BASE COURSE RESILIENT MODULUS FOR THE MECHANISTIC-EMPIRICAL PAVEMENT DESIGN GUIDE

FINAL REPORT

Dr. Dennis R. Hiltunen, P.E.
Principal Investigator

Dr. Reynaldo Roque, P.E.
Faculty Co-Investigator

Dr. Aditya Ayithi
Graduate Student Researcher

DEPARTMENT OF CIVIL & COASTAL ENGINEERING
UNIVERSITY OF FLORIDA

November 2011

UF | UNIVERSITY *of* FLORIDA

DISCLAIMER

The opinions, findings, and conclusions expressed in this publication are those of the authors and not necessarily those of the State of Florida Department of Transportation or the U.S. Department of Transportation.

Prepared in cooperation with the State of Florida Department of Transportation and the U.S. Department of Transportation.

METRIC CONVERSION TABLE

SYMBOL (US)		MULTIPLY BY	TO FIND	SYMBOL (SI)
LENGTH				
in	inches	25.4	millimeters	**mm**
ft	feet	0.305	meters	**m**
yd	yards	0.914	meters	**m**
mi	miles	1.61	kilometers	**km**
AREA				
in^2	squareinches	645.2	square millimeters	**mm^2**
ft^2	squarefeet	0.093	square meters	**m^2**
yd^2	square yard	0.836	square meters	**m^2**
ac	acres	0.405	hectares	**ha**
mi^2	square miles	2.59	square kilometers	**km^2**
VOLUME				
fl oz	fluid ounces	29.57	milliliters	**mL**
gal	gallons	3.785	liters	**L**
ft^3	cubic feet	0.028	cubic meters	**m^3**
yd^3	cubic yards	0.765	cubic meters	**m^3**
MASS				
oz	ounces	28.35	grams	**g**
lb	pounds	0.454	kilograms	**kg**
T	short tons (2000 lb)	0.907	megagrams (or "metric ton")	**Mg (or "t")**
TEMPERATURE (exact degrees)				
°F	Fahrenheit	5 (F-32)/9 or (F-32)/1.8	Celsius	**°C**
FORCE and PRESSURE or STRESS				
lbf	poundforce	4.45	newtons	**N**
lbf/in^2	poundforce per square inch	6.89	kilopascals	**kPa**

SYMBOL (SI)		MULTIPLY BY	TO FIND	SYMBOL (US)
LENGTH				
mm	millimeters	0.039	inches	**in**
m	meters	3.28	feet	**ft**
m	meters	1.09	yards	**yd**
km	kilometers	0.621	miles	**mi**
AREA				
mm^2	square millimeters	0.0016	square inches	**in^2**
m^2	square meters	10.764	square feet	**ft^2**
m^2	square meters	1.195	square yards	**yd^2**
ha	hectares	2.47	acres	**ac**
km^2	square kilometers	0.386	square miles	**mi^2**
VOLUME				
mL	milliliters	0.034	fluid ounces	**fl oz**
L	liters	0.264	gallons	**gal**
m^3	cubic meters	35.314	cubic feet	**ft^3**
m^3	cubic meters	1.307	cubic yards	**yd^3**
MASS				
g	grams	0.035	ounces	**oz**
kg	kilograms	2.202	pounds	**lb**
Mg (or "t")	megagrams (or "metric ton")	1.103	short tons (2000 lb)	**T**
TEMPERATURE (exact degrees)				
°C	Celsius	1.8C+32	Fahrenheit	**°F**
FORCE and PRESSURE or STRESS				
N	newtons	0.225	poundforce	**lbf**
kPa	kilopascals	0.145	poundforce per square inch	**lbf/in^2**

1. Report No.	2. Government Accession No.	3. Recipient's Catalog No.

4. Title and Subtitle	5. Report Date
Base Course Resilient Modulus for the Mechanistic-Empirical Pavement Design Guide	November 2011
	6. Performing Organization Code

7. Author(s)	8. Performing Organization Report No.
Aditya Ayithi, Dennis R. Hiltunen, and Reynaldo Roque	

9. Performing Organization Name and Address	10. Work Unit No. (TRAIS)
Department of Civil and Coastal Engineering University of Florida 365 Weil Hall, P.O. Box 116580 Gainesville, FL 32611-6580	11. Contract or Grant No. BDK-75-977-10

12. Sponsoring Agency Name and Address	13. Type of Report and Period Covered
Florida Department of Transportation 605 Suwannee Street, MS 30 Tallahassee, FL 32399	Final Report June 2008-November 2011
	14. Sponsoring Agency Code

15. Supplementary Notes

16. Abstract

The Mechanistic-Empirical Pavement Design Guidelines (MEPDG) recommend use of modulus in lieu of structural number for base layer thickness design. Modulus is nonlinear with respect to effective confinement stress, loading strain, and moisture. For design purposes, a single effective modulus of a base layer is desirable, and this modulus should be able to approximately account for the nonlinearities. However, the MEPDG does not describe a procedure for determining this single modulus value. This research focused on laboratory characterization of base modulus nonlinearity, developing a nonlinear response model using laboratory data for nonlinear pavement analysis, and a methodology to determine a single effective modulus for a base layer via the nonlinear response model. Resonant column tests were conducted on two base materials used in Florida to characterize shear modulus (G) nonlinearity under different confinements and moisture contents. The suction effect increases G in the strain range of 10^{-5}% to 10^{-1}%, with very significant increases at strain levels below 10^{-3}%. Using laboratory nonlinear modulus data, a nonlinear response model was developed via the Plaxis finite element methodology. The model is an effective means for assessing the effects of unbound material nonlinearity on the response of pavements. A representative modulus can be determined by a backcalculation procedure in which surface deflections from a nonlinear analysis are matched via an equivalent linear analysis. The single effective modulus varies over a range of conditions, including the moisture content of the base, pavement layer thicknesses, and the modulus of the subgrade. There is a significant effect of moisture on the effective modulus of limerock base materials used in Florida and the modulus/moisture relationship employed in the MEPDG underpredicts this increase. An equivalent linear analysis using effective moduli for both an unbound base and the subgrade can predict the structural response of an asphalt surface layer in a flexible pavement. It should be possible to utilize these structural response predictions in the assessment of cracking performance of the surface layer. However, caution is warranted in predicting the structural response of the unbound base and subgrade layers using an equivalent linear analysis. Use of an effective modulus for a nonlinear base layer appears reasonable for very thick pavement structures, but appears to underpredict vertical strain at the top of subgrade as the nonlinearity increases. Use of effective moduli for both a nonlinear base and subgrade appears to underpredict top of subgrade vertical strain even for very thick pavements.

17. Key Word	18. Distribution Statement
Base course, finite element modeling, mechanistic-empirical pavement design, resilient modulus, resonant column testing, small-strain modulus, suction, unsaturated soil mechanics	No Restrictions

19. Security Classif. (of this report)	20. Security Classif. (of this page)	21. No. of Pages	22. Price
Unclassified	Unclassified	259 Pages	

EXECUTIVE SUMMARY

The Mechanistic-Empirical Pavement Design Guidelines (MEPDG) recommend use of material modulus in lieu of structural number for pavement base layer thickness design. Modulus is nonlinear with respect to effective confinement stress, loading strain, and moisture (suction), and modulus nonlinearity should be considered for an efficient base layer design and analysis. For typical design purposes, a single effective modulus value of a base layer is desirable, and this modulus value should be able to approximately account for the nonlinearities of the whole base layer. However, the MEPDG does not describe a procedure for determining this single modulus value. This research study focused on laboratory characterization of base modulus nonlinearity, developing a nonlinear response model using laboratory data for nonlinear pavement analysis, and a methodology to determine a single effective modulus for a base layer via the nonlinear response model.

First, fixed-free and free-free resonant column tests were conducted on two base materials used in the State of Florida to characterize shear modulus (G) nonlinearity in the strain range of 10^{-5}% to 10^{-1}%, including small-level strains, under different loading confinements and moisture contents. The suction effect on nonlinear modulus due to drying was evaluated, and it was found that unsaturated modulus is linear at strains lower than 10^{-5}% and nonlinear thereafter. Compared to dry materials, the presence of moisture in unsaturated material makes it more nonlinear with respect to strain. The suction effect increases G in the strain range of 10^{-5}% to 10^{-1}%, with very significant increases at strain levels below 10^{-3}%. At any given moisture content, additional confinement due to suction does not decrease with an increase in strain. Empirical equations were developed to calculate very small-strain modulus (G_{max}) of dry material. A procedure to calculate an approximate G value at known moisture content, confinement, and strain magnitude was developed.

5

Second, using laboratory nonlinear modulus characterization data, a nonlinear response model was developed via the Plaxis-HSsmall finite element methodology. It was demonstrated that the model is an effective means for assessing the effects of unbound material nonlinearity on the structural response of pavements. Practical pavement design utilizing the MEPDG will require input of a single modulus value to represent unbound base and subgrade materials. A representative modulus can be determined by a backcalculation procedure in which pavement surface deflections from a nonlinear analysis are matched via an equivalent linear analysis. The nonlinearity of unbound base materials is significant and the single effective modulus varies over a range of conditions, including the moisture content of the base, pavement layer thicknesses, and the modulus of the subgrade. There is a significant effect of moisture on the effective modulus of limerock base materials used in Florida. The modulus/moisture relationship employed in the MEPDG underpredicts the significant increase in modulus of Florida limerock base materials when dried below OMC.Use of the MEPDG model will be conservative. An equivalent linear analysis using effective moduli for both an unbound base and the subgrade and based upon matching surface deflections can predict the structural response of an asphalt surface layer in a flexible pavement. It should be possible to utilize these structural response predictions in the assessment of cracking performance of the surface layer. However, caution is warranted in predicting the structural response of the unbound base and subgrade layers using an equivalent linear analysis. Use of an effective modulus for a nonlinear base layer appears reasonable for very thick pavement structures, but appears to underpredict vertical strain at the top of subgrade as the nonlinearity increases due to decreasing thickness, decreasing moisture content, or softening of the subgrade. Use of effective moduli for both a nonlinear base and subgrade appears to underpredict top of subgrade vertical strain even for very thick pavements.

TABLE OF CONTENTS

1.1 Problem Statement

Mechanistic-Empirical Pavement Design Guidelines (MEPDG (2004)) for flexible

pavement structures recommend use of modulus in place of layer coefficient for unbound

aggregate base layer thickness design. Resilient modulus (M_R) and Poisson's ratio (v) are the two

primary input parameters required for thickness design. M_R represents modulus of a material

subjected to repeated traffic loading and can be determined in the laboratory via a standard

testing protocol (AASHTO T307).

Soil is a nonlinear material and its modulus nonlinearity is dependent primarily on

effective confinement stress, loading strain, moisture content (suction) and some other

parameters. MEPDG proposes three different levels of M_R input for pavement design. Level 1

M_R input takes material modulus nonlinearity into account, whereas Level 2 and Level 3 M_R

input assume material is elastic and assigns a single effective elastic modulus value for the whole

layer. However, the nonlinear design analysis response model based on Level 1 nonlinear M_R

input has not been calibrated for practical applications. Thus, it seems that a single effective

elastic modulus approach using either Level 2 or Level 3 M_R input would be most commonly

used in the near future. Therefore, determining this single elastic modulus value is critical for

pavement response model analysis.

However, since soil is a nonlinear material, a single elastic modulus approach should not

discard the importance of modulus nonlinearity. Hence, the single elastic modulus value should

be able to reflect the nonlinear behavior of a base layer under real loading conditions. In parallel,

if we can build a database of either nonlinear modulus parameters, or single effective elastic

modulus values that can also reflect nonlinear behavior approximately, for different types of base

materials, it may not be required to conduct expensive M_R laboratory testing at the initial design stage and the whole design process could be more economical.

MEPDG is primarily based on M_R and its determination via the AASHTO protocol. By following the AASHTO T307 testing procedure, material modulus can be characterized from intermediate (10^{-3}%) to larger strains (10^{-1}%) due to the range of deviatoric stresses applied in this test procedure and the external measurement of loads and deformations. Recent research studies in geotechnical engineering have revealed that it is also necessary to consider modulus nonlinearity at small-level strains ($\leq 10^{-3}$%) along with nonlinearity at intermediate to larger strains, to predetermine accurate pavement responses. Since moduli values at small strain levels cannot be determined via the AASHTO protocol due to procedural limitations, small-strain modulus nonlinearity cannot be characterized. Hence, it is plausible that accurate pavement responses cannot be calculated using moduli values obtained via the AASHTO testing protocol. Therefore, it is desirable to consider an alternative procedure that can characterize material modulus nonlinearity at small-level strains along with intermediate to larger strains.

Moreover, the AASHTO T307 provides a set of M_R values corresponding to different stress levels and strain magnitudes, but not a single elastic modulus value that is required for MEPDG Level 2 and Level 3 material parameter inputs. No methodology is defined either in MEPDG or in the literature about how to determine this single elastic modulus value. Therefore, there is a requirement to develop a proper methodology that can also approximately reflect the modulus nonlinearity.

Suction in partially saturated soils provides additional confinement, which in turn increases soil modulus. Research studies related to the suction effect on soil modulus at different strain levels have revealed that suction can increase modulus at small-level strains very significantly

11

compared to intermediate and large strains. Since it is important to consider modulus nonlinearity at small-level strain, it is important to also consider the suction effect on modulus at small-level strains. The MEPDG incorporates moisture effect (which includes suction effect also) on modulus via the Enhanced Integrated Climatic Model (EICM). The modulus/moisture model in the EICM is developed based on an M_R database for different types of soils. Since these M_R values have been determined via the AASHTO protocol, which can measure modulus at intermediate to large strains only, the EICM does not consider the suction effect at small-level strains. Therefore, it is of interest to develop a pavement response model that can also consider the suction effect at different strain levels including small-level strains.

In view of the above issues regarding testing protocol adequacies, moisture (suction effect) model inabilities, and no properly defined methodology to calculate single effective design modulus for a base layer, there is a necessity to develop: 1) a laboratory testing method for modulus determination that can more accurately characterize modulus nonlinearity at different strain levels including small-level strains, 2) a design methodology to determine a single effective modulus value for MEPDG Level 2 and Level 3 modulus inputs that can also reflect modulus nonlinearity approximately, and 3) a pavement response model that can incorporate the suction effect on modulus at small-level strains, along with intermediate and larger strains.

1.2 Objectives

The primary objective of this research work is to develop a design methodology for characterizing base layer design modulus for use in MEPDG that can address the issues discussed above. More detailed objectives include:

- Conduct a laboratory testing program on selected base materials following a suitable testing methodology that can effectively account for the effects of confinement, strain magnitude, and moisture on nonlinear modulus, including small-strain nonlinear modulus, and can characterize its nonlinear behavior.

12

- Evaluate and quantify the suction effect on nonlinear small-strain modulus.

- Develop an appropriate pavement response model that can utilize the laboratory testing results and account for the above discussed modulus nonlinearity under performance conditions.

- Based on deflections, stresses, and strain responses obtained from a pavement response model, develop a practical design methodology to calculate single effective modulus for whole base layer that can approximate known nonlinearities for use as MEPDG Level 2 and Level 3 material inputs.

- Demonstrate by various techniques that the overall approach, as well as the laboratory test results and pavement response model results, are credible and appear to agree with other known properties and behavior.

1.3 Scope of Research

In the State of Florida, limerock aggregates are commonly used for base layer construction. One limerock material and one non-limerock material were chosen for our testing: 1) Newberry limerock and 2) Georgia granite graded aggregate base. Material collection and specimen preparation were performed following standard procedures.

The fixed-free resonant column torsional shear (fixed-free RC) test method and the free-free resonant column (FFRC) test method were selected for the material testing program. Fixed-free RC tests can determine shear modulus (G) of gravel-type soils at different strain magnitudes including small-level strains. In fixed-free RC testing, compacted specimens can be subjected to required stress confinement. Suction effect can be evaluated by conducting tests on specimens dried to different moisture contents. Therefore, via fixed-free RC testing, modulus nonlinearity of gravelly base soils can be characterized with respect to 1) effective stress confinement, 2) loading strain magnitude including small-level strains, and 3) moisture or suction effect. These tests were conducted on standard size modified Proctor compacted specimens. The FFRC test can determine shear modulus at very small-level strain (G_{max}) at different moisture contents

under no confinement to evaluate the suction effect on G_{max}. Credibility of these testing results is established by comparing them with literature data.

A nonlinear pavement response model was developed via Plaxis-HSsmall, a nonlinear finite element model system that can utilize laboratory testing results. Using our laboratory test results, the response model can characterize material modulus nonlinearity properly with respect to stress confinement, strain magnitude including small-level strains, and moisture or suction effect. Flexible pavement structures with different layer thicknesses or cross-sections were analyzed under performance loading conditions using the nonlinear response model.

A methodology to determine single effective elastic design modulus value for whole base layer that can be utilized as MEPDG Level 2 and Level 3 material parameter input was developed. The single effective base modulus determination methodology was developed such that various pavement responses such as surface deflections, stresses, and strains obtained by nonlinear base modulus analysis, and equivalent linear single elastic base modulus analysis are approximately the same. The effect of base layer nonlinearity on pavement performance is evaluated by comparing the responses obtained from nonlinear base modulus analysis and equivalent linear single base modulus analysis. The effect of subgrade nonlinearity on pavement performance is also briefly evaluated for limited cases.

1.4 Organization of Report

An overview of the remaining chapters of this report is presented here. Chapter 2 gives an overview of resilient modulus (M_R), the M_R testing method and its adequacies, the importance of modulus characterization including small-strain modulus nonlinearity in soils, possible laboratory testing methods, and modulus nonlinearity influencing factors and its importance in geotechnical structural designs. Different models proposed by various researchers to calculate very small-strain modulus and modulus at different strain levels are discussed. Suction effect on

14

small-strain modulus and importance of considering suction effect in determining design modulus is also discussed. Recent research efforts about importance of considering small-strain modulus nonlinearity for geotechnical analysis and design are also discussed.

Different types of materials selected for testing and their properties are presented in Chapter 3. A detailed explanation about specimen preparation methods, for both wet and dry materials, is also given.

In Chapter 4, fixed-free RC and free-free RC test methods used in this research work are presented. Detailed explanations about equipment development background and types of parameters that can be measured with these devices are discussed. Equipment setup, calibration, verification, and limitations are also explained.

Chapter 5 presents testing results obtained from both fixed-free RC and free-free RC tests. Specimen testing conditions including moisture contents, void ratios, and pressure confinements are mentioned. An empirical equation is proposed to calculate very small-strain modulus of dry soils. Suction effect on small-strain modulus is evaluated and an indirect approach to calculate additional confinement due to suction is explained. Based on these testing results, a method to determine approximate modulus at any known moisture content, confinement, and strain magnitude is explained.

Chapter 6 discuses the Plaxis-HSsmall model and required model input parameters. Development of a nonlinear response model for base layer analysis via HSsmall model is discussed, and procedures to obtain input parameters from laboratory testing results are explained.

Chapter 7 presents the base layer nonlinear analysis results and a methodology to determine single effective design modulus for base layer thickness design. Different pavement

cross-sections are analyzed using the HSsmall nonlinear response model. Single effective elastic base moduli values for different pavement structures at different base moisture contents and subgrade moduli are reported and analyzed. The effect of base nonlinearity on pavement response is evaluated.

The potential importance of subgrade nonlinearity in pavement design and analysis is discussed in Chapter 8. A methodology to determine equivalent single elastic modulus for both base and subgrade layers is explained, and the effect of subgrade nonlinearity on pavement response is analyzed briefly for a limited number of structures.

Based on the results presented in Chapters 5, 7 and 8, the primary findings are summarized in Chapter 9, and conclusions and recommendations are presented.

Further test result details are presented in the appendices. Fixed-free RC test results on dry specimens at different void ratios are given in Appendix A. A nonlinear equivalent single effective base moduli database is given in Appendix B. Comparison plots of surface deflection, stress, and strain responses obtained from nonlinear base analysis and equivalent linear base analysis, for different pavement structures is presented in Appendix C. Comparison plots of pavement responses obtained from base and subgrade nonlinearity analysis and equivalent linear analysis are presented in Appendix D.

CHAPTER 2
LITERATURE REVIEW

The primary goal of this research work is to determine the effective base modulus for practical design purposes, while considering modulus nonlinearity. It is proposed to achieve this through laboratory testing and nonlinear modeling. Hence, this literature review concentrates on soil modulus and its influencing factors including suction, modulus at different strain levels including small-level strains and its determination in laboratory, various analytical models developed to determine modulus at different strain levels, the importance of modulus nonlinearity in geotechnical design calculations, and pavement response models.

2.1 Modulus of Particulate Material

Modulus or stiffness is the relationship between change of stress and change of strain, is defined by ratio of stress over strain, and represents resistance to deformation under loading. Being a particulate material, soil modulus is nonlinear and primarily dependent on effective confining stress (σ_c'), strain magnitude (ε), and void ratio (e) (Hardin and Drnevich, 1972; Yasuda and Mastumoto, 1993). In unsaturated soils, modulus is also dependent on moisture content and its suction effect (Wu et al., 1984; Qian et al., 1993; and Cho and Santamarina, 2001).

In a pavement base layer, strain magnitudes are not constant throughout the layer, but are highest near or under the wheel load and diminish to zero moving away from wheel load. Soil modulus is maximum (G_{max} or E_{max}) at strain levels lower than 10^{-4}%, and decreases nonlinearly with an increase in strain (Figure 2-1), generally in an S-shaped pattern. As shown in Figure 2-1, Atkinson and Sallfors (1981) presented a typical modulus reduction curve for soils with an increase in strain, along with different strain levels involved in various types of geotechnical structures. Modulus nonlinearity for different strain levels that can be observed under real

17

loading conditions should be considered for accurate geotechnical design calculations (Atkinson, 1991; Elhakim and Mayne, 2008; and Lehane et al., 2008).
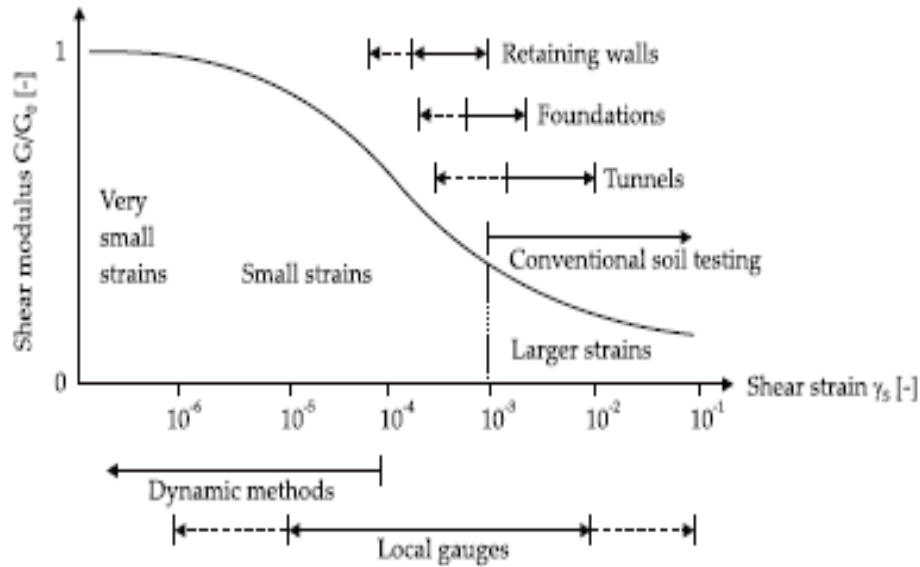

Figure 2-1. Characteristic modulus-strain behavior of soils with typical strain ranges for laboratory tests and structures (from Atkinson and Sallfors, 1991).

2.2 Resilient Modulus

According to MEPDG, resilient modulus (M_R) and Poisson's ratio (ν) are the two basic material parameter inputs required for pavement layer thickness design of a base layer. Behavior of a base or soil subjected to repeated traffic loading in a pavement layer is characterized by M_R. M_R is an elastic modulus based on recoverable strain under repeated loads and is defined as:

$$M_R = \frac{\sigma_d}{\varepsilon_r} \tag{2-1}$$

where σ_d=deviatoric stress and ε_r=recoverable axial strain.

Since its inception in AASHTO 1986 guidelines, much research has been well documented regarding M_R. M_R of soils can be determined in the laboratory via standard testing procedures (e.g., AASHTO T307). For design calculations, M_R of a soil for any given stress condition (θ) can be calculated using the basic constitutive equation:

18

$$M_R = k_1 \times \theta^{k_2} \tag{2-2}$$

in which parameters k_1 and k_2 are material dependent and their values are determined from laboratory testing data. In the standard M_R testing procedure, a specimen is subjected to different predetermined combinations of confinement stress and deviatoric stress and the resulting strain magnitudes are measured using strain gauges placed outside the triaxial testing chamber. Strain magnitudes that can be measured in AASHTO T307 testing are typically in the range of $10^{-3}\%$ and higher.

MEPDG Level 2 and Level 3 design procedures for unbound aggregate base layer thickness design require a single modulus value for the whole layer, which can be obtained from M_R laboratory testing. The laboratory testing produces a set of moduli data corresponding to specific stress and strain levels, but not a single modulus value, and MEPDG does not define a procedure to determine a single modulus value required for design.

To consider modulus nonlinearity with respect to stress and strain in pavement design one first should be able to measure modulus for a wide range of strain levels at any given confinement stress. One of the main challenges in measuring the modulus of soil at small-level strains is choosing the right equipment and testing method for accurate strain measurements Conventional laboratory testing equipments can measure modulus at strains as small as $10^{-3}\%$ with reasonable accuracy, where the strain gauges are placed outside the testing chamber. Moduli corresponding to a strain range of $10^{-5}\%$ to $10^{-3}\%$ can be reliably measured by using local strain gauges attached directly to the sample (Jardine et al., 1984; Atkinson, 1991). However, these local strain gauges cannot measure very small strains (i.e., $\leq 10^{-5}\%$), which correspond to the fundamental material property G_{max}. The AASHTO T307 testing protocol

requires attachment of the strain gauges outside of the testing chamber. Thus, the accuracy of strain measurements less than $10^{-3}\%$ becomes questionable in a standard M_R test.

2.3 Modulus Characterization for Complete Range of Strains

Past research efforts have shown that nonlinearity of soil for a wide range of strains including small-level strains needs to be considered for accurate settlement/deformation predictions in soils (Jardine et al., 1984; Atkinson, 1991; Elhakim and Mayne, 2008; and Lehane et al., 2008). It is now well acknowledged that strain/deformation predictions for geotechnical structures (e.g., footings, retaining walls, braced excavations) are often not at an acceptable level of accuracy, and one of the primary reasons for this inaccuracy is choosing a single linear elastic modulus value to represent the soil behavior. A numbers of analytical models have been developed to calculate G at different strain levels, using G_{max} as the benchmark, and these are discussed in following sections.

2.3.1 Small-Strain Modulus (G_{max} or E_{max})

Over the past several decades, a large number of research investigations have been conducted and documented on G_{max} of sands, silts, and clay soils and its influencing factors. Hardin and Richart (1963) measured longitudinal and shear wave velocities (V_s) of Ottawa sand, crushed quartz sand and crushed quartz silt at small-strain levels using free-free and fixed-free resonant column methods. They found that V_s for sands varied with approximately the ¼ power of confining pressure. At very small-strain, V_s of sands is a function of mean effective confining pressure (σ_c) and void ratio (e), and can be expressed as:

$$V_s = (170 - 78.2 \times e)\sigma_c^{1/4} \text{, for } \sigma_c < 2000 \text{ psf} \tag{2-3}$$

$$V_s = (119 - 56.0 \times e)\sigma_c^{3/10} \text{, for } \sigma_c > 2000 \text{ psf} \tag{2-4}$$

where the units of V_s are ft/sec (fps).

Hardin and Drnevich (1972) conducted resonant column tests on different types of soils to analyze the effects of confining pressure, strain amplitude, void ratio, number of loading cycles, degree of saturation, and thixotropy. They found that shear modulus decreases and damping ratio increases very rapidly with increase in strain amplitude. The rate of decrease or increase in G_{max} depends on many parameters and a single relationship between modulus or damping and strain amplitude is not sufficient. For very small strain amplitudes, modulus varies with 0.5 power of effective mean principal stress, but at larger strains modulus depends primarily on strength of soil and the variation is more nearly with 1.0 power. Modulus and damping ratio decreases with increase in void ratio and the effect is accounted by:

$$F(e) = \frac{(2.973 - e)^2}{(1 + e)}$$

(2-5)

where e is void ratio. Shear modulus decreases for cohesive soils and increases for cohesionless soils with increase in number of loading cycles. Degree of saturation has no effect on modulus of cohesionless soils. In cohesive soils, modulus increases rapidly with decrease in degree of saturation.

Hardin and Drnevich (1972) have clearly shown that moduli values for sands are strongly influenced by three main factors: confining pressure, strain magnitude, and void ratio.

Seed et al. (1986) investigated shear moduli and damping characteristics of soils via cyclic undrained triaxial tests and derived an empirical equation to determine G_{max} as:

$$G_{max} = 1000 \, (K_2)_{max} (\sigma'_c)^{n_G}$$

(2-6)

They found that values of $(K_2)_{max}$ for dense well-graded gravels are likely to range from 80-180, compared with the range of about 55-80 for sands, and gradation does not have much influence on shear moduli of gravels. They developed a normalized shear modulus versus shear strain curve for gravels similar to the curve for sands, and the curve for gravels is slightly flatter

compared to sand (Figure 2-2). Based on in situ shear wave velocity measurements, shear moduli

of gravelly soils are between 1.25 and 2.5 times greater than that of sands.
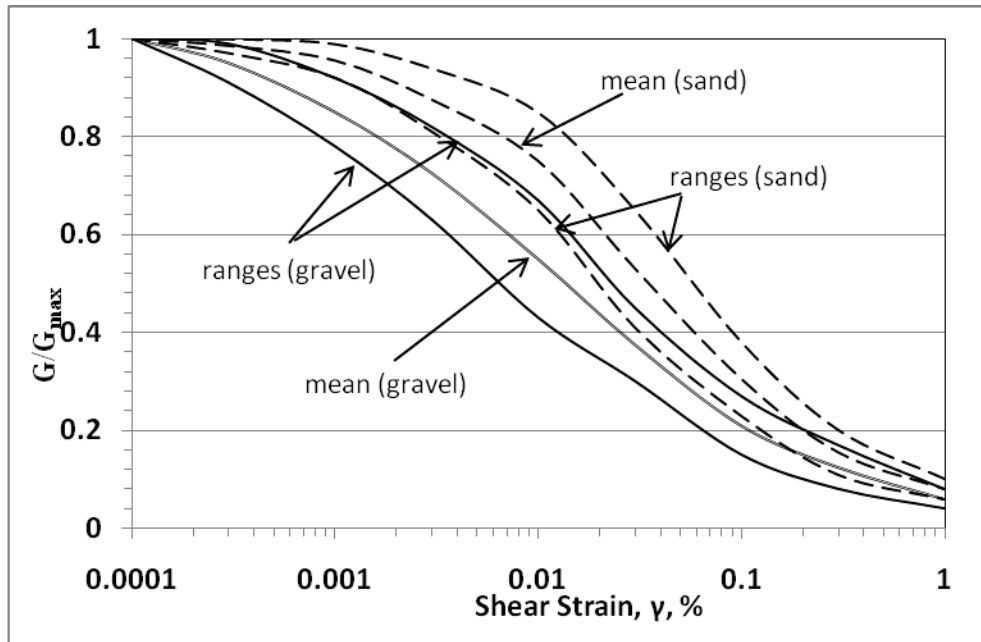
Figure 2-2. G/G_{max} versus log γ curves of gravelly sandy soils reported by Seed et al. (1986).

Hardin and Richart (1963) proposed the following empirical formula to calculate G_{max} for

known void ratio (e) and confinement (σ_c):

$$G_{max} = A_G F(e)(\sigma_c')^{n_G} \tag{2-7}$$

where A_G and n_G are material constants, $F(e)$ is function of void ratio, and σ_c' is effective mean

principal stress.

2.3.2 Shear Modulus (G) at Different Strain Levels

Kokusho (1987) pointed out that as the grain size increases the rate of reduction in strain-

dependent modulus becomes high at a smaller strain level.

Yasuda and Matsumoto (1993) conducted cyclic torsional simple shear tests and cyclic

triaxial tests to investigate the dynamic deformation characteristics of sand and rock fill

materials. They found that G can be expressed as a function of shear strain, void ratio, and

confining stress. They also found that the absolute value of G for the rock fill materials is substantially higher than sand under the same relative density. The alteration of G of rock fill material occurred at smaller strains than for sands.

Yasuda et al. (1996) conducted large-scale cyclic triaxial tests on undisturbed and reconstituted specimens obtained from the river bed gravel foundation of an embankment dam to determine G in the strain range of 10^{-6} to 10^{-3}. Undisturbed specimens of size 300 mm in diameter and 550 mm in height were sampled by using a freezing method. From their testing investigation, they found that G_{max} of undisturbed specimens was 1.5 to 2 times greater than reconstituted specimens. They reported that this difference was due to cementation and fabric produced by the effects of the geological time of sedimentation in undisturbed specimens. The G/G_{max} versus γ relationship was marked by almost identical declining tendencies in both undisturbed and reconstituted specimens (Figure 2-3), thus the G versus γ relationship for undisturbed specimens can be determined from in situ G_{max}.

Lin et al. (2000) investigated shear modulus (G) and damping ratio (D) of gravelly cobble deposits. They conducted resonant column and cyclic triaxial tests to obtain G for a strain range of 10^{-4} to 1%. They observed a decrease of G with increase in γ for $\gamma \leq 0.1\%$, an increase in G thereafter (Figures 2-4 and 2-5), and attributed this behavior to a gap gradation of the soils tested. Gravel cobble deposits contain 80% gravel and the remaining is filling material. When they artificially increased the proportion of filling material, G decreased with an increase in strain as previously mentioned. G increases as the maximum particle size (D_{max}) increases and also with an increase in confining pressure (Figure 2-6). There is no significant effect of either D_{max} or σ_c on the G/G_{max} versus γ relationship. Based on their testing data, they developed an empirical equation to calculate G_{max} of a deposit at different confining pressures as shown in Figure 2-7.
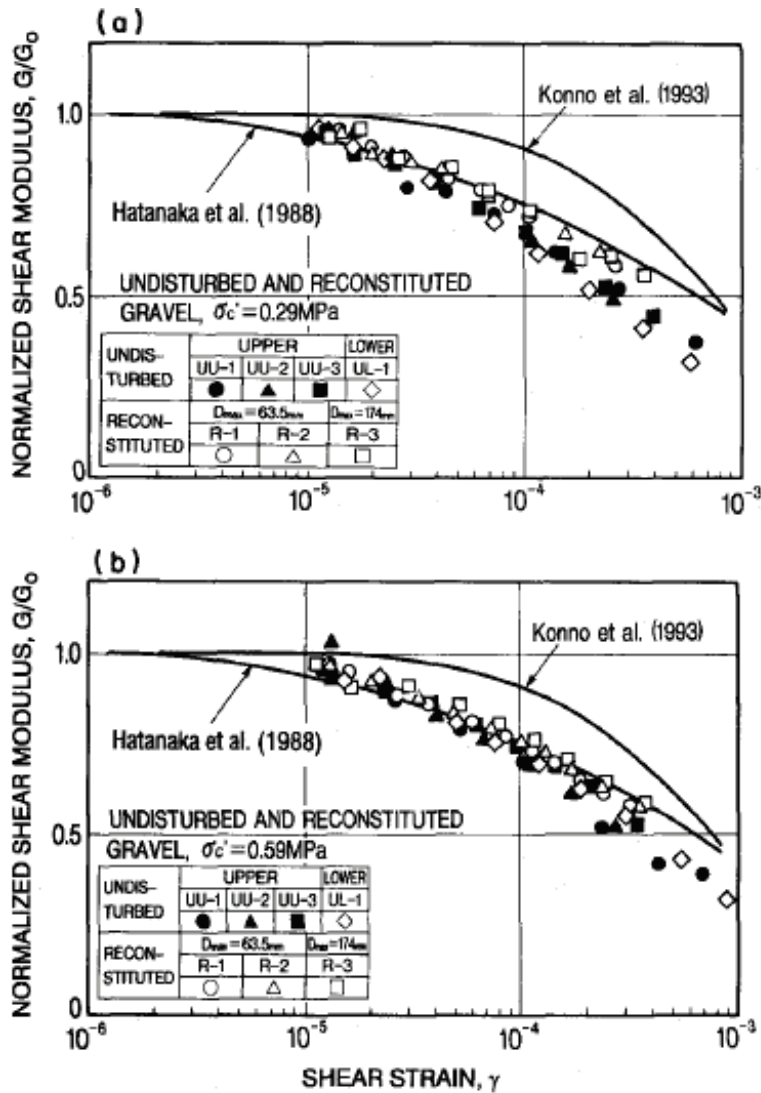
Figure 2-3. G/G$_{max}$ versus log γ curves of undisturbed and reconstituted riverbed gravel for: (a) σ$_c$=0.29 MPa and (b) σ$_c$=0.59 MPa (from Yasuda et al., 1996).

Menq (2003) conducted free-free resonant column tests on sandy and gravelly soils and measured G in the strain range of 10^{-5} to 10^{-1}%. He observed G$_{max}$ at strains less than 10^{-4}% for gravels and at strains less than 10^{-3}% for sands. Normalized modulus versus strain curves for gravels are flatter than for sand and follow the same trend as reported by Seed et al. (1986) (Figure 2-8).

24
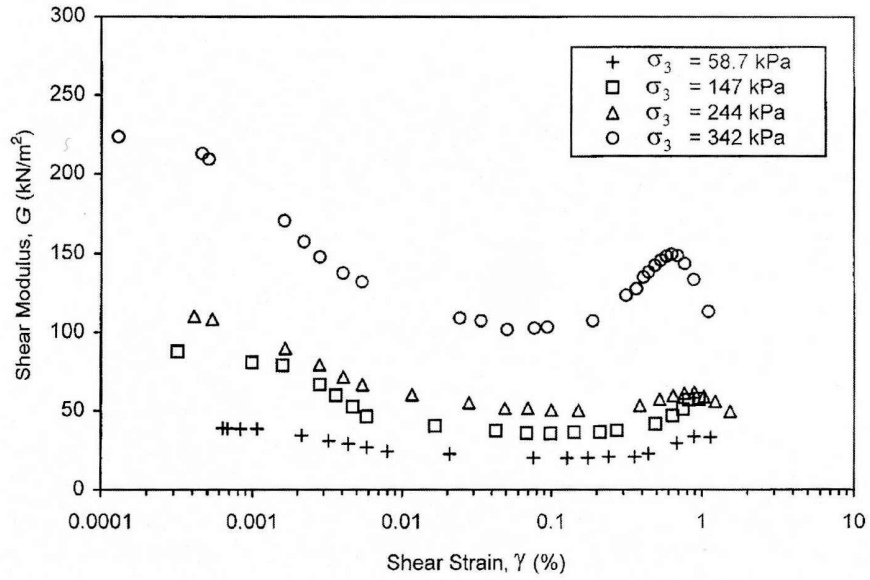
Figure 2-4. Effect of σ_3 on the G-γ relationship (d_{max} = 1.27 cm) (from Lin et al., 2000).
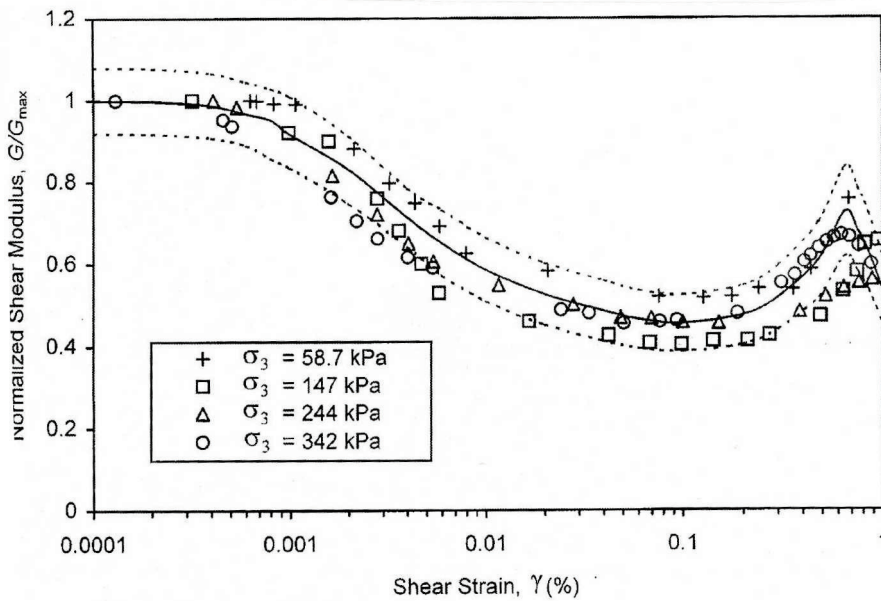
Figure 2-5. Variation of normalized shear modulus with shear strain (d_{max}= 1.27 cm) (from Lin et al., 2000).

25
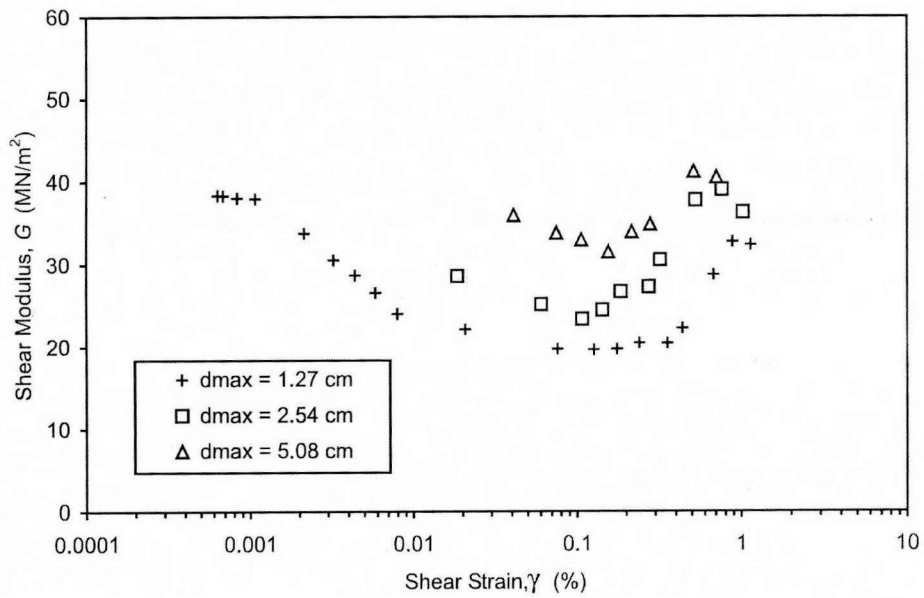
Figure 2-6. G-γ relationship (σ_3 = 58.7 kN/m^2) (from Lin et al., 2000).
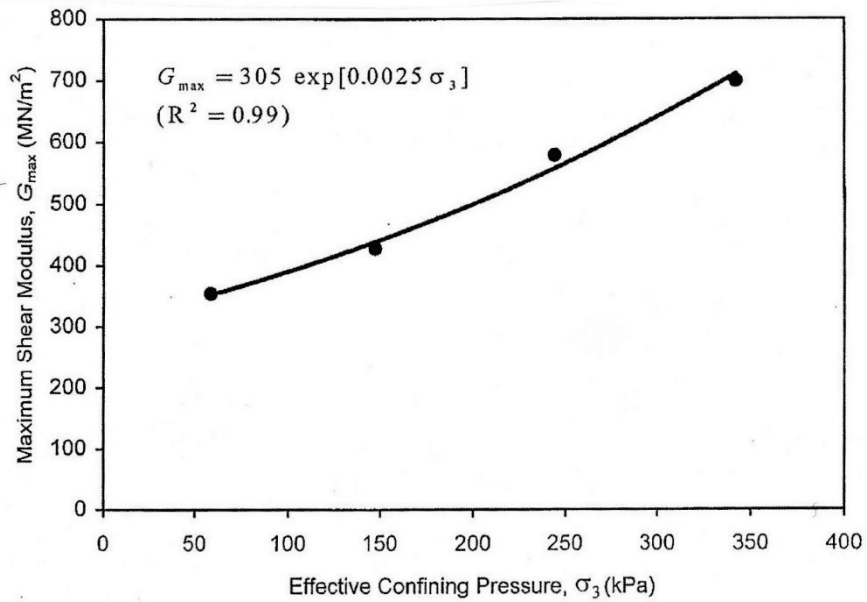
Figure 2-7. Variation of G$_{max}$ of the field deposit with σ_3 (from Lin et al., 2000).
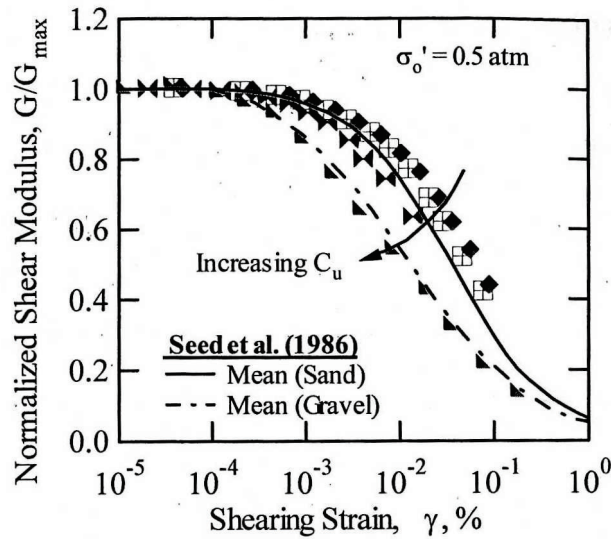
Figure 2-8. G/G_{max} – log γ relationship for gravelly soils (from Menq, 2003).

Gravelly soils are commonly used in base layer construction. Many researchers investigated small-strain modulus of sands, silts and clays, but few efforts have been made to determine moduli of gravel-type soils. Being a large size aggregate, testing on gravel requires 4 inch to 6 inch diameter specimens and large size equipment, which makes testing complicated and is one reason for the lack of literature about moduli of gravels.

2.3.3 Analytical Models to Estimate Shear Modulus at Different Strain Levels

A general hyperbolic form of the stress-strain relation to estimate G at shear strain γ can be written as:

$$\frac{G}{G_{max}} = \frac{1}{1+\frac{\gamma}{\gamma_r}},$$

(2-9)

where $\gamma_r - reference\ strain = \frac{\tau_{max}}{G_{max}}$.

Hardin and Drnevich (1972), based on their testing database for different types of soils, modified the hyperbolic expression as:

$$\frac{G}{G_{max}} = \frac{1}{1+\gamma_h} \qquad\qquad\qquad (2\text{-}10)$$

where $\gamma_h = \frac{\gamma}{\gamma_r}\left[1 + a\,e^{-b\left(\frac{\gamma}{\gamma_r}\right)}\right]$ and a and b are soil constants. They proposed a = -0.5 and b= -

0.16 for clean dry sands, and a comparison between measured and calculated values is shown in

Figure 2-9.
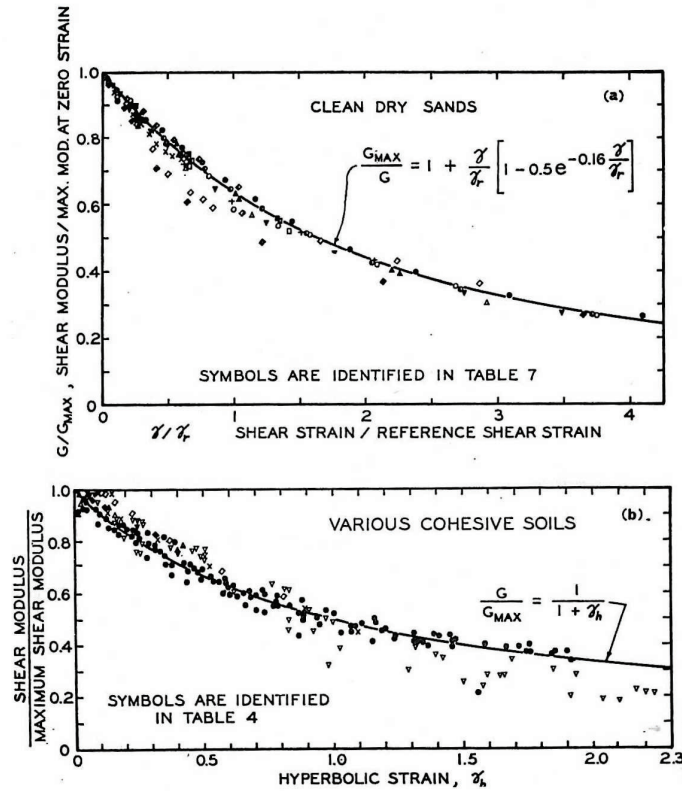
Figure 2-9. Comparison of calculated and measured values of normalized shear modulus (from Hardin and Drnevich, 1972).

Hardin and Kalinski (2005) found that the G/G_{max} versus strain (γ) relationship for gravels

varies with confinement stress level, whereas the G/G_{max} versus γ/γ_r (normalized strain)

relationship is independent of stress level. Thus, it is more convenient to use γ/γ_r instead of γ for

the modulus reduction relationship for gravels, which is similar to sands as proposed by Hardin

and Drnevich (1972).

Rollins et al. (1998) conducted an experimental program on gravels and reviewed results of 15 testing programs from the literature and concluded that the normalized shear modulus curve is dependent on confining pressure and independent of sample disturbance, relative density and gradation. Based on 15 different testing results data, they proposed a best-fit hyperbolic curve model as given below and shown in Figure 2-10.

$$\frac{G}{G_{max}} = \frac{1}{[1.2+16\gamma(1+10^{(-20\gamma)})]}$$

(2-11)
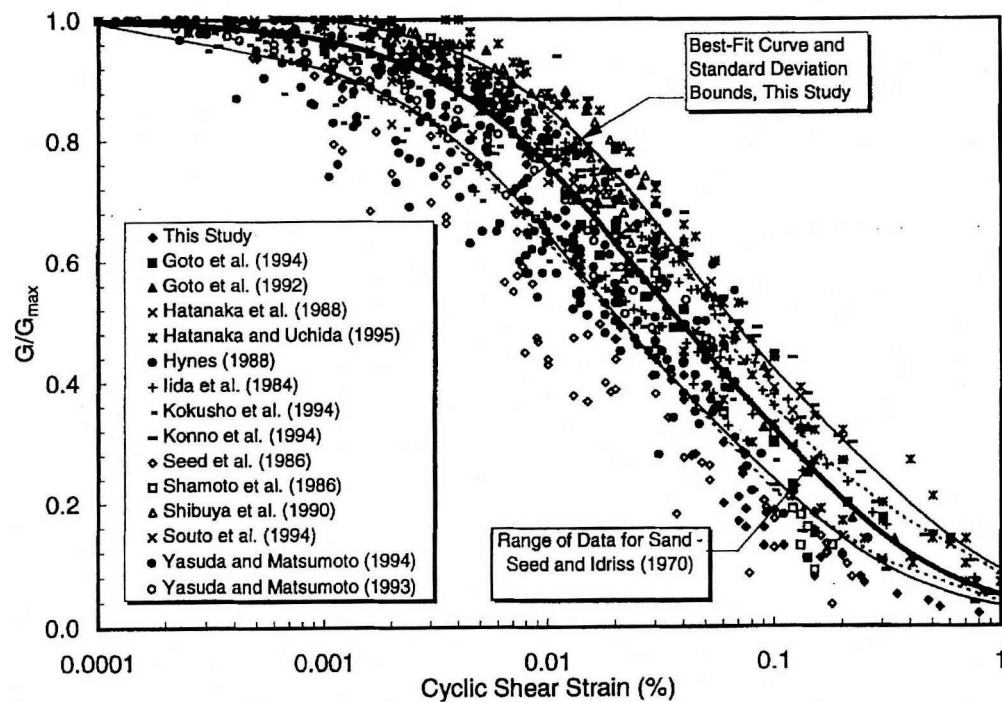
Figure 2-10. Data points defining G/G_{max} versus γ relationship for gravelly soils based on testing by all 15 investigators along with best-fit curve and ± one standard deviation bounds for entire data set (from Rollins et al., 1998).

From their testing results, they observed an increase in G with increase in gravel content (Figure 2-11). They also observed that the G/G_{max} versus γ curve moves from the low end to high end with an increase in confining pressure (Figure 2-12). According to their review, for gravels, at

shear strain lower than 10^{-4}%, shear modulus and damping remain constant and shear modulus is at its maximum, i.e., G_{max}.
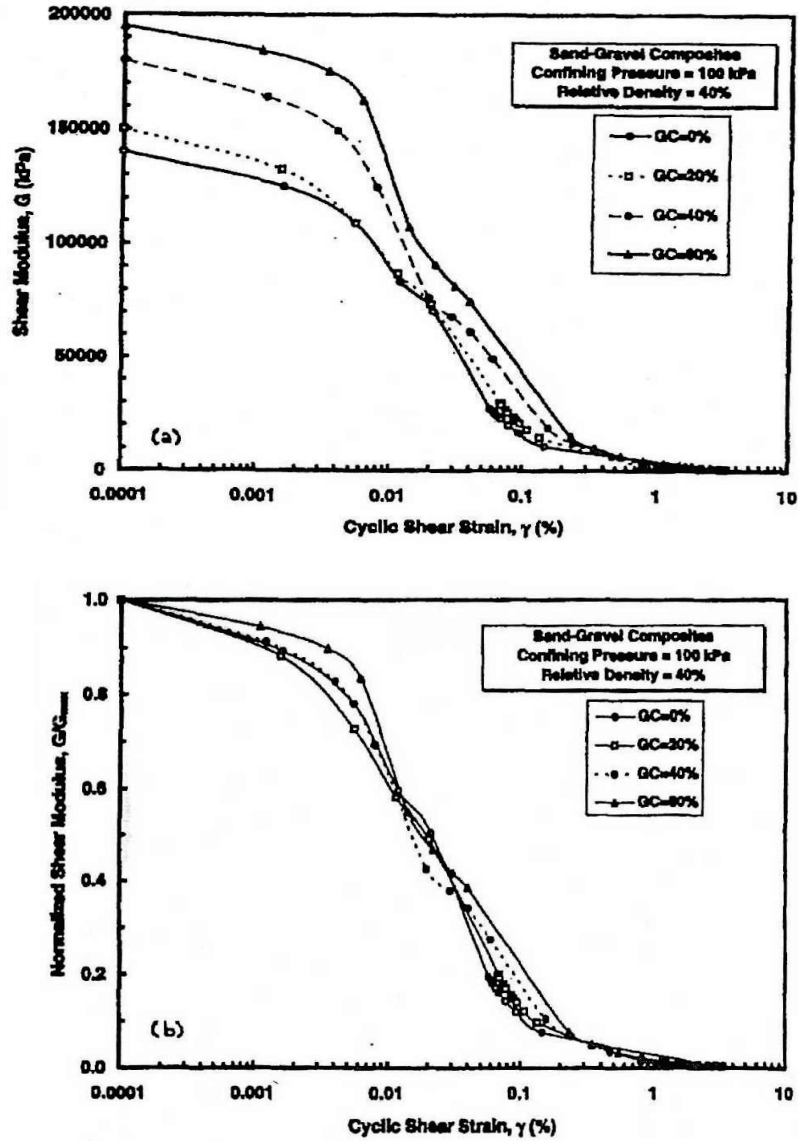
Figure 2-11. (a) G versus γ curves and (b) G/G_{max} versus γ curves determined for test specimens containing 0, 20, 40 and 60% gravel size particles (from Rollins et al., 1998).

Santos and Correia (2001) proposed a modified Hardin-Drnevich hyperbolic relationship to calculate shear modulus for different strain levels:

$$\frac{G}{G_0} = \frac{1}{1 + a \left| \frac{\gamma}{\gamma_{0.7}} \right|}$$

(2-12)

where G_0 = maximum shear modulus, a = 0.385, and $\gamma_{0.7}$ = shear strain at $G = 0.7 \times G_0$. They

recommended that normalization of shear strain (γ) with reference threshold shear strain ($\gamma_{0.7}$)

makes it possible to define almost a unique strain-dependent stiffness degradation curve for sand

and clays. Their proposed stiffness degradation curve with higher and lower limits is shown in

Figure 2-13.
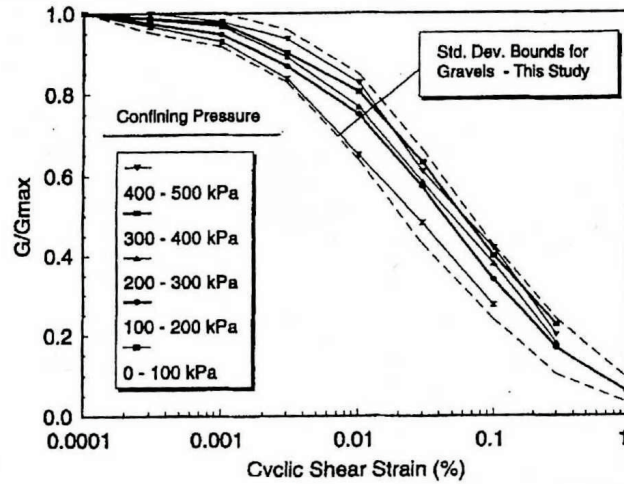
Figure 2-12. Mean curves defining G/G_{max} versus γ relationships for gravelly soils at various
confining pressures along with standard deviation boundaries for reduced data set
(from Rollins et al., 1998).
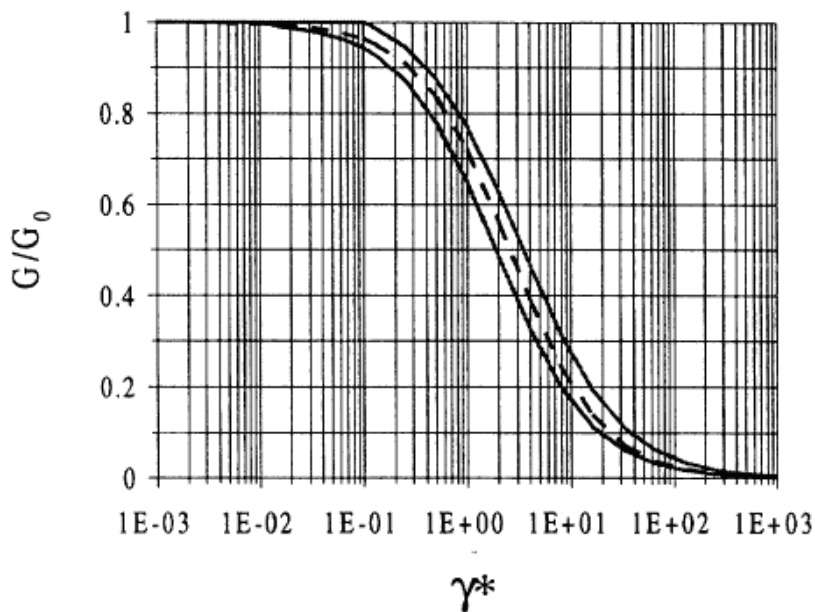
Figure 2-13. Shear modulus degradation curve proposed by Santos and Correia (2001).

2.4 Influence of Suction on Soil Modulus

Wu et al. (1984) conducted resonant column tests on fine-grained cohesionless soils to investigate capillary effects on G_{max}. For their testing, they used 3.6 cm diameter and 8 cm height specimens compacted at required different moisture contents and void ratios. Specimens were tested at 24.8, 49 and 98 kPa confinement pressure. For a given void ratio, starting from dry, they found G_{max} increases with an increase in degree of saturation to a peak value, and then decreases thereafter with further increase in moisture content. The degree of saturation where G_{max} is at peak is called the optimum degree of saturation. Capillary effects were greatest for soils with smallest effective grain diameter (D_{10}) and at the lowest confining pressure (σ_c'). They determined that an effective additional confinement provided due to capillary suction is almost equal to 1.6 m of overburden of completely saturated soils, and found that the maximum capillary suction occurred between 5% and 20% moisture content.

Qian et al. (1993) conducted an experimental investigation of capillary effects on low-strain shear modulus (strains lower than 10^{-5}) of partially saturated sands. They ran Hall-type resonant column tests on 14 sands with different gradations (four natural sands and remaining man-made from these four natural sands) to study the effect of void ratio (e), confining pressure (σ), grain shape and grain size distribution. Specimens were prepared at different moisture contents and void ratios, similar in procedure to that followed by Wu et al. (1984). They found that capillary effects increase small-strain shear modulus significantly and more pronounced for soils with low void ratio. Optimum degree of saturation increases with an increase in void ratio and is not affected by confinement while the influence capillarity decreases with confinement.

Picornell and Nazarian (1998) conducted bender element tests on specimens of coarse sand, fine sand, silt, and clay prepared by separating a local soil into size fractions to investigate the effect of soil suction on low-strain shear modulus (G_{max}) of soils. Predetermined soil suction

was applied on specimens at different moisture contents using a pressure-plate apparatus. They observed that as the soil particle size decreases, there is a progressive increase of saturated and residual moisture contents. As the moisture content decreases from saturated, G_{max} increases for sands by a factor of 1.8, for silts by a factor of 2.5, and for clays by a factor of 10. The larger effect in clay specimens was attributed to presence of flatly particles that deform under forces imposed by the menisci, resulting in an increase in number of contact points where menisci can develop and act.

Cho and Santamarina (2001) conducted microscale particle level studies to investigate capillary effects on low-strain stiffness at different moisture contents. They conducted bender element tests on i) glass beads, ii) a mixture of kaolinite and glass beads , iii) granite powder, and iv) sandboil sand. They also conducted microscale experimental study on menisci failure and recovery. Shear wave velocities (Vs), measured from bender element tests for the above four materials at different degree of saturation are shown in Figure 2-14. Some of the conclusions of their study were:

- The contribution of capillarity to interparticle forces involves both matric suction and surface tension.

- An equivalent effective stress due to capillary forces increases with decreasing moisture content, decreasing particle size, and increasing coordination.

- Remolding is not an appropriate specimen preparation method (as followed by Wu et al., 1984 and Qian et al., 1992) to study the behavior of low moisture content soils, since drying influences particle contact forces.

- Observed strains for menisci failure are in the range of $\varepsilon = 0.01$ to 1 and higher than the threshold strain for sands, so partial saturation is a stabilizing force for the soils skeleton. This strain at menisci failure decreases with a decrease in moisture content.

- On the other hand, small menisci may fail before reaching the strain at peak strength of soils. Thus, capillary forces at low moisture contents cause an increase in low strain stiffness of soils, but may not contribute to the peak strength.

33
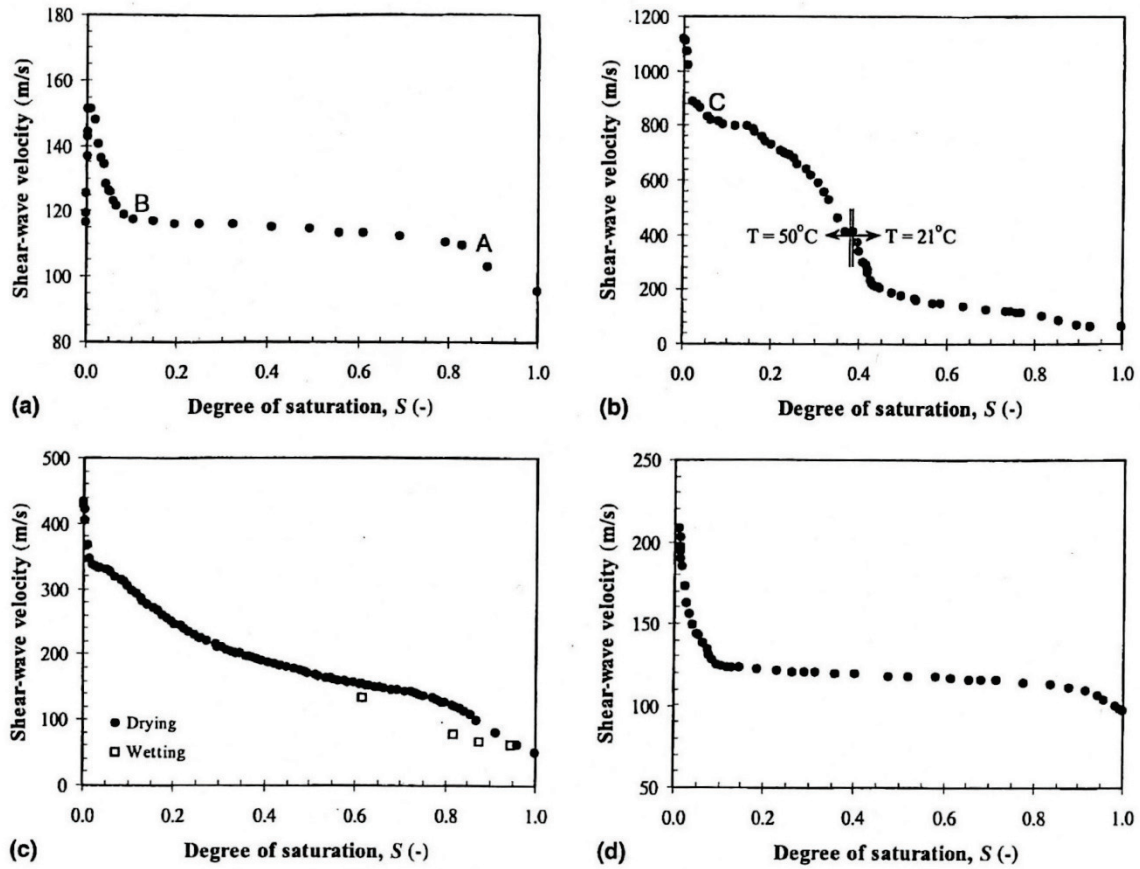
Figure 2-14. Shear wave velocity versus degree of saturation for different materials: (a) clean glass beads, (b) mixture of Kaolinite and glass beads, (c) granite powder, (d) sand boil sand (from Cho and Santamarina, 2001).

Toros (2008) investigated suction effects on small-strain Young's modulus (E_{max}) of Florida base course gravelly soils. He conducted free-free resonant column (FFRC) tests on 6 inch ×12 inch cylindrical specimens of Miami limerock, Newberry limerock, Ocala limerock, Loxahatchee shell rock, and Georgia granite, which are typically used base layer materials in the State of Florida. Samples were compacted at optimum moisture content and exposed to four different conditions: i) laboratory, ii) outside, iii) constant moisture, and iv) wetting and drying. For drying, specimens were placed in an oven, and for wetting, oven dried specimens were soaked in a water filled tank. He investigated the time effect on E_{max} at constant moisture,

moisture content effect on E_{max} at laboratory ambience, outside ambience and oven drying and water soaked wetting ambience.

Under constant moisture condition, E_{max} increases with time (Figure 2-15). Toros (2008) hypothesized that the behavior observed could be due to increased suction or negative pore water pressure that occurs as the water in the material redistributes following compaction into more preferential positions within the inter-particle void spaces. This increased suction effectively adds confining stress to the particulate material and thereby increases the resistance to deformation (stiffness).
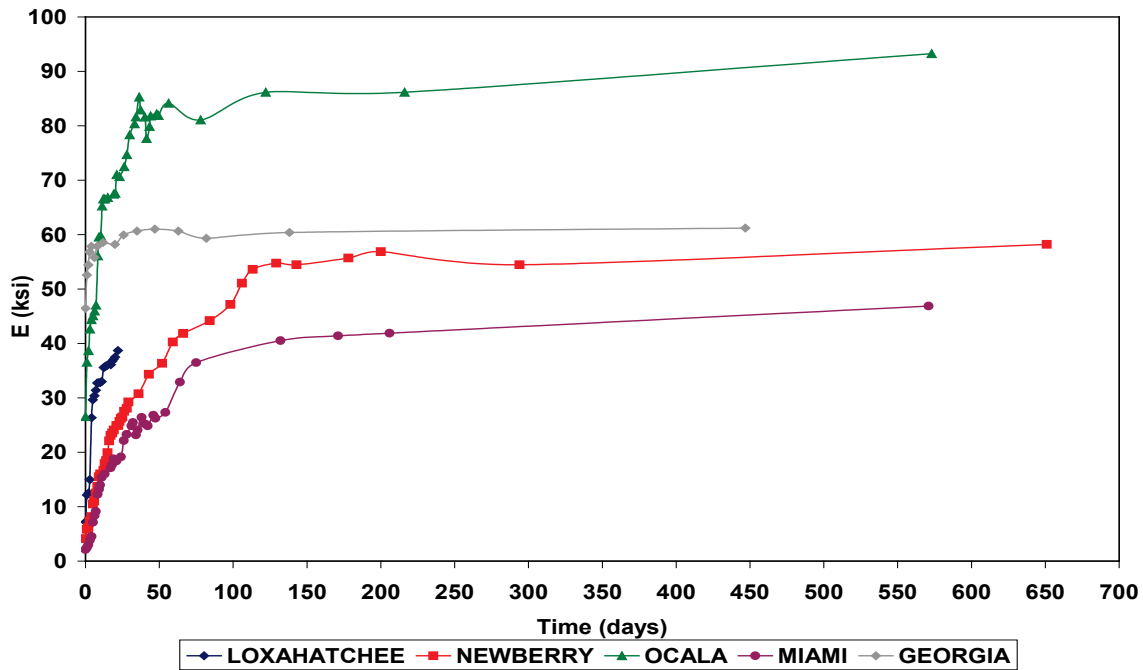
Figure 2-15. FFRC test results of specimen exposed to constant moisture (from Toros, 2008).

In both laboratory and oven drying methods, E_{max} increased significantly with a decrease in moisture content (Figure 2-16 and 2-17). This stiffening with drying was explained by an increase in suction, which effectively increases confinement and hence modulus. Regardless of the drying method, the Miami limerock changed the most, and this behavior is partially explained by the fact that this material is coarsest, well graded, and at low void ratio.
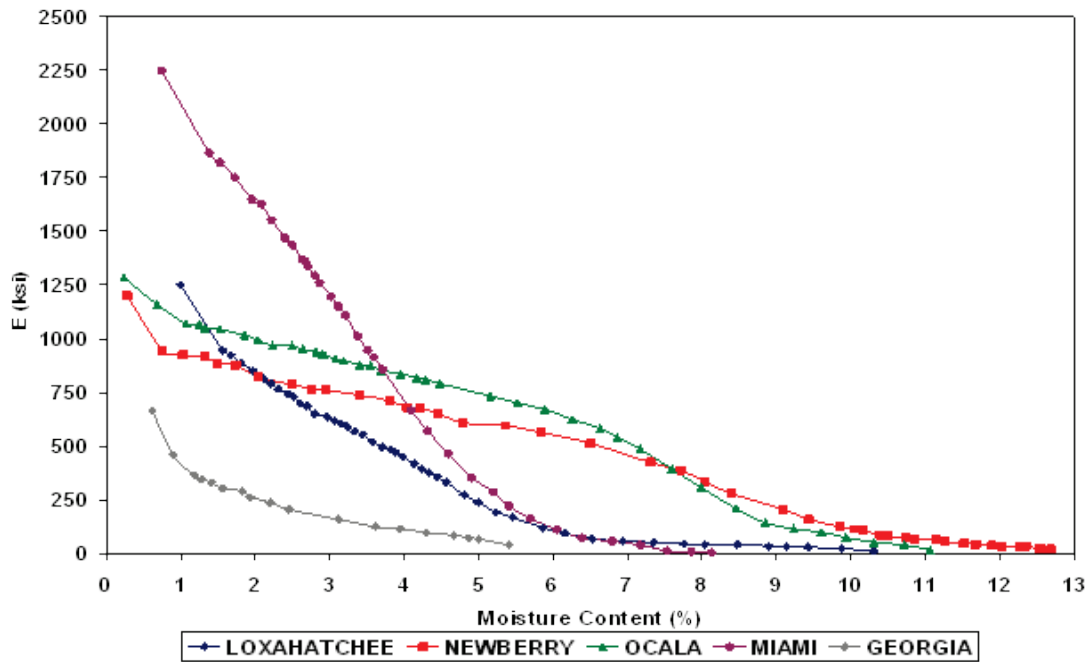
Figure 2-16. FFRC test results of specimens exposed to laboratory ambient (from Toros, 2008).
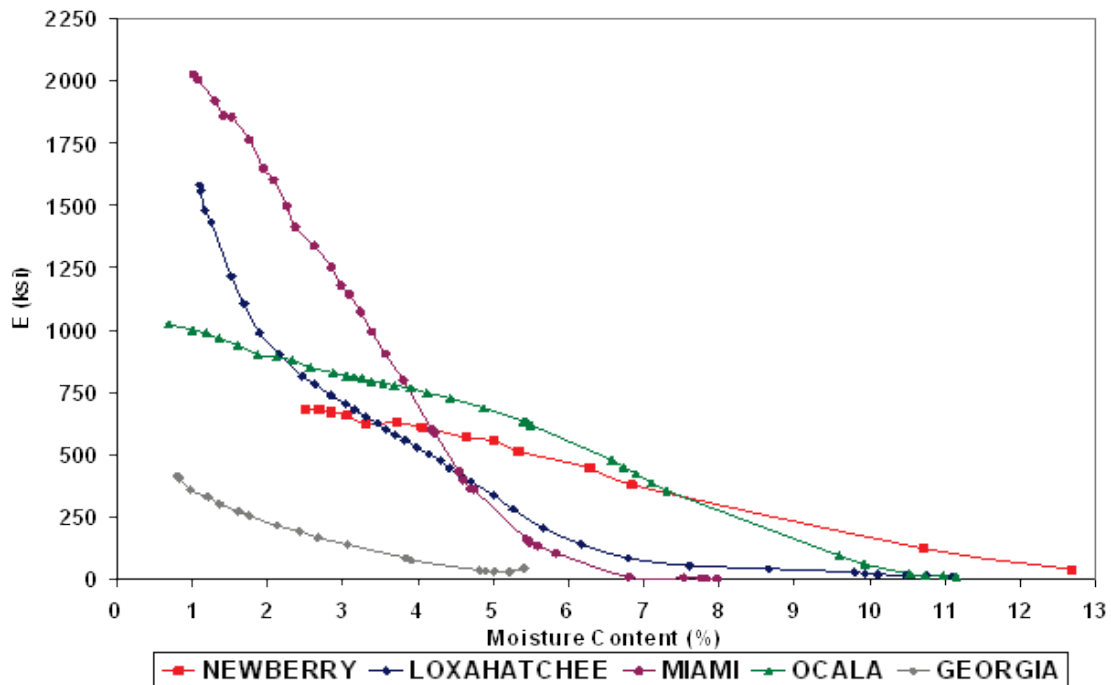
Figure 2-17. FFRC test results of each material during first cycle of oven drying (from Toros, 2008).

36

Drying and wetting responses do not follow the same relationship and there is a hysteretic phenomenon whereby a different modulus is measured while drying to certain moisture content compared to while wetting to the same moisture content (Figure 2-18). This hysteretic phenomenon is well known in unsaturated soil mechanics where the suction values reached at common moisture content are different between drying and wetting.
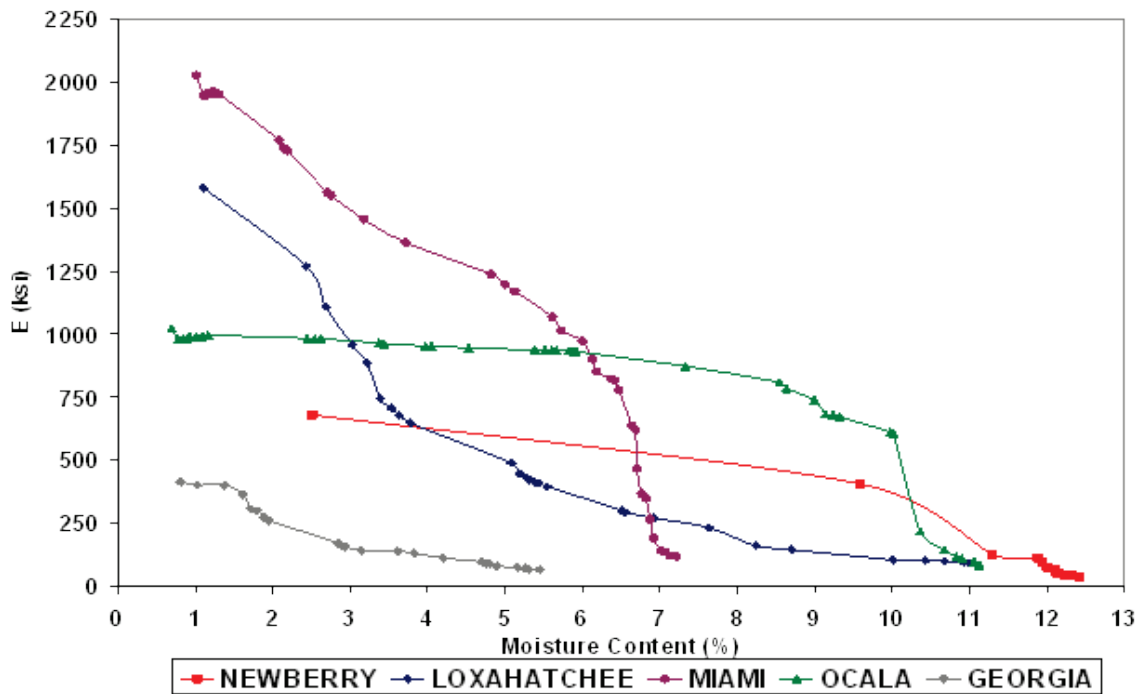
Figure 2-18. FFRC test results of each material during first cycle of wetting (from Toros, 2008).

The MEPDG incorporates the suction effect on M_R of unbound aggregate via the Enhanced Integrated Climatic Model (EICM). The EICM model is based on a M_R laboratory testing database, and incorporates the suction effect at M_R laboratory testing strain levels only (i.e., higher than 10^{-3}%) and does not consider the suction effect for a complete range of strains including very small-level strains. Moreover, this model is developed based on testing data obtained from limited selected base soils only.

2.5 Importance of Small-Strain Modulus Nonlinearity

Recent research studies in geotechnical engineering have increased the awareness of considering modulus nonlinearity for a complete range of strain levels in realistic prediction of ground deformations and surface settlements in geotechnical structures such as footings, braced excavations, etc. (Jardine et al., 1986; Atkinson, 1991; Elhakim and Mayne, 2008; and Lehane et al., 2008).

Jardine et al. (1986) studied the influence of nonlinear stress-strain characteristics in soil-structure interaction. They used laboratory measured nonlinear stress-strain properties for a finite element analysis of footings, pile excavations, and pressuremeter tests to assess the influence of small-strain nonlinearity in comparison with linear elastic behavior. From their study they concluded that although linear elasticity remains a convenient tool for expressing measurements of soil stiffness, unless the nonlinear nature of soil is taken into account, interpretation of field measurements can be misleading. Also, small-strain nonlinearity has a significant influence on interpretation of equivalent elastic moduli of in situ deformation tests.

Elhakim and Mayne (2008) developed a logarithmic modulus reduction algorithm to model and calculate soil modulus at different strain levels using G_{max} as the benchmark. By incorporating these nonlinear moduli at different strain levels in settlement analysis calculations, they were able to predict load-displacement response of footing on soft clay very close to the actual field measured load-displacement curve (Figure 2-19).

Lehane et al. (2008) conducted load tests on four different size footings on Perth sand. For their settlement predictions, they incorporated modulus nonlinearity for different strain levels including small-level strains via the Plaxis-HSsmall model. They found that foundation settlements predicted with Plaxis-HSsmall model are much better than existing standard linear design methods and, in some cases, close to actual measured load test settlements (Figure 2-20).

In their analysis they observed that settlement predictions performed with in situ measured parameters are more accurate than predictions performed with laboratory determined parameters. Settlements predicted with laboratory parameters were larger than settlements predicted using measured parameters by as much as a factor of four in some cases.
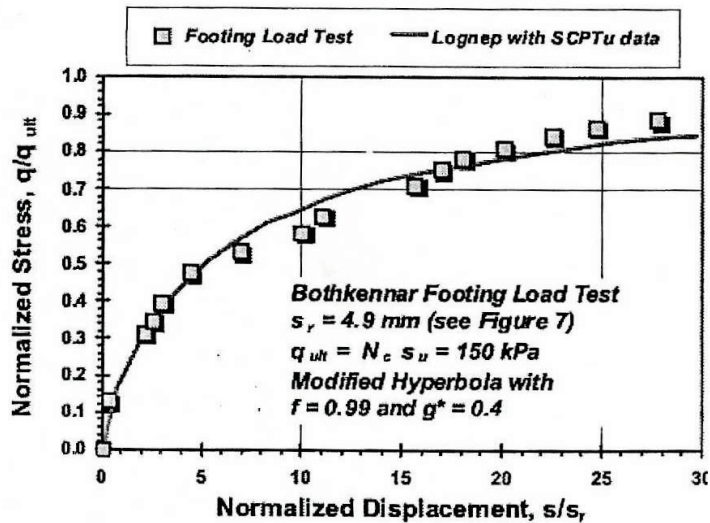
Figure 2-19. Load-displacement curves at Bothkennar footing test fitted using the proposed model (from Elhakim and Mayne, 2008).

2.6 Pavement Response Models

2.6.1 MEPDG Nonlinear Response Model

MEPDG recommends considering modulus nonlinearity of base soils for Level 1 material parameter inputs. A nonlinear finite element response model for base layer analysis developed for the MEPDG calculates nonlinear resilient modulus using the following equation:

$$M_R = k_1 p_a \left(\frac{\theta - 3k_6}{p_a}\right)^{k_2} \left(\frac{\tau_{oct}}{p_a} + k_7\right)^{k_3}$$

(2-13)

where Θ = bulk stress at the peak of loading, τ_{oct} = octahedral shear stress at the peak of loading, p_a = atmospheric pressure, and k_1 through k_7 are material parameters that should be determined from M_R laboratory data.

Equation 2-13 results in different M_R values for different stress levels based on the corresponding stress state. These moduli values are appropriate for the limited strain range that can be measured in laboratory testing, but not a complete range of strains including small-level strains required for more accurate material nonlinear modeling.
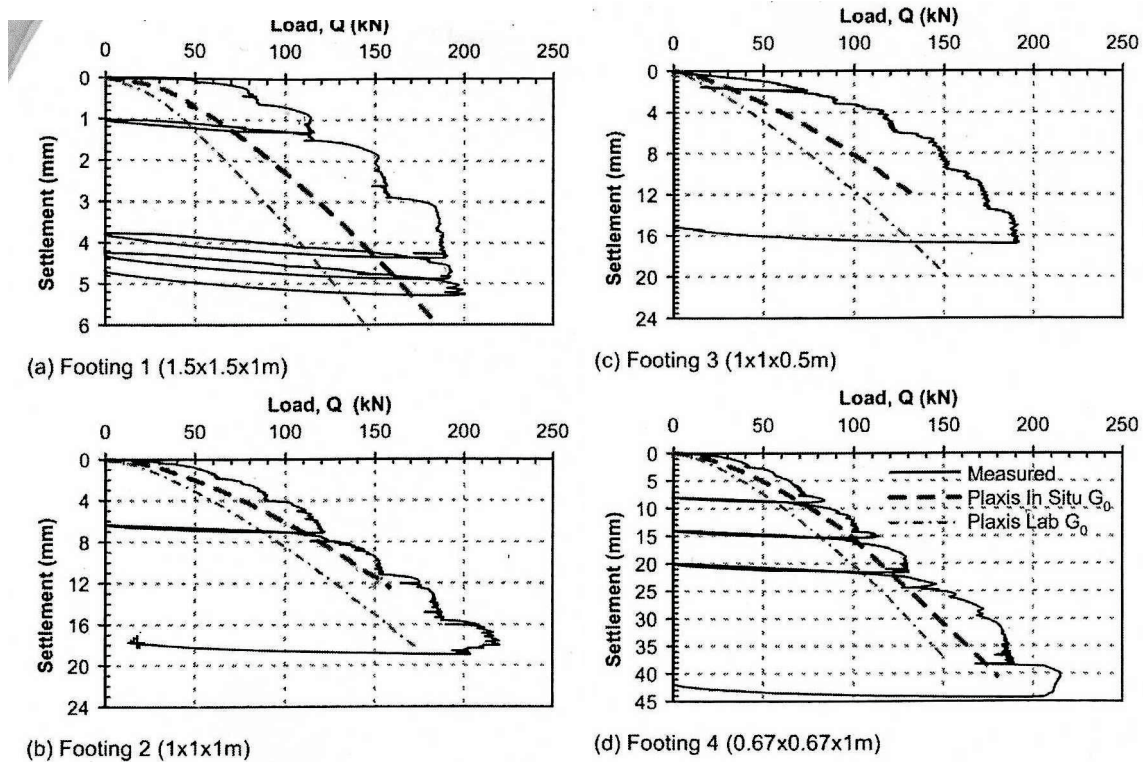
Figure 2-20. Comparison of measured foundation load settlement response at Shenton Park to prediction using Plaxis-HSsmall model (from Lehane et al., 2008).

2.6.2 Effective Modulus Determination

Roque et al. (1992) performed a comprehensive analysis to determine whether linear elastic layer analysis can be used to accurately predict the nonlinear response of pavements. They performed nonlinear analysis using the finite element computer program ILLIPAVE to predict nonlinear response of pavement structure. Surface deflections obtained from nonlinear analysis were used to backcalculate equivalent elastic moduli using BISAR. A design load of 40 kN was used for the analysis.

40

For nonlinear analysis, the asphalt surface layer was considered elastic and both base and subgrade were considered nonlinear. ILLIPAVE uses stress dependent nonlinear moduli for nonlinear analysis. For better predictions and comparison, the upper 0.30 m of the subgrade was modeled as a separate layer. Comparison of surface deflections, stresses, and strains between nonlinear analysis and backcalculated linear analysis was made. They found that, within the surface layer, fairly accurate predictions of deflections, stress, and strain equal to nonlinear analysis could be made when a single effective layer modulus was used to represent the surface and base layers. Nonlinear response of the subgrade could be represented by two elastic layers and corresponding effective layer moduli.

2.6.3 Plaxis-HSsmall Model

Plaxis-HSsmall model is a commercially available software that can implement modulus nonlinearity in soils with respect to both stress confinement and strain magnitude. HSsmall model considers nonlinear modulus at different strain levels (as high as 10^1) including very small-level strain (i.e., $\leq 10^{-6}$). Lehane et al (2008) used this approach for nonlinear modeling of soil under footings for settlement predictions and obtained fairly accurate results. Input parameters required for nonlinear modulus modeling can be obtained from resonant column testing, and it is proposed to use Plaxis-HS small for development of a nonlinear pavement response model. HSsmall model characteristics, background, and required input parameters are explained in detail in Chapter 6.

2.7 Closing Remarks

Conclusions of this literature review are:

- G_{max} of dry soils is primarily dependent on confining pressure (σ_c) and void ratio (e), whereas G also depends on strain. Gradation and maximum aggregate size are some of the other secondary influencing parameters.

- Different empirical relationships have been developed to calculate G_{max} and hyperbolic models are available to calculated G at different strain levels. Normalization of G with G_{max} nullifies the effect of confinement.

- An increase in suction due to drying of aggregate can increase modulus significantly.

- Consideration of nonlinear small-strain modulus in geotechnical design and analysis improves soil deformation/settlement predictions. G_{max} can be considered as a benchmark for soil modulus nonlinearity.

- Nonlinear small-strain stiffness can have significant influence on determination of equivalent elastic modulus used for linear design and analysis.

- It may be possible to determine a single effective modulus that can approximate nonlinearities for a range of pavement structures and loads.

The first objective of this research study was to characterize modulus nonlinearity of

selected base soils via a suitable laboratory testing program. The laboratory testing methodology

should be selected such that it can effectively account for confinement stress, loading strain

magnitude, and moisture content effects on nonlinear modulus, including small-strain nonlinear

modulus.

In the literature review of Chapter 2, various research studies conducted to determine

nonlinear small-strain shear modulus of sands and gravelly soils via resonant column testing

were discussed. Based on the literature review and testing requirements, the fixed-free and free-

free resonant column tests were selected for our laboratory testing. Background, mechanisms,

and limitations of these testing methods are discussed in this chapter.

3.1 Fixed-Free Resonant Column Testing

The fixed-free resonant column torsional shear test (fixed-free RC) is a dynamic testing

method that can determine material nonlinear shear modulus (G) under different confinement

pressures and at very small to medium-level strains.

3.1.1 Background and Testing Mechanism

The resonant column method is based on a one-dimensional wave equation derived from

the theory of linear elastic vibration. For our testing, a fixed-free resonant column torsional shear

(fixed-free RCTS) testing device was used where both resonant column and torsional shear tests

can be preformed, but only fixed-free resonant column (fixed-free RC) mechanics was utilized.

In a fixed-free RC device, the soil column is fixed at the base and free to rotate at the top, and an

external cyclic torsional load is applied to the top of the specimen. During testing, the loading

frequency is gradually changed until maximum response (strain amplitude) is found. The lowest

frequency at which maximum strain amplitude is obtained is the fundamental frequency (ω_n) of the soil specimen and driving system for that specific applied torsional load. This fundamental frequency is a function of soil modulus, specimen geometry, and characteristics of the resonant column device.

3.1.2 Shear Modulus (*G*)

The governing equation of motion for the fixed-free resonant column test idealized in Figure 3-1a for torsional vibration with a Kelvin-Voigt soil model is derived as follows. The torque (T) applied to an elastic soil cylinder that generates an angle of twist (dθ) along an incremental length of the specimen (dz) can be expressed as:

$$T = GJ \frac{\partial \theta}{\partial z} \tag{3-1}$$

(a)   (b)
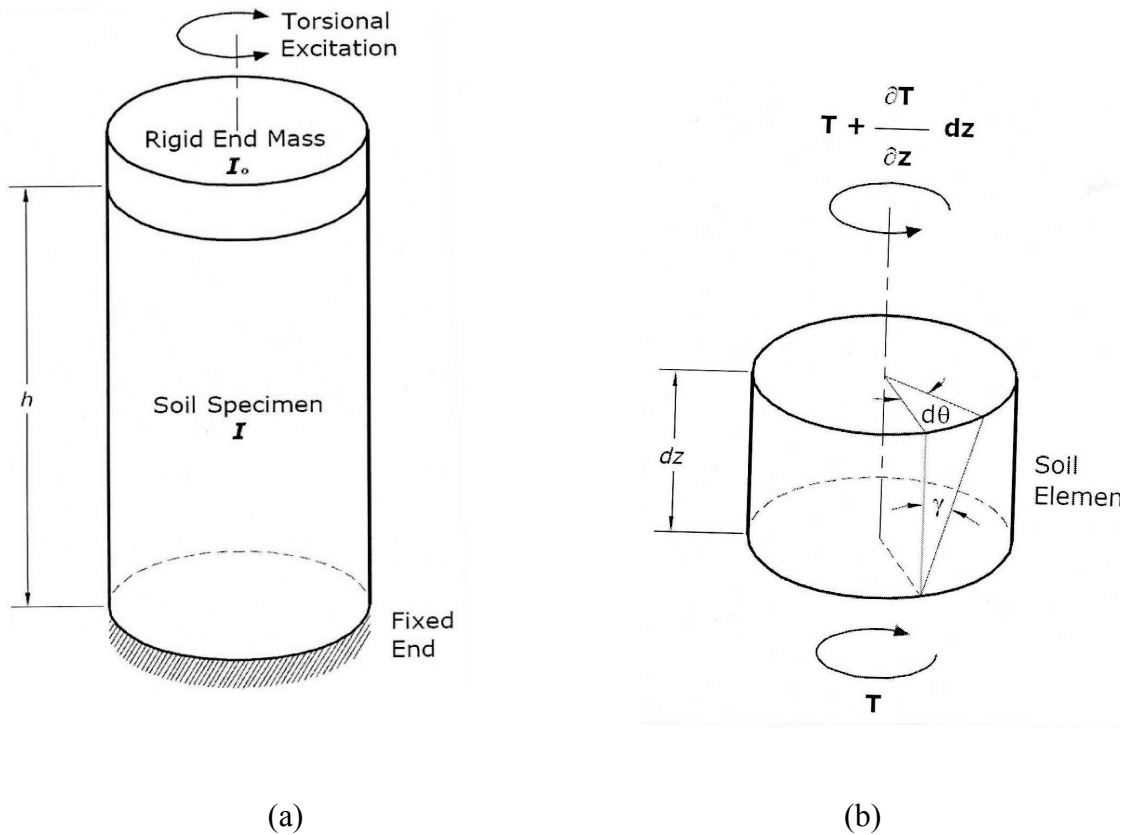
Figure 3-1. Fixed-free RC: (a) idealized testing specimen and (b) differential soil element.

where G = shear modulus of the soil and J= polar moment of inertia of the cross-sectional area .

From Figure 3-1b, the torque on two faces of the soil element are T and T+$\frac{dT}{dz}$. Using the torque (T) from Equation 3-1, we obtain:

$$\frac{\partial T}{\partial z}\, dZ = GJ\, \frac{\partial^2 \theta}{\partial^2 z} \tag{3-2}$$

Applying Newton's second law to the motion of the soil column and equating this net torque to the product of the mass polar moment of inertia and the angular acceleration produces:

$$\frac{\partial T}{\partial z}\, dZ = I\, \frac{\partial^2 \theta}{\partial t^2} = \rho J dz\, \frac{\partial^2 \theta}{\partial t^2} \tag{3-3}$$

where I = mass moment of inertia=$\rho\, J\, dz$ and ρ = soil mass density. From soil mass density (ρ) and shear wave velocity (V_s), shear modulus (G) can be calculated as:

$$G = \rho\, V_s^{\,2} \tag{3-4}$$

Substituting $\frac{\partial T}{\partial z}$ from Equation 3-3 and using Equation 3-4, we obtain the wave equation in torsion for an elastic rod:

$$\frac{\partial^2 \theta}{\partial z^2} = \frac{1}{V_s^2}\, \frac{\partial^2 \theta}{\partial t^2} \tag{3-5}$$

The general solution to Equation 3-5 is found using separation of variables as:

$$\theta\,(z,t)=\left[A \sin\left(\frac{w}{V_s}\, z\right) + B \cos\left(\frac{w}{V_s}\, z\right)\right] * e^{i\omega_n t} \tag{3-6}$$

where ω_n=natural circular frequency and A and B = constants that depend on the boundary conditions of the soil column. The boundary conditions in this fixed-free RC system are: 1) the angular displacement at the bottom (fixed end) is zero, and 2) the torque at the top of the soil specimen (free end) is equal but opposite of the inertia torque of the drive system. By solving Equation 3-1 via substituting these known boundary equations, the resulting expression is:

$$\frac{I}{I_0} = \frac{\omega_n h}{V_s} \tan\left(\frac{\omega_n h}{V_s}\right)$$

(3-7)

where I=mass moment of inertia of soil column, I_0= mass moment of inertia of drive system, and

h=height of specimen. Once the shear wave velocity (V_s) is determined from Equation 3-7, shear

modulus (G) can be calculated from Equation 3-4.

3.1.3 Shear Strain (γ)

The shear strain in a cylindrical resonant column loaded in torsion varies from zero at the

center line of the specimen to a maximum value at its outer edge as shown in Figure 3-2. Since a

single or unique value of shear strain amplitude with the measured shear modulus (G) is

required, conventionally r_{equ} is assumed as 2/3 of r_0 for solid specimens with radius r_0. Shear

strain ($\gamma_{(r)}$) is then calculated as follows:

$$\gamma_{(r)} = \frac{r_{equ}\theta_{max}}{h}$$

(3-8)

where r_{equ} =equivalent radius of specimen=$\frac{2}{3}r_0$, r_0=radius of solid specimen, θ_{max} =maximum

angle of twist=$\frac{x}{r_{sensor}}$, r_{sensor}=distance of target center (or fiber optic sensor) from specimen's

central axis, and x=radial displacement of target. The radial displacement is measured by a fiber

optic sensor system, which can measure strains in the range of 10^{-5}% to 10^{-1}%.

3.1.4 Equipment Setup

The fixed-free RC equipment consists of a Perspex cylindrical chamber with leakproof top

and bottom covering plates at the ends of the chamber (Figures 3-3 and 3-4). The bottom cap of

the specimen is attached firmly to the chamber's bottom plate, and the top end of the specimen is

left free to rotate, establishing the fixed- and free-end boundary conditions. A torsional loading

motor is attached to the specimen's top cap and includes a supporting system. A fiber optic

sensor target to measure radial displacements is also attached to top cap. This target extends out

from the top cap in a radial direction. The fiber optic sensor cable is attached to one of chamber

supporting rods and positioned facing the target. This sensor system measures the radial

displacements of the target produced by the torsional loading. Finally, the entire testing chamber

unit is fixed firmly to a loading frame for stability. Tests can be run and controlled through a

software program that sends control signals to the resonant column interface and servo amplifier

unit (Figure 3-5a), which controls the torsional loading motor and the amount of load to be

applied. Air confinement can be applied via a pressure control panel (Figure 3-5b). The fiber

optic sensor system (Figure 3-5c) sends target displacement information back to the controlling

software, which calculates the resonant frequency (ω_n) and other test parameters (Figure 3-6).
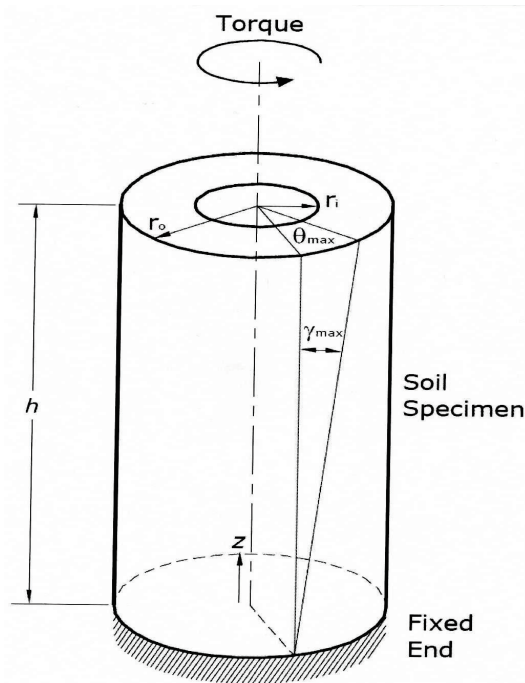
Figure 3-2. Shear strain in soil specimen.

Figure 3-3. Fixed-free RC equipment.
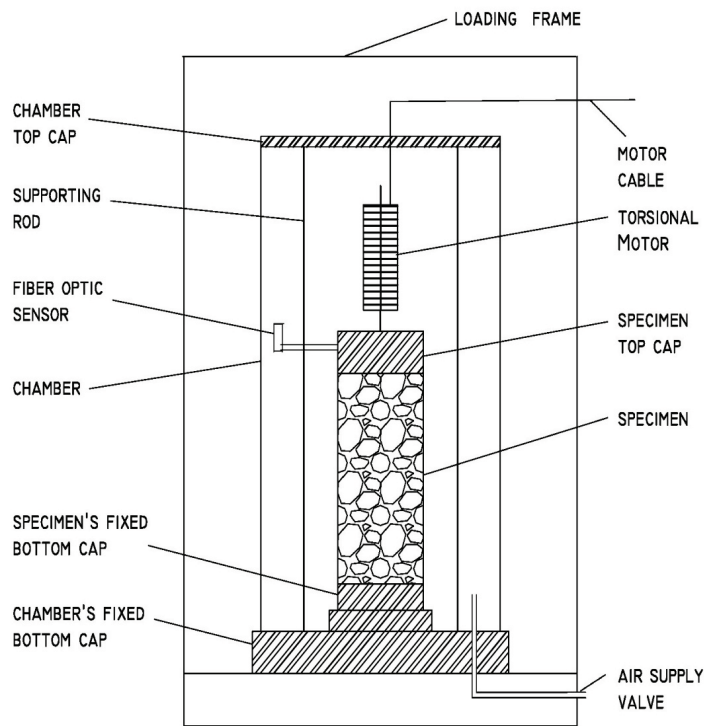
Figure 3-4. Sectional view of fixed-free RC testing equipment.

(a)
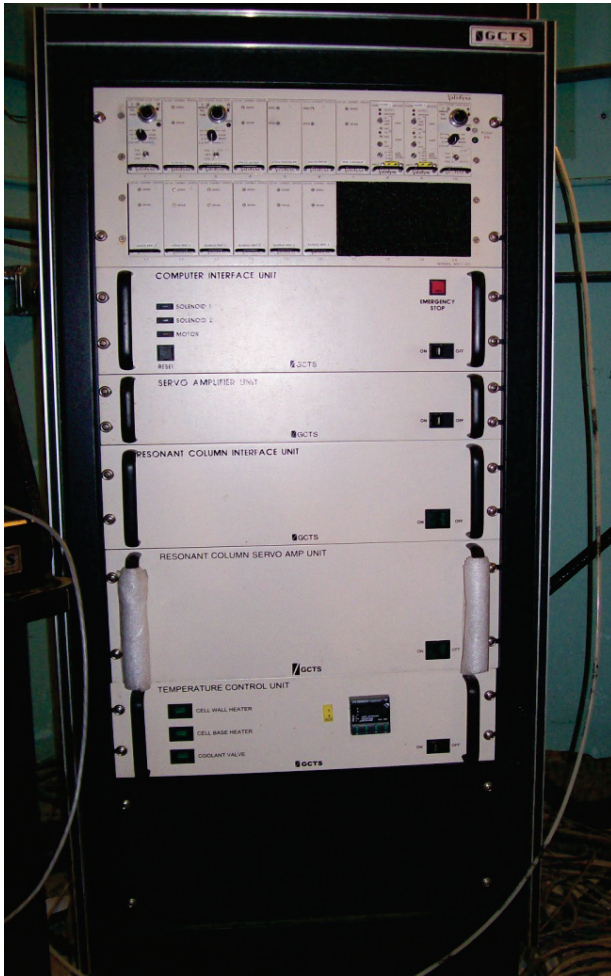
(b)

(c)

Figure 3-5. Controlling units of fixed-free RC equipment: (a) resonant column interface unit and servo amplifier unit, (b) pressure control panel, and (c) fiber optic sensor placed facing the target attached to specimen.
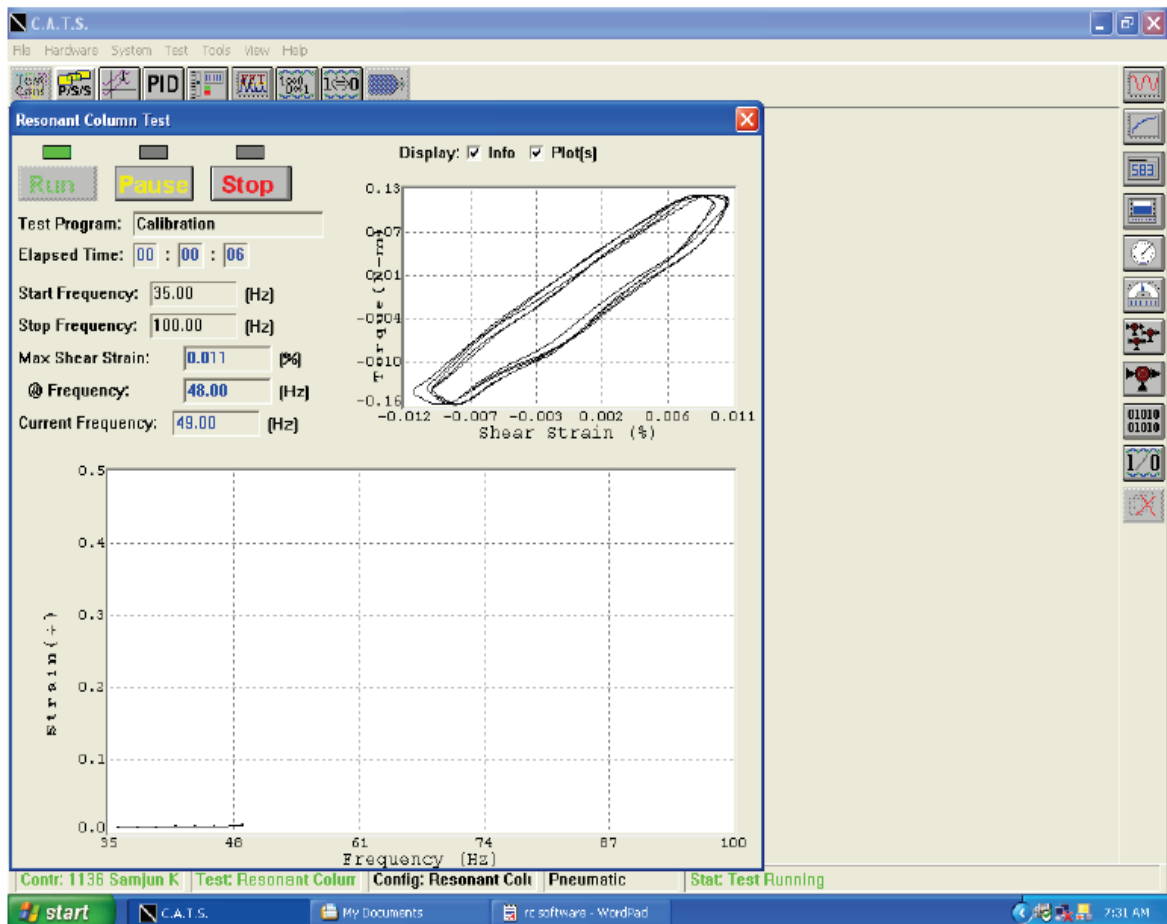
Figure 3-6. Real-time test execution window showing resonant frequency and loading loop.

3.1.5 Calibration of the Drive System

When a torsional load is applied during testing, the torsional motor rotates the top specimen cap along with the testing specimen. The weight of the cap and motor, combined with the specimen weight, form the total weight of the testing system. To nullify the effects of the top specimen cap and motor weight and to determine the properties of specimen alone, calibration of driving system is required.

Calibration of the driving system is performed using a metallic specimen (Figure 3-7) that is assumed to have zero or close to zero damping and a constant torsional stiffness (k). From Newton's second law, the mass moment of inertia is related to the natural or resonant frequency (ω_n) as follows:

$$I = \frac{k}{\omega_n^2} \tag{3-9}$$
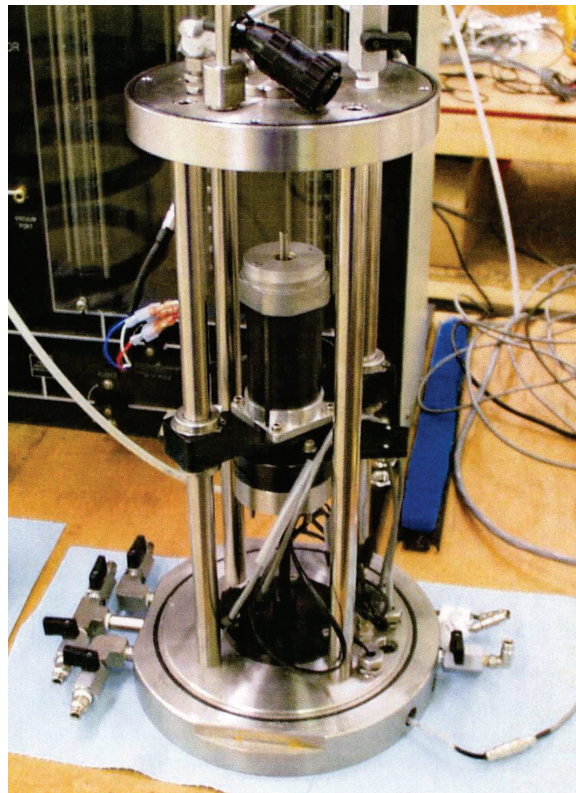
Figure 3-7. Calibration specimen with added mass.

The recommended procedure to find the mass moment of inertia of the driving system (I_0) is to perform two resonant column tests with the metal calibration specimen, one by itself and the other with an added mass. After performing a frequency sweep with constant force amplitude to find the resonant frequency, the solutions will be:

$$\text{Without added mass: } I_0 + I_{cal} = \frac{k}{\omega_1{}^2} \tag{3-10}$$

$$\text{With added mass : } I_0 + I_{cal} + I_{mass} = \frac{k}{\omega_2{}^2} \tag{3-11}$$

where I_0=mass moment of inertia of the drive system and any other fixture that will be used during actual soil testing, I_{cal} = mass moment of inertia of the calibration specimen, I_{mass} = mass moment of inertia of the added mass, ω_1 = resonant frequency of calibration specimen without the added mass, and ω_2 = resonant frequency of calibration specimen with the added mass. By combining Equations 3-10 and 3-11, we get:

$$I_0 = \frac{(I_{cal} + I_{mass})\omega_2^2 - I_{cal}\omega_1^2}{\omega_1^2 - \omega_2^2} \tag{3-12}$$

3.1.6 Limitations Experienced with the Testing Equipment

The maximum frequency that can be applied using the torsional loading motor of the fixed-free RC equipment is 300 Hz, thus only specimens with a resonant frequency less than 300 Hz can be tested with this equipment. Part of our testing program (explained in detail in Chapter 5) was to run tests on specimens compacted at optimum moisture content and then dried to different moisture contents. However, after drying specimens to below certain moisture contents (as explained in later chapters), the resonant frequency exceeded 300 Hz due to an increase in modulus. As a result, we were able to determine material modulus down to limiting moisture contents below the optimum moisture content (OMC), but not to a completely dry condition.

3.1.7 Equipment Credibility Verification

After installation, the equipment was subjected to verification to assess that the testing measurements were crdeible. This verification was performed by conducting tests on Ottawa sand, since experimental results determined for shear modulus are available in the literature, thus our testing results can be compared with literature data for verification.

Verification tests were conducted on 4 inch diameter and 8 inch height Ottawa sand specimen compacted to a minimum void ratio (e_{min}) of 0.435. This compacted specimen was subjected to six different confining pressures (σ_c) of 50, 100, 150, 200, 250, and 300 kPa. Shear modulus (G) at strain levels in the strain range of $10^{-4}\%$ to $10^{-1}\%$ were measured at each confinement, and these results are shown in Figures 3-8 and 3-9.

Using the very small-strain modulus (G_{max}) (i.e., G at $\gamma = 10^{-4}\%$) data at different confining pressures, G_{max} versus $\log(\sigma_c)$ data was developed and is shown in Figure 3-9. From this plot, an empirical relationship to calculate G_{max} was developed in the form proposed by Hardin and Richart (1963):

$$G_{max} = A_G F(e)(\sigma_c')^{n_G} \qquad (2\text{-}5)$$

where A_G and n_G are material constants, $F(e) = (2.17\text{-}e)^2/(1+e)$, and G_{max} and σ_c' are in kPa. From our testing data, we obtained:

n_G=0.5165

e=0.435

F(e)=2.098

By substituting values of F(e) and n_G in Equation 2-5, and solving it with the testing data, an empirical equation to calculate G_{max} was obtained:

$$G_{max} = (5350)\,(2.098)(\sigma_c')^{0.5165} \qquad (3\text{-}13)$$
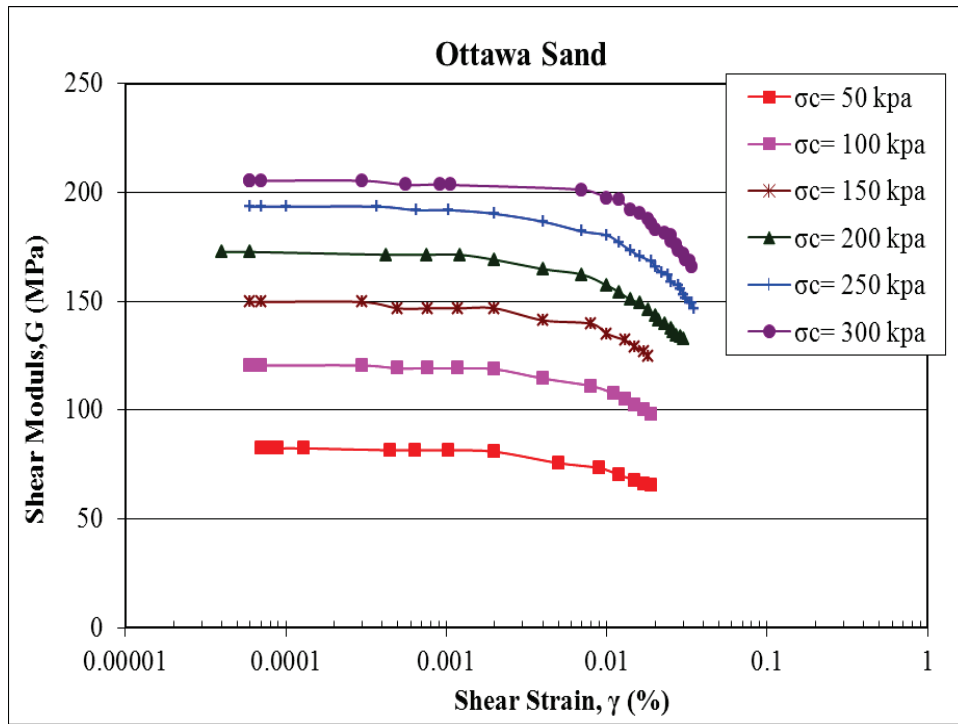
Figure 3-8. Shear modulus versus shear strain curves at different confining pressures for Ottawa sand.
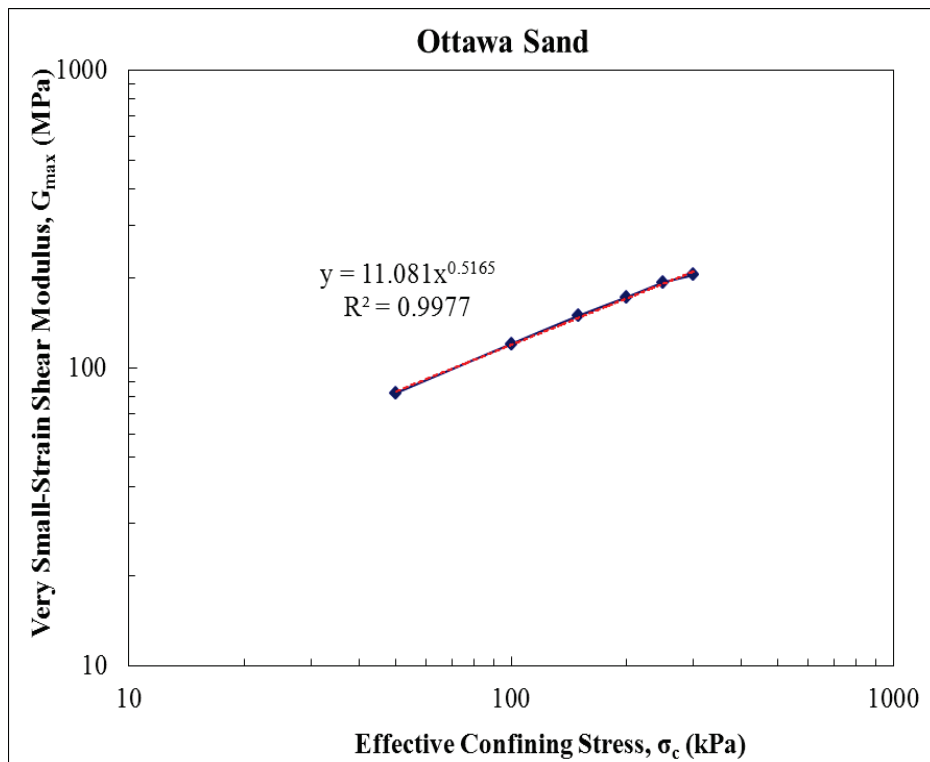
Figure 3-9. G_{max} versus log σ_c relationship for Ottawa sand.

An $n_G = 0.5165$ obtained from our testing matches well with the literature data for Ottawa sand (Hardin and Richart, 1963; Menq, 2003). Also, the value of $A_G = 5350$ falls in the range of 3300 to 9000 for sands (Menq, 2003). Thus, by comparing Ottawa sand testing results with literature data, our fixed-free RC equipment data appears to be credible.

3.2 Free-Free Resonant Column Testing (Free-Free RC)

Free-free RC testing method (Kim and Stokoe, 1992; Menq, 2003; Toros, 2008) was used to determine very small-strain modulus (i.e., $\leq 10^{-5}\%$) of Florida base materials at different moisture contents. This test can be conducted very quickly on laboratory compacted specimens. Further, the free-free RC test is nondestructive, and thus can be conducted on the same specimen at different moisture contents by drying it as required.

3.2.1 Background and Mechanism

Two different types of stress wave measurements can be conducted on a solid rod with free-free RC testing: 1) resonance measurements, and 2) direct-arrival measurement. With known specimen dimensions and measured resonance frequency (ω_n), Young's modulus (E) can be determined using Equations 3-14 and 3-15:

$$V_c = 2\, \omega_n\, l \tag{3-14}$$

$$E = \rho\, V_c^2 = \rho\, (2\, \omega_n\, l)^2 \tag{3-15}$$

where V_c = unconstrained compression wave velocity and l=length of specimen.

The travel time (Δt) of a constrained compression wave is determined via direct-arrival measurement, from which constrained compression wave velocity (V_p) is calculated as:

$$V_p = \frac{l}{\Delta t} \tag{3-16}$$

where l=length of the specimen, and Δt = measured travel time of constrained compression wave. With known constrained compression wave velocity (V_p) and unit mass of the specimen (ρ), constrained modulus (M) can be calculated as:

$$M = \rho v_p{}^2 = \rho\left(\frac{\ell}{\Delta t}\right)^2 \tag{3-17}$$

With known constrained and unconstrained wave velocities, Poisson's ratio (v) can also be calculated as:

$$\upsilon_{ME} = \frac{1-\left(\dfrac{v_p}{v_c}\right)^2 + \sqrt{\left(\left(\dfrac{v_p}{v_c}\right)^2 - 1\right)^2 + 8\times\left(\dfrac{v_p}{v_c}\right)^2\left(\left(\dfrac{v_p}{v_c}\right)^2 - 1\right)}}{4\times\left(\dfrac{v_p}{v_c}\right)^2} \tag{3-18}$$

Finally, with known Poisson's ratio (v), Young's modulus (E), and constrained modulus (M), shear modulus (G) can be calculated as:

$$G = \frac{E}{2(1+\upsilon)} \tag{3-19}$$

$$G = \frac{2M\upsilon - M}{2(\upsilon - 1)} \tag{3-20}$$

For our free-free RC testing, we used the same equipment used by Toros (2008) to measure very small-strain modulus of Florida base materials. Detailed background and mechanism explanations about free-free RC testing and equipment verification are given in Toros (2008).

3.2.2 Equipment Setup

Modified Proctor compacted specimens without any confinement of casing or membrane are tested with this equipment. Following the testing procedure of Toros (2008), our free-free RC testing system consists of a dynamic signal analyzer (DSA) or (oscilloscope), an instrumented

impact hammer, and an accelerometer (transducer). Specimens are oriented horizontally and suspended with flexible straps to achieve free-free boundary conditions (Figure 3-10). The excitation point with impact hammer is at the center of one end of the specimen, and the location of the accelerometer is at the center of other end of the specimen. The accelerometer is glued to the specimen.

The main difference between our testing procedure and Toros (2008) is confinement with casing around the specimen (Figure 3-11). Toros (2008) tested 6 inch diameter and 12 inch height specimens with plastic casing, whereas we tested 4 inch diameter and 8 inch height naked specimens without any confining casing.
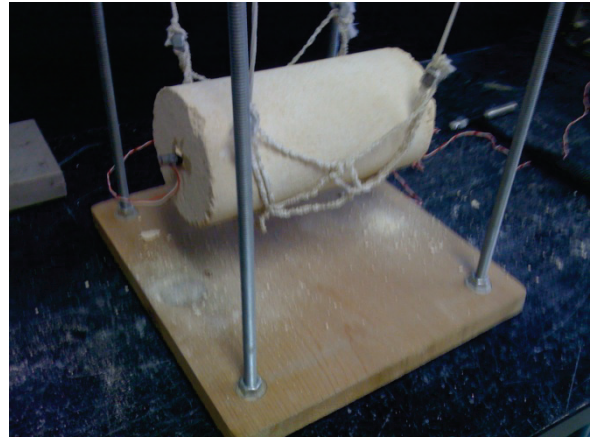
|(a)|(b)|

Figure 3-10. Free-free resonant column test equipment setup: (a) overall setup and (b) specimen with transducer and instrumented impact hammer.

|(a)|(b)|
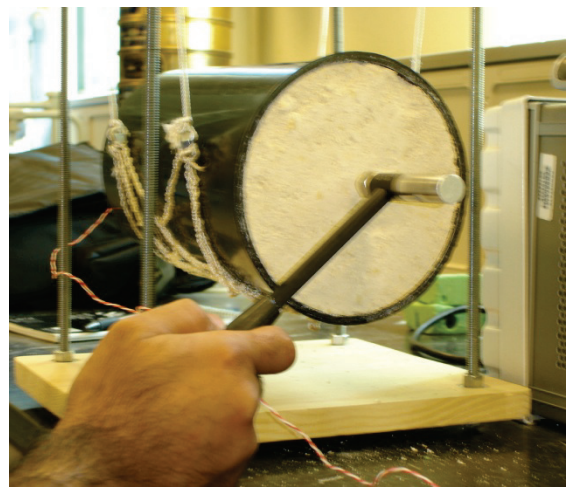
Figure 3-11. Free-rree resonant column testing specimen: (a) without confinement casing and (b) with confinement casing (from Toros, 2008).

CHAPTER 4
MATERIALS AND SPECIMEN PREPARATION

In the State of Florida, limerock aggregates are commonly used for base layer construction. For our testing, one limerock and one non-limerock material were selected: Newberry limerock and Georgia graded aggregate. A detailed description about their source, particle size distribution, basic parameters, and specimen preparation are given in this chapter.

4.1 Materials

4.1.1 Sources

Newberry limerock and Georgia granite graded aggregate base were selected for our testing. Material sources for these two materials are given in Table 4-1.

Table 4-1. List of materials used for testing and their sources.

Material	Mine Number/Source	Type
Newberry limerock	26-002	Limerock
	Newberry Quarry	
Georgia granite	GA-178	Granite
Graded Aggregate Base (GAB)	Macon Quarry	

Representative samples of these selected materials were collected by FDOT SMO (Florida Department of Transportation State Materials Office) staff from sources identified in Table 4-1, and following FDOT standard method, i.e., Florida Methods 1 (FM 1) T-002 that is similar to AASHTO T2.

4.1.2 Characterization

The collected samples were transported in bags to the FDOT SMO laboratory for further characterization and testing. Before testing, the transported sample bags were placed in a thermostatically-controlled drying oven at a temperature of 110 ºF until the samples were friable.

After these oven dried samples cooled, sieve analysis and other basic parameter tests were

conducted. Representative samples of these two materials are shown in Figure 4-1.

Sieve analysis was performed following the procedures in AASHTO T27. The grain size

distribution for particles larger than the #200 sieve (i.e., 0.075 mm) is shown in Figure 4-2.

(a)   (b)

Figure 4-1. Representative samples of (a) Georgia granite and (b) Newberry limerock.
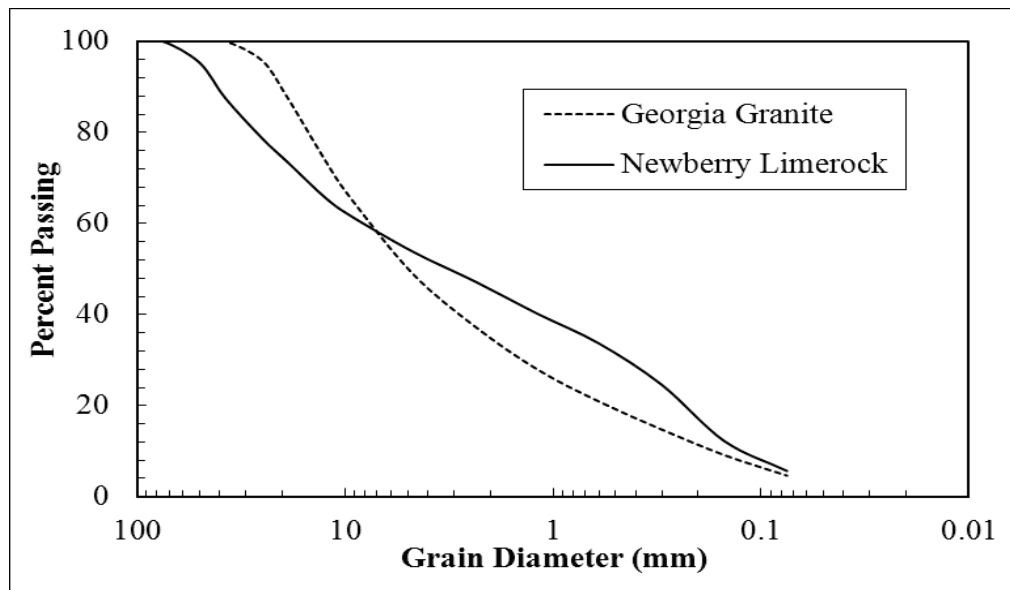
Figure 4-2. Grain size distribution.

The specific gravity of fine and coarse aggregates were performed following the procedures FM 1 T-084 and T-085, which are similar to the AASHTO T084 and T085 procedures, respectively. Atterberg limits were determined following AASHTO T90 for plastic limit and plasticity index and AASHTO T89 for liquid limit. These basic material parameters are presented in Table 4-2.

Table 4-2. Basic material parameters.

Parameter	Georgia granite	Newberry limerock
Unified soil classification	GW-GM	GM
D_{50} (mm) - mean grain size	5	3
D_{10} (mm) - effective grain size	0.16	0.13
C_u- the coefficient of uniformity	50	61.5
C_c- the coefficient of curvature	1.76	0.15
G - specific gravity	2.74	2.72
Maximum dry density (kN/m^3) ($\gamma_{dry\ max}$)	22.08	18.21
Optimum moisture content (OMC) (%)	5.5	13
Void ratio at OMC (e_{OMC})	0.20	0.45
Plastic limit	NP	NP
Plasticity index	NP	NP
Liquid limit	NP	NP

where: $C_u = D_{60} / D_{10}$, $C_c = (D_{30})^2/ (D_{60} \times D_{10})$

4.2 Specimen Preparation and Installation

Fixed-free RC tests were conducted on both dry and wet (partially saturated) compacted cylindrical specimens and free-free RC tests were conducted on wet compacted specimens. The 4 inch (10.16 cm) diameter by 8 inch (20.32 cm) height specimens were prepared following standard methods for specimen preparation and detailed explanation is given in the following sections.

Aggregate passing through the ¾-inch sieve only was used for specimen preparation. After oven drying the mine collected samples, aggregate that does not pass through ¾-inch sieve was

separated and sent through a limerock crusher, so that all the aggregate is smaller than ¾ inch. This crushed aggregate was mixed with uncrushed aggregate and the entire material was used for specimen preparation satisfying the gradation requirements.

4.2.1. Dry Specimens

4.2.1.1 Dry Specimen Preparation

Dry specimens were used in fixed-free RC testing and were prepared at three different void ratios for each material as presented in Table 4-3. The dry specimens were prepared using a split mold and membrane. Initially, a split mold with membrane on the inner wall of the mold was attached to the resonant column bottom cap (pedestal) (Figure 4-3a). Next, dry aggregate was placed inside the split mold and compacted by dropping a loading hammer manually (Figure 4-3b). The amount of energy required (i.e., weight of hammer, height of drop, and number of layers) to compact the dry aggregate to obtain required void ratio was determined by trial and error. Following compaction, to keep the specimen intact after removal of the split mold, vacuum was applied through the bottom drainage line (Figure 4-3c).

Table 4-3. Selected void ratios for dry specimen testing.

Material	Void Ratio (e)		
	1 (e $_{OMC}$)	2	3
Newberry limerock	0.45	0.50	0.55
Georgia granite	0.20	0.25	0.29

4.2.1.2 Dry Specimen Installation

For dry specimens, after completing compaction, the top cap with vertical and horizontal serrations was placed firmly to achieve proper contact grip between the soil and cap. Friction due to the serrations on both the top and bottom caps provides a good grip and the entire soil column rotates as a single integral unit when the torsional load is applied. After attaching the top cap and

loading motor, a confinement chamber was placed and the required air confinement was applied through a pressure control panel (Figure 4-3d). Once the dry compacted specimen was stablized by the externally applied air confinement, the vacuum line was disconnected.

4.2.2 Wet (Partially Saturated) Specimens

4.2.2.1 Wet Specimen Preparation

Wet specimens were compacted at optimum moisture content (OMC) using a modified Proctor compactor (Figure 4-4a). Before compaction, the soil-water mixture was soaked for at least 12 hours in a nylon-sheet-covered container (Figure 4-4b) to seek a uniform distribution of water throughout the soil mixture. After soaking, the mixture was compacted in a standard size mold used for making 4 inch diameter and 8 inch height specimens (Figure 4-4c). The number of layers and the number of blows required for each layer were estimated based on ASTM D1557, Test Method for Laboratory Compaction Characteristics of Soils Using Modified Effort. The specimens were compacted in six layers and 36 blows per layer, which meets the required compaction effort of 2700 kN-m/m^3 according to ASTM D1557. After extruding from the compaction mold, the specimen was covered with a 0.012-inch thick rubber membrane and allowed to sit for 12 hours in an air-tight container at room temperature before testing.

4.2.2.2 Wet Specimen Installation

For the wet OMC compacted specimens, the top and bottom caps were glued to the specimen using Bondo. This glue material was selected such that it should not influence the testing measurements (i.e., resonant frequency) and material properties. Next, the bottom cap of the specimen was attached firmly to the chamber's bottom plate, and the top end of the specimen is left free to rotate. Finally, the torsional loading motor was attached to the top cap with the supporting system .

Figure 4-3. Dry specimen compaction and installation: (a) split mold with membrane inside, (b) split mold with dry compacted limerock, 9c) after application of vacuum, and (d) after installation of chamber and external confinement application.

Figure 4-4. Wet specimen compaction: (a) modified Proctor compactor with 4 inch diameter and 8 inch height specimen mold, (b) soaked aggregate trays with nylon cover sheet, and (c) compacted wet specimens of 4 inch diameter and 8 inch height.

CHAPTER 5
EXPERIMENTAL RESULTS AND ANALYSIS

The first objective of this research work was characterization of base soil modulus nonlinearity with respect to confinement stress, loading strain and moisture content via laboratory testing. To achieve this objective, fixed-free resonant column tests (fixed-free RC) and free-free resonant column (free-free RC) tests were conducted on selected representative base soils. Testing mechanisms and their background were explained in detail in Chapter 3. Base soils selected for testing, their basic properties characterization, and specimen preparation methods were explained in Chapter 4.

Fixed-free RC tests were conducted on both dry and unsaturated (wet) compacted specimens of Newberry limerock and Georgia granite to determine shear modulus (G) under different confinement pressures and at strain levels as small as 10^{-5}% (very small-level strains) and as high as 10^{-1}% (medium level strains). Free-free RC tests were conducted on unsaturated (wet) compacted specimens of Newberry limerock and Georgia granite to determine very small-strain shear modulus (G_{max}) under no confinement. Specimen testing conditions such as moisture content, confinement pressure, and strain magnitude are explained in the following sections, and experimental results are discussed and analyzed.

5.1 Fixed-Free Resonant Column Torsional Shear Testing

5.1.1 Dry Specimen Testing Results

Dry compacted specimens of Newberry limerock and Georgia granite were tested at three different void ratios (Table 4-3) to investigate the effect of void ratio. A specimen at each void ratio was subjected to four different confining pressures of 50, 100, 150, and 200 kPa to investigate confinement effect. Shear modulus (G) versus shear strain (γ) testing results for e_{OMC}

(i.e., e=0.45 for Newberry limerock and e=0.20 for Georgia granite) are shown in Figures 5-1

and 5-2, and plots corresponding to the remaining two void ratios are presented in Appendix A.

Based on literature (Seed et al., 1986; Menq, 2003; and Atkinson, 2000) for dry gravels,

strains less than 10^{-4}% are referred as very small-level strains and the corresponding shear

modulus is at its maximum (i.e., G_{max}). Thus, by considering G value at $\gamma = 10^{-5}$% as G_{max},

normalized shear modulus (G/G_{max}) versus shear strain curves are developed and shown in

Figures 5-3 and 5-4.

From Figures 5-1 and 5-2, it can be observed that:

- At constant confining pressure, modulus decreases with an increase in strain magnitude. At constant strain magnitude, modulus increases with increases in confinement and the rate of increase is maximum at very small-strain (i.e., 10^{-5}%). Modulus is maximum (i.e., G_{max}) and elastic at strains lower than 10^{-4}% and starts decreasing thereafter with an increase in strain. Modulus decreases linearly in the strain range of 10^{-4}% to 10^{-3}% and nonlinearly thereafter. Menq (2003) reported similar results for gravelly soils. Seed et al. (1986) and Rollins et al. (1998) also observed that in gravelly soils G starts decreasing from 10^{-4}% strain with increase in strain magnitude.

- Based on Ottawa sand testing results (Figure 3-7a) and literature database, the modulus of sands are maximum and elastic at strains smaller than 10^{-3}% and decrease thereafter with an increase in strain. By comparing results of gravelly soils with sands, it can be concluded that presence of gravel size aggregates increases nonlinearity in modulus reduction. This agrees with the findings of Seed et al. (1986) and Menq (2003).

- The difference in moduli at different confining pressures and for the same strain magnitude decreases with an increase in strain. This indicates that the confinement effect on modulus decreases with an increase in strain magnitude. At strains higher than 10^{-1}% modulus does not vary significantly with respect to either an increase in strain or an increase in confinement. This observation indicates that at larger strains (i.e., 10^{-1}% and higher) pressure confinement and strain magnitude have no significant influence on moduli of gravelly soils.

- For both soils, modulus reduction curves at constant confinement are flatter for 50 kPa and 100 kPa compared to 150 kPa and 200 kPa. This behavior implies that nonlinearity of modulus reduction increases with increases in confinement. Pestana and Salvati (2006) reported similar behavior for Monterey sand.
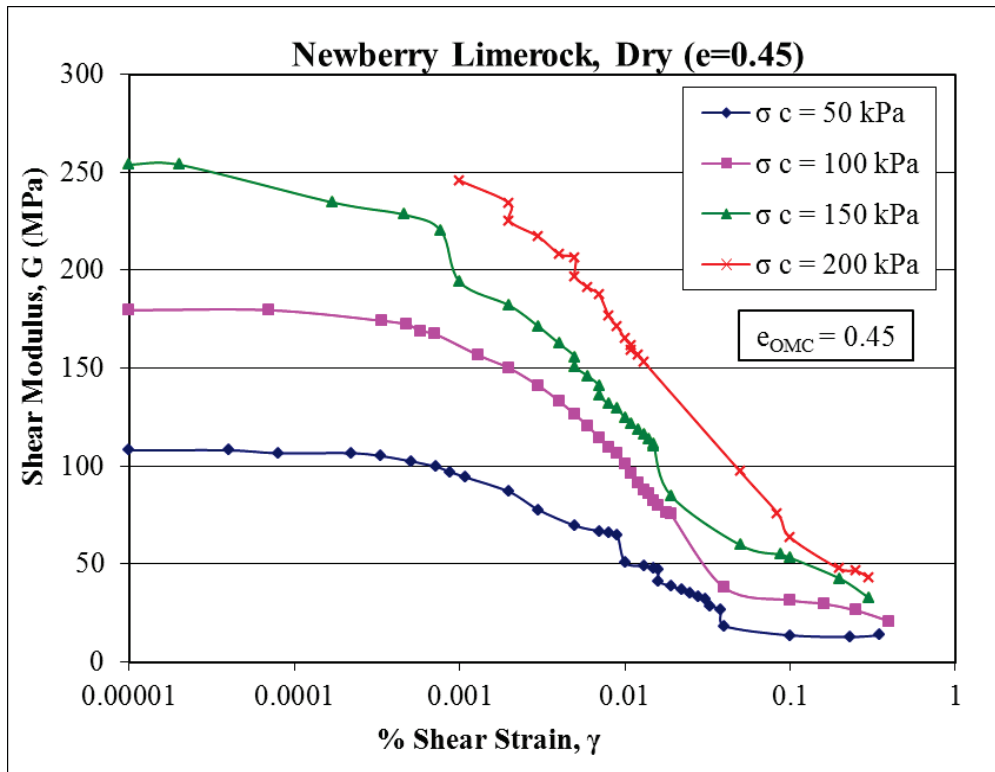
Figure 5-1. Shear modulus (G) versus shear strain (γ) curves for dry Newberry limerock at e_{OMC} (i.e., e = 0.45).
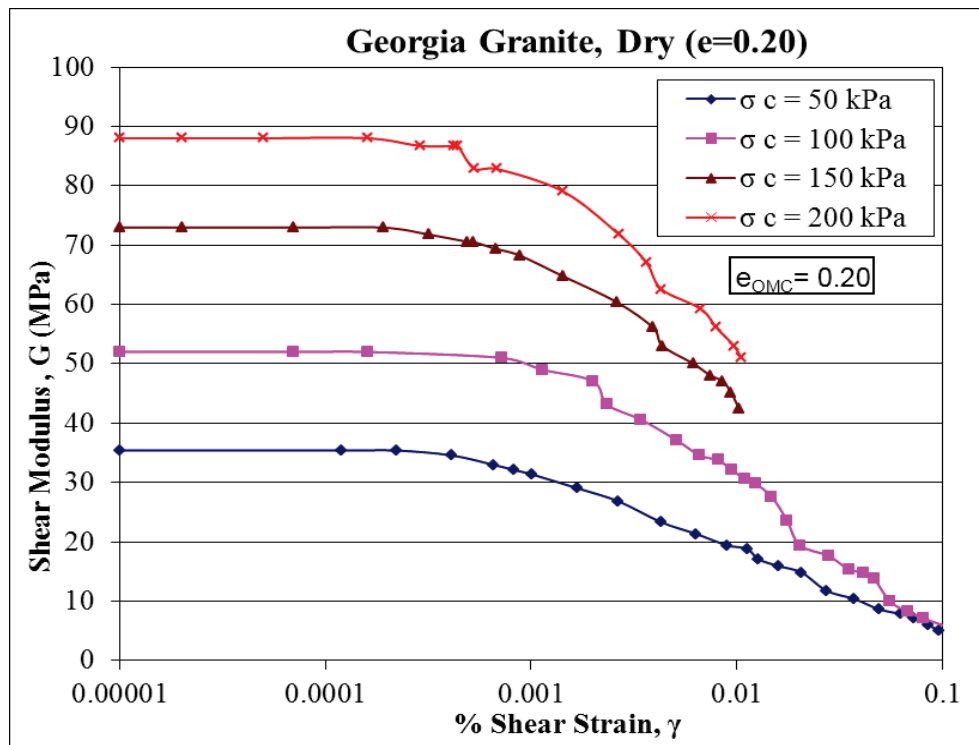
Figure 5-2. Shear modulus (G) versus shear strain (γ) curves for dry Georgia granite at e_{OMC} (i.e., e=0.20).
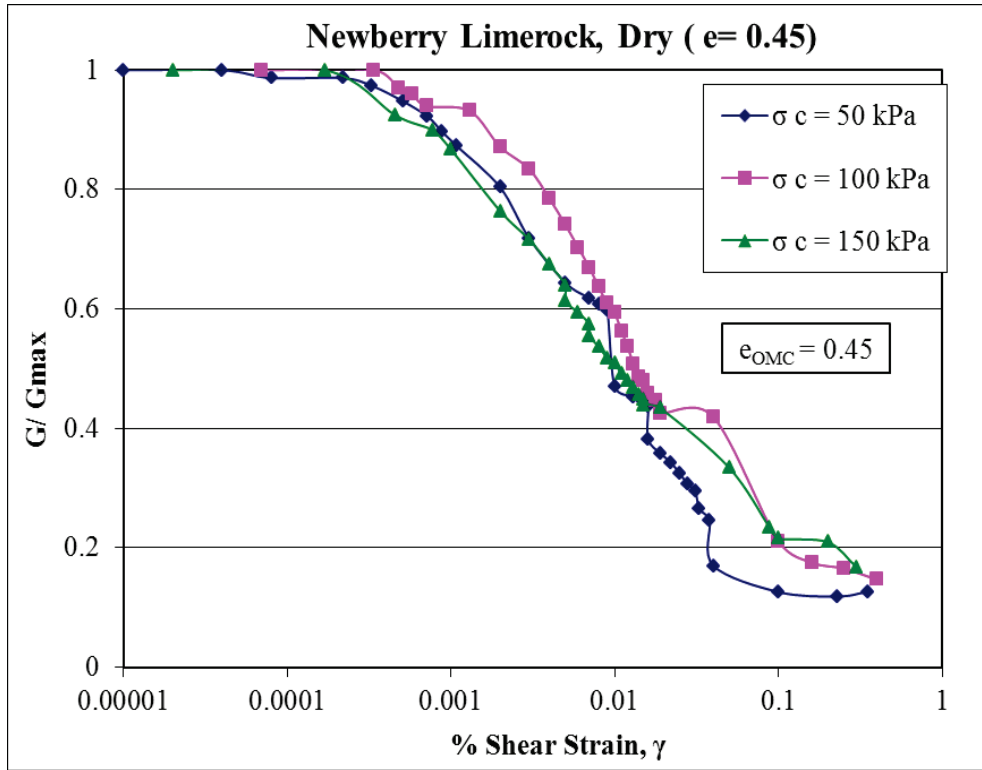
Figure 5-3. G/G$_{max}$ versus shear strain (γ) curves at e = e$_{OMC}$ for Newberry limerock.
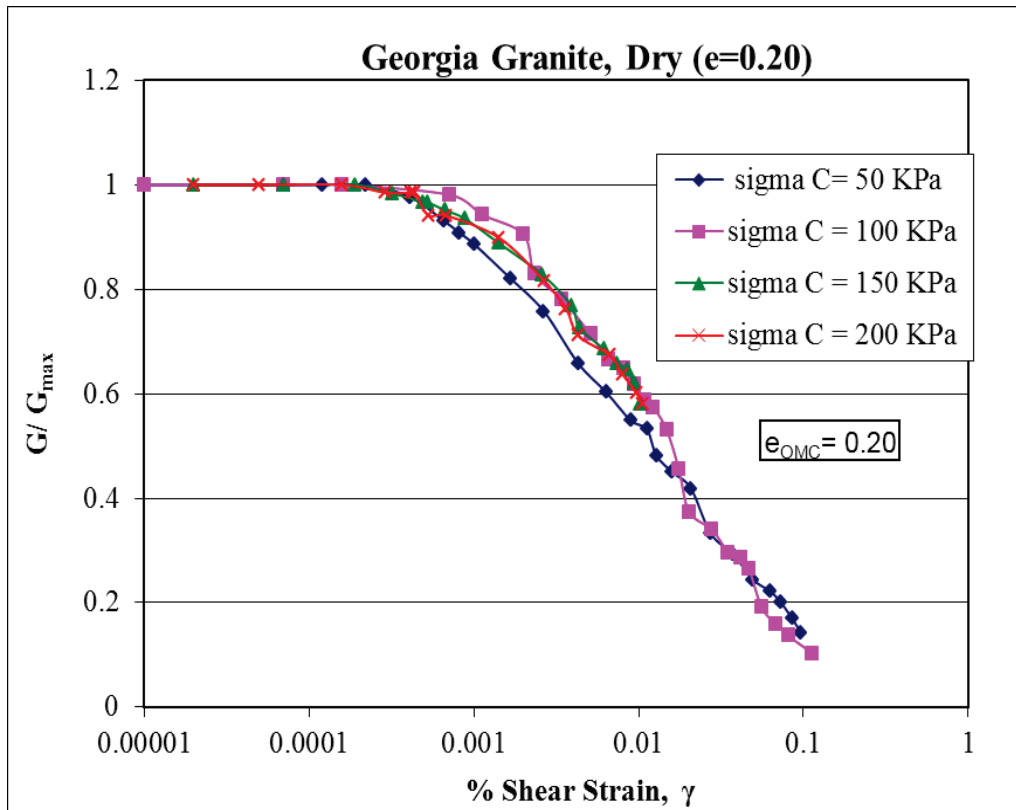
Figure 5-4. G/G$_{max}$ versus shear strain (γ) curves at e = e$_{OMC}$ for Georgia granite.

69

G/G$_{max}$ normalized curves for any confining pressure (Figures 5-3 and 5-4) are very similar, indicating that rate of decrease in modulus with increase in strain does not depend on confining pressure. In Figure 5-5, normalized data points for both materials lie well within the maximum and minimum ranges of gravel soils reported by Seed et al. (1986). Lin et al. (2000) (Figure 2-5) and Yasuda and Matsumoto (1993) (Figure 2-3) reported similar behavior for gravelly soils. However, Rollins et al. (1998) reported that, G/G$_{max}$ versus γ curves are different for different confinements and move from the low end of the data range towards the high end with an increase in confinement (Figure 2-12). They also point out that the deviation between various confinements are relatively small and use of a best-fit hyperbolic curve for any confining pressure would not likely cause significant error.

G$_{max}$ values (G at 10^{-5}% strain) at different void ratios (e) and different confining pressures are plotted on a log-log plot of modulus versus confining pressure and shown in Figures 5-6 and Figure 5-7. Empirical equations in the form of Equation 2-5 were derived for each material by plotting a trend line for the set of G$_{max}$ values at different void ratios as shown in Figure 5-8. The empirical equations for each material are as follows:

- Newberry limerock: $G_{max} = (2575) F(e) (\sigma_c)^{0.772}$ (5-1)

- Georgia granite: $G_{max} = (816) F(e) (\sigma_c)^{0.6638}$ (5-2)

where G$_{max}$ and σ$_c$ are in kPa. It is noted that shear modulus of Newberry limerock is proportional to pressure confinement to the power of 0.702 while Georgia granite is proportional to pressure confinement to the power of 0.6638. These values agree well with values report in literature, i.e., in the range of 0.5-0.85 for gravel type soils (Menq, 2003). These equations can be used to calculate G$_{max}$ of dry material under any confining pressure and void ratio (e).
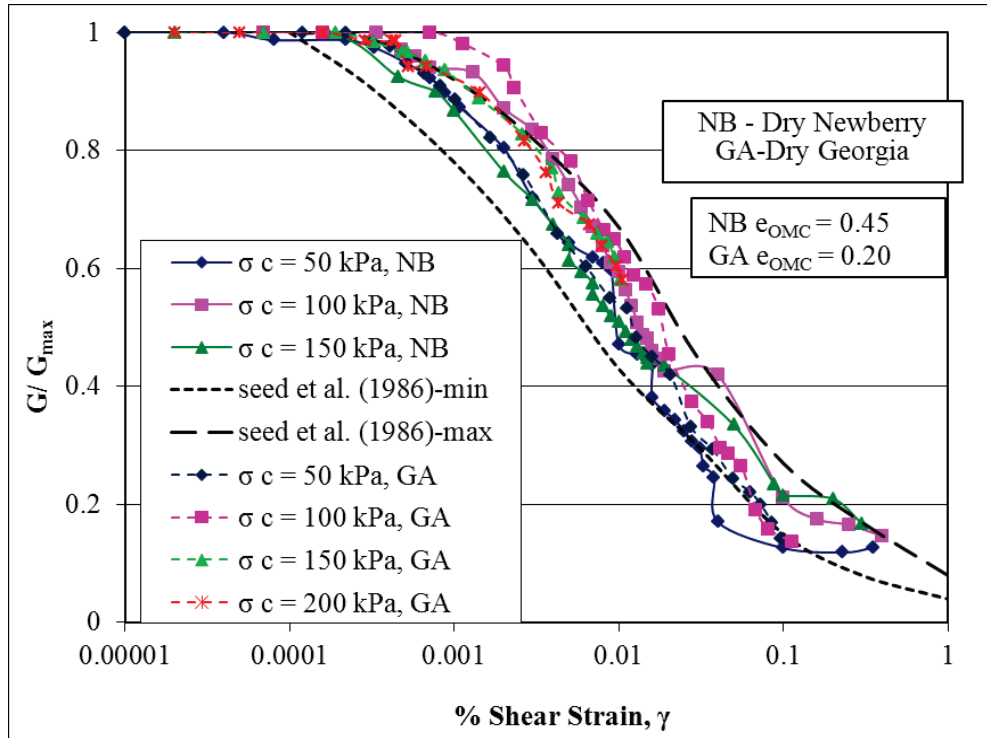
Figure 5-5. Comparison of G/G_{max} versus shear strain (γ) data of Newberry limerock and Georgia granite with Seed and Idriss (1986) maximum and minimum limits.
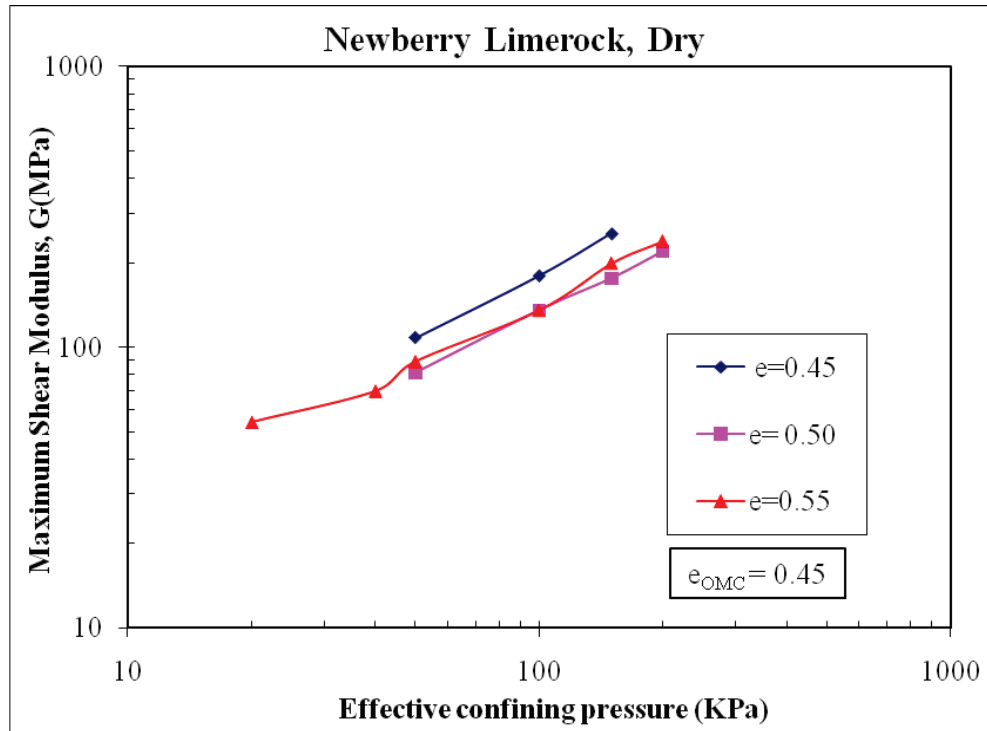
Figure 5-6. G_{max} versus confining pressure for Newberry limerock at different void ratios.
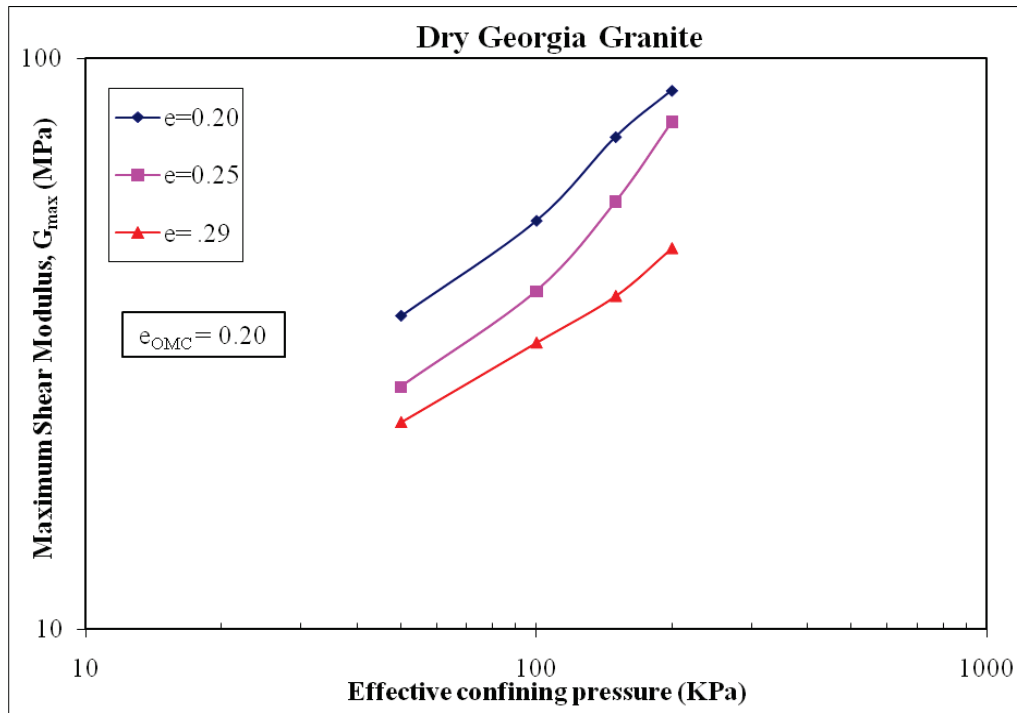
Figure 5-7. G_{max} versus confining pressure for Georgia granite at different void ratios.
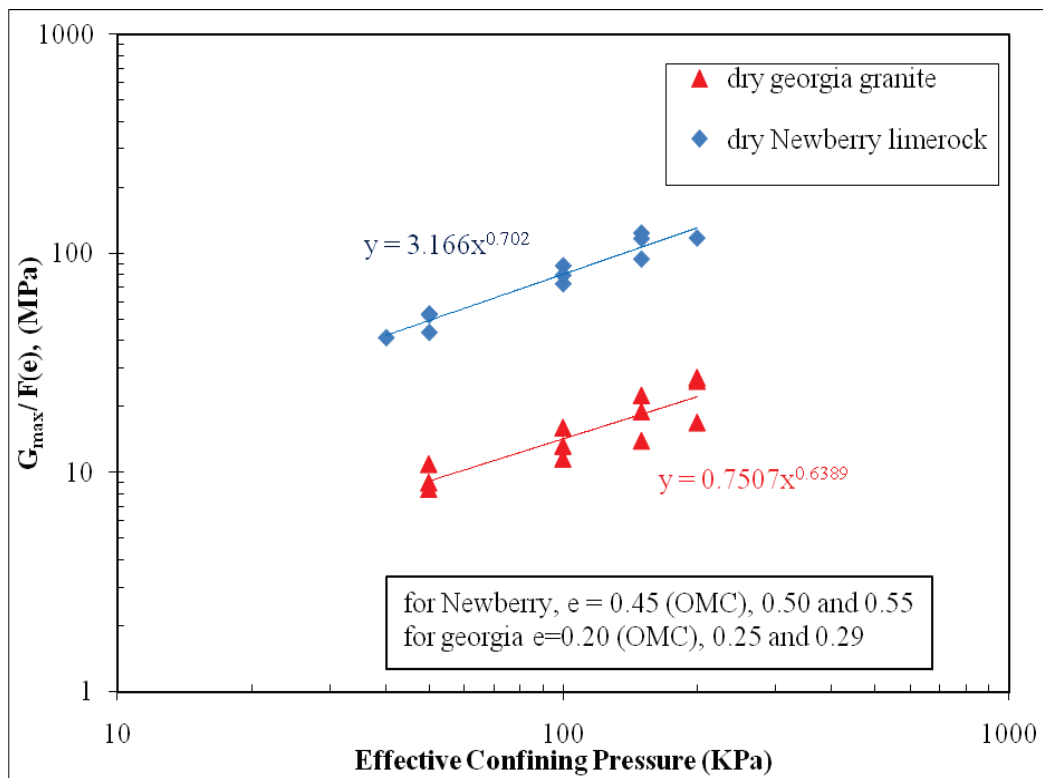
Figure 5-8. G_{max} empirical equations for Newberry limerock and Georgia granite.

5.1.2 Unsaturated (Wet) Specimen Testing Results

The primary goals of conducting fixed-free RC tests on unsaturated specimens is to characterize modulus nonlinearity at different moisture contents and strain levels, and to evaluate the suction effect due to drying on modulus. Based on previous research investigations conducted by Toros (2008), very small-strain modulus (G_{max}) of base course soils increases with a decrease in moisture content. He dried OMC compacted specimens in different environments and tested them at different moisture contents during the process of drying, starting from OMC to nearly zero moisture content. Cho and Santamarina (2001) reported that specimen drying simulates actual drying in real field conditions and makes the material stiffer compared to compacting the specimen at required moisture content. Thus, the modulus of the material is higher in case of dried specimen than in the case of compacted specimen at required moisture content. Hence, to simulate actual field conditions for our testing, we achieved different moisture contents by drying OMC compacted specimens.

For our testing program, 4-in. by 8-in. cylindrical specimens were compacted at OMC using modified Proctor compaction. These OMC compacted specimens were allowed to dry in laboratory environment (i.e., at room temperature) by leaving them without any membrane cover. Specimens dried to different moisture contents in this method were tested to determine modulus at different shear strain levels, from as low as 10^{-5}% (very small-strain) and as high as 10^{-1}% (medium to large strains).

5.1.2.1 Equipment Limitations

As previously explained in section 3.1.6, the stiffness capacity of the fixed-free resonant column apparatus is reached at a resonant frequency of 300 Hz. Based on this limitation, the specimen moisture contents that could be tested are given in Table 5-1.

Table 5-1. List of unsaturated specimen moisture contents.

Material	Void ratio at OMC (e_{OMC})	Moisture content at saturation (%)	Tested moisture content (%)	Degree of saturation, S_r (%)
Newberry limerock	0.45	16.5	13	78.6
			12	72.5
			11	66.5
			10	60.4
Georgia granite	0.2	7.3	5.5	75.3
			4.5	61.7
			3.5	48

5.1.2.2 Confinement Effect on Unsaturated Specimens

Similar to dry specimen testing, initially it was planned to test unsaturated specimens under confinement pressures of zero (i.e., no confinement), 50, 100, 150, and 200 kPa. However, for tests conducted on unsaturated specimens under confinement, no increase in modulus was observed for an increase in confinement. This is explained by a buildup of pore pressure inside the specimens, as the specimens could only be tested in an undrained condition due to limitations with the testing apparatus. Thus, as an alternative, the modulus of unsaturated material under actual confinement can be calculated approximately by an indirect method that is explained in a later section of this chapter.

5.1.2.3 Results and Analysis

Shear modulus versus strain plots of unsaturated specimens tested at different moisture contents under no confinement are shown in Figure 5-9 for Newberry limerock and in Figure 5-10 for Georgia granite. The dry specimen testing curve corresponding to 50 kPa confining pressure is also included for comparison purposes. From these plots it can be observed that:
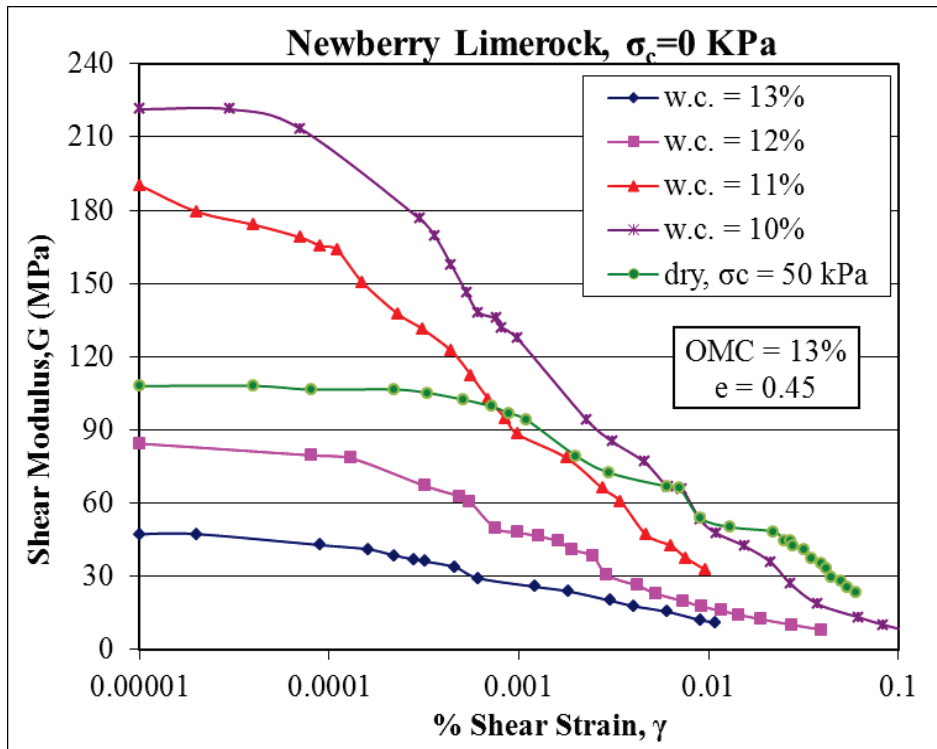
Figure 5-9. Shear modulus (G) versus shear strain (γ) curves for Newberry limerock at different moisture contents.
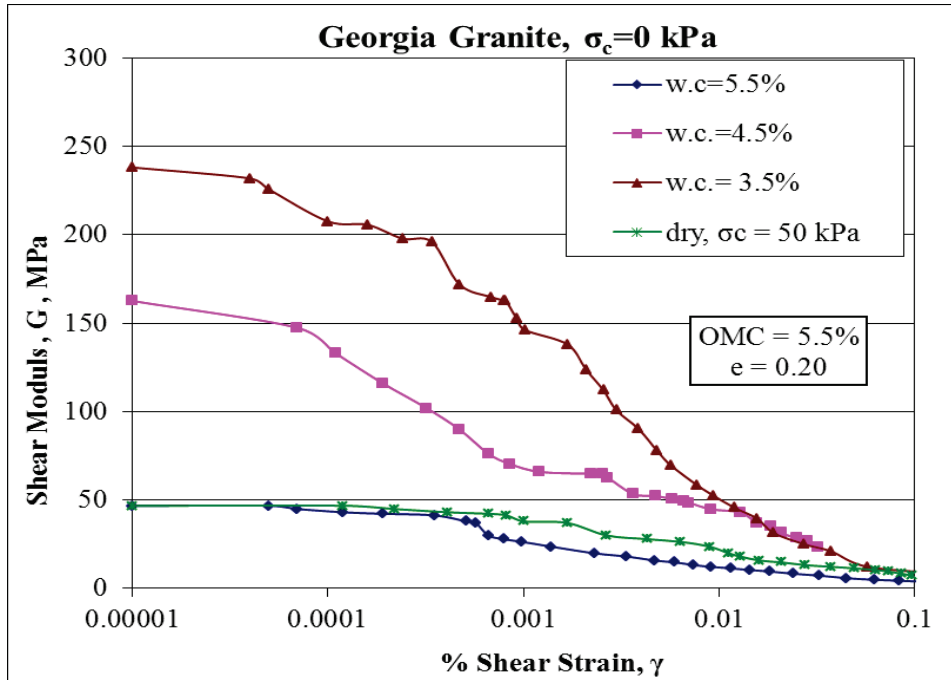
Figure 5-10. Shear modulus (G) versus shear strain (γ) curves for Georgia granite at different moisture contents.

- At constant strain magnitude, modulus increases with a decrease in moisture content and is maximum (i.e., G_{max}) at very small-strain (i.e., 10^{-5}%). G versus γ curves at different moisture contents behave similar to the dry curves at different pressure confinements presented in Figure 5-1 and Figure 5-2. Since the void ratio is the same for both dry and wet specimens (i.e., @e_{OMC}), the increase in G with decrease in moisture content is likely due to an increase in effective confinement, i.e., suction or negative pore pressure. Although no pore pressure measurements were obtained to prove the presence of suction, research investigations by Wu et al. (1984), Qian et al. (1993), and Cho and Santamarina (2001) report that a decrease in moisture content increases suction and thus additional confinement. This phenomenon is also well explained in unsaturated soil mechanics (Lu and Likos, 2004).

- At different moisture contents, the difference in moduli at the same strain magnitude decreases with an increase in strain, similar to dry soils. This implies that the suction confinement effect decreases with an increase in strain.

- G decreases at a faster rate with increase in γ in low-moisture-content specimens compared to high-moisture-content specimens. This could be due to a failure of suction menisci at lower strains in low moisture content specimens. Cho and Santamarina (2001), from their microscale particle menisci studies, reported that the strain at menisci failure decreases with a decrease in moisture content and small menisci may fail before the strain at peak strength of soil. Hence, at low moisture contents, small suction menisci cause high small-strain modulus and modulus decreases at a faster rate due to early menisci failure.

- In a dry condition, shear modulus is maximum (i.e, G_{max}) at 10^{-4}% strain and decreases to 0.15 G_{max} at 10^{-1}% strain. Whereas in an unsaturated condition, shear modulus is maximum at 10^{-5}% strain and decreases to 0.075 G_{max} at 10^{-1}% strain. This implies that in unsaturated gravelly soils, the presence of moisture increases nonlinearity in modulus reduction and modulus starts decreasing from 10^{-5}% strain. Menq (2003) observed this same behavior in gravelly soils. An increase in modulus nonlinearity is probably due to a water lubrication effect, which reduces inter particle frictional contact forces, allowing easier and irreversible soil particle movement, even at strains lower than 10^{-4}%.

- Similar to dry specimens, in wet specimens at strains of 10^{-1}% and higher the difference in moduli at different moisture contents is very minimal. This implies that a suction confinement effect on modulus becomes less significant at higher strains.

- In case of Newberry limerock, G_{max} at 13% (OMC) and 12% moisture contents is lower than that of dry case at 50 kPa pressure confinement, which implies that additional confinement due to suction is less than 50 kPa at 13% and 12% moisture content and higher than 50 kPa at moisture content 11% and lower. Similarly, in case of Gerogia Granite, G_{max} at 5.5% (OMC) moisture content is almost equal to G_{max} of dry soil at 50 kPa, which means at moisture contents lower than 5.5%, confinement due to suction is greater than 50 kPa. Additional confinement provided due to suction is calculated and corresponding results are shown in a later section.

Normalized curves of G/G_{max} versus logarithmic shear strain (γ) for both dry and wet specimens are shown in Figure 5-11 and Figure 5-12. From these plots, it can be observed that in the case of dry specimens, normalized curves for any confining pressure are very similar. This indicates that the rate of decrease in modulus with increase in strain does not depend on confining pressure. In the case of unsaturated specimens, normalized curves for any moisture content are also very similar. This indicates that the rate of decrease in modulus of unsaturated specimens with an increase in strain does not depend on moisture content and its suction effect. It is also observed that the normalized curves for unsaturated specimens are below those of dry specimens, and this indicates that the rate of decrease in modulus with increase in strain is higher in unsaturated soils and hence the modulus nonlinearity is higher in an unsaturated condition. Based on microscale particle level studies of Cho and Santamarina (2001), higher modulus nonlinearity in unsaturated specimens is due to early failure of small menisci at very small-level strains. Menq (2003) observed the same difference in case of dry and partially saturated gravelly soils behavior.

Shear modulus (G) normalized with shear modulus at OMC (G_{OMC}) versus moisture content plots for different strain levels are shown in Figures 5-13 and Figure 5-14. At any given strain magnitude, the increase in G/G_{OMC} with decrease in moisture content is approximately the same. In other words, additional confinement provided due to the suction effect (various magnitudes at different moisture contents) is not changing, i.e., it is the same at different strain levels. It appears that, unsaturated material under additional confinement due to suction, behaves similar to dry material under external constant confinement. Cho and Santamrina (2001) reported in their particle level studies that menisci failure strains (ε=0.01 to 1) are higher than threshold strains for sands. Since strain magnitudes are smaller than threshold strains, Cho and
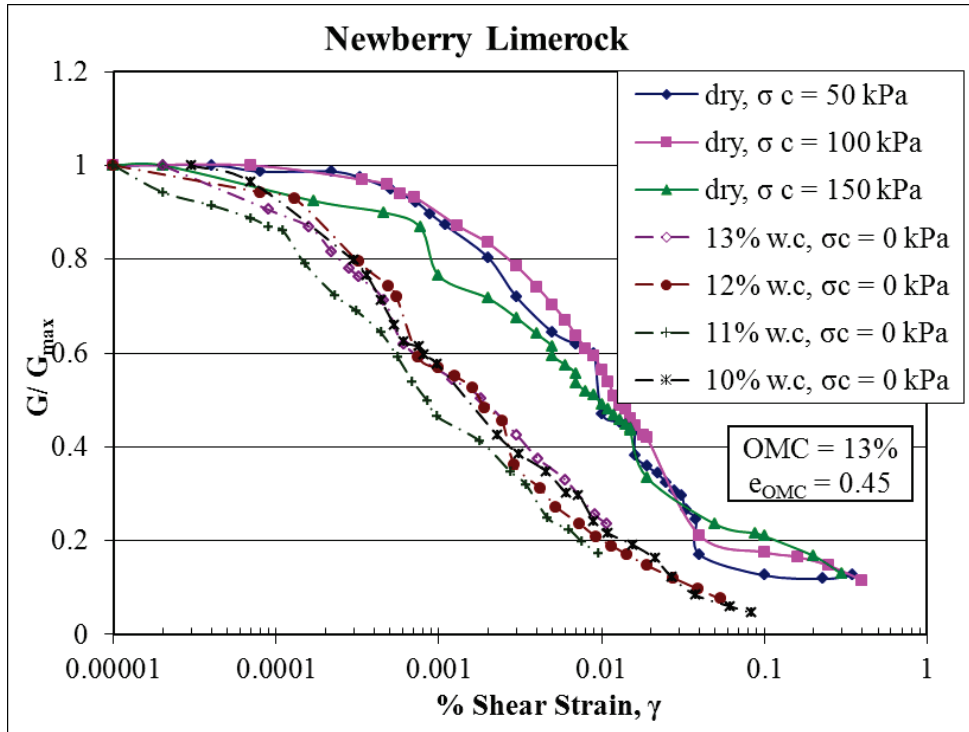
Figure 5-11. G/G$_{max}$ versus shear strain curves for Newberry limerock for both dry and wet specimens.
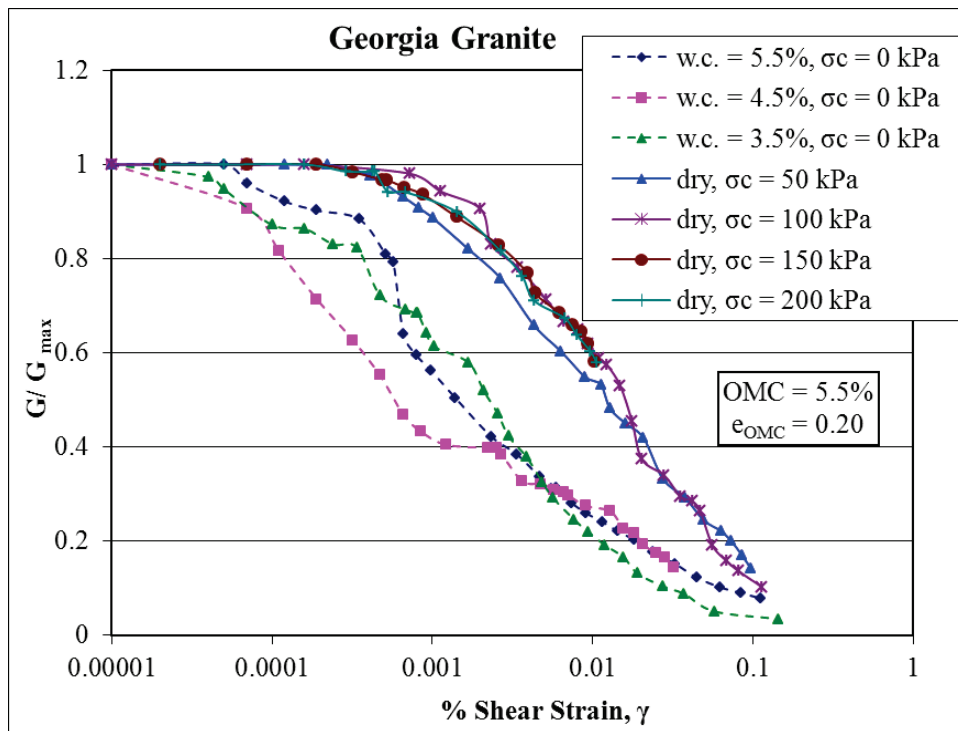
Figure 5-12. G/G$_{max}$ versus shear strain curves for Georgia granite for both dry and wet specimens.
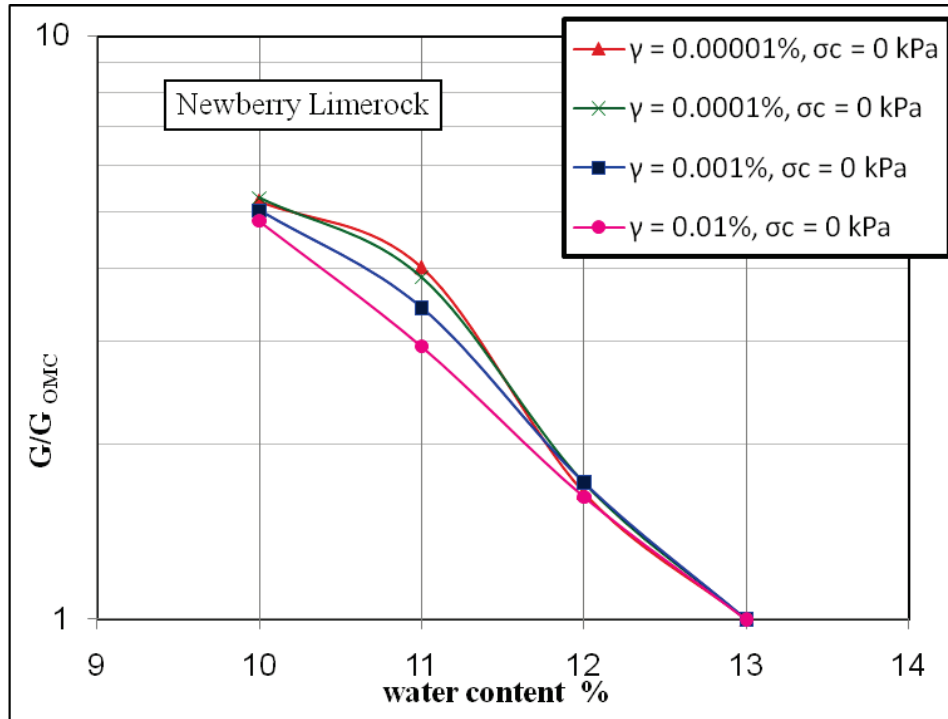
Figure 5-13. G/G$_{OMC}$ versus moisture content at different strain levels for Newberry limerock.
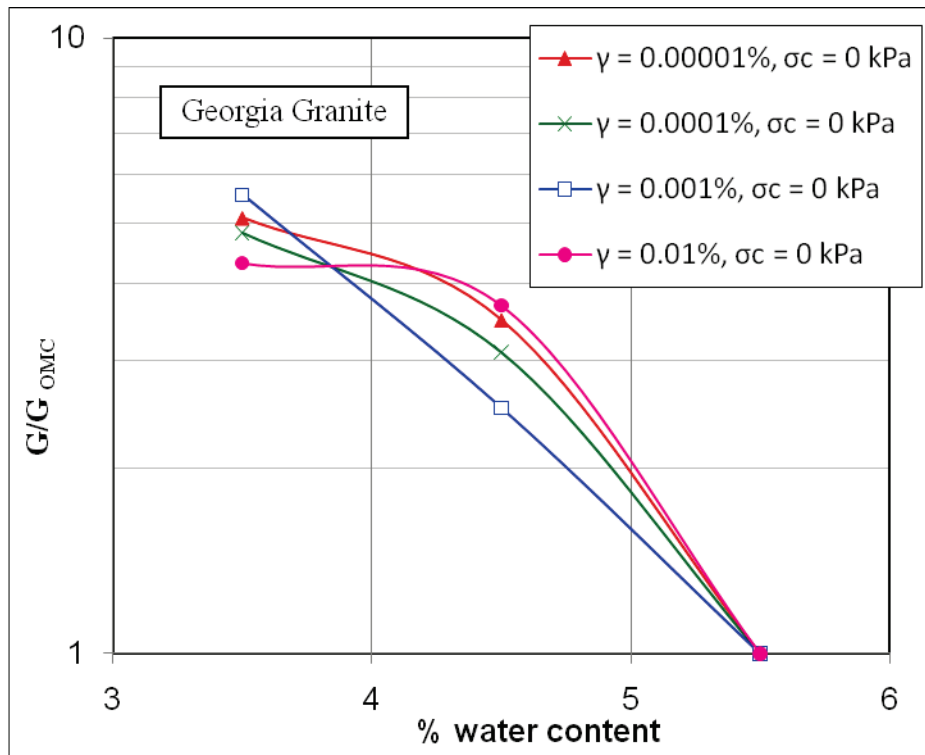
Figure 5-14. G/G$_{OMC}$ versus moisture content at different strain levels for Georgia granite.

Santamarina's findings support our observations that the suction effect remains the same irrespective of strain magnitude. A further detailed particle study is required to analyze the strain level effect on menisci failure and its suction effect.

5.1.2.4 Additional Confinement Pressure Due to Suction

By comparing dry and wet specimen testing results, the additional confinement pressure provided by suction can be evaluated and a detailed procedure is explained below.

From dry specimen testing results, Equations 5-1 and 5-2 were derived to calculate G_{max} (i.e., G at $\gamma = 10^{-5}\%$) of dry material at different confining pressures. At e_{OMC}, G_{max} for any chosen confining pressure can be calculated using Equations 5-1 and 5-2. By substituting the unsaturated specimen G_{max} value obtained at a given moisture content into these equations, the confinement pressure required to obtain the dry specimen's G_{max} can be calculated. Following this procedure, the additional effective stress or confinement due to suction at different moisture contents or degree of saturation was determined and are shown in Figures 5-15 and 5-16. It can be observed that the increase in additional confinement for decreasing moisture content is much higher in Georgia granite compared to Newberry lime rock. This is due to low e_{OMC} and a higher reduction in degree of saturation (S_r) in Georgia granite. For the same amount of reduction in moisture content, in soils with low void ratio the degree of saturation reduces more rapidly than soils with high void ratio. As the degree of saturation decreases faster, suction magnitude increases proportionally faster and hence an increase in additional confinement at a faster rate.

5.2 Free-Free Resonant Column Testing

Free-free resonant column (free-free RC) tests were run on modified Proctor compacted specimens of Newberry limerock and Georgia Granite under no confinement to measure very small-strain Young's modulus (E). OMC compacted specimens were placed in a laboratory environment and tested at different moisture contents during drying, starting at OMC and down
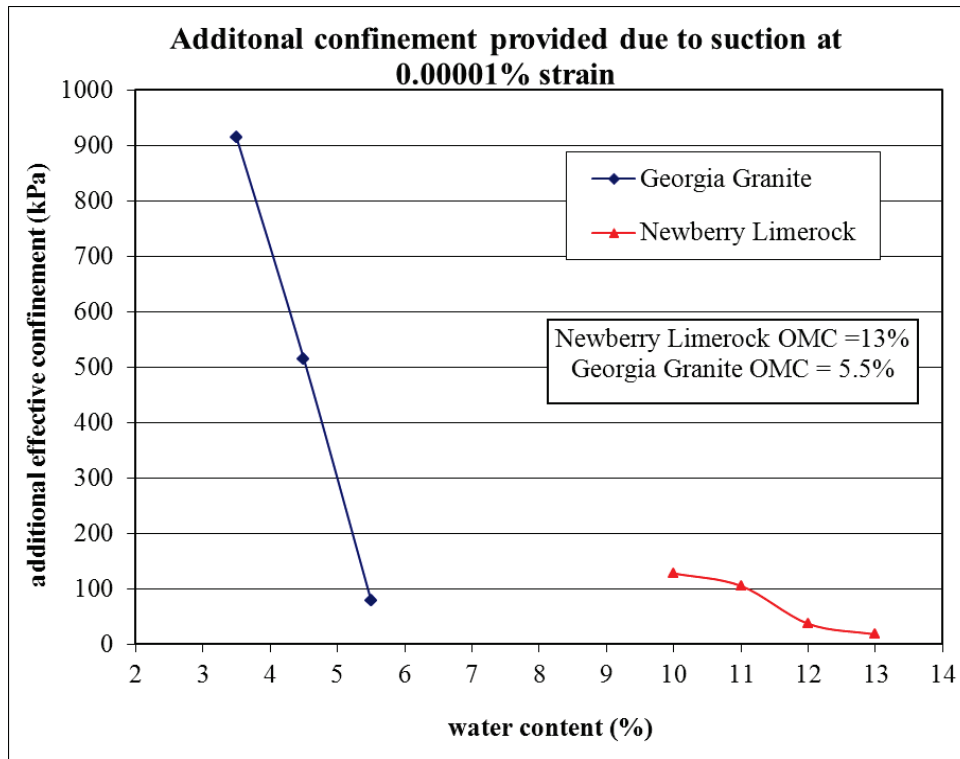
Figure 5-15. Additional confinement provided due to suction at 10^{-5}% strain at different moisture contents.
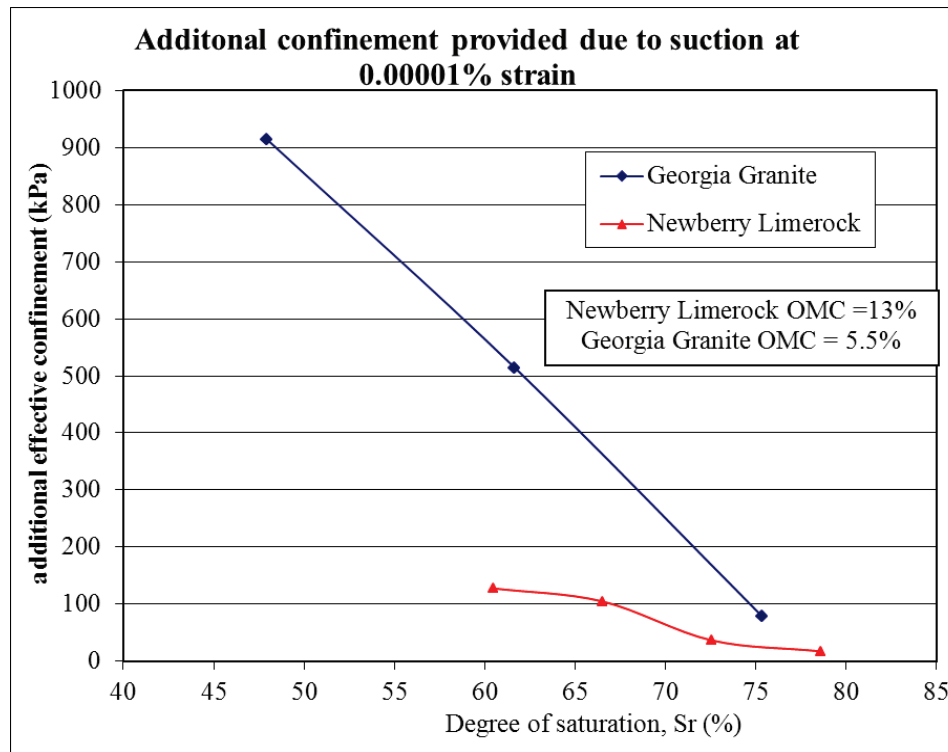
Figure 5-16. Additional confinement provided due to suction at 10^{-5}% strain at different degrees of saturation.

81

to nearly zero. Toros (2008) conducted similar tests, but used a plastic cylindrical case around the specimens that likely provides some confinement. Results are presented, compared, and discussed in the following sections.

5.2.1 Results and Discussion

Free-free RC with no confinement test results for both Newberry lime rock and Georgia granite are shown in Figures 5-17 and 5-18, respectively. These results show that in both materials very small-strain Young's modulus (E_{max}) increases with a decrease in moisture content. These trends are similar to results reported by Toros (2008). Toros (2008) concluded that the increase in modulus with decrease in moisture content is probably due to an increase in additional confinement due to suction. Free-free results are compared with fixed-free RC test results at very small-strain (i.e., 10-5%) and free-free RC results of Toros (2008) and presented in Figures 5-19 and 5-20. It can be observed that:

- Fixed-free RC moduli values at 10^{-5}% strain are nearly equal to those of free-free RC results at corresponding moisture contents. This implies that the strain magnitudes of free-free RC testing are close to 10^{-5}%. A close observation of these plots suggests that fixed-free RC moduli values are slightly higher. This difference is possibly due to the weight of motor and top specimen cap attached to specimen top in fixed-free RC testing, which might provide some actual confinement, hence resulting in slightly higher moduli values compared to free-free RC moduli values at no confinement.

- At the same moisture content, the Toros (2008) free-free RC moduli values are higher than our free-free RC moduli values. The materials and method of compaction were the same for both tests with the only difference being the casing confinement. Our free-free RC tests were run on specimens with no casing and Toros (2008) free-free RC tests were run on specimens with plastic mold. Toros compacted specimens in plastic cylindrical molds and tested specimens with the mold. These plastic cylinders might provide some confinement around the side surface of the specimen, which might have resulted in higher moduli values compared to that of specimens with no confinement.
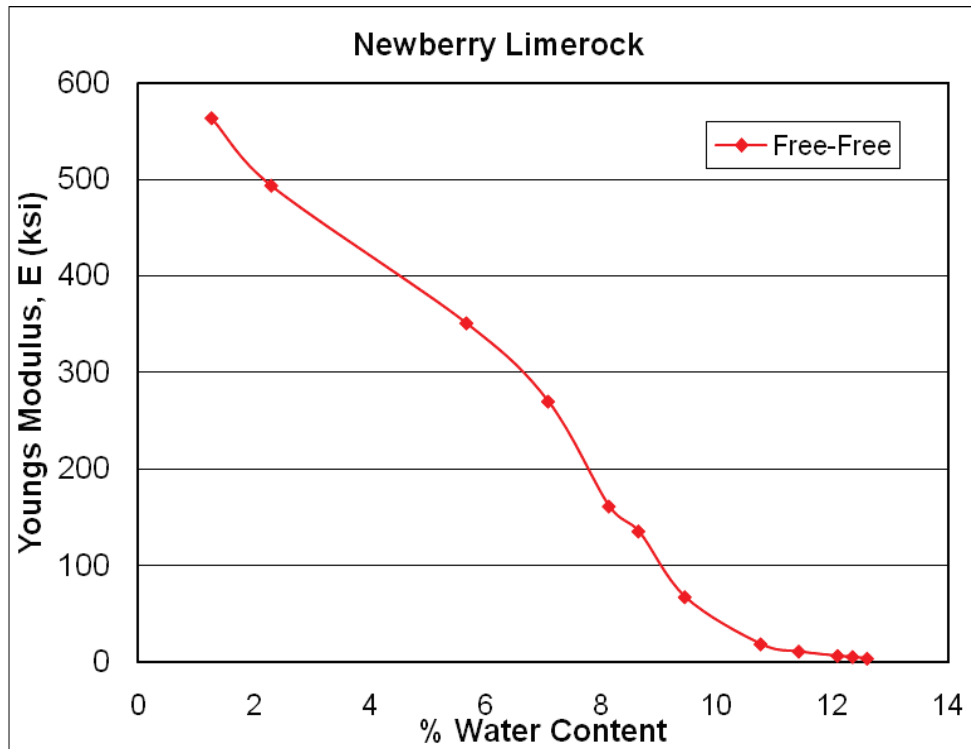
Figure 5-17. Young's modulus versus moisture content results from free-free RC test on Newberry limerock.
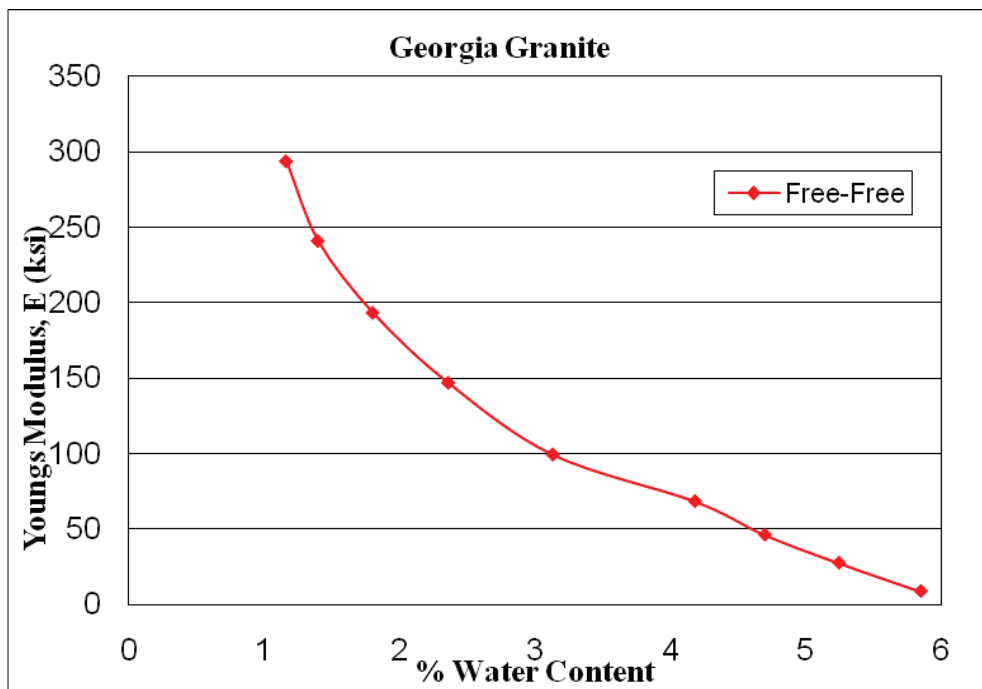
Figure 5-18. Young's modulus versus moisture content results from free-free RC test on Georgia granite.
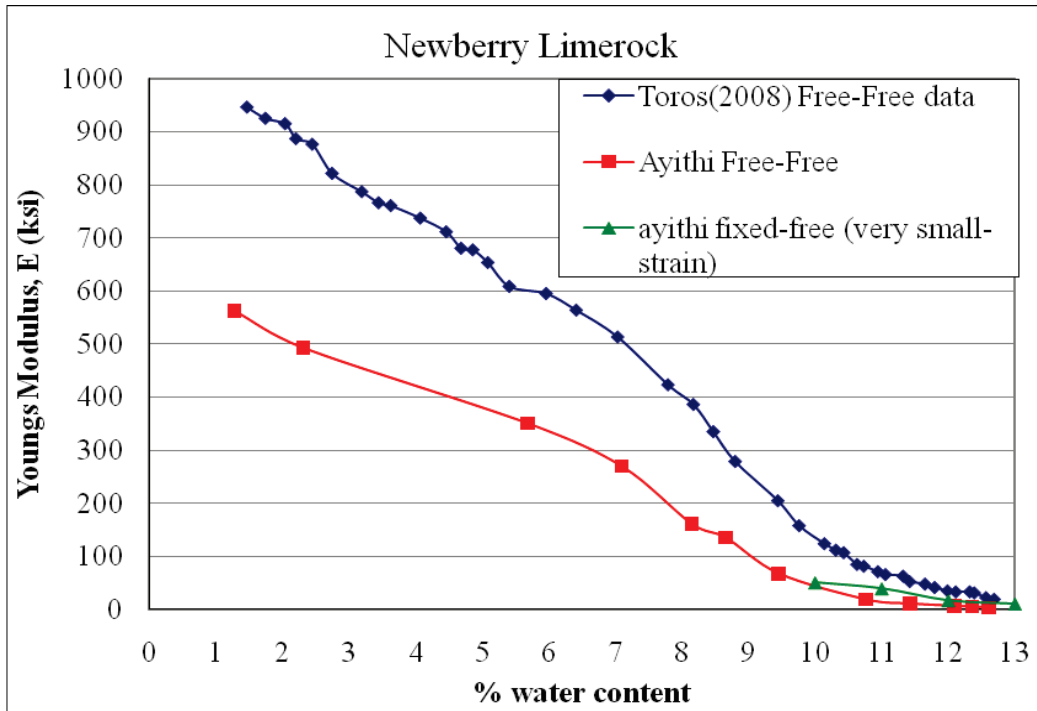
Figure 5-19. Comparison of Newberry limerock free-free RC test data with fixed-free RC at very small-strain data and Toros (2008) data.
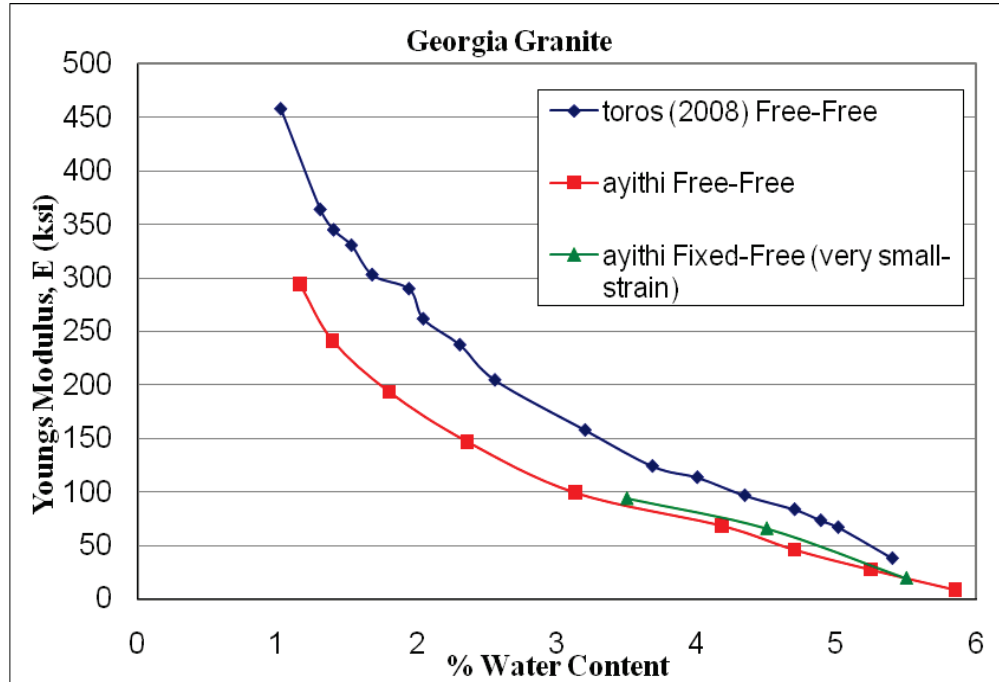
Figure 5-20. Comparison of Georgia granite free-free RC test data with fixed-free RC at very small-strain data and Toros (2008) data.

5.2.2 Method to Estimate Approximate Modulus

G_{max} of dry material can be determined via Equations 5-1 and 5-2, which were derived based on dry material fixed-free RC testing results. By knowing G_{max} at any moisture content under no confinement (either from fixed-free RC or free-free RC) and substituting this value in Equation 5-1 or 5-2, the additional effective stress provided due to suction can be calculated by following the procedure explained in section 5.1.2.4. By adding this additional confinement stress to the initial confinement where where an estimate of modulus is required, an approximate G_{max} value can be calculated via Equations 5-1 and 5-2. From Figures 5-11 and 5-12, it is understood that G/G_{max} versus strain curves behave similarly at any moisture content. Thus, after calculating G_{max} at a given confinement and moisture content using Equations 5-1 and 5-2, the value of G/G_{max} at a required strain level can be determined from Figures 5-11 and 5-12, from which an approximate value of G can be calculated.

5.3 Closing Remarks

- G_{max} of dry Newberry limerock and dry Georgia Granite at e_{OMC} and known confinement can be determined using Equations 5-1and 5-2.

- Shear modulus of dry gravelly soils is maximum and elastic at strains lower than $10^{-4}\%$ and starts decreasing linearly in the strain range of $10^{-4}\%$ to $10^{-3}\%$ and nonlinearly thereafter. The presence of gravel size aggregate makes modulus of gravelly soils more nonlinear compared to sands.

- In unsaturated gravelly soils, capillary suction confinement increases with a decrease in moisture content and has significant effect on G_{max}.

- Shear modulus of unsaturated gravelly soils is maximum at $10^{-5}\%$ strain and decreases thereafter with an increase in strain. The presence of moisture increases modulus nonlinearity in unsaturated gravelly soils compared to dry gravelly soils.

- In dry gravelly soils, the rate of decrease in G with an increase in strain is independent of confinement pressure. In unsaturated gravelly soils, the rate of decrease in G with increase in strain is independent of moisture content and its suction confinement.

- In unsaturated gravelly soils, at any moisture content, the suction effect on G does not change with an increase in strain.

- Strain magnitudes generated in free-free RC testing are approximately 10^{-5}% and corresponding moduli are nearly equal to very small-strain moduli obtained from fixed-free RC testing.

- At 10^{-5}% strain, additional confinement due to suction can be as high as 900 kPa, which is equivalent to 39 m of overburden pressure confinement. Since confinement due to suction can influence soil modulus significantly, it is important to consider suction effects in determination of base layer design modulus.

CHAPTER 6
NONLINEAR FINITE ELEMENT MODELING OF BASE LAYER

One of the main objectives of this research study was to develop a nonlinear pavement response model that can utilize the laboratory testing results presented in Chapter 5 and incorporate base modulus nonlinearity with respect to effective stress confinement, loading strain, and moisture content. The Plaxis Hardening Soil small model (Plaxis-HSsmall), a nonlinear finite element model software was selected for our nonlinear analysis. A detailed discussion of its features, suitability for our analysis, and analysis methodology are presented in this chapter.

6.1 Plaxis-Hardening Soil-Small Model (Plaxis-HSsmall Model)

Plaxis is a special purpose two-dimensional finite element computer program used to perform deformation and stability analysis for various types of geotechnical applications. Either a plain strain or an axisymmetric model may model real situations.

HSsmall model is an elastoplastic type of hyperbolic model and incorporates strain dependent stiffness moduli simulating the different reaction of soils to small strain (i.e., strains below 10^{-3}%) and large strains (i.e., strains above 10^{-1}%). Soil modulus behaves elastic at very small-strains (i.e., lower than 10^{-4}%) and decreases nonlinearly with an increase in strain amplitude. Figure 6-1 shows an example of a typical S-shaped soil modulus reduction curve.

The most frequently used hyperbolic model to estimate nonlinear modulus reduction in soils (Figure 6-1), including both small and large strains, is the Hardin-Drnevich relationship:

$$\frac{G}{G_{max}} = \frac{1}{1+\left|\frac{\gamma}{\gamma_r}\right|} \tag{6-1}$$

where threshold strain is quantified as:

$$\gamma_r = \frac{\tau_{max}}{G_{max}} \tag{6-2}$$
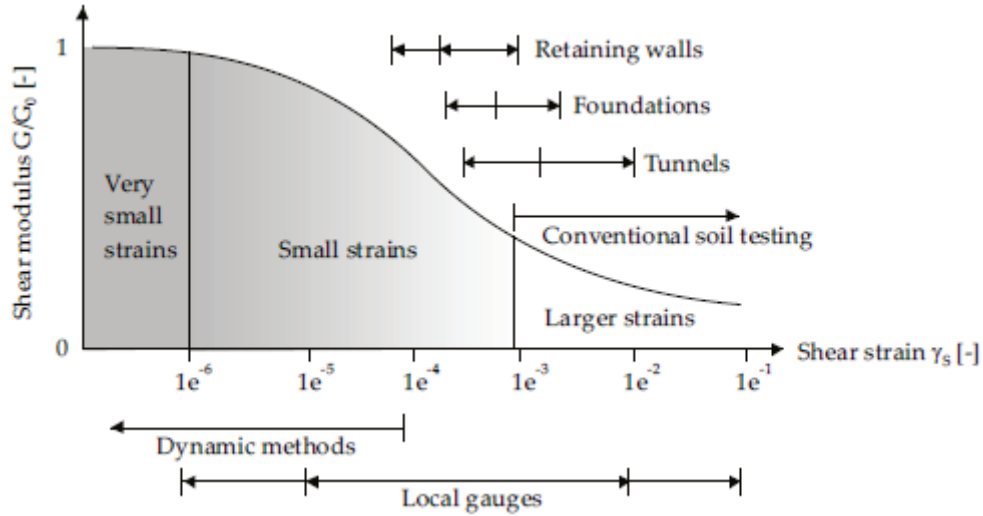
Figure 6-1. Characteristic modulus versus strain behavior of soil with typical strain ranges for laboratory tests and structures (from Atkinson and Sallfors, 1991).

HSsmall uses a modified Hardin-Drnevich relationship proposed by Santos and Correia (2001):

$$\frac{G}{G_{max}} = \frac{1}{1+a\left|\frac{\gamma}{\gamma_{0.7}}\right|} \qquad (6\text{-}3)$$

where $\alpha = 0.385$ and $\gamma_{0.7}$ is the shear strain at $G = 0.7 * G_{max}$. Figure 6-2 shows the fit of the relationship (Equation 6-3) with Santos and Correia (2001) testing data. Therefore, two parameters are needed to describe the modulus behavior at small strains:

- The initial or very small-strain modulus G_{max}

- The shear strain level $\gamma_{0.7}$

Some additional basic characteristics of the HSsmall model include:

- Stress-dependent stiffness according to a power law (input parameter m)

- Plastic straining due to primary deviatoric loading (input parameter $E_{50}{}^{ref}$)

- Plastic straining due to primary compression (input parameter $E_{oed}{}^{ref}$)

- Elastic unloading/reloading (input parameters $E_{ur}{}^{ref}$ and ν_{ur})

- Failure according to the Mohr-Coulomb model (iInput parameters c, φ and ψ)

- Nonlinear reduction of small-strain modulus (input parameters G_{max} and $\gamma_{0.7}$)
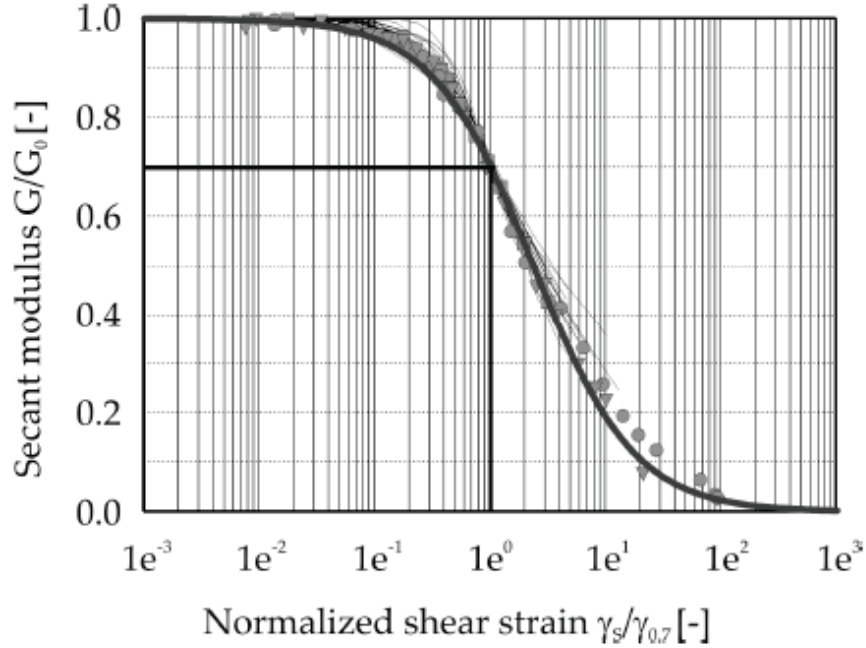
Figure 6-2. Results from modified Hardin-Drnevich relationship compared to test data by Santos and Correia (2001).

6.1.1 Parameters of HSsmall Model

The input parameters required for the HSsmall model are presented in Table 6-1. All stiffness related parameters (i.e., G_{max}^{ref}, E_{50}^{ref}, E_{oed}^{ref} and E_{ur}^{ref}) are defined at a particular reference stress at which they are determined in laboratory testing. Based on the stiffness value defined at a particular reference stress, Plaxis-HSsmall model calculates stiffness values at any required stress for given conditions using the following equations:

$$G_{max} = G_{max}^{ref} \left(\frac{c \, cos\varphi - \sigma_1' \, sin \, \varphi}{c \, cos \, \varphi + p^{ref} \, sin \, \varphi} \right)^m \tag{6-4}$$

$$E_{50} = E_{50}^{ref} \left(\frac{c \, cos\varphi - \sigma_3' \, sin \, \varphi}{c \, cos \, \varphi + p^{ref} \, sin \, \varphi} \right)^m \tag{6-5}$$

$$E_{ur} = E_{ur}^{ref} \left(\frac{c \, cos\varphi - \sigma_3' \, sin \, \varphi}{c \, cos \, \varphi + p^{ref} \, sin \, \varphi} \right)^m \tag{6-6}$$

$$E_{osd} = E_{osd}^{ref} \left(\frac{c \, cos\varphi - \sigma_1' \, sin \, \varphi}{c \, cos\varphi + p^{ref} \, sin \, \varphi} \right)^m \tag{6-7}$$

Table 6-1. Input parameters of Plaxis-HSsmall model.

Failure parameters	
c	Cohesion
φ	Angle of internal friction
ψ	Angle of dilatancy

Basic parameters for nonlinear small-strain stiffness	
G_{max}^{ref}	Initial or very small-strain modulus at reference stress
$γ_{0.7}$	Shear strain level at which shear modulus G is reduced to 70% of G_{max}

Basic parameters for soil stiffness	
E_{50}^{ref}	Secant stiffness in standard drained triaxial test
E_{oed}^{ref}	Tangent stiffness for primary oedometer loading
E_{ur}^{ref}	Unloading /reloading stiffness (default $E_{ur}^{ref} = 3\ E_{50}^{ref}$)
m	Power for stress-level dependency

Advanced parameters	
$ν_{ur}$	Poisson's ratio for unloading-reloading (default $ν_{ur} = 0.2$)
p_{ref}	Reference stress for stiffness
K_0^{nc}	K_0 -value for normal consolidation (default $K_0^{nc} = 1\text{-}\sinφ$)
R_f	Failure ratio q_f/q_a (default $R_f = 0.9$)
$σ_{tension}$	Tensile strength (default $σ_{tesnsion} = 0$ stress units)
$c_{increment}$	As-in Mohr-Coulomb model (default $c_{incememt} = 0$)

where $σ_1' $ = vertical stress at which test was conducted and $σ_3' $ = confining stress or minor

principal stress at which test was conducted. Based on parameter values for different soils found

in the literature (Benz, 2006 and Lehane et al., 2008), it can be approximated that $E_{ur} = E_{max}/3 =$

$G_{max}\ 2\ (1+v)/3$. The Plaxis-HSsmall model manual suggests $E_{50} = E_{oed} = E_{ur}/3$ by default.

6.1.2 Compatibility of Plaxis-HSsmall Model Modulus Reduction

In order to use Plaxis-HSsmall model for Newberry limerock and Georgia granite, it was

necessary to check the compatibility between the HSsmall model nonlinear modulus reduction

curve and modulus reduction curves from our laboratory testing. For both materials, G/G_{max}

versus $\gamma/\gamma_{0.7}$ curves were developed following the Santos and Correia (2001) modified hyperbolic

curve (Equation 6-3), and comparisons are shown in Figure 6-3. It can be concluded that the

HSsmall model hyperbolic curve can be used to represent the nonlinear small-strain modulus

reduction behavior of Newberry limerock and Georgia granite.
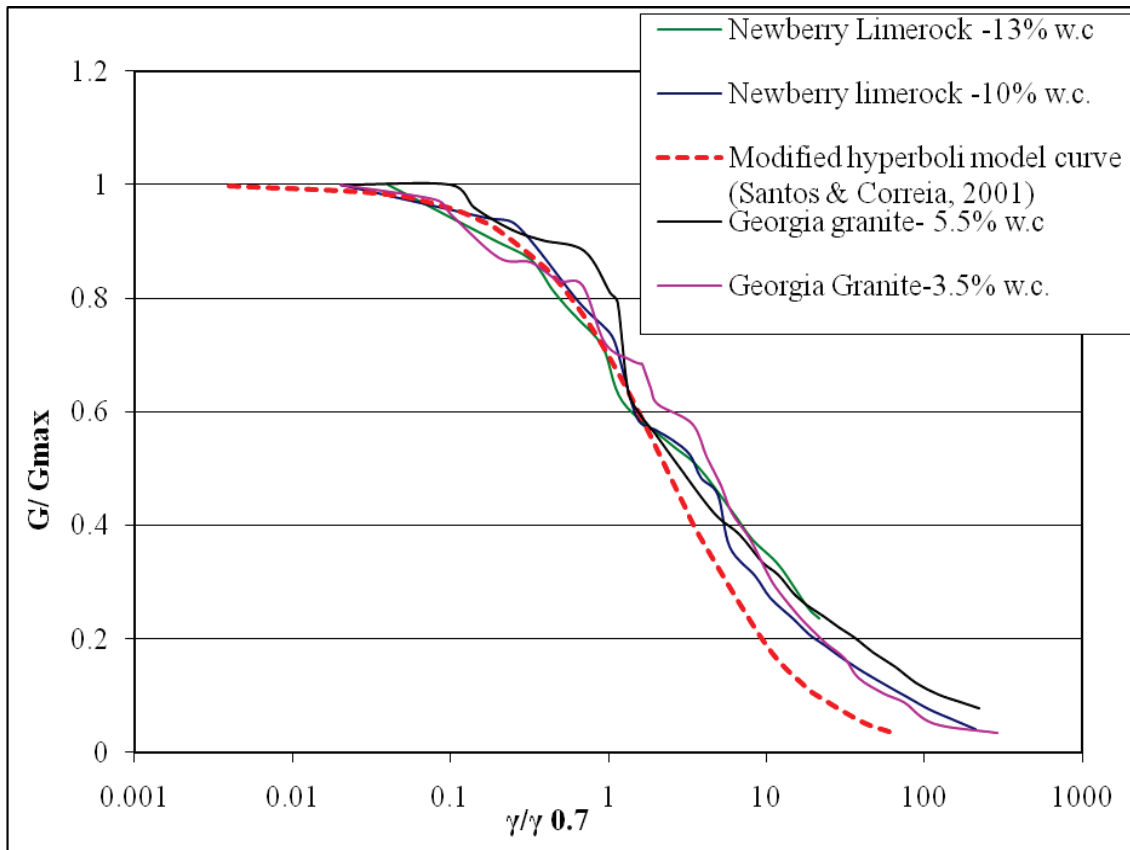
Figure 6-3. Comparison of Newbery limerock and Georgia granite data with Santos and Correia
(2001) modified hyperbolic curve.

6.2 Flexible Pavement Nonlinear Response Model

The primary basis of our finite element model for flexible pavement is adapted from

MEPDG (2004), Appendix-RR (Finite Element Procedures for Flexible Pavement Analysis).

Some of the main features of MEPDG (2004) finite element model are:

- Axisymmetric model

- Static single wheel load with 150 mm radius circular cross-sectional area and 550 kPa tire contact stress

- Vertical side boundaries are 10 to 12 radii from center of wheel load and horizontal bottom boundaries are 50 radii below the top of surface layer

- Linear elastic surface asphalt concrete (AC) layer and linear elastic subgrade layer

- Nonlinear base layer

These MEPDG features were implemented for our pavement model and explained in detail in the following sections.

6.2.1 Axisymmetric Model

An axisymmetric model with 15-node triangular elements was chosen for the pavement modeling and a typical pavement cross-section and FE mesh is shown in Figure 6-4. The size of the elements, i.e., fineness of mesh, was selected such that: 1) there is a smooth continuity of resulting stresses and strains between two adjacent elements and 2) the time required for processing is not too long. Since the surface AC layer and subgrade layer are considered elastic, the fineness of mesh is critical for the base layer. Vertical side boundaries are at least 12 radii (i.e., > 1.8 m) from load center and the bottom horizontal boundary is at least 50 radii (i.e., 7.5 m) below the top of AC layer. It was also eunsured that the location of boundaries has no influence on the resulting deformations by checking that the deformations near boundaries are either zero or almost zero. Vertical side boundaries were fixed horizontally and allowed to move vertically. Horizontal boundaries were fixed both in the horizontal and vertical directions.

6.2.2 Pavement Cross-Sections

A total six different pavement cross-sections with different layer thicknesses were considered for nonlinear analysis (Table 6-2 and Figure 6-5).
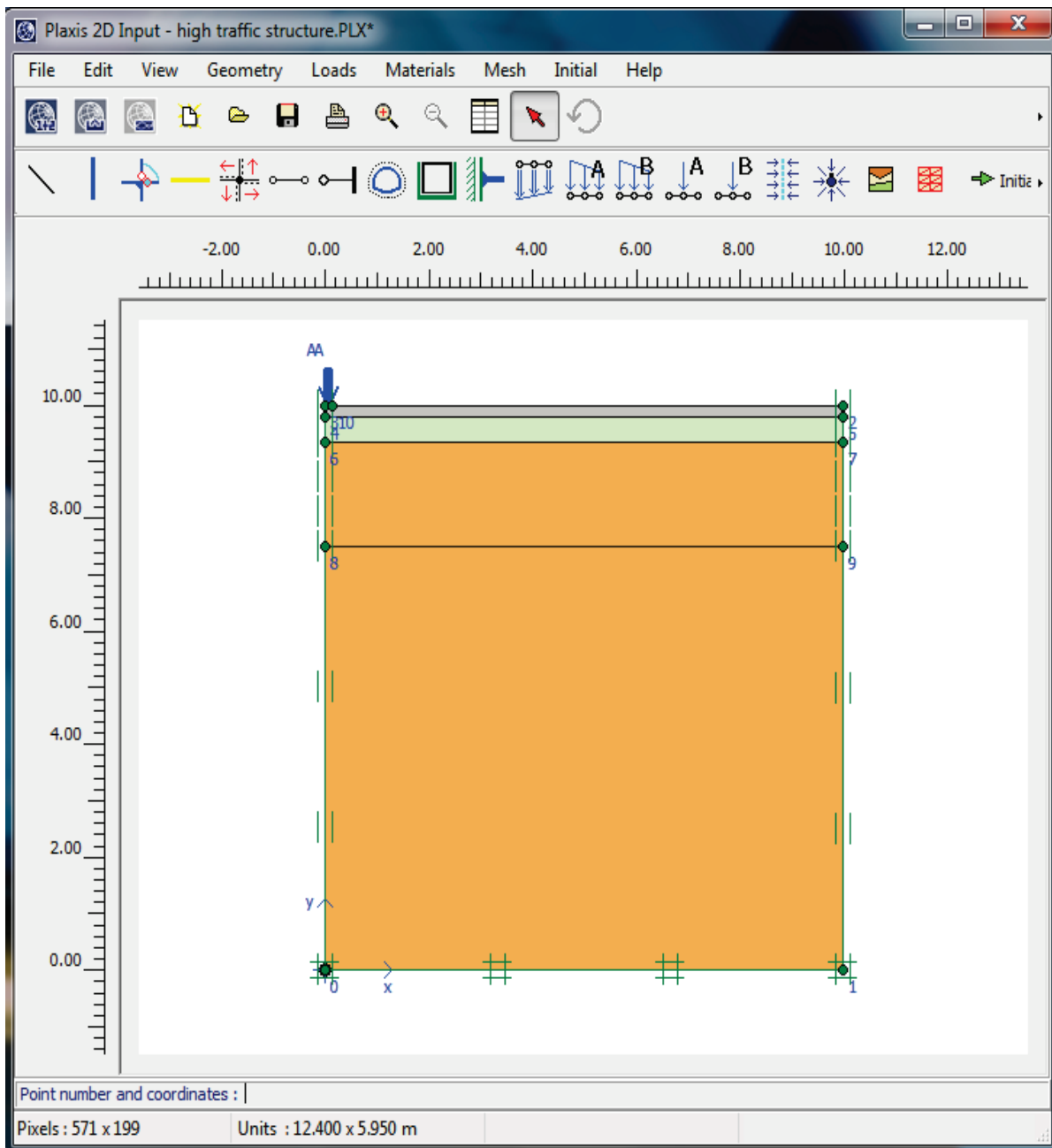
Figure 6-4a. Typical Plaxis-HSsmall model cross-section used for nonlinear analysis.

Connectivities
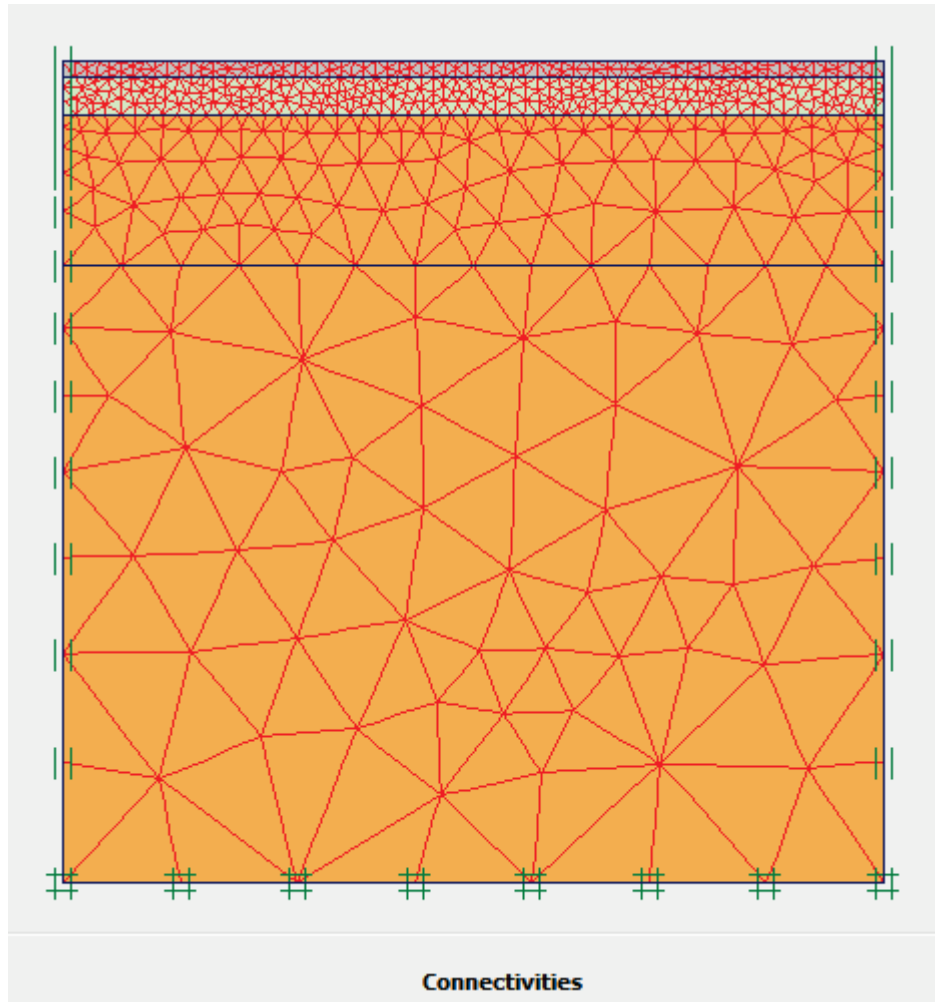
Figure 6-4b. Typical HSsmall model finite element mesh of a pavement cross-section.

6.2.3 Loading Conditions

A circular single wheel with 150 mm radius and 550 kPa of static contact stress was the only

loading condition considered for this analysis.

6.2.4 Input Parameters for Surface and Subgrade Layers of Flexible Pavement

Since the focus was on modulus nonlinearity of base layer, the AC surface and subgrade

were modeled as linear elastic, and we utilized the MEPDG finite element analysis for material

property selection. Three elastic moduli for AC and four elastic moduli for subgrade were chosen

for the analsis (Table 6-3).

Table 6-2. Pavement structures considered for analysis.

Structure Number	Asphalt Concrete Surface Thickness (mm)	Base Thickness (mm)
1	200	450
2	200	300
3	100	450
4	100	300
5	100	200
6	50	300

Table 6-3. Material input parameters for surface asphalt concrete and subgrade layers.

	Elastic Modulus (MPa)	Poisson's ratio (ν)	Unit weight (kN/m^3)
Asphalt Concrete	12500 3000 1000	0.39	23
Subgrade	125 70 50 30	0.32	18

6.3 Initial Plaxis-HSsmall Pavement Model Runs and Recalibration

Before conducting pavement response analyses via a nonlinear response model, it was desirable to check the model applicability and accuracy by comparing against known in situ measured pavement results. However, we found that no such data exists in conjunction with nonlinear base material properties. We did find that in situ measured results were available from Perth footing field studies conducted by Lehane et al. (2008) and these results were selected for our model verification. Lehane et al. (2008) conducted load tests on four footings built in Perth sand and made in situ measurement of actual settlements for each footing. Comparison of

settlements obtained from their in situ measurements and settlement predictions from HSsmall

model for footing 1 was utilized for our verification.

Structure-1

AC — 200 mm (8")

Base — 450 mm (18")

Subgrade

Structure-2

AC — 200 mm (8")

Base — 300 mm (12")

Subgrade

Structure-3

AC — 100 mm (4")

Base — 450 mm (18")

Subgrade

Structure-4

AC — 100 mm (4")

Base — 300 mm (12")

Subgrade

Structure-5

AC — 100 mm (4")

Base — 200 mm (8")

Subgrade

Structure-6

— 50 mm (2")

Base — 300 mm (12")

Subgrade
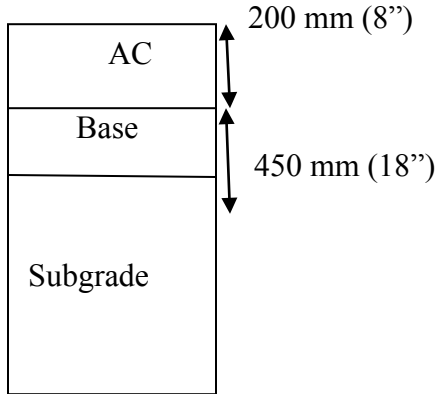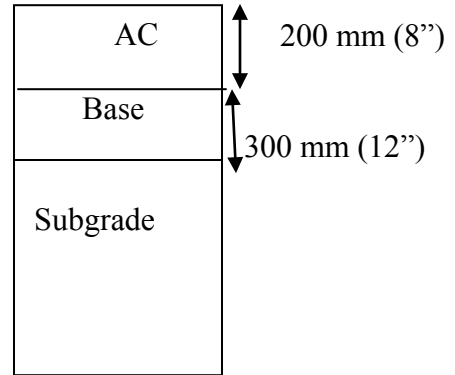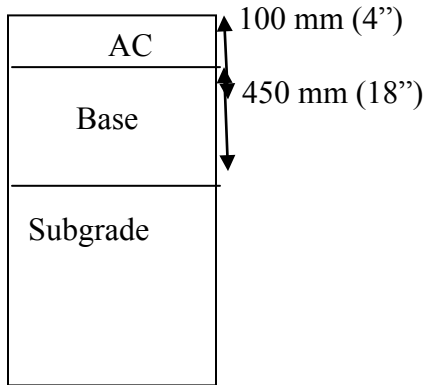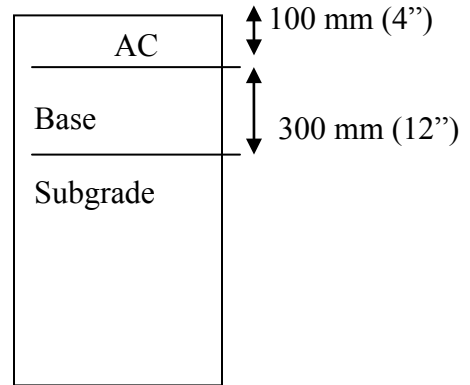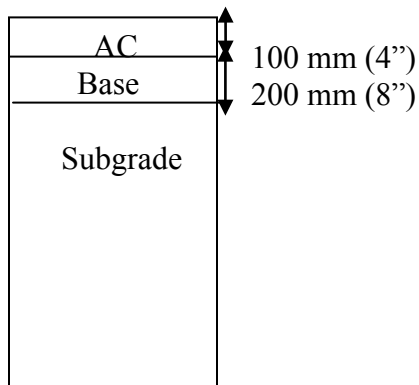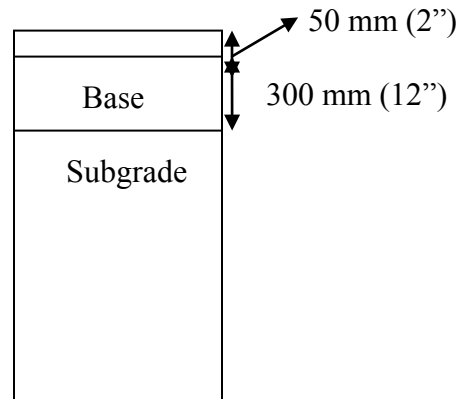
Note: AC = Asphalt Concrete

Figure 6-5. Cross-sections considered for nonlinear base pavement analysis.

6.3.1 Footing Model Analysis and Verification

Similar to Lehane's finite element model, a footing 1 (1.5 m×1.5 m×1 m) nonlinear response model was developed via Plaxis-HSsmall model (Figure 6-6). The material properties used by Lehane were used for our model (Table 6-4), and the footing model was subjected to loads similar to actual field test loads. The settlement predictions are compared with actual measured settlements in Figure 6-7a. This initial nonlinear analysis comparison revealed that the HSsmall model is soft and predictions are overestimated. Lehane et al. (2008) reported similar observations. Thus, we decided to recalibrate the Plaxis model by equating the model and field results.
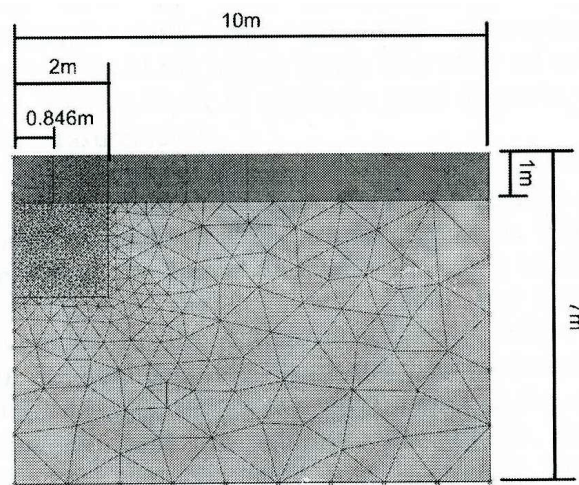
Figure 6-6. Finite element mesh used for model recalibration analysis (footing 1 from Lehane et al., 2008).

6.3.2 Model Recalibration

From Section 6.1.1, it is understood that G_{max}^{ref} and $\gamma_{0.7}$ are the basic model input parameters for HSsmall model should be determined from laboratory testing. Other stiffness parameters, i.e., E_{50}^{ref}, E_{oed}^{ref}, E_{ur}^{ref} and m, are useful in analysis at larger strains. Plaxis recommends using default values for these stiffness parameters that are calculated from G_{max}^{ref}, $\gamma_{0.7}$ and Possion's ratio (ν).

Table 6-4. Input parameters for footing settlement predictions (from Lehane et al. 2008).

Parameter	Unit	Value
γ	kN/m^3	18
P_{ref}	kPa	100
E_{50}^{ref}	MPa	20
E_{oed}^{ref}	MPa	20
E_{ur}^{ref}	MPa	45
G_0^{ref}	MPa	160
m		0.5
c	kPa	1
φ		35°
ψ		0
ν_{ur}		0.2
$\gamma_{0.7}$		2.50E-05

One possible to way to recalibrate our response model was to modify these input

parameters such that actual footing settlements were equal to model predicted settlements. Since

G_{max}^{ref}, $\gamma_{0.7}$ and m were determined from our laboratory testing, these parameters were utilized

directly. Alternatively, it was decided to modify the remaining non-measured stiffness

parameters, i.e., E_{50}^{ref}, E_{oed}^{ref} and E_{ur}^{ref}, to recalibrate the response model. These non-measured

stiffness parameters were modified by trial and error to achieve an equivalence between model

and actual settlements. Following this adjustment, the recalibrated parameters shown in Table 6-

5 are compared with the original parameters, and a comparison of settlement prediction after

recalibration is shown in Figure 6-7b.

6.4 Recalibrated Nonlinear Input Parameters

Based on recalibration carried out in Section 6.3.2, input parameters for materials used in

our analysis were modified accordingly and the details are discussed in the following paragraphs.
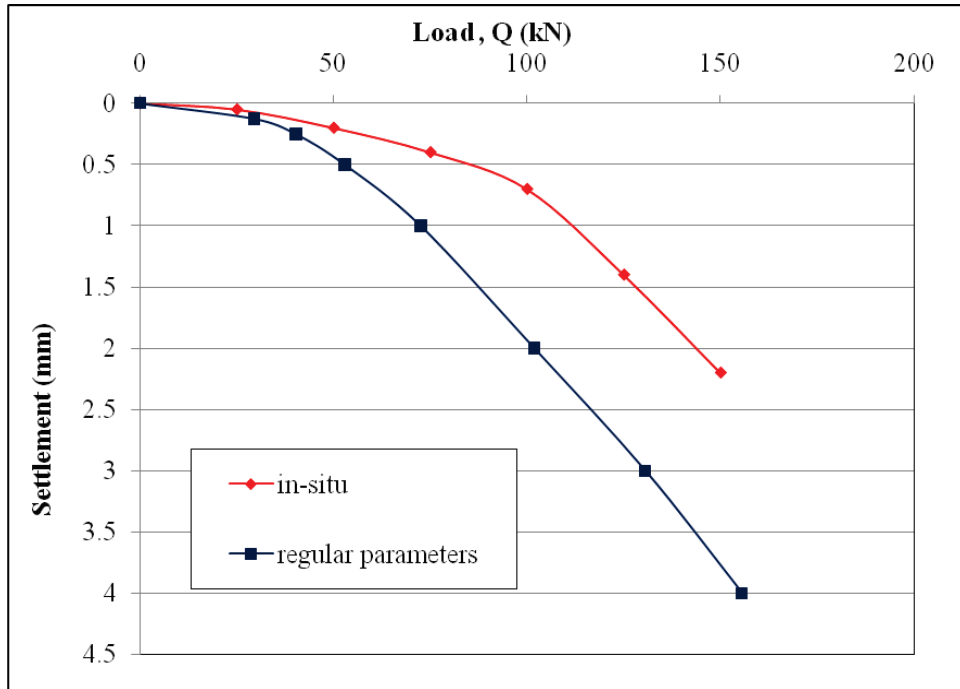
Figure 6-7a. Comparison of actual settlements with settlements predicted using suggested
parameters and Plaxis-HSsmall footing model.
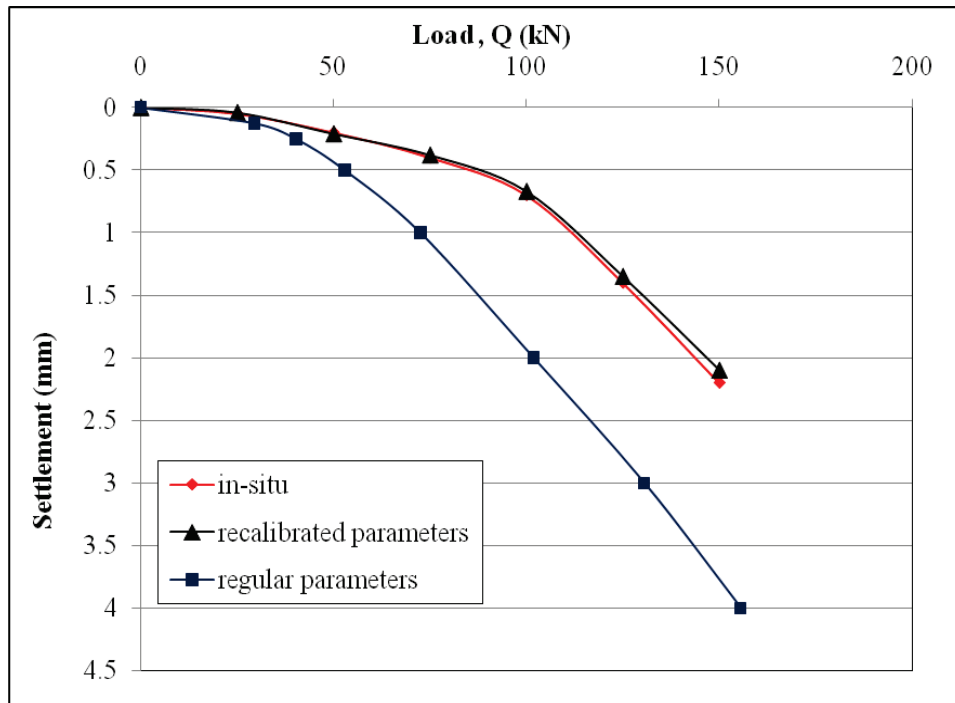
Figure 6-7b. Comparison of actual settlements with settlements predicted using recalibrated
parameters and Plaxis-HSsmall footing model.

Table 6-5. Comparison of suggested and modified material parameters.

Stiffness Parameter	Suggested Values	Modified Values Through Calibration
The initial or very small-strain modulus at reference stress	G_{max}	G_{max}
Secant stiffness in standard drained triaxial test	E_{50}	$E_{ur}/3$
Tangent stiffness for primary oedometer loading	E_{oed}^{ref}	$E_{ur}/3$
Unloading /reloading stiffness (default $E_{ur}^{ref} = 3\ E_{50}^{ref}$)	E_{ur}	$0.85\ E_{max}$ *

Note: * $E_{max} = 2\ (1+\nu)G_{max}$

6.4.1 Recalibrated Parameters of Newberry Limerock and Georgia Granite

The recalibrated input parameters for Newberry limerock and Georgia granite are presented in Tables 6-6 and Table 6-7, respectively. As explained in Chapters 3 and 4, compacted unsaturated specimens of Newberry limerock and Georgia granite were tested at different moisture contents under no confinement. Thus, the reference stress (p_{ref}) for model input was specified as a very low value of 1 kPa (zero is not a possible input). The value of m indicates the stiffness dependence on stress, and was obtained from testing results of the dry material (Figure 5-6). G_{max} was obtained from fixed-free RC tests conducted on Newberry limerock at 13, 12, 11, and 10% moisture contents; G_{max} for moisture contents lower than 10% were obtained from free-free RC test results. The G_{max} values for Georgia granite were all obtainted from fixed-free RC tests.

Table 6-6. Recalibrated HSsmall input parameters for Newberry limerock.

Newberry limerock						
Moisture content (%)	13	12	11	10	8	5.5
G_{max} (MPa)	47.38	84.48	190.3	221.39	449.61	906.536
$\gamma 0.7$	5.E-06	5.E-06	5.E-06	5.E-06	5.E-06	5.E-06
P_{ref} (kPa)	1	1	1	1	1	1
E_{max} (MPa)	132.66	234.85	525.23	606.61	1227.44	2465.78
E_{ur} (MPa)	112.76	199.63	446.44	515.62	1043.32	2095.91
E_{oed} (MPa)	56.38	99.81	223.22	257.81	521.66	1047.96
E_{50} (MPa)	56.38	99.81	223.22	257.81	521.66	1047.96
m	0.702	0.702	0.702	0.702	0.702	0.702
γ (kN/m^3)	21.42	20.45	20.2	20	19.64	18.95
ν	0.4	0.39	0.38	0.37	0.365	0.36

Table 6-7. Recalibrated HSsmall input parameters for Georgia granite.

Georgia granite			
Moisture content (%)	5.5	4.5	3.5
G_{max} (MPa)	46.67	162.65	238.22
$\gamma 0.7$	5.E-06	5.E-06	5.E-06
P_{ref} (kPa)	1	1	1
E_{max} (MPa)	133.48	455.42	657.49
E_{ur} (MPa)	113.45	387.11	558.86
E_{oed} (MPa)	56.73	193.55	279.43
E_{50} (MPa)	56.73	193.55	279.43
m	0.6389	0.6389	0.6389
γ (kN/m^3)	21.42	20.45	20.2
ν	0.43	0.4	0.38

6.4.2 Input Parameters for Miami Limerock

Miami limerock is another base layer material commonly used in the State of Florida. Studies by Toros (2008) on Miami limerock reported that its modulus behavior is relatively different from other limerocks available in Florida and increases tremendously with drying compared to other limerocks. Therefore, it was decided to also perform nonlinear model analysis on Miami limerock.

Since fixed-free resonant column tests were not conducted on Miami limerock, G_{max} versus moisture content curves from free-free RC testing results of Toros (2008) were utilized herein. These results were adjusted for an assumed influence of casing confinement to produce approximate free-free test moduli values for Miami limerock with no casing confinement (Figure 6-8). HS-Small model parameters were then developed and are reported in Table 6-8.
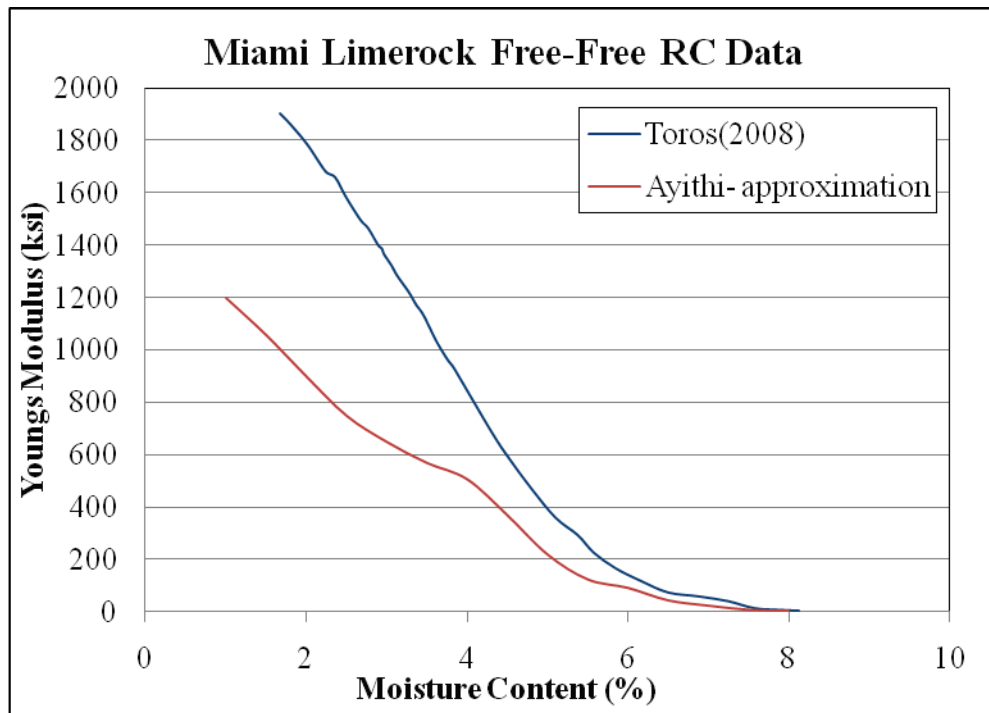
Figure 6-8. G_{max} versus moisture content for Miami limerock.

Table 6-8. Recalibrated HSsmall input parameters for Miami limerock.

	Miami limerock		
Moisture content (%)	8	6	4
G_{max} (MPa)	12.22	226.95	1286.8
$\gamma 0.7$	5.E-06	5.E-06	5.E-06
P_{ref} (kPa)	1	1	1
E_{max} (MPa)	35.19	640.00	3500.10
E_{ur} (MPa)	29.91	544.00	2975.08
E_{oed} (MPa)	14.96	272.00	1487.54
E_{50} (MPa)	14.96	272.00	1487.54
m	0.702	0.702	0.702
γ (kN/m^3)	21.42	20.45	20.2
ν	0.44	0.41	0.36

6.5 Demonstration of Response Model Nonlinear Behavior

One of the main objectives of developing this response model and recalibrated material parameters was to incorporate both stress-dependent and strain-dependent modulus nonlinearity in base layer nonlinear analysis.

6.5.1 Demonstration of Input Parameter Nonlinearity

For nonlinear soils, deformations or strains should increase nonlinearly with an increase in load. This nonlinearity is demonstrated in Figure 6-9 for the footing 1 model discussed above using Newberry limerock HSsmall parameters at 10% moisture content.

6.5.2 Demonstration of Pavement Model Nonlinearity

As a further demonstation of nonlinearity, the pavement model shown in Figure 6-4a was subjected to different wheel loads via a change in contact pressure from 350 to 800 kPa. Surface deflection profiles obtained from this analysis are plotted in Figure 6-10. The deflection basins vary nonlinearly with load, which demonstrates the nonlinearity of the pavement model.
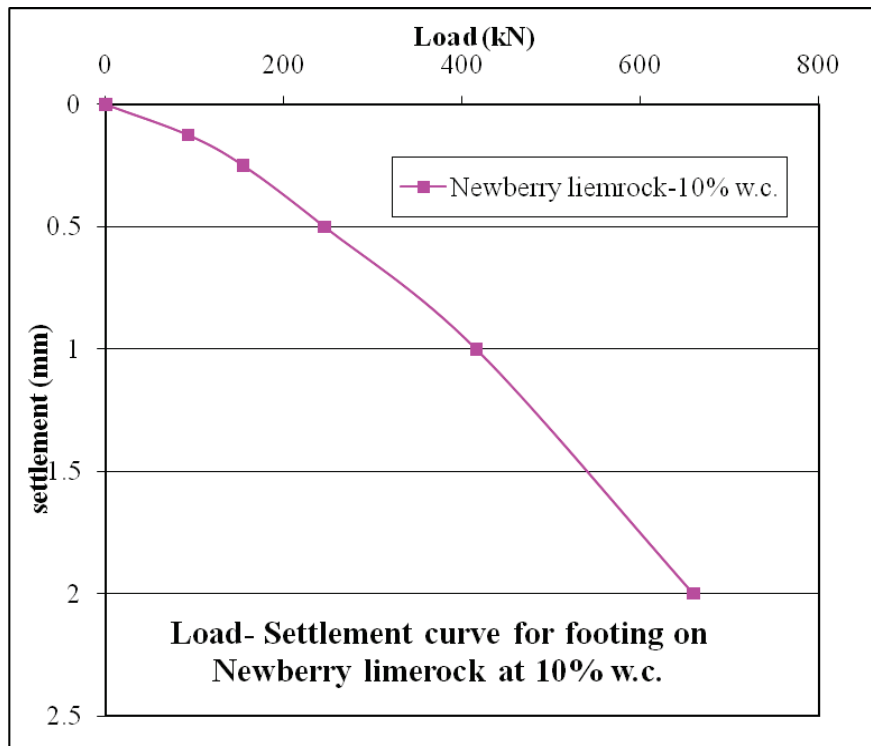
Figure 6-9. Load versus settlement curve to demonstrate material input parameters nonlinearity.
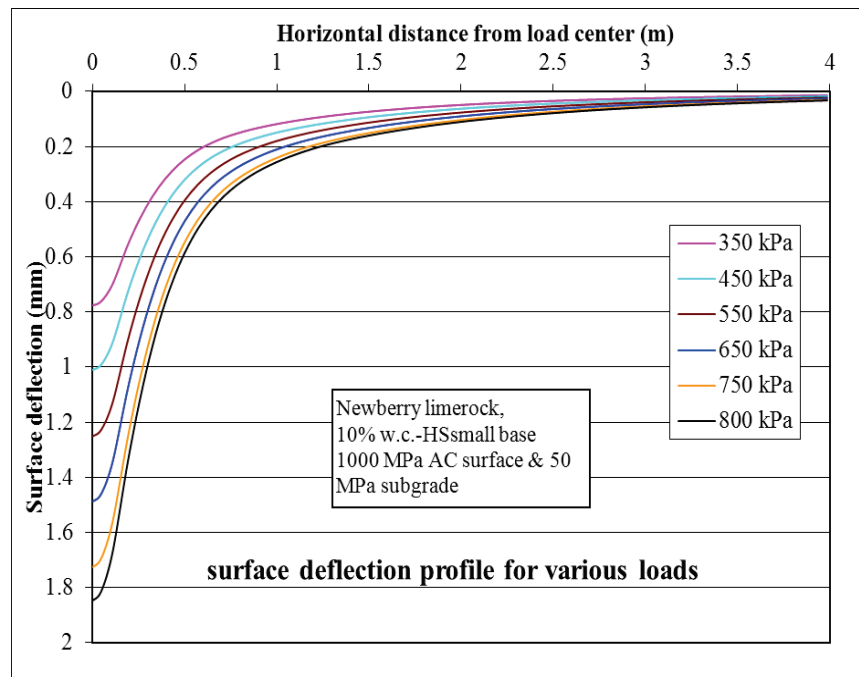
Figure 6-10. Pavement surface deflection basins for different loads demonstrating pavement model nonlinearity.

CHAPTER 7
BASE LAYER NONLINEAR MODELING RESULTS

Characterization of modulus nonlinearity of base soils via a laboratory testing program was discussed in Chapter 5. Using these laboratory test results, a nonlinear response model for pavement analysis was developed via Plaxis. Model development, model characteristics and calibration, pavement cross-sections proposed for analysis, material parameters, and verification and demonstration of model nonlinearity are presented in Chapter 6. With a nonlinear model now available, the next objective was to develop a methodology to calculate an effective, linear elastic modulus for the whole base layer that can approximate known nonlinearities and can be used for MEPDG Level 2 and Level 3 design inputs for practical design applications. Effective modulus determination and the influence of moisture content, subgrade modulus, and overall structural cross-section on effective modulus are discussed in this chapter.

7.1 Effective Base Modulus Determination

7.1.1 Methodology

To derive an effective elastic modulus value for a base layer, it is proposed to use pavement surface deflection as the single matching criterion between a nonlinear and a linear analysis. For nonlinear analysis, both AC surface and subgrade layers are considered linear and the base layer is considered nonlinear. Using the maximum surface deflection obtained from a nonlinear analysis as the criterion, an equivalent, linear elastic modulus value for the whole base layer is determined by trial and error. Once the effective base modulus is determined, pavement responses obtained at critical locations (Figure 7-1) for both linear and nonlinear cases can be compared to examine the influence of the simplification.
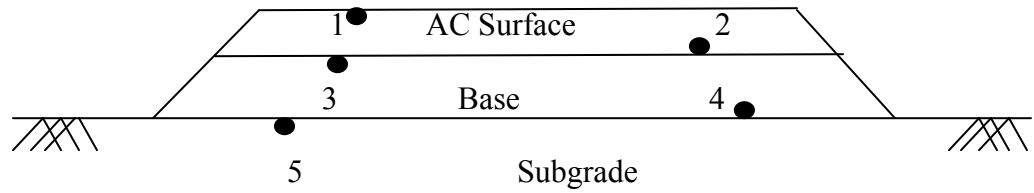
Figure 7-1. Critical locations for pavement response analysis (1=top of AC surface layer, 2=bottom of AC surface layer, 3=top of base layer, 4=bottom of base layer, and 5=top of subgrade layer).
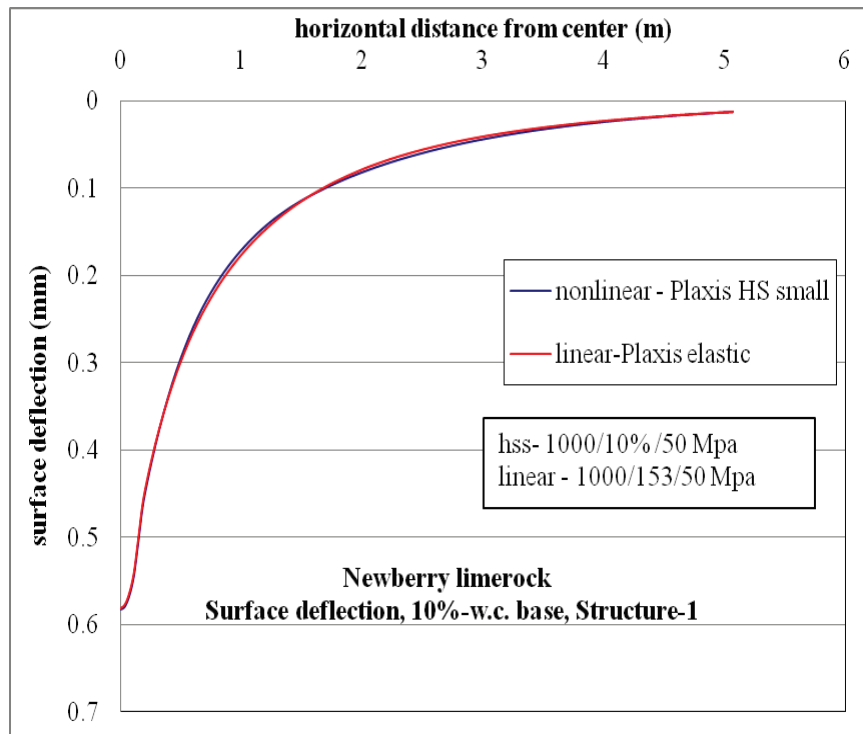
Figure 7-2. Surface deflection basin comparison for nonlinear and linear cases.

7.1.2 Surface Deflection Matching

To illustrate via an example, nonlinear analysis via the Plaxis-HSsmall nonlinear pavement response model (Chapter 6) was performed on Structure 1 (Figure 6-5) with the base layer at 10% moisture content. The AC surface layer and subgrade layer were considered elastic with moduli of 1000 MPa and 50 MPa, respectively. From the nonlinear analysis a maximum surface

deflection of 0.582 mm was obtained under a wheel load of 550 kPa. Keeping the elastic moduli of the surface and subgrade layers the same, an effective modulus for the base layer was determined by trial and error using a linear analysis for the base layer and producing the same maximum surface deflection of 0.582 mm. For this case, the surface deflection basins for the nonlinear and linear models are plotted in Figure 7-2 where it is observed that the entire surface deflection basins are in good agreement.

7.1.3 Nonlinear Reduction of Effective Modulus with Increase in Load

In mechanics, it is well known that the modulus of a particulate material decreases nonlinearly with an increase in strain or load. One of the main objectives of our research work was to incorporate this modulus nonlinearity in pavement design. Hence, it is of interest to demonstrate that the effective modulus of a base layer decreases nonlinearly with an increase in load. The results of such a demonstration are shown Figures 7-3 and 7-4. The analyses were performed for Structure 1 and Structure 4 using Newberry limerock base at 13% and 10% moisture contents and Georgia granite base at 5.5% and 3.5% moisture contents. The moduli of the AC surface layer and subgrade layer were 1000 MPa and 50 MPa, respectively. The effective base modulus at each load level was determined using the procedure described above. It is clearly observed that the effective base modulus decreases nonlinearly with an increase in load. It is also observed that the modulus nonlinearity increases with a decrease in moisture content.

7.2 Effective Design Moduli

7.2.1 Effective Moduli Data

Nonlinear analyses were conducted viathe Plaxis-HSsmall response model on six different pavement structures presented in Figure 6-5 and using material parameters listed in Tables 6-6, 6-7, and 6-8 for Newberry limerock, Georgia granite, and Miami limerock. The AC surface layer was considered elastic with a modulus of 1000 MPa. Elastic modulus values presented in Table
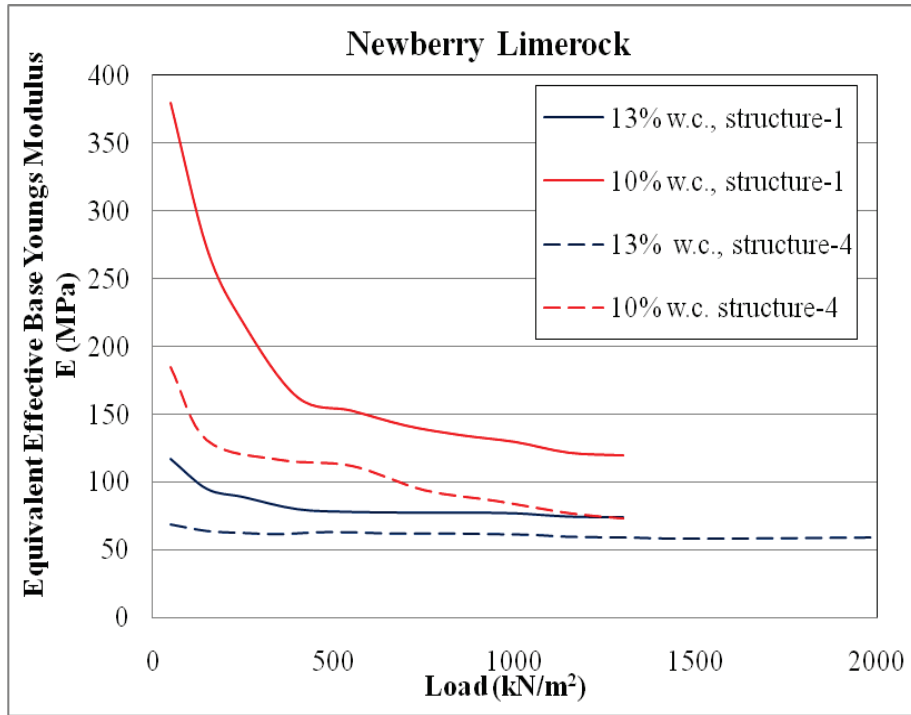
Figure 7-3. Nonlinear variation of effective modulus with increase in load for Newberry limerock base at 13% and 10% moisture contents.
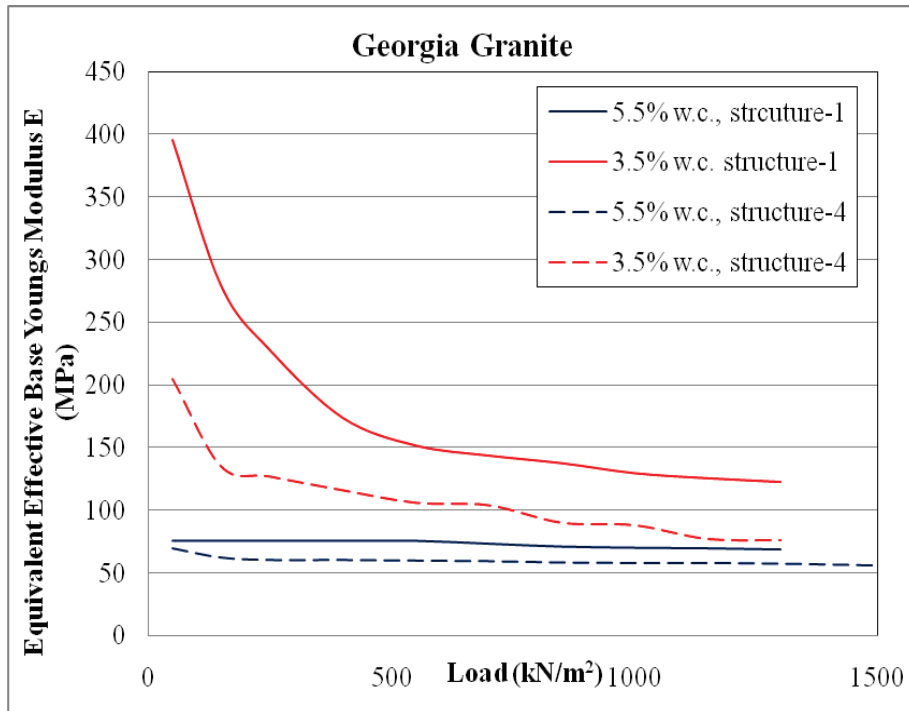
Figure 7-4. Nonlinear variation of effective modulus with increase in load for Georgia granite base at 5.5% and 3.5% moisture contents.

6-3 were assigned to subgrade layer to analyze the effect of subgrade on base layer effective

modulus. The methodology described in section 7.1.1 was followed to determine the effective

design moduli presented in Tables 7-1 to 7-3.

Table 7-1. Effective moduli (in MPa) for different pavement structures and subgrade moduli for Newberry limerock base.

Subgrade Modulus (MPa)	Structure	Moisture Content (%)					
		13	12	11	10	8	5.5
30	1	65	79	112	118	142	171
	2	58	70	92	94	118	139
	3	54	67	90	101	108	130
	4	49	60	69	70	76	78
50	1	79	102	140	153	196	230
	2	74	92	120	125	155	178
	3	66	89	112	124	148	168
	4	62	80	108	112	123	132
	5	73	---	100	---	---	102
	6	76	---	90	---	---	107
70	1	90	117	170	175	230	267
	2	85	109	143	149	184	207
	3	73	100	135	142	195	205
	4	71	96	129	135	139	144
125	1	108	157	227	241	310	387
	2	107	147	210	220	278	308
	3	93	141	214	220	281	311
	4	84	127	196	206	228	240
	5	105	---	189	---	---	209
	6	103	---	180	---	---	187

Table 7-1 presents effective moduli values for Newberry limerock, Table 7-2 for Georgia

granite, and Table 7-3 for Miami limerock. Following the procedure explained in section 5.2.2

and using Equations 5-1 and 5-2, maximum Young's modulus (E_{max}) values of base soil were

calculated at the middle depth of base layer. Effective moduli values, corresponding $E_{max,}$ and the

ratio of effective to maximum modulus (i.e., E/E_{max}) are presented in Appendix B. It can be

observed that E/E_{max} decreases with a decrease in moisture content, which indicates that modulus

nonlinearity increases with a decrease in moisture content.

Table 7-2. Effective moduli (in MPa) for different pavement structures and subgrade moduli for
Georgia granite base.

Subgrade Modulus (MPa)	Structure	Moisture Content (%)		
		5.5	4.5	3.5
30	1	63	104	117
	2	56	94	104
	3	54	88	100
	4	46	74	75
50	1	76	135	152
	2	70	112	124
	3	66	115	119
	4	60	100	106
70	1	86	155	178
	2	82	135	150
	3	73	133	162
	4	67	123	137
125	1	112	210	243
	2	105	195	220
	3	90	207	220
	4	84	184	220

Table 7-3. Effective moduli (in MPa) for different pavement structures and subgrade moduli for
for Miami limerock base.

Subgrade Modulus (MPa)	Structure	Moisture Content (%)		
		8	6	4
50	1	30	168	337
	4	6	54	159
125	1	31	260	545
	4	7	122	320

7.2.1.1 Influence of Moisture Content on Effective Modulus

For Structures 1 to 6 and at constant subgrade modulus, the variation of effective modulus with decreasing moisture content is shown in Figures 7-5, 7-6, and 7-7 for Newberry limerock, Georgia granite, and Miami limerock, respectively. From these plots it can be observed that effective base modulus increases significantly with decreasing moisture content similar to our laboratory test results. Among the three base materials, Miami limerock base has the highest effective modulus values. From the laboratory testing results, it is observed that the increase in small-strain modulus due to suction also is highest for Miami limerock.

7.2.1.2 Influence of Subgrade Modulus on Effective Modulus

From the column plots in Figures 7-5, 7-6, and 7-7 it can be observed that for any given structure and base moisture content, the effective base modulus increases with an increase in subgrade modulus. This behavior can be explained by fundamentals of pavement mechanics. Pavement deformation is mainly dependent on subgrade modulus and deformation decreases with an increase in subgrade modulus. As the subgrade modulus increases,the magnitude of the deviatoric stresses acting on the base layer decreases. Since base soil modulus is nonlinear and increases with a decrease in deviatoric stress (or shear strain), the base layer effective modulus increases with an increase in subgrade modulus.

7.2.1.3 Influence of Structure Type on Effective Modulus

The variation of effective modulus for different pavement structures and subgrade moduli is shown in Figures 7-8, 7-9, and 7-10 for Newberry limerock, Georgia granite, and Miami limerock, respectively. It can be observed, at any given moisture content and subgrade modulus combination, the effective modulus is dependent on structure type, i.e., layer thicknesses. As the layer thicknesses vary, the magnitude of the deviatoric stress transferred from the top to bottom
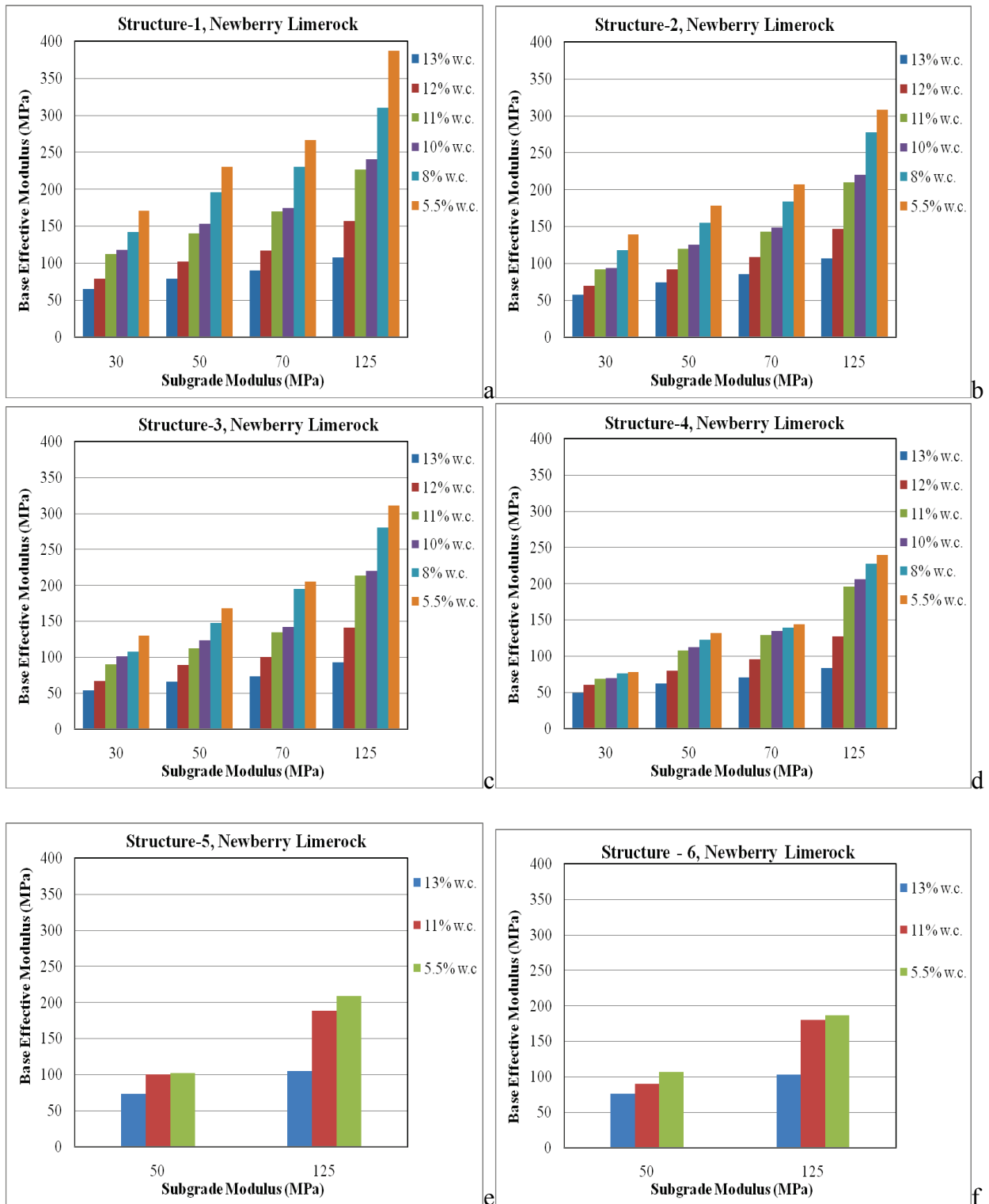
Figure 7-5. Newberry limerock effective base modulus versus subgrade modulus relationship for different moisture contents and structures: (a) Structure 1, (b) Structure 2, (c) Structure 3, (d) Structure 4, (e) Structure 5, and (f) Structure 6.
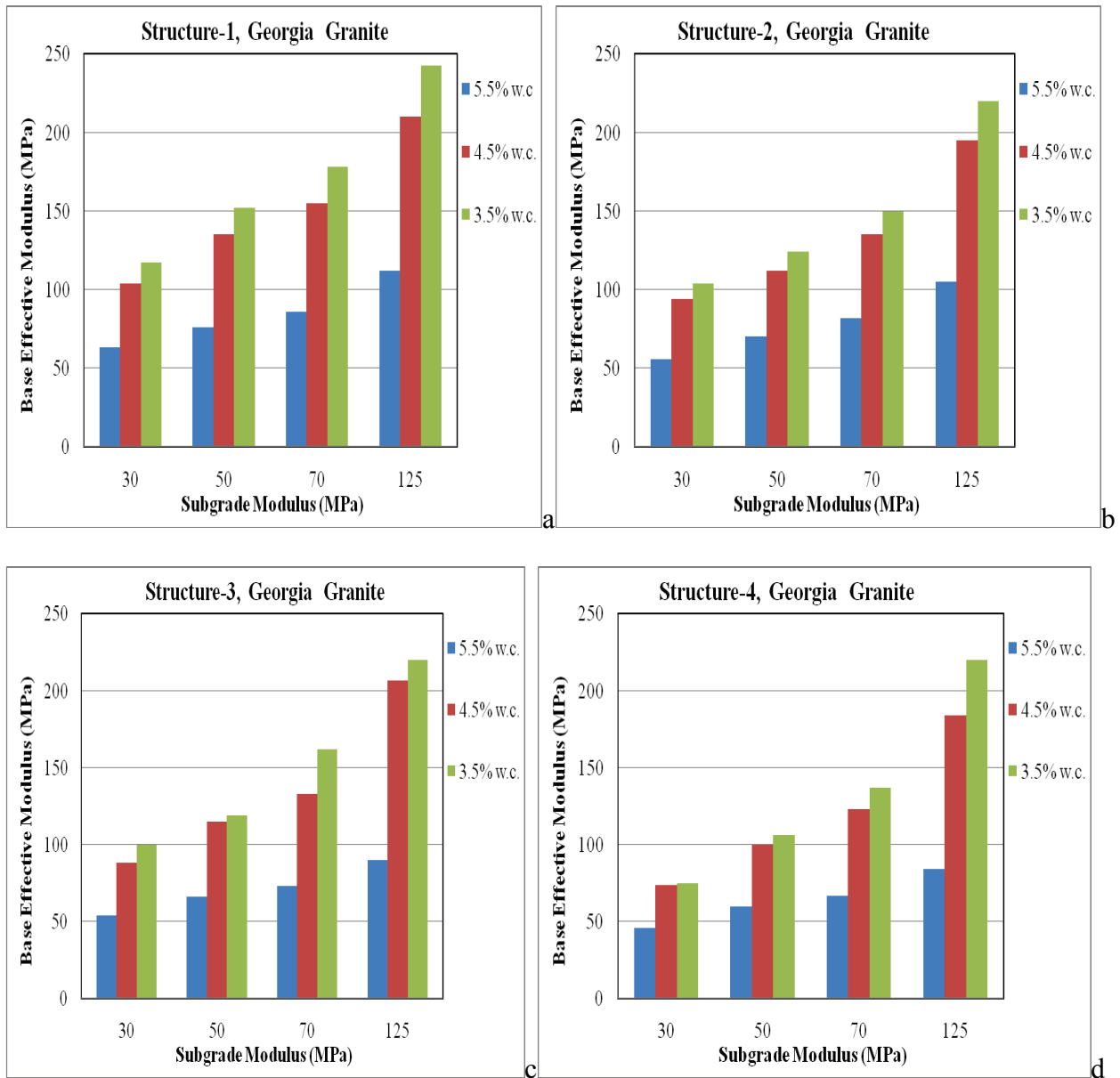
Figure 7-6. Gerogia granite effective base modulus versus subgrade modulus for different moisture contents and structures: (a) Structure 1, (b) Structure 2, (c) Structure 3, and (d) Structure 4.
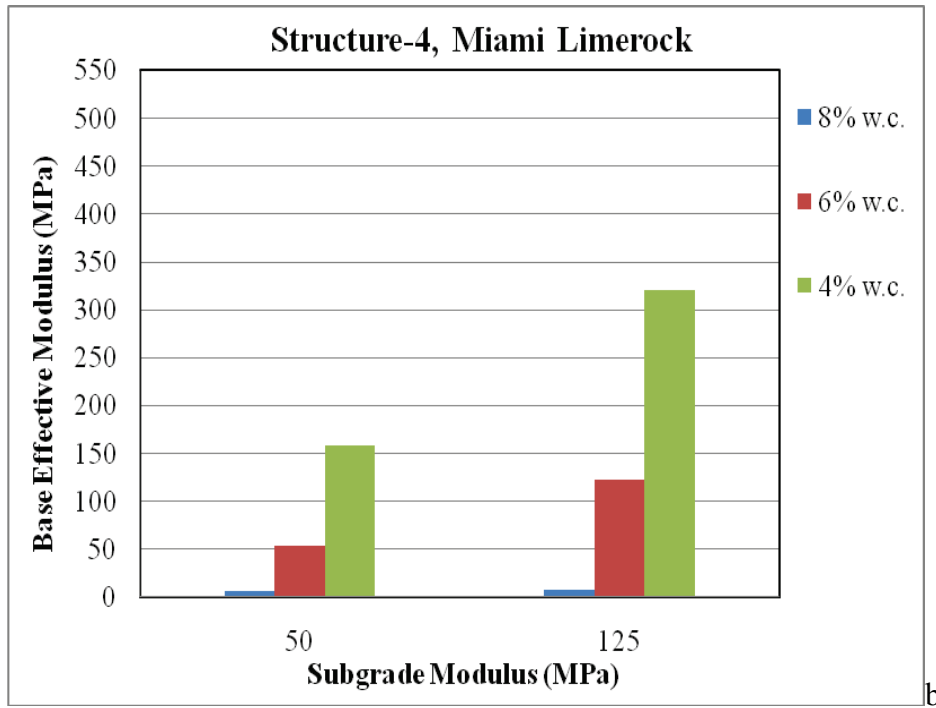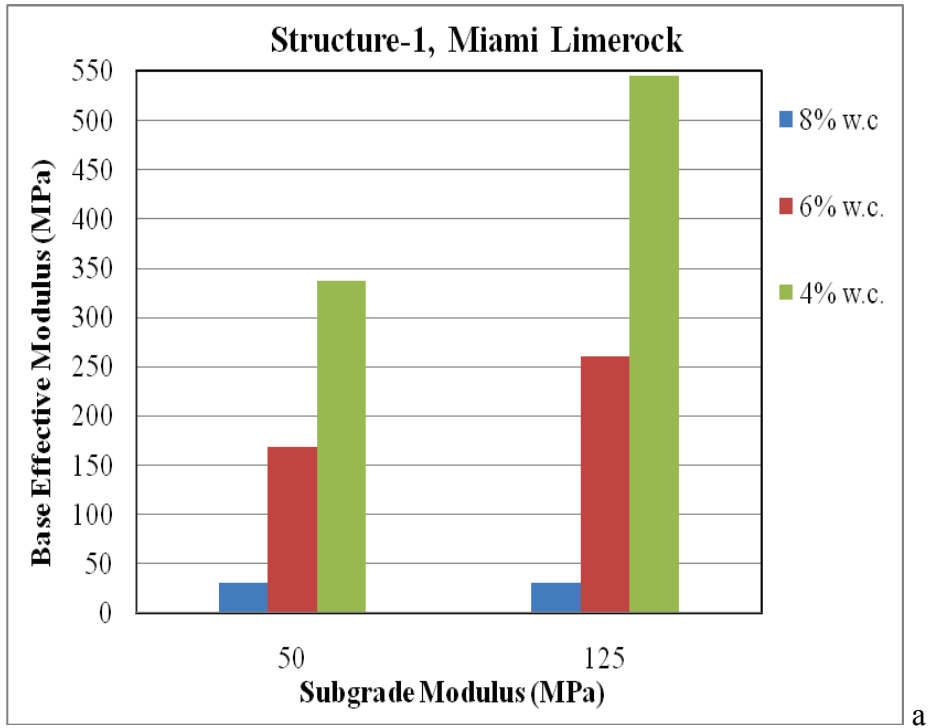
Figure 7-7. Miami limerock effective base modulus versus subgrade modulus for different moisture contents and structures: (a) Structure 1and (b) Structure 4.
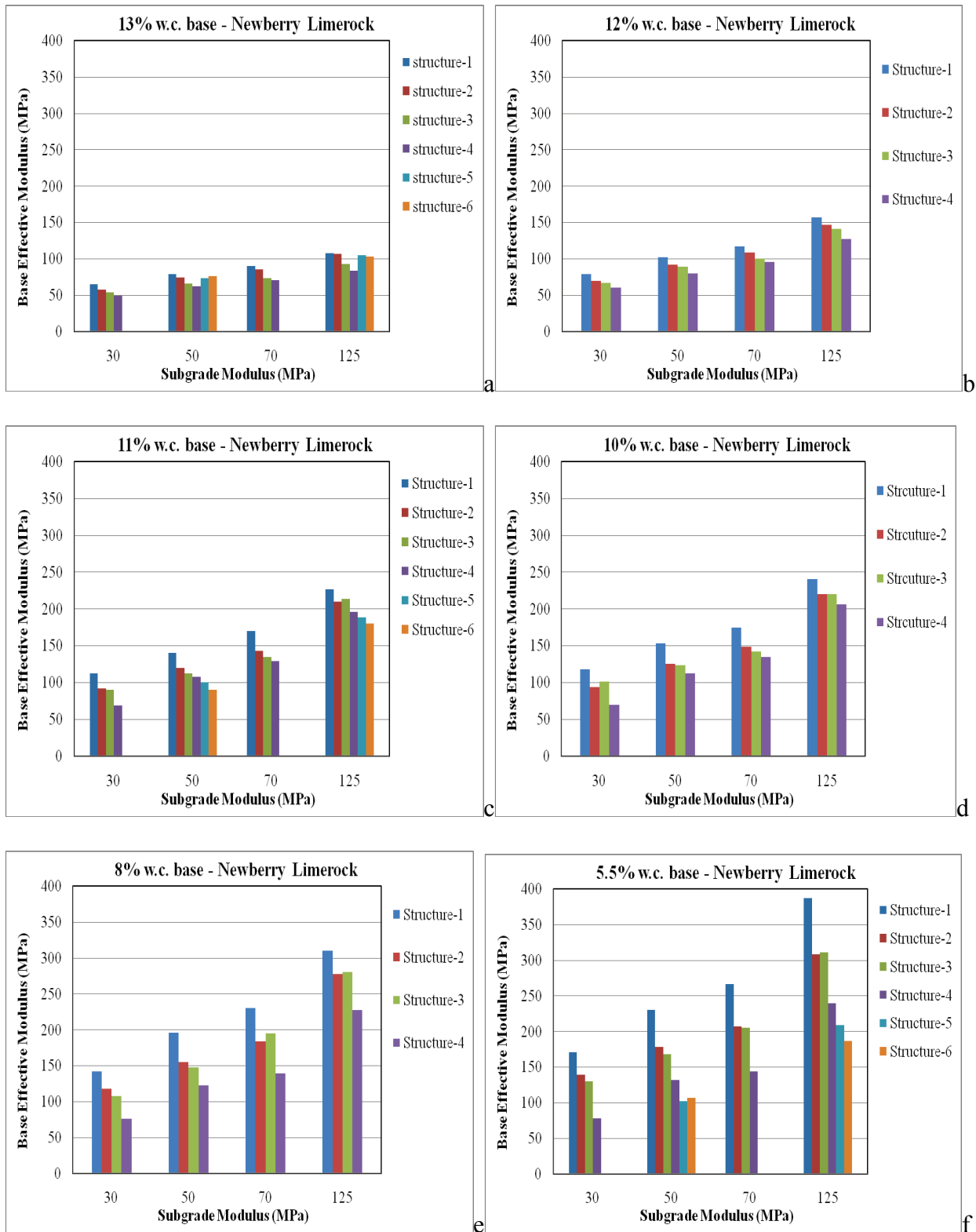
Figure 7-8. Newberry limerock effective base modulus versus subgrade modulus for different structures and at constant moisture contents of: (a) 13%, (b) 12%, (c) 11%, (d) 10%, (e) 8%, and (f) 5.5%.
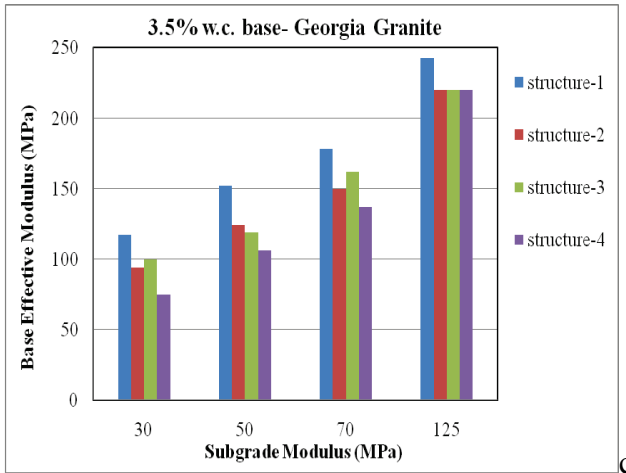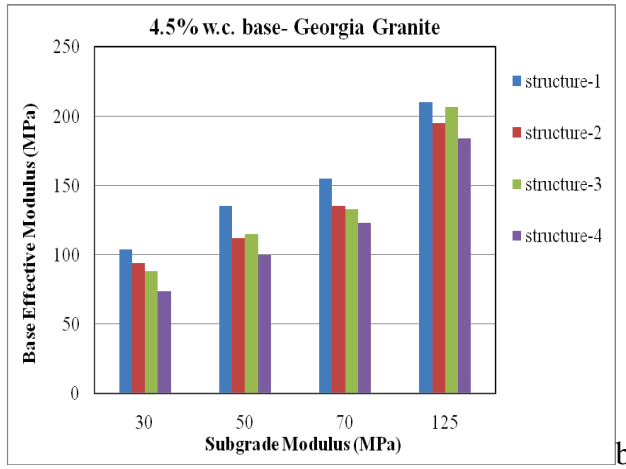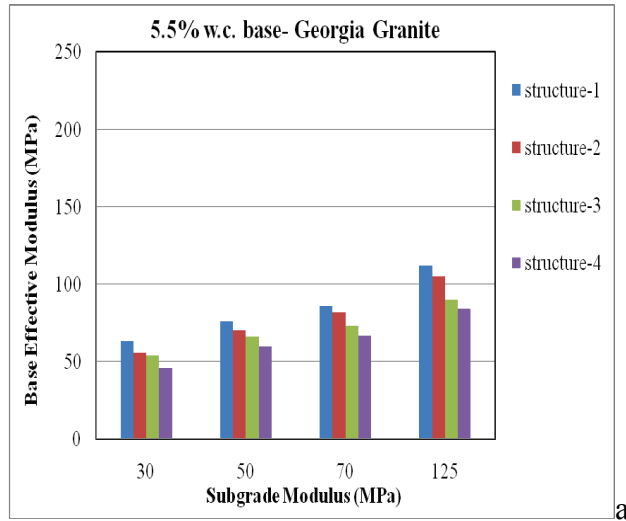
Figure 7-9. Georgia granite effective base modulus versus subgrade modulus for different structures and at constant moisture contents of: (a) 5.5%, (b) 4.5%, and (c) 3.5%.
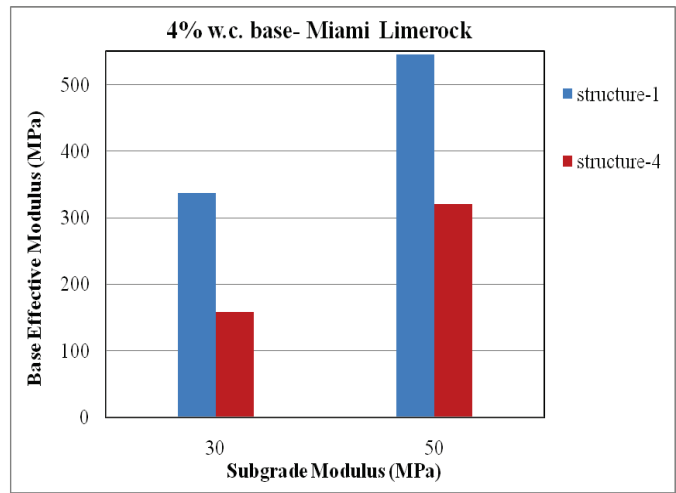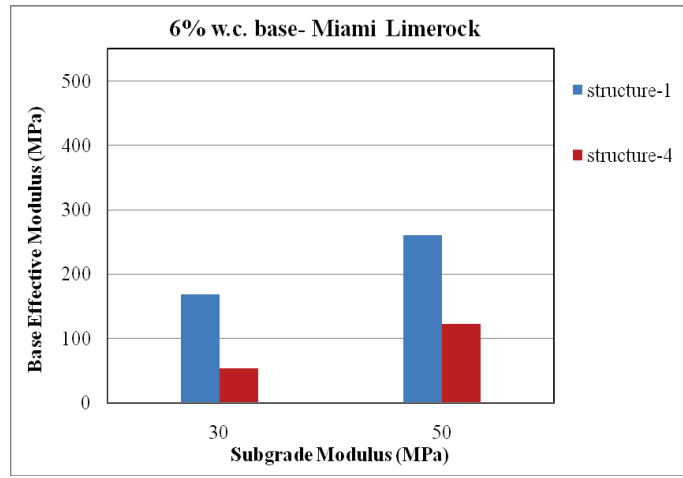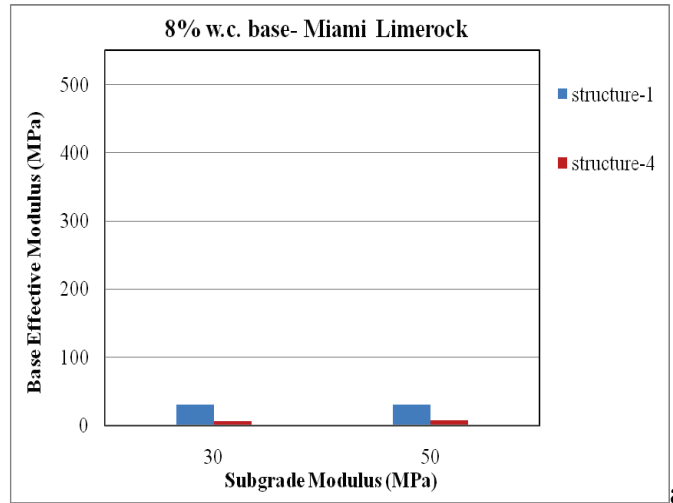
Figure 7-10. Miami limerock effective base modulus versus subgrade modulus for different structures and at constant moisture contents of: (a) 8%, (b) 6%, and (c) 4%.

layers also varies. Usually, as the thickness of a layer increases, the deviatoric stress transferred to the layer beneath it decreases, and the corresponding modulus increases.

7.2.1.4 Comparison of Effective Design Moduli for Different Materials

Effective design moduli obtained at 8% moisture content for Newberry limerock, 3.5% for Georgia granite, and 4% for Miami limerock are compared with modulus values at their respective optimum moisture contents (OMC) in Figure 7-11. These plots provide insight on the effect that drying has on the effective modulus of each material. It is observed that Miami limerock behaves very differently as its effective modulus increases at a much faster rate as the material dries out. At OMC, the effective modulus of Miami limerock is much lower than that of Newberry limerock and Georgia granite, but as the material dries out, its modulus increases significantly faster compared to the other two materials.

To further compare the three materials, normalized effective base moduli obtained at different base moisture contents are compared in Figure 7-12a for Structure 1 and Figure 7-12b for Structure 4. Each plot contains results for subgrade moduli of 50 MPa and 125 MPa. The effective modulus (E) at each moisture content is normalized with the effective modulus at optimum moisture content (E_{opt}), and the normalized modulus is plotted versus the reduction in degree of saturation due to drying from optimum moisture content. Again, it is observed that the Newberry limerock and Georgia granite exhibit similar behavior whereas the Miami limerock displays a much faster rate of increase in modulus upon drying. Toros (2008) also observed very significant increases in E_{max} of Miami limerock as the material dries out as compared to Newberry limerock and Georgia granite.

7.2.1.5 MEPDG Moisture Effect Model

The MEPDG (2004) recommends the following generalized regression model to predict the influence of moisture on resilient modulus (M_R):
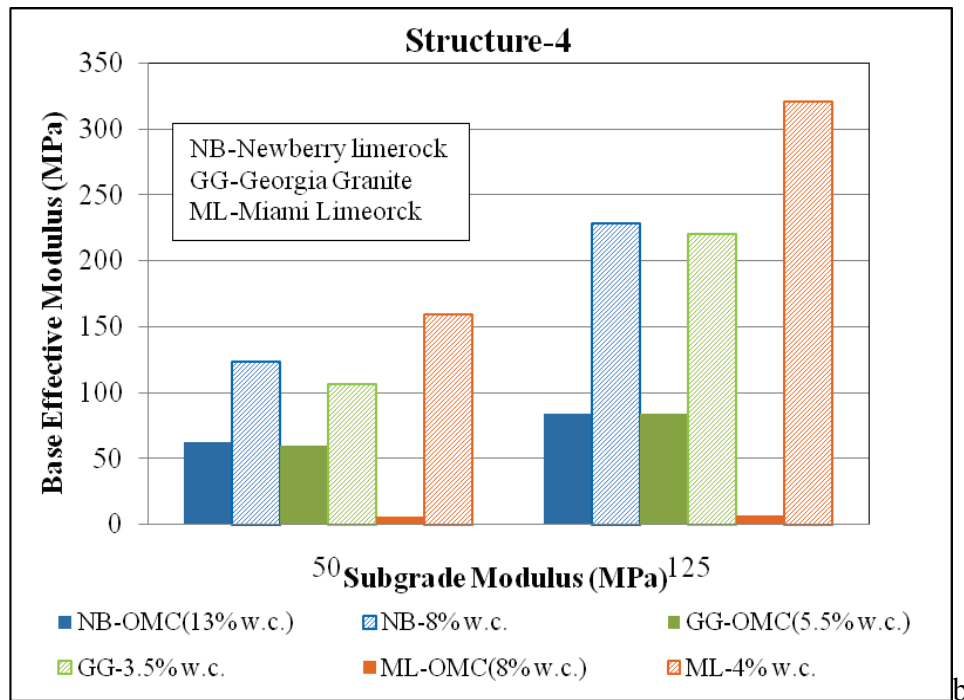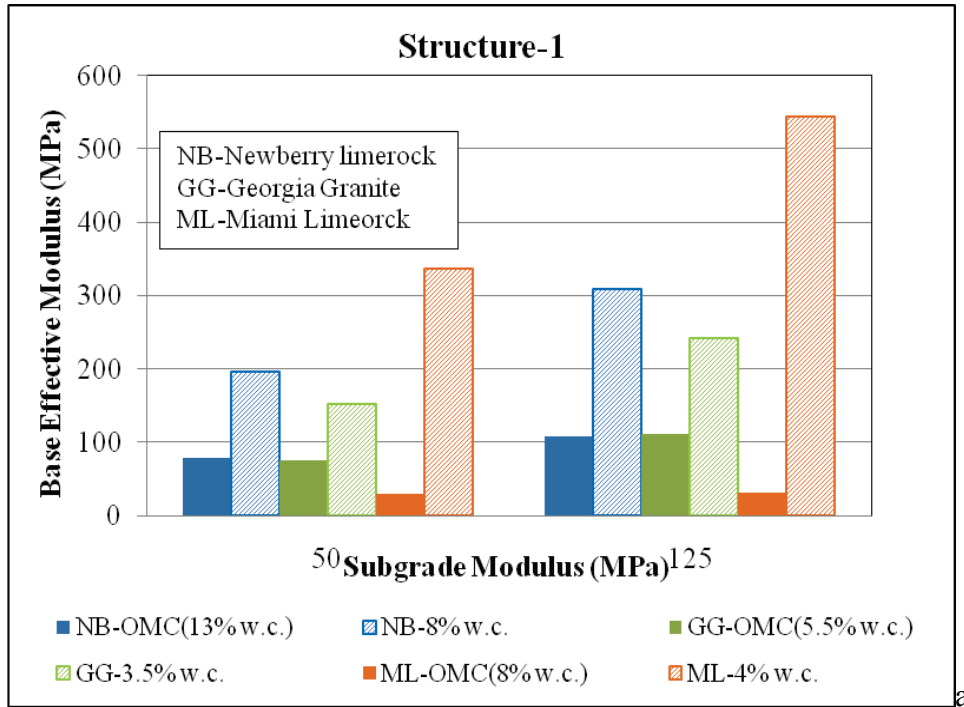
Figure 7-11. Comparsion of effetive moduli of all three materials at different base moisture contents and twosubgrade moduli for: (a) Structure1 and (b) Structure 4.

119
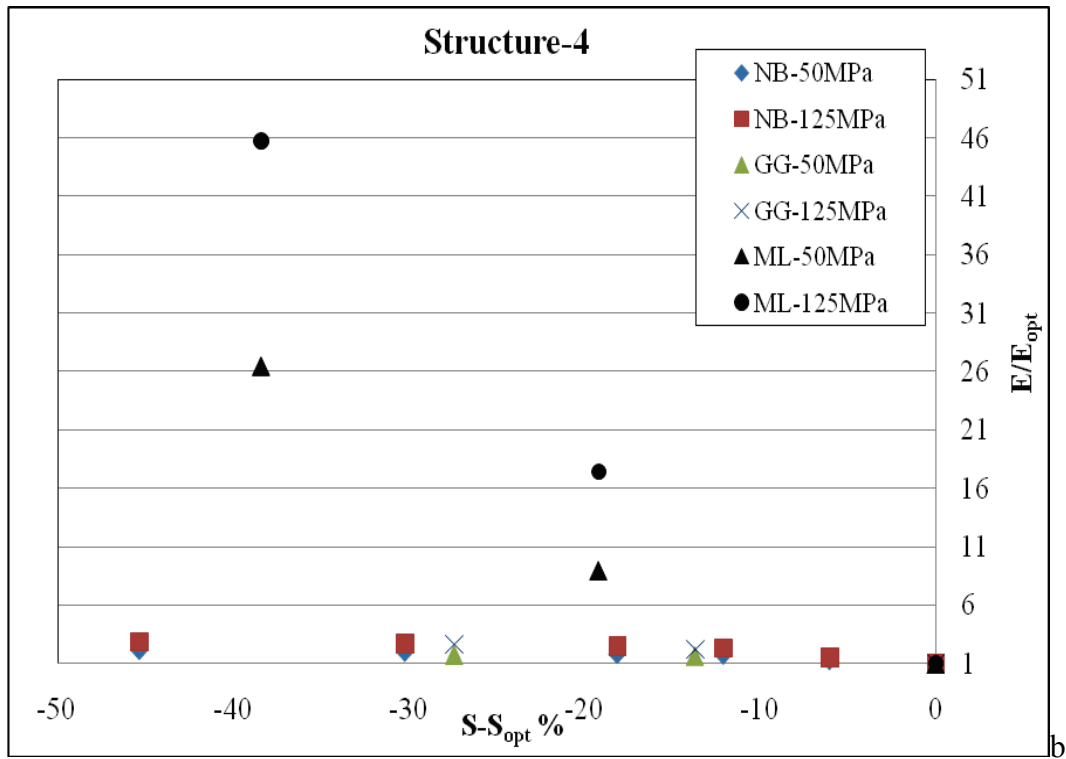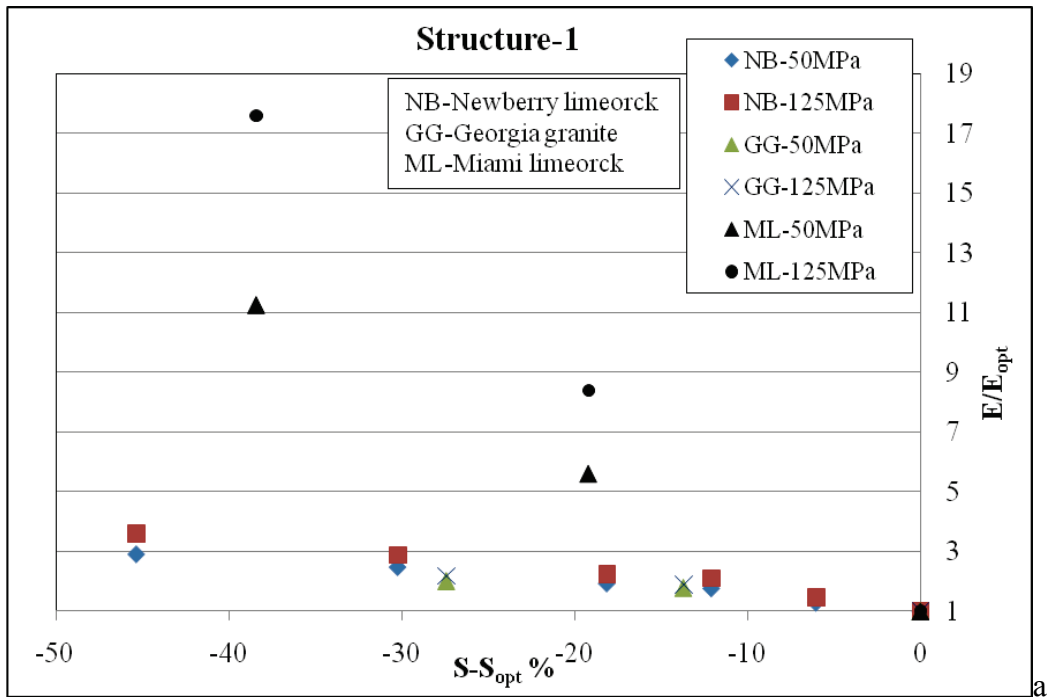
Figure 7-12. Comparsion of normalized effetive moduli of all three materials with subgrade moduli of 50 MPa and 125 MPa and for: (a) Structure 1and (b) Structure 4.

120

$$\log\frac{M_R}{M_{Ropt}} = a + \frac{b - a}{1 + EXP(\beta + k_s \cdot (S - S_{opt}))}$$

<div align="right">(7-1)</div>

For coarse grains soils a=-0.3123, b=0.3, β=-0.0401, and k_s=6.8157. It is of interest to determine if the MEPDG model can accurately estimate the modulus of Florida base materials by comparing model predictions with the effective moduli values previously presented in Tables 7-1, 7-2, and 7-3. Figures 7-13, 7-14, and 7-15 compare MEPDG modulus predictions with effective moduli for Newberry limerock, Georgia granite, and Miami limerock, respectively, and for selected pavement structures and subgrade moduli shown in the legend. The moduli are shown normalized using the modulus at optimum moisture content (E_{opt} or $M_{R\ opt}$), and the results are plotted versus the reduction in degree of saturation due to drying from optimum moisture content. It is observed that the modulus value from the MEPDG model can increase up to two times upon drying from optimum moisture content whereas the effective moduli values for our materials all experience a larger increase. In the case of Miami limerock the increase can be as much as 45 times over the range of moisture contents evaluated by our analyses. In general, for structures with low subgrade modulus (50 MPa), effective moduli are near the MEPDG model values. However, as the subgrade modulus increases, E/E_{opt} values are much higher than those from the MEPDG model, and up to 3.5 times for Newberry limerock, 2.5 times for Georgia granite, and 47 times for Miami limerock. From these observations it can be concluded that the MEPDG model does not well represent the moisture/suction effect for Florida base materials. Use of the MEPDG model would be a conservative estimate at best.
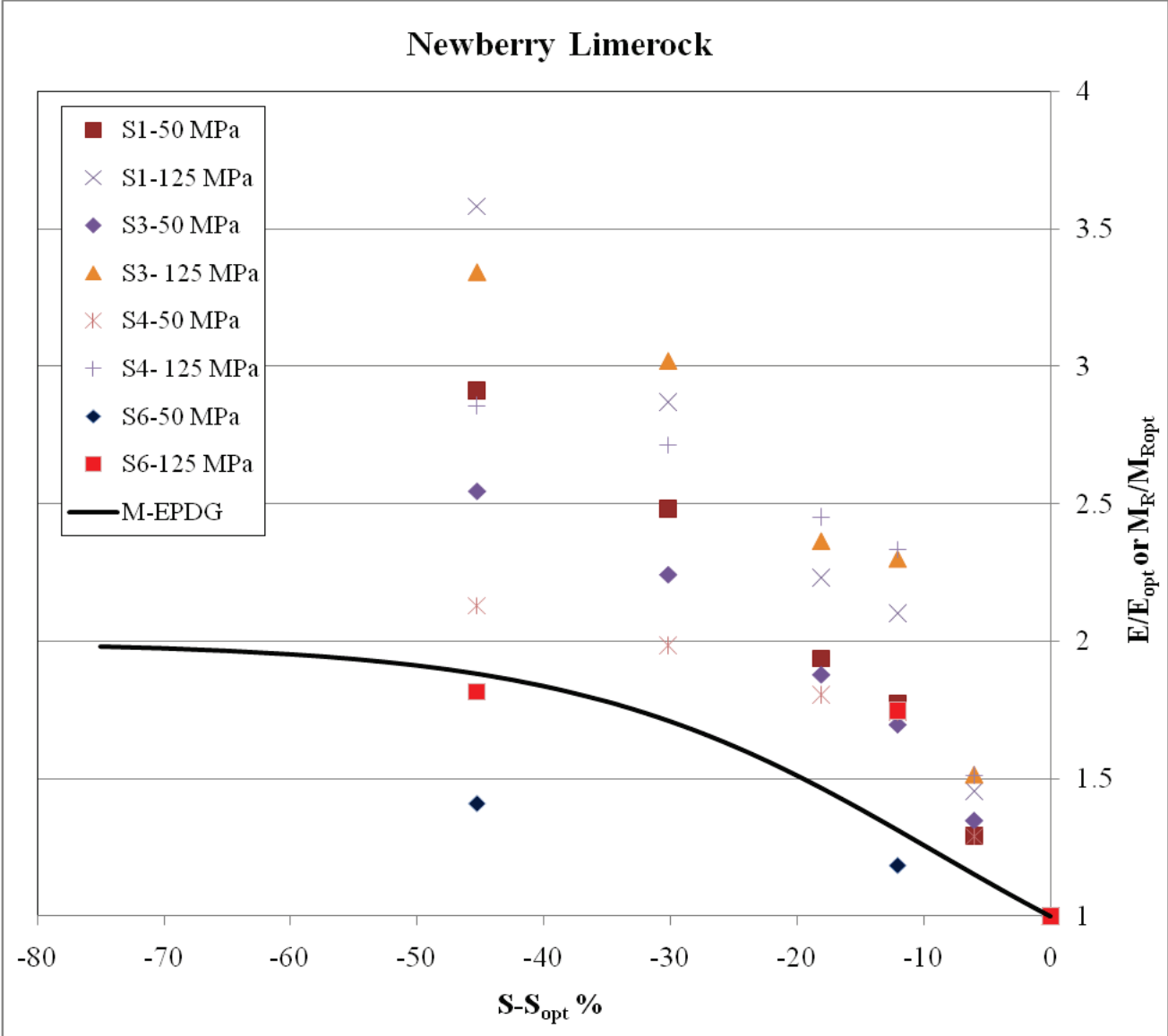
Figure 7-13. Comparison of Newberry limerock effective base moduli with MEPDG model.
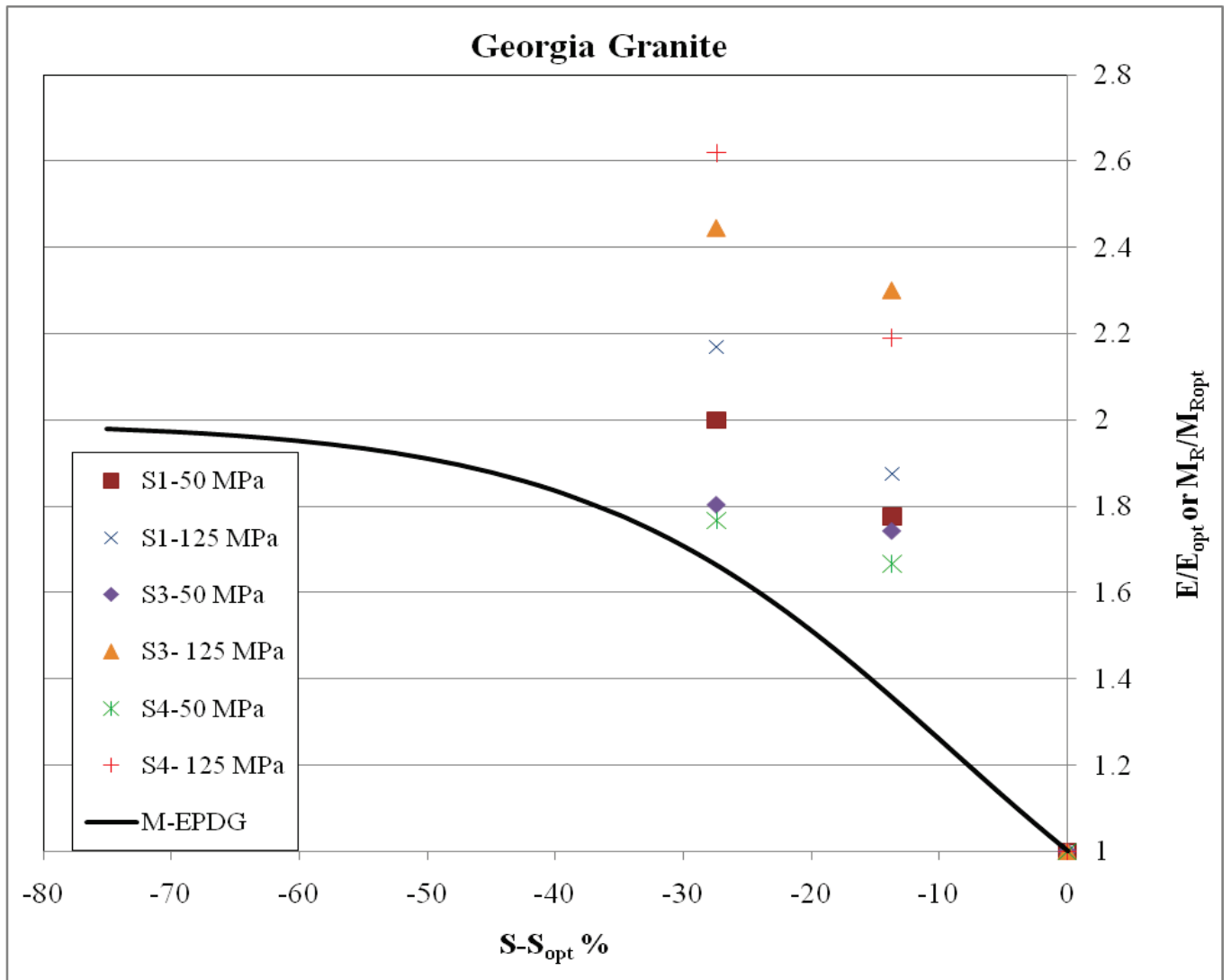
Figure 7-14. Comparison of Georgia granite effective base moduli with MEPDG model.
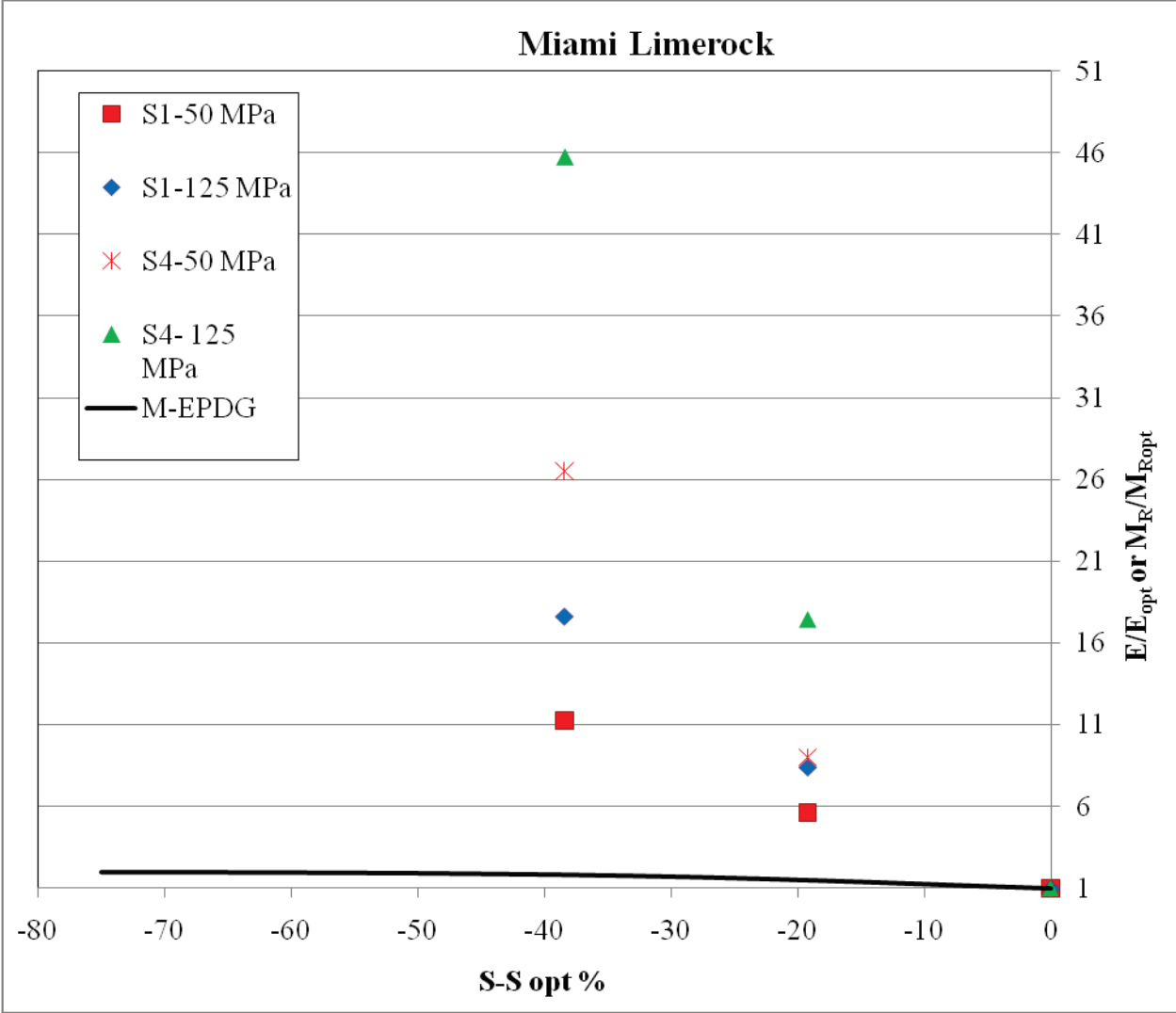
Figure 7-15. Comparison of Miami limerock effective base moduli with MEPDG model.

7.3 Comparison of Nonlinear and Equivalent Linear Responses

A methodology to determine an effective design modulus for a base layer was developed by equating maximum surface deflection between a nonlinear and linear response analysis. It was also demonstated that the complete surface deflection basin generated from a nonlinear analysis and a corresponding equivalent linear analysis match well. As a next step, it is of interest to compare other pavement responses generated from the nonlinear and equivalent linear analysis models to more fully assess the applicability of the effective modulus in lieu of a nonlinear analysis. For this purpose, pavement responses at critical locations obtained from nonlinear and corresponding equivalent linear analysis are compared.

Responses obtained from nonlinear and corresponding equivalent linear analyses at several locations within a pavement structure (Figure 7-1) were as follows:

- Surface deflection

- Horizontal stress (σ_{xx}) and strain (ε_{xx}) at top of AC layer

- Horizontal stress (σ_{xx}) and strain (ε_{xx}) at bottom of AC layer

- Vertical stress (σ_{yy}) and strain (ε_{yy}) at top of base layer

- Vertical stress (σ_{yy}) and strain (ε_{yy}) at bottom of base layer

- Vertical stress (σ_{yy}) and strain (ε_{yy}) at top of subgrade layer

The basis for selecting these responses for comparison is found in the fundamentals of pavement mechanics. Surface cracking and rutting are two important distresses that occur in pavement structures. Surface cracking is primarily dependent on the horizontal strain (ε_{xx}) at the bottom of AC layer, and rutting is dependent on vertical strain (ε_{yy}) at the top of subgrade layer. Comparison of these two responses for nonlinear and linear analyses can illustrate whether adopting an effective modulus in place of nonlinear analysis would influence the rutting and

125

cracking performance of a pavement. Surface deflection was chosen as the criterion of equivalency between the nonlinear and equivalent linear analysis and a comparison will illustrate the accuracy of the match. The remaining stress and strain responses provide further information regarding how well the stresses and strains at different layer intersections agree between the nonlinear and equivalent linear analyses.

A complete demonstration of pavement responses obtained from nonlinear and equivalent linear analysis of selected pavement structures (Table 7-4) with an AC surface modulus of 1000 MPa, a subgrade modulus of 50 MPa, and base materials at specified moisture contents are presented in Appendix C. Because it is particuraly important, the horizontal strain (ε_{xx}) at the bottom of AC layer of Structure 1 and Structure 4 with different base moisture contents is compared in Figure 7-16a for Newberry limerock and Figure 7-16b for Georgia granite. Similarly, the vertical strain (ε_{yy}) at the top of subgrade layer is shown in Figure 7-17a for Newberry limerock and Figure 7-17b for Georgia granite.

Table 7-4. List of pavement structures analyzed for response comparisons.

Base Material	Type of Structure	Moisture Content (%)
Newberry limerock	1 and 4	13
		10
		8
		5.5
Georgia granite	1 and 4	5.5
		3.5

From the surface deflection plots (Figures C-1 to C-8 for Newberry limerock and Figures C-89 to C-92 for Georgia granite), it can be observed that the surface deflection profiles for nonlinear and equivalent linear analyses match well. This demonstates that the procedure for

126

determining an effective modulus based upon matching the maximum surface deflection also results in a more general matching of the complete surface deflection profile.

From the comparison plots of horizontal tensile strain (ε_{xx}) at bottom of AC layer (Figure 7-16), it can be observed that the nonlinear analysis and the equivalent linear case with an effective base modulus produce similar results. This suggests that an equivalent linear analysis can produce an accurate prediction of pavement response in the AC surface layer. This may also suggest that the cracking performance of a flexible pavementcan be reasonably assessed via a linear elastic analysis of the pavement so long as appropriate effective elastic moduli are chosen for the analysis.

Comparison plots of vertical strain (ε_{yy}) at the top of subgrade for nonlinear and equivalent linear cases are compared in Figure 7-17. In the case of Structure 1 and for both materials at different moisture contents, it can be observed that the nonlinear analysis and the equivalent linear case with an effective base modulus produce similar results. In the case of Structure 4, the top of subgrade strains from the nonlinear analysis are higher than the corresponding equivalent linear analysis, and this difference increases with a decrease in moisture content. This suggests that the base material nonlinearity becomes more important with a decrease in moisture content. Since structre 4 is thinner than Structure 1, this also suggests that material nonlinearity increases as the structure thickness decreases, which should be expected. Thus, as the base nonlinearity increases with a decrease in structure thickness or a decrease in base layer moisture content, an effective elastic modulus based upon matching surface deflection should be used with caution. According to pavement mechanics, vertical strain at the top of subgrade is a strong indicator of rutting performance. Thus, the differences in strain might suggest that a linear elastic analysis would overestimate rutting performance. However, this could only be demonstrated by

127

comparing a rutting performance analysis conducted via a suitably-calibrated nonlinear model with a similar model based upon a linear elastic analysis. Such a comparision is beyond the scope of this investigation. Finally, it should also be noted that the differences in strain found in these comparisons are probably accentuated due to the choice of a relatively soft subgrade modulus of 50 MPa. A softer subgrade is expected to increase the nonlinear behavior similar to the effect of decreasing the structure thickness.
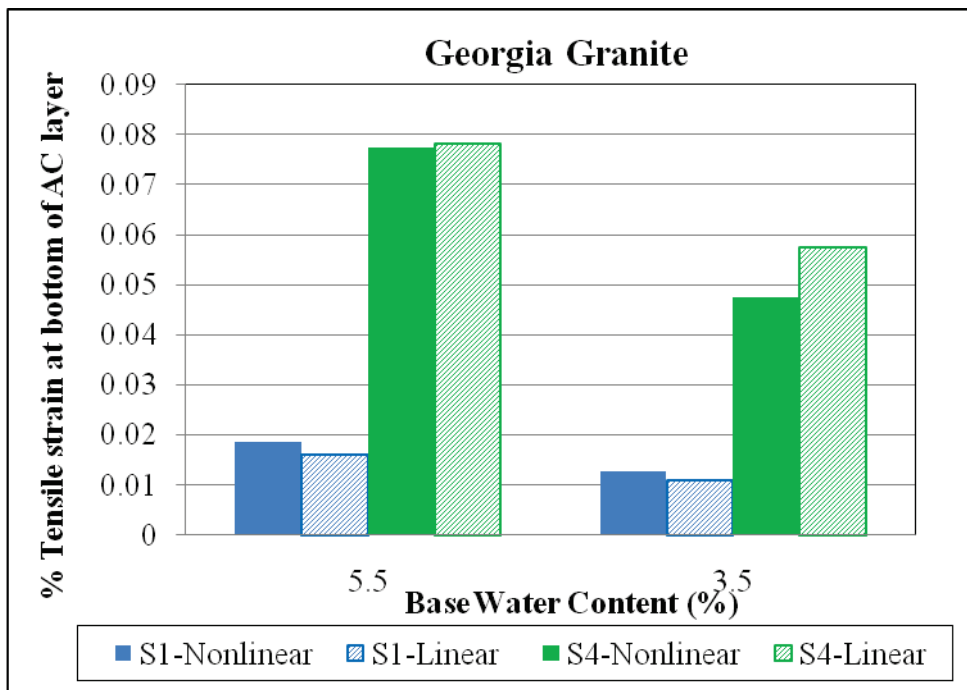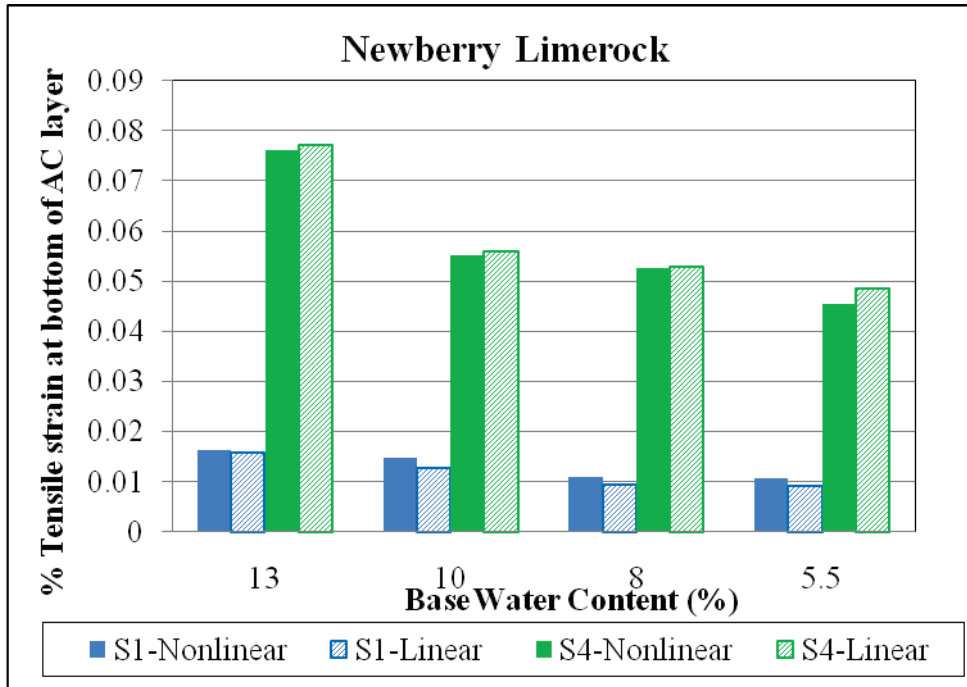
Figure 7-16. Comaprision of horizontal tensile strain at bottom of AC layer for Structure 1 and Structure 4 and for different base moisture contents: (a) Newberry limerock and (b) Georgia granite.

129
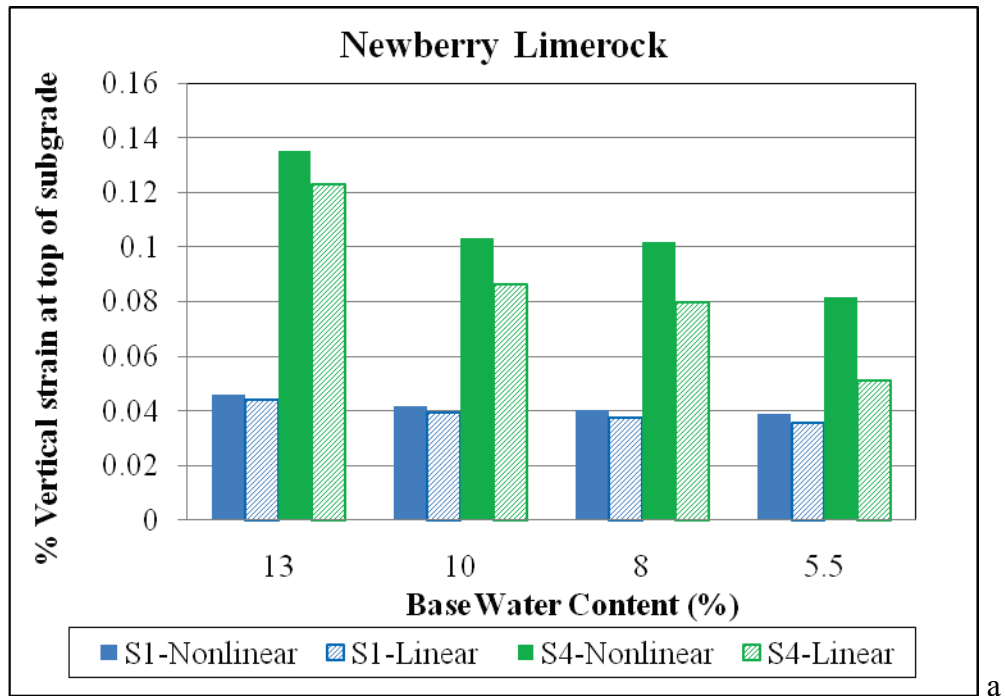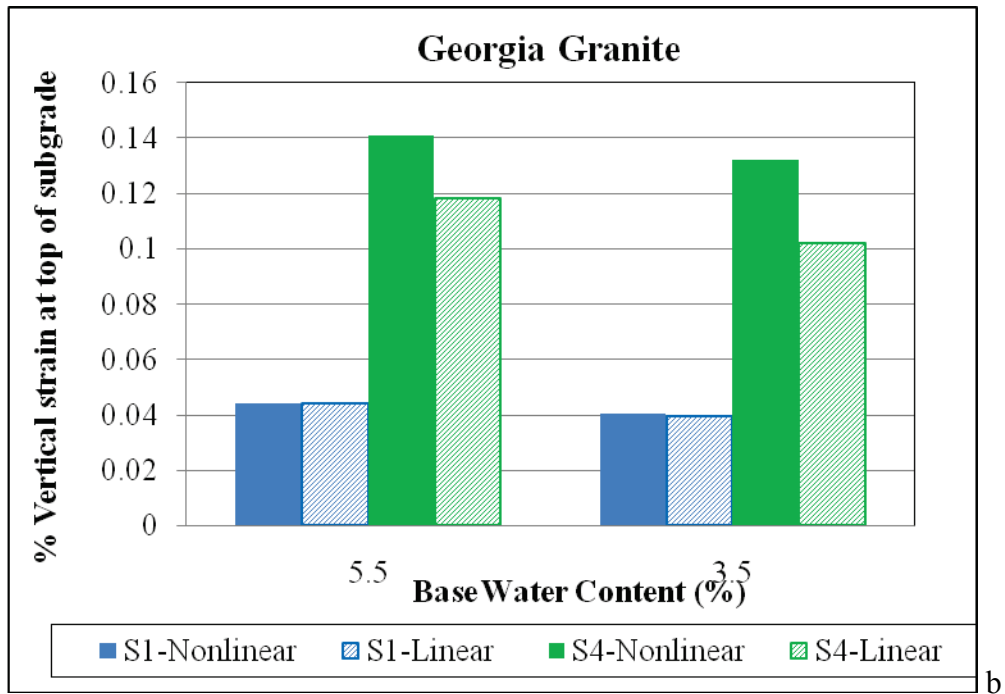
Figure 7-17. Comaprision of vertical compressive strain at top of subgrade for Structure 1 and Structure 4 and for different base moisture contents: (a) Newberry limerock and (b) Georgia granite.

CHAPTER 8
NONLINEAR MODELING OF SUBGRADE LAYER

It was demonstrated in Chapter 7 that by keeping both the AC surface and subgrade layers elastic, and incorporating nonlinearity just in the base layer, results in more vertical strain at the top of subgrade compared to an equivalent linear analysis. Since subgrade soils are also nonlinear materials, it is expected that incorporating modulus nonlinearity in the subgrade layer may result in increased vertical strain. Hence, we conducted an analysis incorporating nonlinearity in both the base and subgrade layers and the results are shown in the following sections.

8.1 Determination of Effective Modulus for Base and Subgrade Layers

8.1.1 Methodology

Two cases are modeled and compared herein:

- A pavement with a linear elastic AC surface layer, nonlinear base, and nonlinear subgrade.

- A pavement with a linear elastic AC surface layer, equivalent elastic base, and equivalent elastic subgrade.

Similar to the analysis in Chapter 7, to derive effective moduli for both nonlinear base and nonlinear subgrade, pavement surface deflection was used as the matching criterion. Since both base and subgrade layers are considered nonlinear, deriving effective moduli for both layers by a trial and error method based on surface deflection is more difficult. Hence, we used a Falling Weight Deflectometer (FWD)-type analysis procedure that can backcalculate elastic modulus values for multiple layers using a surface deflection basin and layer thicknesses as inputs. The surface deflection basin for the backcalculation was produced by the Plaxis-HS small model for nonlinear base and nonlinear subgrade. Pavement responses obtained from the nonlinear analysis were then compared with an equivalent linear analysis using the effectivie moduli.

8.1.2 Material Parameters and Structural Inputs

Two pavements, Structure 1 and Structure 4 (Figure 6-5), were considered for this analysis, and material moduli used for different layers are presented in Table 8-1. For the subgrade layer, Ottawa sand was chosen for the nonlinear analysis since this material was tested as part of the laboratory testing program (Figure 3-7), and HSsmall input parameters for the sand are presented in Table 8-2.

Table 8-1. Material properties for nonlinear base and nonlinear subgrade analysis.

Pavement Layer	Material	Modulus (MPa)
Surface	AC	1000
Base	Newberry limerock	Values at 13, 12, 11, and 10% moisture
	Georgia granite	Values at 5.5, 4.5, and 3.5% moisture
Subgrade	Ottawa sand	HS small parameters are given in Table 8-2.

Table 8-2. HS small model parameters for Ottawa sand.

Parameter	Value
G_{max} (MPa)	120
$\gamma_{0.7}$	5.0E-04
P_{ref} (kPa)	100
E_{max} (MPa)	316.80
E_{ur} (MPa)	269.28
E_{oed} (MPa)	134.64
E_{50} (MPa)	134.64
m	0.5
γ (kN/m^3)	18.11
ν	0.32

8.1.3 Surface Deflection Basin Matching

By way of example, nonlinear analysis via the Plaxis-HSsmall response model was performed on Structure 1 with Newberry limerock base at 10% moisture content and Ottawa sand subgrade. From the analysis, a maximum surface deflection of 0.62 mm was obtained for a wheel load of 550 kPa. Using this surface deflection basin, effective moduli for the surface, base, and subgrade layers were backcalculated via the FWD-type analysis (Figure 8-1). The surface deflection basins for both the nonlinear and equivalent linear cases are compared in Figure 8-2 where it is observed that the basins match very well.
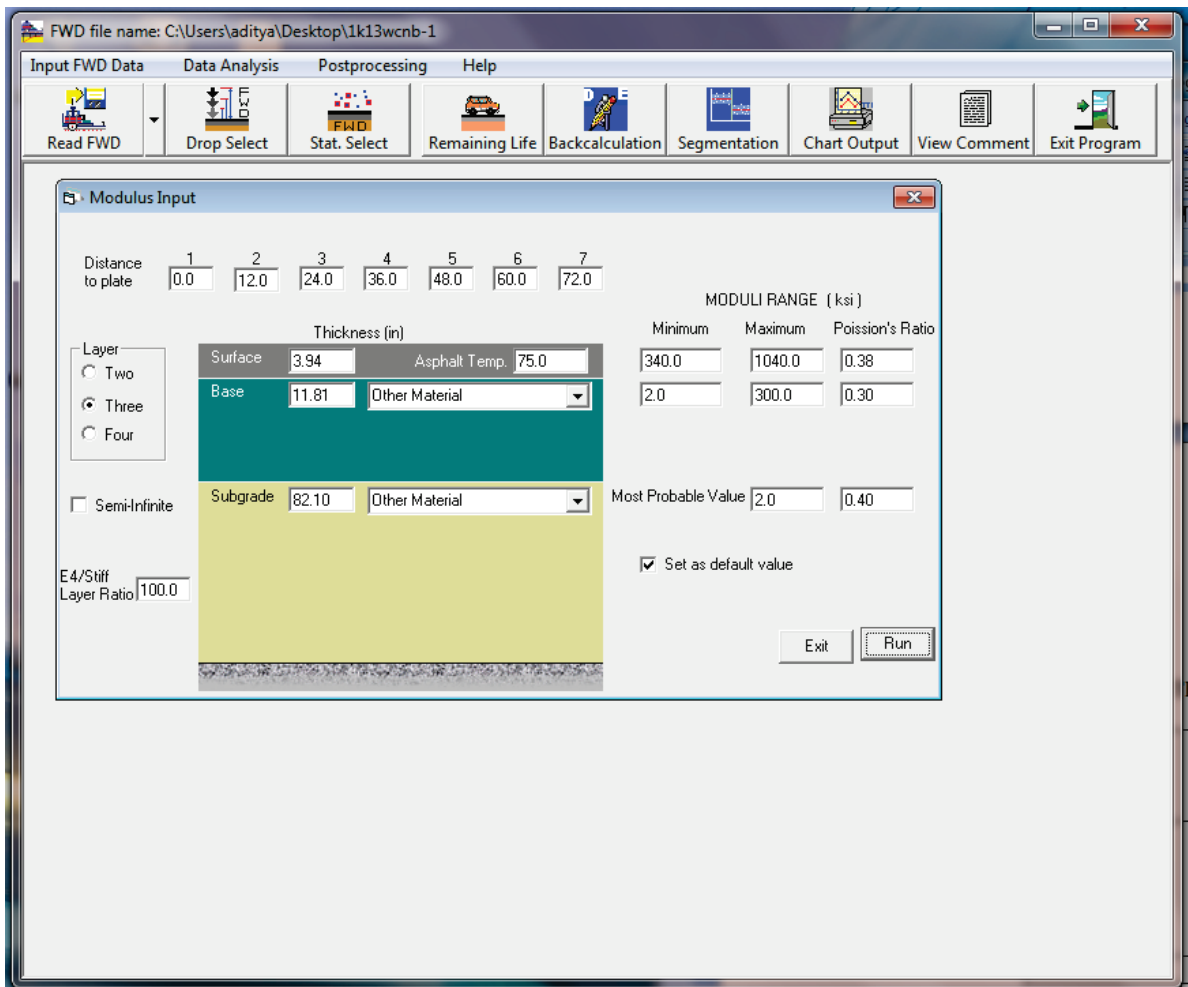
Figure 8-1. FWD analysis of Structure 4.
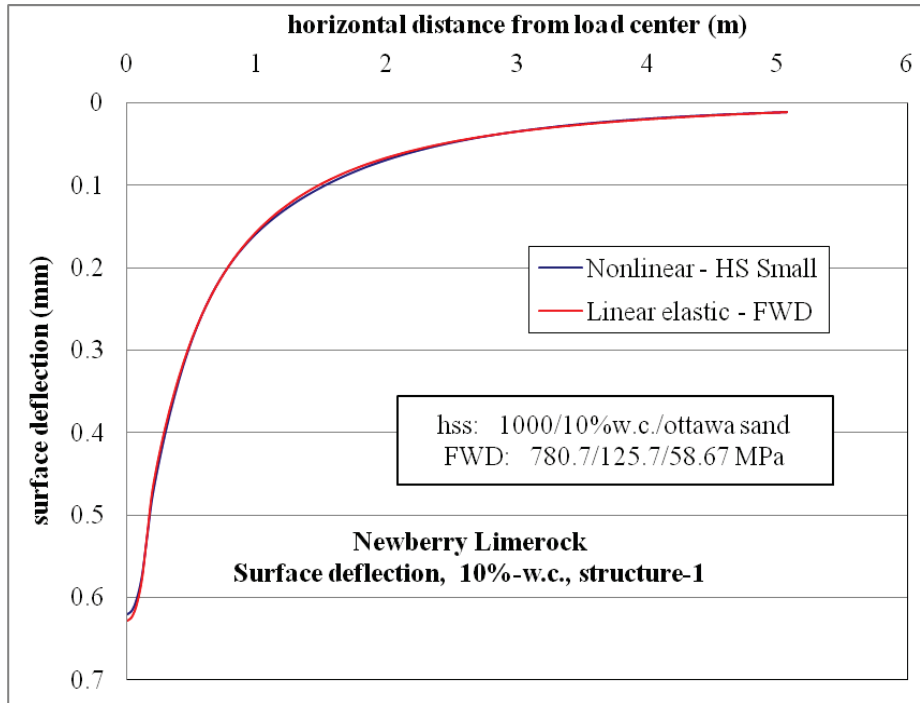
Figure 8-2. Nonlinear and linear surface deflections for Structure 1 with 10% moisture base and Ottawa sand subgrade.

8.2 Comparison of Nonlinear and Equivalent Linear Analysis Results

8.2.1 Effective Moduli Values for Base and Subgrade

Backcalculated effective moduli values for Structure 1 and Structure 4 with different moisture contents of Newberry limerock base and Ottawa sand subgrade are presented in Tables 8-3 and Table 8-4. Similar results for Georgia granite base and Ottawa sand subgrade are presented in Tables 8-5 and 8-6.

First, for the base layer, it is observed that effective moduli values increase with material drying as expected. When we compare the backcalculated base effective moduli results with those from Chapter 7, here the effective modulus for any moisture content is smaller than the corresponding value obtained with an elastic subgrade of 50 MPa (Tables 7.1 to 7.3). This decrease in base effective modulus suggests an additional effect of subgrade nonlinearity that causes greater strain and lower effective moduli.

134

Table 8-3. Equivalent elastic moduli for Structure 1 with Newberry limerock base and Ottawa sand subgrade.

	Structure 1	
Layer	Nonlinear Plaxis-HSsmall Model Analysis (MPa)	Linear Analysis (MPa)
AC Surface Layer	1000	862
Base	13%	67.75
Subgrade	Ottawa sand	54.95
AC Surface Layer	1000	858.12
Base	12%	86.60
Subgrade	Ottawa sand	55.64
AC Surface Layer	1000	795.10
Base	11%	124.24
Subgrade	Ottawa sand	53.92
AC Surface Layer	1000	780.686
Base	10%	125.69
Subgrade	Ottawa sand	58.67

Table 8-4. Equivalent elastic moduli for Structure 4 with Newberry limerock base and Ottawa sand subgrade.

	Structure 4	
Layer	Nonlinear Plaxis-HSsmall Model Analysis (MPa)	Linear Analysis (MPa)
AC Surface Layer	1000	1073.79
Base	13%	24.82
Subgrade	Ottawa sand	44.61
AC Surface Layer	1000	1099.37
Base	12%	31.44
Subgrade	Ottawa sand	43.85
AC Surface Layer	1000	1012.98
Base	11%	42.06
Subgrade	Ottawa sand	43.85
AC Surface Layer	1000	1019.66
Base	10%	42.33
Subgrade	Ottawa sand	44.26

Table 8-5. Equivalent elastic moduli for Structure 1 with Georgia granite base and Ottawa sand subgrade.

	Structure 1	
Layer	Nonlinear Plaxis-HSsmall Analysis (MPa)	Linear FWD Analysis (MPa)
AC Surface Layer	1000 (elastic)	851.77
Base	5.5%	61.36
Subgrade	Ottawa sand	55.80
AC Surface Layer	1000 (elastic)	823.99
Base	4.5%	114.04
Subgrade	Ottawa sand	58.67
AC Surface Layer	1000 (elastic)	820.82
Base	3.5%	124.00
Subgrade	Ottawa sand	56.67

Table 8-6. Equivalent elastic moduli for Structure 4 with Georgia Granite base and Ottawa sand subgrade.

	Structure 4	
Layer	Nonlinear Plaxis-HSsmall Analysis (MPa)	Linear Analysis (MPa)
AC Surface Layer	1000 (elastic)	1058
Base	5.5%	24.54
Subgrade	Ottawa sand	44.5
AC Surface Layer	1000 (elastic)	1005.32
Base	4.5%	40.47
Subgrade	Ottawa sand	44.68
AC Surface Layer	1000 (elastic)	944.44
Base	3.5%	46.19
Subgrade	Ottawa sand	45.02

Next, backcalculated effective moduli for the subgrade layer are in the range of 55 to 60 MPa for Structure 1 and 42 to 44 MPa for Structure 4. The decrease in subgrade effective modulus in Structure 4 indicates an increase in subgrade nonlinearity due to the decrease in structure thickness and is consistent with pavement mechanics fundamentals.

For Structure 1, backcalculated effective moduli for the base layer are greater than the moduli of the subgrade, whereas for Structure 4, backcalculated effective moduli for the base

layer are usually lower than that of the subgrade. As noted above, the decrease in structure

thickness increases modulus nonlinearity and results in lower effective moduli for the base.

Finally, backcalculated elastic moduli for the AC surface layer are in the range of 800 MPa

for Structure 1 and 1050 MPa for Structure 4, while the modulus value assigned to the AC layer

in the nonlinear analysis was 1000 MPa.

8.2.2 Comparison of Nonlinear and Equivalent Linear Pavement Responses

As in Chapter 7, pavement responses obtained at important locations in the pavement

structure were compared for the nonlinear and corresponding equivalent linear analyses. A list of

cases that were analyzed is given in Table 8-7, and the entire collection of nonlinear and

equivalent linear response comparison plots are presented in Appendix D. For example, the

horizontal strain at the bottom of AC layer for Structure 1 and with different base moisture

contents are compared in Figure 8-3a for Newberry limerock and Figure 8-3b for Georgia

granite. Similarly, comparison plots for vertical strain at the top of subgrade layer are shown in

Figure 8-4a for Newberry limerock and Figure 8-4b for Georgia granite.

Table 8-7. List of pavement structures analyzed for response comparis.

Base Material	Structure	Moisture Content (%)
Newberry limerock	1	13
		10
	4	10
Georgia granite	1	5.5
		3.5

From surface deflection (Figures D-1 to D-3 for Newberry limerock and Figures D-34 to

D-35 for Georgia granite), it can be observed that the surface deflection profiles for nonlinear

and equivalent linear analyses match well. This demonstates that the procedure for determining effective moduli based upon matching surface deflection is successful.

From the comparison plots of horizontal tensile strain at the bottom of AC layer (Figure 8-3a and 8-3b), it can be observed that the horizontal strains for the nonlinear case are similar to the equivalent linear case with backcalculated effective moduli. Similar to the results in Chapter 7, this suggests that an equivalent linear analysis can produce an accurate prediction of pavement response in the AC surface layer. This may also suggest that the cracking performance of a flexible pavementcan be reasonably assessed via a linear elastic analysis of the pavement so long as appropriate effective elastic moduli are chosen for the analysis.

From the comparison plots of vertical strain at the top of subgrade (Figure 8-4a and 8-4b), it can be observed that vertical strains for the nonlinear case are almost two times greater than the corresponding values for the equivalent linear analysis. Since these results come from Structure 1, the thickest pavement, it is expected that the deviations would be even larger for thinner pavement structures. This indicates that the subgrade behavior cannot be modeled well with an equivalent linear analysis based upon matching surface deflection when both base and subgrade nonlinearity is taken into account.
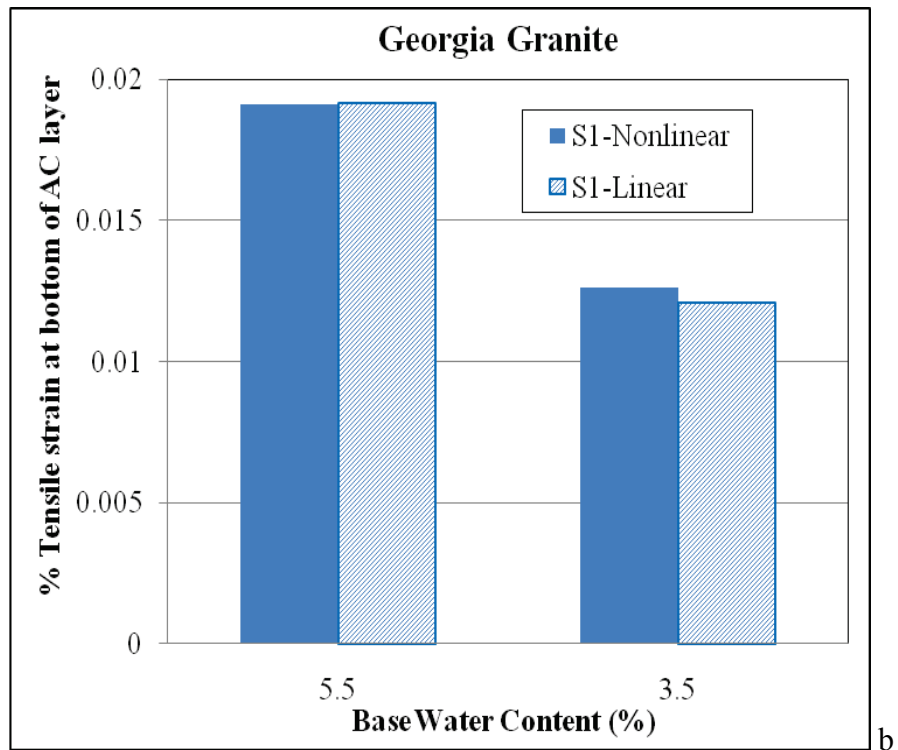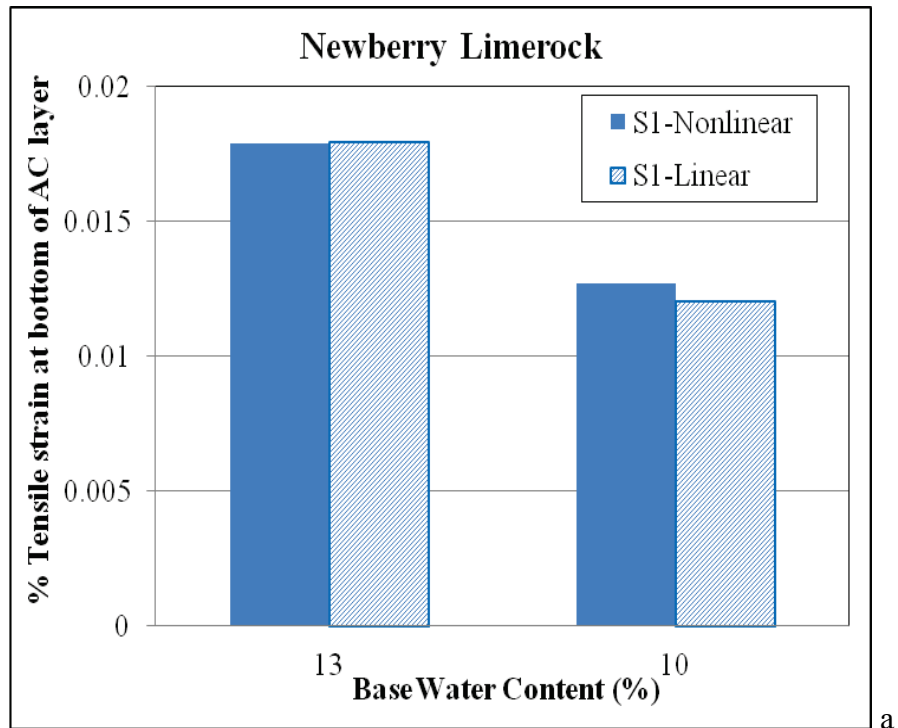
Figure 8-3. Horizontal tensile strain at bottom of AC layer of Structure 1 with Ottawa sand subgrade and two base moisture contents for: (a) Newberry limerock and (b) Georgia granite.
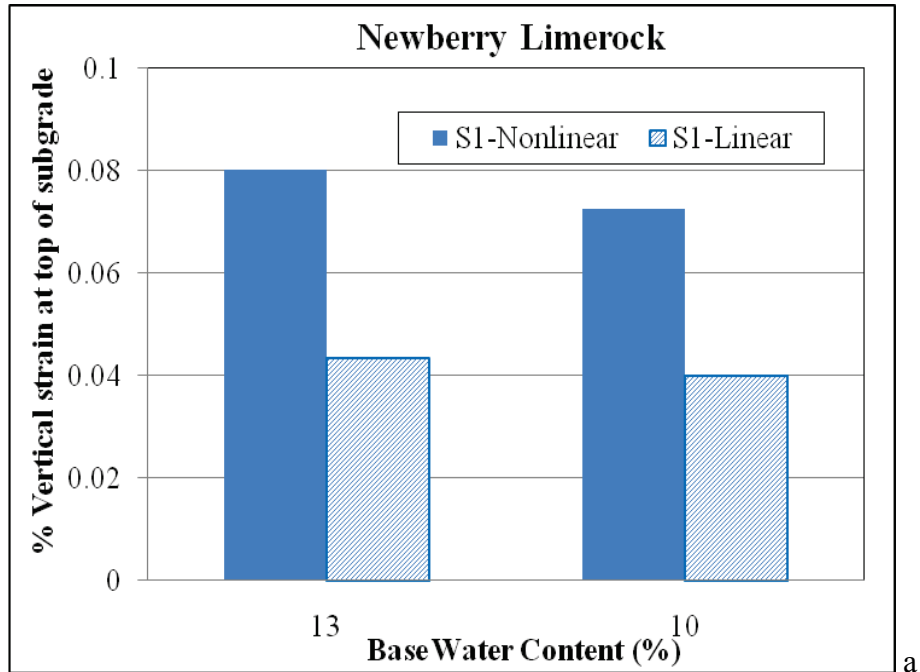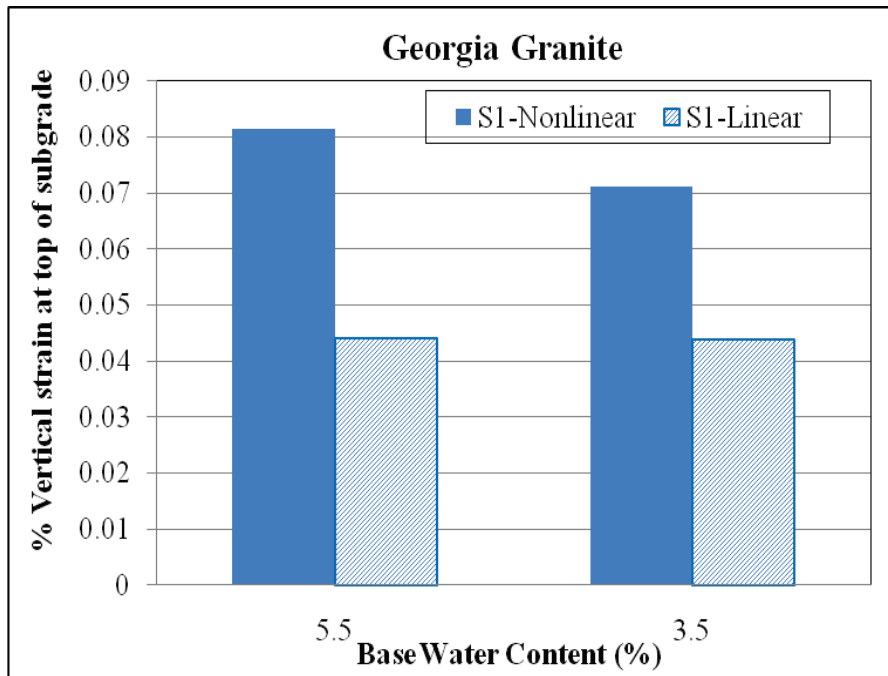
Figure 8-4. Vertical compressive strain at top of subgrade for Structure 1 with Ottawa sand subgrade and two base moisture contents for: (a) Newberry limerock and (b) Georgia granite.

CHAPTER 9
CONCLUSIONS

9.1 Summary of Findings

The primary goal of this research investigation was to develop a methodology to determine a single effective modulus of a base layer that can approximate known material modulus nonlinearities and can be used as MEPDG Level 2 or Level 3 material parameter input. In order to achieve this goal a laboratory testing program was conducted on base materials and a nonlinear response model was developed using the laboratory testing results. First, a laboratory testing program was conducted on two base materials used in the State of Florida to characterize modulus nonlinearity with respect to stress, strain, including small-level strains, and moisture content. Fixed-free resonant column torsional shear (fixed-free RC) tests that can measure shear modulus in the strain range of $10^{-5}\%$ to $10^{-1}\%$ while varying pressure confinement and moisture content were conducted on modified Proctor compacted cylindrical specimens of Newberry limerock and Georgia granite. Second, utilizing these laboratory tested parameters, a nonlinear finite element pavement response model that can account for the modulus nonlinearities was developed via the Plaxis-HSsmall model. Various types of pavement structures with nonlinear base and elastic AC surface and subgrade layers were analyzed for single wheel loading via the nonlinear response model. Based on pavement responses obtained from this nonlinear analysis, a methodology was developed to determine an effective elastic modulus for the base layer that can approximately account for nonlinearity. The influence of base layer nonlinearity on pavement response was evaluated, and the influence of both base and subgrade modulus nonlinearity on pavement response was also evaluated for a few selected pavement structures. The following sections provide a discussion of the findings in more detail.

9.1.1 Laboratory Testing on Unbound Aggregate Base Materials

Limerock is commonly used for pavement base layer construction in the State of Florida. Newberry limerock and Georgia granite were selected for laboratory testing, representing one limerock aggregate and one non-limerock graded aggregate. Fixed-free resonant column torsional shear tests (fixed-free RC) and free-free resonant column test methods were followed. The fixed-free RC equipment was updated to measure strains as small as 10^{-5}% using a fiber optic sensor. Credibility of this updated apparatus was evaluated and verified by conducting tests on Ottawa sand specimens and comparing sand test results with data available in the literature. Fixed-free RC were conducted on modified Proctor specimens of Newberry limerock and Georgia granite to investigate the influence of effective confinement stress, loading strain, including small-level strains, and moisture content. Modulus in the strain range of 10^{-5}% to 10^{-1}% was measured to analyze small-strain modulus nonlinearity of these materials. Specimens were dried in a laboratory environment and tested at different moisture contents in the process of drying. Additional effective confinement due to suction at different moisture contents was evaluated. Empirical equations to calculate maximum shear modulus (G_{max}) of dry materials were developed. An approximate methodology to calculate shear modulus at any given effective confinement, strain level, and moisture content was also proposed. Free-free resonant column tests were also conducted on compacted specimens to determine very small-strain modulus (i.e., G_{max} at $\leq 10^{-5}$% strain) at different moisture contents ranging from OMC to near dry condition. Based upon the laboratory testing program, the following findings have been derived:

- For dry materials, the shear modulus of Newberry limerock is proportional to pressure confinement to the power of 0.702, and for Georgia granite the modulus is proportional to pressure confinement to the power of 0.6389.

- For dry materials, the shear modulus is maximum and elastic at strains lower than 10^{-4}%, starts decreasing linearly in the strain range of 10^{-4}% to 10^{-3}%, and decreases nonlinearly

142

thereafter. The presence of gravel-size aggregate makes modulus more nonlinear compared to sands.

- The G_{max} of dry Newberry limerock and dry Georgia granite at known void ratio (e) and confinement (σ_c) can be determined using the following empirical equations:

  Newberry limerock: $G_{max} = (2575) \, F(e) \, (\sigma_c)^{0.772}$

  Georgia granite: $G_{max} = (816) \, F(e) \, (\sigma_c)^{0.6638}$

  where $F(e) = \dfrac{(2.17-e)^2}{(1+e)}$

- In an unsaturated condition, the shear modulus is maximum at 10^{-5}% strain, and starts decreasing thereafter with an increase in strain.

- In a dry condition, shear modulus is maximum (i.e , G_{max}) at 10^{-4}% strain, and decreases to 0.15 G_{max} at 10^{-1}% strain. Whereas, in an unsaturated condition, shear modulus is maximum at 10^{-5}% strain, and decreases to 0.075 G_{max} at 10^{-1}% strain. Compared to the dry material, the presence of moisture increases modulus nonlinearity.

- In unsaturated soils, a decrease in moisture content due to drying provides additional suction confinement and increases G_{max} significantly.

- Additional confinement due to suction at different moisture contents is material specific and needs to be evaluated separately for each material for accurate modulus nonlinearity characterization.

- In dry materials, the rate of decrease in G (i.e., G/G_{max}) with increase in strain is approximately independent of confinement pressure. In unsaturated materials, the rate of decrease in G with increase in strain is independent of moisture content and its suction confinement.

- In an unsaturated condition, at any given moisture content, the suction effect on G does not change with an increase in strain over the range of strains tested in the laboratory.

- The strains generated in free-free RC testing are approximately in the range of 10^{-5}%, and corresponding moduli are nearly equal to the small-strain moduli from fixed-free RC tests.

9.1.2 Nonlinear Response Model and Base Layer Nonlinear Modeling and Analysis

Utilizing the laboratory testing data as material inputs, a nonlinear finite element response

model that can account for modulus nonlinearity was developed via the Plaxis-HSsmall model.

This response model can incorporate modulus nonlinearity with respect to effective stress

confinement, strain magnitude, including small-level strains, and moisture content. From some

initial pavement modeling and analysis exercises via the Plaxis-HSsmall, it was observed that the response model behaves too soft, and as a result produces high deformations. Hence, the response model was recalibrated using Lehane et al. (2008) footing analysis results. Input parameters of the HSsmall model were recalibrated such that Lehane's footing analysis produces deformations matching with measured footing settlements. This recalibrated nonlinear response model was used for further pavement base layer modeling and analysis. Based on laboratory testing data of Newberry limerock, Georgia granite, and Miami limerock, calibrated material input parameters for the nonlinear response model were developed and functional capabilities of the response model to incorporate modulus nonlinearity were illustrated.

To single out the influence of base layer modulus nonlinearity on pavement response, the AC surface layer and subgrade were considered elastic, and the base layer was considered nonlinear. Using the maximum surface deflection as the matching criterion between nonlinear and linear analysis, a methodology to determine an effective elastic modulus that can approximate the nonlinearities of the base layer was developed. An effective moduli database for a range of pavement structures, subgrade moduli, and base moisture contents was developed from repeated runs of the nonlinear response model, and the influence of moisture content, subgrade modulus, and structure type (thickness) on effective modulus was evaluated. Effective moduli values of the three materials were compared with each other, and also compared with the MEPDG moisture (suction) model to assess the suitability of the MEPDG model for our base materials. Nonlinear and equivalent linear pavement responses obtained at critical locations were compared to evaluate the applicability of base layer effective modulus as a substitute for a more complete nonlinear analysis. Based upon the base layer nonlinear modeling and analysis results, the following findings have been derived:

- The effective base modulus increases significantly with a decrease in moisture content and the rate of increase is material specific.

- Our laboratory testing data showed that a decrease in moisture content increases the additional confinement caused by suction, which in turn increases small-strain modulus. This increase in small-strain modulus is being reflected on effective modulus and hence single effective modulus increases with a decrease in moisture content.

- For any given structure and base moisture content, the effective base modulus increases with an increase in subgrade modulus, i.e., the effective design modulus of a base layer at any given moisture content depends on modulus of the subgrade that supports the base layer.

- At any given moisture content and subgrade modulus combination, the base layer effective modulus is dependent on thicknesses of the pavement layers. As the thicknesses vary, the magnitude of wheel load deviatoric stresses transferred from the top to bottom layers also varies. Since modulus is nonlinear with respect to stress, effective modulus also varies.

- Among the three materials evaluated, Miami limerock behaves differently, and its effective modulus increases at a significantly faster rate as the material dries. At OMC, the effective modulus of Miami limerock is much lower than that of Newberry limerock and Georgia granite. But, as the material dries, its modulus increases at a faster rate compared to the other two materials. Therefore, an increase in design modulus with material drying is material specific. Since modulus tests are generally conducted at OMC, it is important to take this behavior into account.

- With the MEPDG modulus/moisture model, modulus can increase with a decrease in moisture content a maximum of two times the modulus at optimum moisture content. Effective base moduli derived for our materials change at a faster rate. E/E_{opt} values increase up to 3.5 times for Newberry limerock, 2.5 times for Georgia granite, and 47 times for Miami limerock. E/E_{opt} values for our materials are determined only for a decrease in degree of saturation down to 40%, and can potentially increase further with a further decrease in degree of saturation. The current MEPDG modulus/moisture model does not appear to incorporate the moisture/suction effect accurately for these Florida base materials.

- Surface deflection profiles for nonlinear and equivalent linear analyses match well and serve as an effective means for determining an equivalent elastic modulus.

- Horizontal strain at the bottom of AC layer for nonlinear base modulus case is approximately equal to the equivalent linear case with effective base modulus. This suggests that an equivalent linear analysis can produce an accurate prediction of pavement response in the AC surface layer.

- For vertical strain at the top of subgrade, base nonlinearity increases with a decrease in structure thickness or a decrease in base moisture content, and an effective elastic modulus based upon matching surface deflection should be used with caution.

9.1.3 Nonlinear Modeling and Analysis of Base and Subgrade Layers

Nonlinear modeling and analysis of both base and subgrade layers were conducted for a few pavement structures to evaluate the effect of both sources of nonlinearity on pavement response. For this nonlinear modeling, the AC surface layer was considered elastic. Since material properties were measured in the laboratory testing program, Ottawa sand was chosen as the subgrade material. Considering the surface deflection basin obtained from nonlinear analysis as the matching criterion, an FWD-type backcalculation method was followed to determine equivalent elastic moduli for all layers. Equivalent elastic moduli were then used for linear analysis of the pavement structures, and pavement responses obtained from nonlinear analysis and equivalent linear analysis were compared. Based upon these results, the following findings have been derived:

- Backcalculated subgrade moduli for nonlinear subgrade structures are in the range of 40 to 44 MPa. By comparing the backcalculated effective base moduli of these nonlinear subgrade structures with that of the same structures with 50 MPa elastic subgrade, the effective modulus of base layer with nonlinear subgrade is significantly lower than effective modulus of base layer with 50 MPa elastic subgrade, indicating the subgrade nonlinearity has a significant influence on the base behavior as well.

- Surface deflection profiles for nonlinear and equivalent linear analyses match well and serve as an effective means for determining equivalent elastic moduli.

- Horizontal strain at the bottom of AC layer for nonlinear base and subgrade case is approximately equal to the equivalent linear case with effective base moduli. This suggests that an equivalent linear analysis can produce an accurate prediction of pavement response in the AC surface layer.

- For vertical strain at the top of subgrade, the vertical strains for the nonlinear case are almost two times greater than the corresponding values for the equivalent linear analysis. Since these results come from Structure 1, the thickest pavement, it is expected that the deviations would be even larger for thinner pavement structures. This indicates that the subgrade behavior cannot be modeled well with an equivalent linear analysis based upon matching surface deflection when both base and subgrade nonlinearity is taken into account.

9.2 Conclusions

Based on the findings outlined above, the following conclusions are appropriate:

- The fixed-free resonant column methodology can determine the modulus nonlinearity of base materials over a wide range of strains, from very small strains of less than $10^{-5}\%$ to strains as large as $10^{-1}\%$.

- Modulus nonlinearity can be characterized on both dry base materials and on wet materials over a practical range of moisture contents. The modulus increases significantly with a decrease in moisture content. It appears that a decrease in moisture content due to drying creates suction, which provides significant additional effective confinement. The suction effect can increase nonlinear modulus significantly up to strain levels as high as $10^{-2}\%$.

- The free-free resonant column methodology can accurately determine the modulus of base materials at very small strains and over a wide range of moisture conditions.

- The Plaxis HSsmall finite element methodology is an effective means for assessing the effects of unbound pavement material nonlinearity on the structural response of pavements.

- Practical pavement design utilizing the MEPDG will require input of a single modulus value to represent unbound base and subgrade materials. A representative modulus can be determined by a backcalculation procedure in which pavement surface deflections from a nonlinear analysis are matched via an equivalent linear analysis.

- The nonlinearity of unbound base materials is significant and the single effective modulus will vary over a range of conditions, including the moisture content of the base, pavement layer thicknesses, and the modulus of the subgrade.

- There is a significant effect of moisture on the modulus of base materials used in Florida, particularly those composed of limerock. The modulus/moisture relationship employed in the MEPDG underpredicts the significant increase in modulus of Florida limerock base materials when dried below OMC. Use of the MEPDG model will be conservative.

- An equivalent linear analysis using effective moduli for both an unbound base and the subgrade and based upon matching surface deflections can predict the structural response of an asphalt surface layer in a flexible pavement. It should be possible to utilize these structural response predictions in the assessment of cracking performance of the surface layer.

- However, caution is warranted in predicting the structural response of the unbound base and subgrade layers using an equivalent linear analysis. Use of an effective modulus for a nonlinear base layer appears reasonable for very thick pavement structures, but appears to underpredict vertical strain at the top of subgrade as the nonlinearity increases due to decreasing thickness, decreasing moisture content, or softening of the subgrade. Use of effective moduli for both a nonlinear base and subgrade appears to underpredict top of subgrade vertical strain even for very thick pavements.

9.3 Recommendations

The following recommendations are suggested after reviewing all of the findings and conclusions previously discussed:

- The MEPDG recommends resilient modulus (M_R) as the primary input for characterizing unbound base materials. For Level 1, the parameters that describe the nonlinear results from an M_R test are expected, while for Levels 2 and 3, a single elastic modulus is required for base characterization. However, the ASSHTO protocol for determination of M_R from a laboratory test does not provide characterization of the material over a complete range of strains. In addition, the MEPDG does not provide a methodology for determining a single elastic modulus from M_R test results. The resonant column tests conducted in this research characterized the base materials over a wide range of strains and moisture conditions. A procedure was developed for determining an effective elastic modulus for a base material that can be utilized in Levels 2 and 3 of the MEPDG. These results can be used for the design of pavements in Florida. However, two important issues may require further consideration.

- First, the resonant column tests were conducted on freshly compacted laboratory specimens. Toros (2008) demonstrated that significant time-dependent increases in modulus occur in base materials following initial construction, even at constant moisture content. For example, the very small-strain modulus may increase by more than a factor of 10 for some Florida limerock materials (Figure 2-17). This phenomenon provides a likely explanation for the observation that the effective moduli reported in Chapters 7 and 8 are low for moisture contents at or near OMC. Thus, the effective moduli appropriate for typical field conditions should account for this time-dependent behavior. The required adjustment is approximately equivalent to utilizing effective moduli reported herein at moisture conditions significantly drier than OMC. For example, an effective modulus for Newberry limerock for Structure 4 (a typical Florida pavement) at a moisture content of 5.5% is consistent with the expected conditions in the field at OMC. The effective modulus reported in Table 7.1 is 240 MPafor these conditions and at a subgrade modulus of 125 MPa (typical Florida subgrade). This effective modulus value approximates the modulus that would be attained at OMC following time-dependent increases at constant moisture. Further increases in modulus would be expected if the material dried following initial construction. While these observations are approximate, they provide an initial recommendation for input values of effective modulus for use in Levels 2 and 3 MEPDG design. Certainly further laboratory experiments, field experiments, and model studies are warranted to refine and corroborate these preliminary recommendations.

- Second, it is clear from the work reported herein that the behavior of pavement base materials is complicated by several significant nonlinear relationships, and the idea that a base layer can be easily represented by a single modulus value should be used with caution. On the one hand, the methodology reported herein for determination of a single effective modulus that can account approximately for these nonlinearities can significantly simplify pavement design with regard to the base layer. The nonlinear equivalent single

effective base modulus methodology can be implemented in the MEPDG for determining Level 2 and Level 3 material parameter inputs. However, the methodology is itself complicated in its current form, requiring at minimum a nonlinear finite element pavement response model. Yet, it appears likely that this methodology could be itself replaced by a simpler empirically-based relationship following a more exhaustive parametric study with the finite element model. At the very least, base course small-strain modulus nonlinearity and the moisture suction effect on it should be implemented in pavement design procedures. The AASHTO resilient modulus protocol will not capture this behavior since the modulus is not measured at the appropriate small strains. Underestimation of the modulus versus moisture behavior by the MEPDG modulus/moisture model may be due to the fact that this empirical model is based upon laboratory resilient modulus values determined by the AASHTO protocol.

- The effective modulus procedure documented herein is based upon the Plaxis-HSsmall nonlinear response model that has been compared with and calibrated against only one field test result of a shallow foundation on sand. While the one calibration check is quite positive, a more comprehensive calibration procedure based upon pavement examples would seem most appropriate. In general, there are very limited examples available in the literature of comparisons between pavement response models and field test results, and most of the examples are for linear elastic pavement response models. It is common to assume the pavement responses are accurate, and then to provide calibration adjustment coefficients between response and observed performance. However, this approach does not properly identify the sources of the discrepancies, and makes it near impossible to know what aspect of the system requires further improvement since much of the error is lumped together in one or a small number of coefficients.

- As noted above, the analysis results presented herein certainly reveal that both base and subgrade particulate materials exhibit significant nonlinear behavior with respect to both loading and environmental variables. As shown, these nonlinearities may not have significant effect on the cracking performance of asphalt concrete flexible pavements. However, the nonlinearities can have a significant effect on the responses within the base and subgrade layers, and these responses typically play a significant role in the determination of permanent deformation, i.e., rutting. However, the effect of these response differences on performance cannot be clearly identified utilizing performance models that were developed around linear elastic pavement response models. Rather, a performance analysis that is properly coupled with a nonlinear pavement response model should be utilized to more carefully evaluate the potential effect on performance.

- Two additional considerations may be warranted regarding the development of an equivalent linear elastic model utilizing effective moduli. First, the significant effects of nonlinearity on pavement response in the subgrade were conducted for pavement structures with a relatively soft (50 MPa) subgrade. Further analyses utilizing stiffer (and possibly more realistic for Florida conditions) subgrades may reveal that the influence of base and subgrade nonlinearity is not as large as shown herein. Second, the development of effective moduli were based upon matching surface deflections. It is possible that an alternative criterion can be discovered that would provide better agreement between nonlinear and equivalent linear elastic analysis for the responses in the base layer and subgrade.

- It is clear from both the laboratory test results and from the effective modulus values backcalculated from pavement responses that the moduli values of a base layer are strongly affected by moisture. Based upon the results presented herein, the current MEPDG utilizes a modulus/moisture relationship that does not appear well suited for the three Florida base materials investigated. While the results for Miami are based mostly on data from free-free resonant column tests, and not more complete fixed-free tests, the MEPDG relationship significantly underestimates the potential stiffening upon drying of this material. The previous research project on base stiffening conducted by the UF researchers showed that this stiffening upon drying of the Miami material can lead to the material having a consistency of a lean concrete, where a core of the material can be extracted from a pavement intact. The fundamentals of this material behavior should be more fully investigated and explained. Does the Miami material develop higher suction pressures than the other materials? Is the stiffening response due to suction more significant because of inherent material particle characteristics, such as a rougher texture?

- This research work is limited to axisymmetric modeling of a pavement structure subjected to single-wheel loading. It may be further extended to three-dimensional modeling of a pavement structure, under multiple wheel and axle loads, and for more appropriate tire/contact pressure scenarios for more accurate nonlinear modeling of soil element stress state and further performance analysis.

LIST OF REFERENCES

Atkinson, J.H. (2000), "Non-liner Soil Stiffness in Routine Design," *Geotechnique,* 50(5), 487-508.

Atkinson, J.H. and Sallfors, J. (1991), "Experimental Determination of Stress-Strain-Time Characteristics in Laboratory and In-situ Tests," *Proceedings of Tenth European Conference on Soil Mechanics and Foundation Engineering*, Rotterdam, Netherlands, 915-958.

Cho, G.C. and Santamarina, J.C. (2001), "Unsaturated Particulate Materials – Particle Level Studies," *Journal of Geotechincal and Geoenvironmental Engineering*, 127(10), 84-96.

Elhakim, A.F. and Mayne, P.W. (2008), "Footing Stress-Displacement Response Using Small-Strain Modulus," *Proceedings of the Fourth International Symposium on Deformation Characteristics of Geomaterials,* Atlanta*,* 937-944.

Hardin, B.O. and Drnevich, V.P. (1972), "Shear Modulus and Damping in Soils: Measurement and Parameter Effects," *Journal of Soil Mechanics and Foundations Division*, 98(SM6), 603-624.

Hardin, B.O. and Drnevich, V.P. (1972), "Shear Modulus and Damping in Soils: Design Equations and Curves," *Journal of Soil Mechanics and Foundations Divison*, 98(SM7), 667-692.

Hardin, B.O. and Kalinski, M.E., (2005), "Estimating Shear Modulus of Gravelly Soils," *Journal of Geotechincal and Geoenvironmental Engineering*, 131(7), 867-873.

Hardin, B.O. and Richart, F.E., Jr. (1963). "Elastic Waves in Granular Soils," *Journal of Soil Mechanics and Foundation Division*, 89(SM1), 33-65.

Huang, Y.H. (1993), *Pavement Analysis and Design*, Prentice Hall, New Jersey, 805 pp.

Huang, W., Yang, S, Kung, J.H.S., and Lin, H. (2006), "Effect of Matric Suction on Resilient Modulus of Compacted Subgrade Soils,", *Transportation Research Board 85th Annual Meeting Compendium of Papers, CD-ROM,* 21 pp.

Jardine, R.J., Fourie. A., Maswoswe. J. and Burland, J.B. (1984), "Field and Laboratory Measurement of Soil Stiffness," *Proceedings of 11th International Conference on Soil Mechanics and Foundation Engineering*, San Francisco, 2, 511-514.

Jardine, R.J., Potts, D.M., Fourie A.B., and Burland, J.B., (1986), "Studies of the Influence of Non-linear Stress-Strain Characteristics in Soil-Structure Interaction," *Geotechnique,* 36(3), 377-396.

Kim, D. S. and Stokoe, K. H., II (1992), "Characterization of Resilient Modulus of Compacted Subgrade Soils Using Resonant Column and Torsional Shear Tests," *Transportation Research Record 1369,* TRB, Washington, D. C., 83-91.

Kokusho, T. (1987), "In-Situ Dynamic Soil Properties and Their Evaluations," *Proceedings of the 8th Asian Regional Conference on Soil Mechanics and Foundation Engineering*, Kyoto, 2, 215-240.

Lehane, B.M., Doherty, J.P., and Schneider, J.A. (2008), "Settlement Prediction for Footings on Sand," *Proceedings of the Fourth International Symposium on Deformation Characteristics of Geomateriasl,* Atlanta, 133-150.

Lin, S., Lin, P.S., Luo, H., and Juang, C.H. (2000), "Shear Modulus and Damping Ratio Characteristics of Gravelly Deposits," *Canadian Geotechnical Journal*, 37, 638-651.

Lu, N. and Likos, W. J. (2005), *Unsaturated Soil Mechanics,* John Wiley & Sons Inc, New York, 556 pp.

Menq, F. Y. (2003), "Dynamic Properties of Sandy and Gravelly Soils," *Ph.D. Dissertation*, The University of Texas at Austin, May, 363 pp.

MEPDG (2004), "Guide for Mechanistic-Empirical Design of New and Rehabilitated Pavement Structures, NCHRP, March.

Picornell, M. and Nazarian, S. (1998), "Effect of Soil Suction on the Low-Strain Shear Modulus of Soils," *Proceedings of 2nd International Conference on Unsaturated Soils: UNSAT'98*, Beijing, China, 102-107.

Pestana, J.M. and Salvati, L.A. (2006), "Small-Strain Behavior of Granular Soils: Model for Cemented and Uncemented Sands and Gravels," *Journal of Geotechincal and Geoenvironmental Engineering*, 132 (8), 1071-1081.

Qian, X., Gray, D.H., and Richard, W. (1993), "Voids and Granulometry: Efefcts on Shear Modulus of Unsaturated Sands," *Journal of Geotechnical Engineering*, 119 (2), 295-314.

Rollins, K.M., Evans, M.D., Dielhl, N.B., and Daily, W.D. (1998), "Shear Modulus and Damping Relationships for Gravels," *Journal of Geotechincal and Geoenvironmental Engineering,* 124(5), 396-405.

Roque, R., Romero, P., and Hiltunen, D.R. (1992), "The Use of Linear Elastic Analysis to Predict the Nonlinear Response of Pavements," *Proceedings of 7th International Conference on Asphalt Pavements*, Nottingham, U.K., 295-310.

Santos, J.A. and Correia, A.G. (2001), "Reference Threshold Shear Strain for Soil: Its Application to Obtain a Unique Strain-Dependent Shear Modulus Curve for Soil," *Proceedings of the 15th International Conference on Soil Mechanics and Geotechnical Engineering,* Istanbul, 267-270.

Seed, H.B., Wong, R.T., Idriss, I.M., and Tokimatsu, K. (1986), "Moduli and Damping Factors for Dynamic Analyses of Cohesionless Soils," *Journal of Geotechnical Engineering* , 112(12), 1016-1032.

Toros, U. (2008), "Effects of Moisture and Time on Stiffness of Unbound Aggregate Base Coarse Materials," *Ph.D. Dissertation*, The University of Florida, May 2008, 199 pp.

Wu, S., Gray, D.H., and Richart, F.E., Jr. (1984), "Capillarity Effects on Dynamic Modulus of Sands and Silts," *Journal of Geotechnical Engineering*, 110 (9), 1188-1203.

Yasuda, N. and Matsumoto, N. (1993), "Dynamic Deformation Characteristics of Sands and Rockfill Materials," *Canadian Geotechnical Journal,* 30, 745-757.

Yasuda, N., Ohat, N., and Nakamura, A. (1996), "Dynamic Deformation Characteristics of Undisturbed Riverbed Gravels," *Canadian Geotechnical Journal,* 33, 237-249.
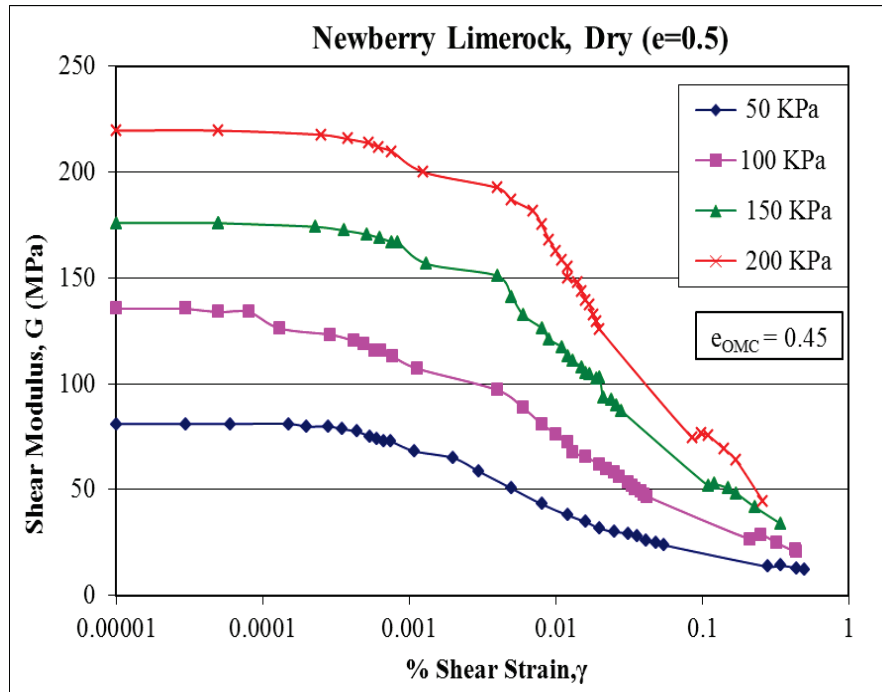
Figure A-1. Shear Modulus (G) versus % Shear strain (γ) curves for dry Newberry limerock at e=0.5.
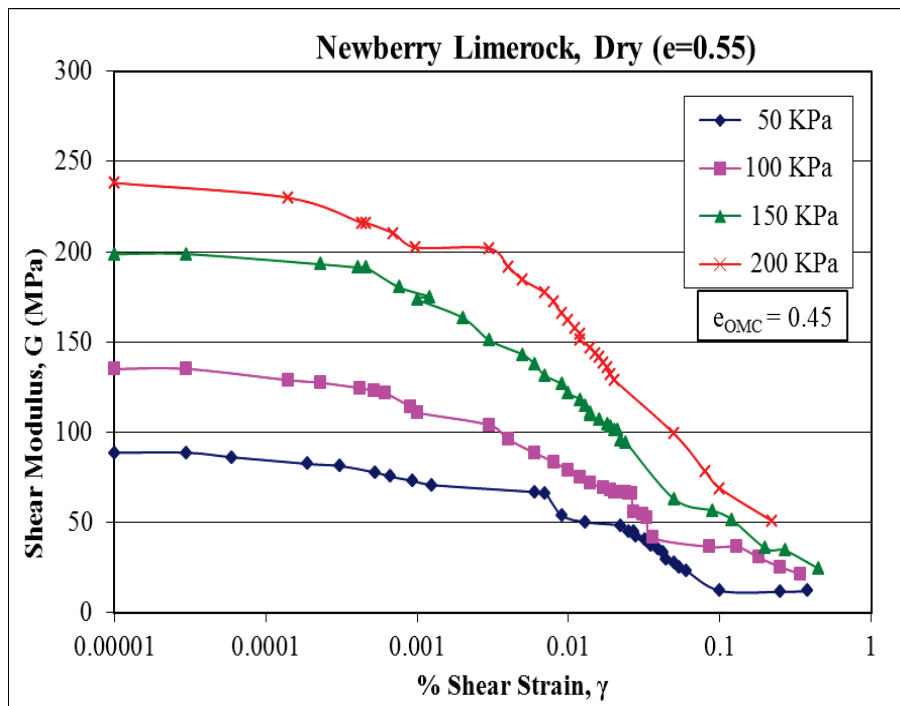
Figure A-2. Shear Modulus (G) versus % Shear strain (γ) curves for dry Newberry limerock at e=0.55.
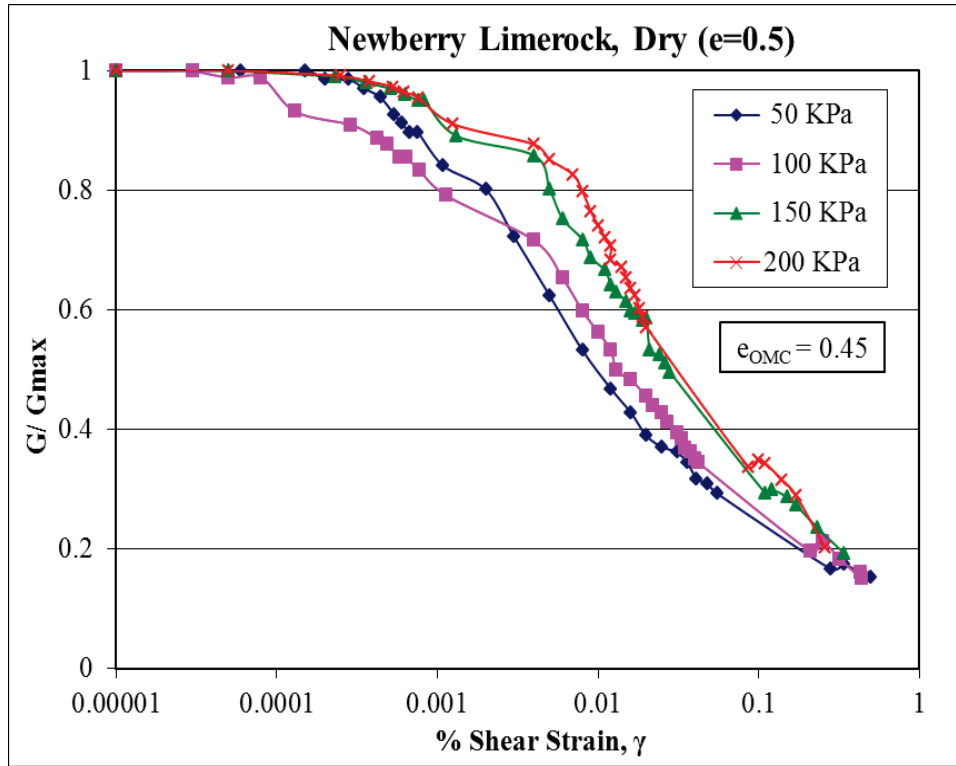
Figure A-3. G/G_{max} versus % shear strain(γ) curves at e=0.5 for Newberry limerock.
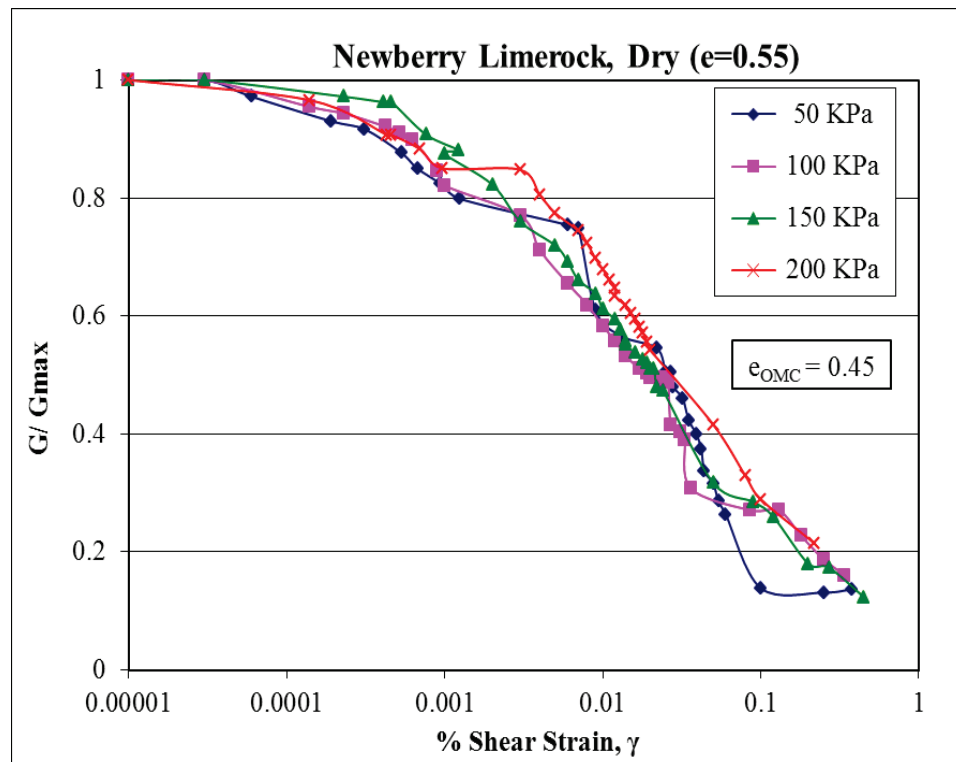
Figure A-4. G/G_{max} versus % shear strain (γ) curves at e=0.55 for Newberry limerock.

155
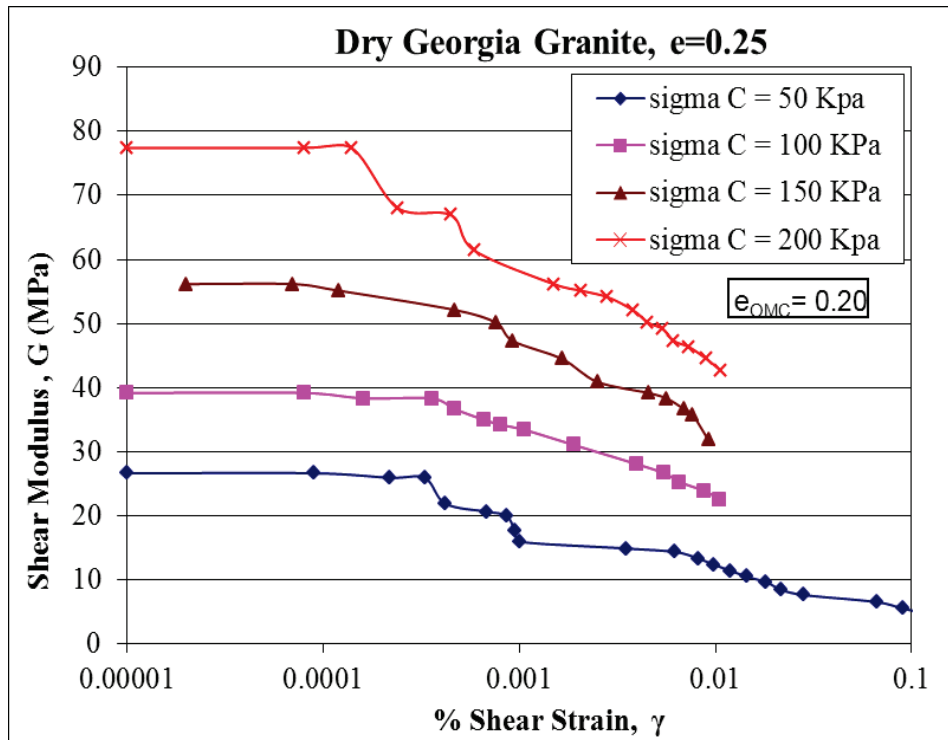
Figure A-5. Shear Modulus (G) versus % Shear strain (γ) curves for dry Georgia granite at e=0.25.
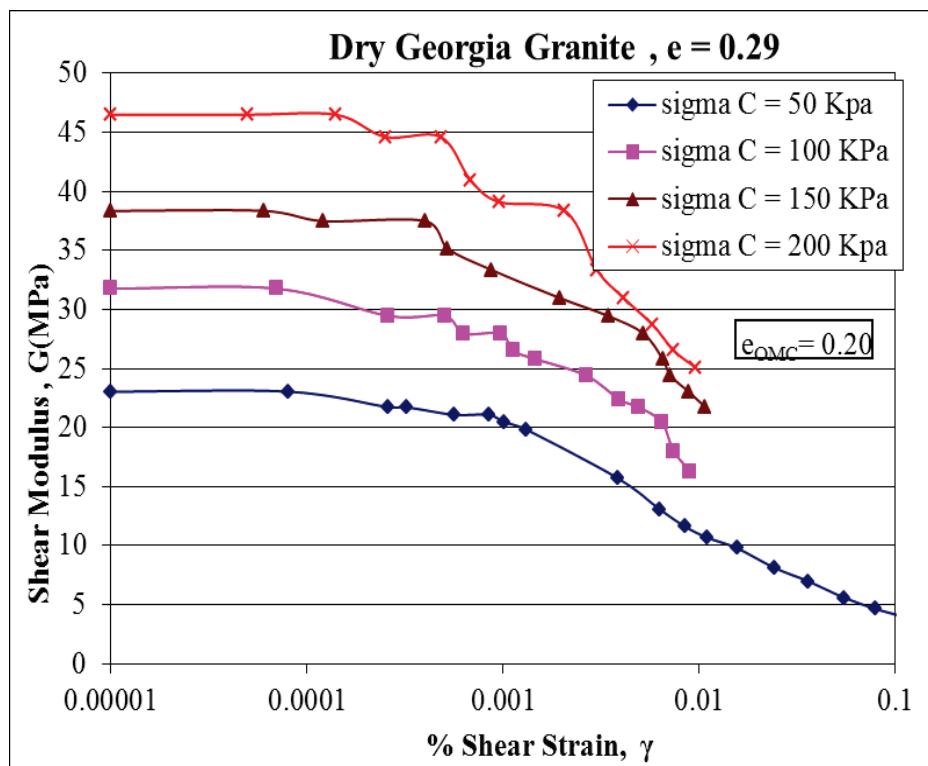
Figure A-6. Shear Modulus (G) versus % Shear strain (γ) curves for dry Georgia granite at e=0.29.
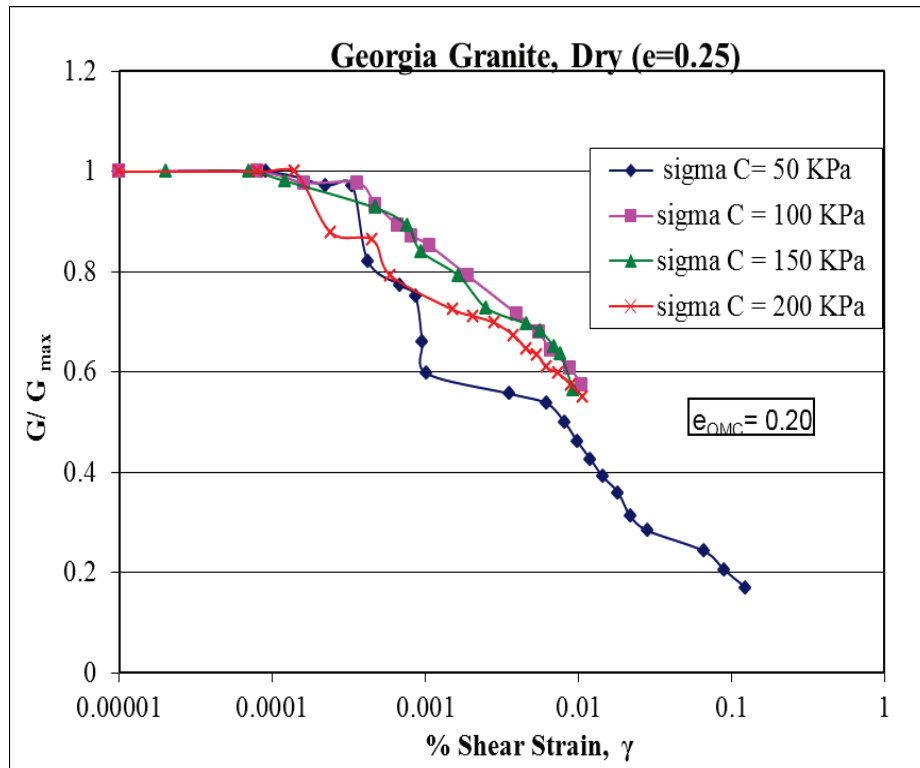
Figure A-7. G/G$_{max}$ versus % shear strain(γ) curves at e=0.25 for Georgia granite.
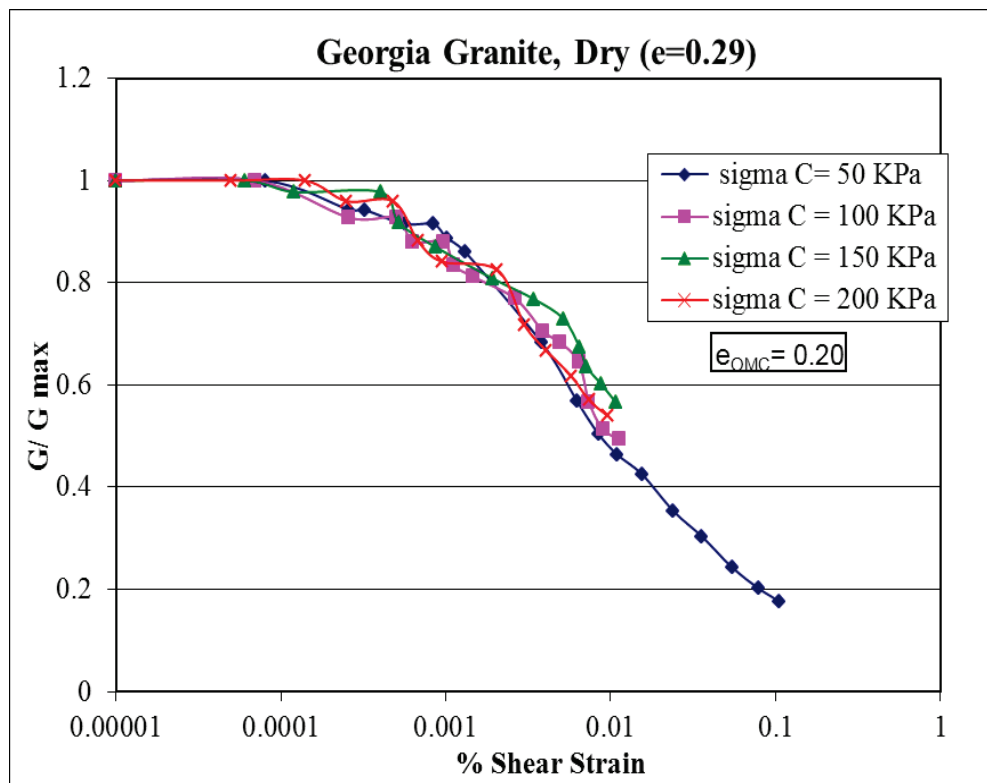
Figure A-8. G/G$_{max}$ versus % shear strain(γ) curves at e=0.29 for Georgia granite.

APPENDIX B
NONLINEAR EQUIVALENT LINEAR EFFECTIVE BASE MODULI DATA FOR
DIFFERENT TYPES OF BASE SOILS

Table B-1. For Structure-1, nonlinear equivalent linear effective moduli data for Newberry
limerock base layer.

			Structure-1			
			Base Layer Moisture Content			
	13%	12%	11%	10%	8%	5.5%
E_{max} (MPa)*	179.82	272.05	548.75	631.12	1249.55	2487.10
Case 1: 50 MPa subgrade						
base E (MPa)	79	102	140	153	196	230
E/E_{max}	0.44	0.37	0.26	0.24	0.16	0.09
Case 2: 30 MPa subgrade						
base E (MPa)	65	79	112	118	142	171
E/E_{max}	0.36	0.29	0.20	0.19	0.11	0.07
Case 3: 70 MPa subgrade						
base E (MPa)	90	117	170	175	230	267
E/E_{max}	0.50	0.43	0.31	0.28	0.18	0.11
Case 4: 125 MPa subgrade						
base E (MPa)	108	157	227	241	310	387
E/E_{max}	0.60	0.58	0.41	0.38	0.25	0.16

* E_{max}- Maximum Young's modulus is calculated for in situ overburden stress
at middle height of base layer

Table B-2. For Structure-2, nonlinear equivalent linear effective moduli data for Newberry limerock base layer.

			Structure-2			
			Base Layer Moisture Content			
	13%	12%	11%	10%	8%	5.5%
E_{max} (MPa)*	170.45	264.114	542.403	625.074	1245.22	2483.69
Case 1: 50 MPa subgrade						
base E (MPa)	74	92	120	125	155	178
E/E_{max}	0.43	0.35	0.22	0.20	0.12	0.07
Case 2: 30 MPa subgrade						
base E (MPa)	58	70	92	94	118	139
E/E_{max}	0.34	0.27	0.17	0.15	0.09	0.06
Case 3: 70 MPa subgrade						
base E (MPa)	85	109	143	149	184	207
E/E_{max}	0.50	0.41	0.26	0.24	0.15	0.08
Case 4: 125 MPa subgrade						
base E (MPa)	107	147	210	220	278	308
E/E_{max}	0.63	0.56	0.39	0.35	0.22	0.12

Table B-3. For Structure-3, nonlinear equivalent linear effective moduli data for Newberry limerock base layer.

			Structure-3			
			Base Layer Moisture Content			
	13%	12%	11%	10%	8%	5.5%
E_{max} (MPa)*	166.819	260.58	539.487	622.215	1242.78	2481.57
Case 1: 50 MPa subgrade						
base E (MPa)	66	89	112	124	148	168
E/E_{max}	0.40	0.34	0.21	0.20	0.12	0.07
Case 2: 30 MPa subgrade						
base E (MPa)	54	67	90	101	108	130
E/E_{max}	0.32	0.26	0.17	0.16	0.09	0.05
Case 3: 70 MPa subgrade						
base E (MPa)	73	100	135	142	195	205
E/E_{max}	0.44	0.38	0.25	0.23	0.16	0.08
Case 4: 125 MPa subgrade						
base E (MPa)	93	141	214	220	281	311
E/E_{max}	0.56	0.54	0.40	0.35	0.23	0.13

Table B-4. For Structure-4, nonlinear equivalent linear effective moduli data for Newberry limerock base layer.

	Structure-4					
	Base Layer Moisture Content					
	13%	12%	11%	10%	8%	5.5%
E_{max} (MPa)*	158.3	253.46	533.84	616.7	1238.44	2478.16
Case 1: 50 MPa subgrade						
base E (MPa)	62	80	108	112	123	132
E/E_{max}	0.39	0.32	0.20	0.18	0.10	0.05
Case 2: 30 MPa subgrade						
base E (MPa)	49	60	69	70	76	78
E/E_{max}	0.31	0.24	0.13	0.11	0.06	0.03
Case 3: 70 MPa subgrade						
base E (MPa)	71	96	129	135	139	144
E/E_{max}	0.45	0.38	0.24	0.22	0.11	0.06
Case 4: 125 MPa subgrade						
base E (MPa)	84	127	196	206	228	240
E/E_{max}	0.53	0.50	0.37	0.33	0.18	0.10

Table B-5. For Structure-5, nonlinear equivalent linear effective moduli data for Newberry limerock base layer.

	Structure-5		
	Base Layer Moisture Content		
	13%	11%	5.5%
E_{max} (MPa)*	152.538	530.054	2457.67
Case 1: 50 MPa subgrade			
base E (MPa)	73	100	102
E/E_{max}	0.48	0.19	0.04
Case 2: 125 MPa subgrade			
base E (MPa)	105	189	209
E/E_{max}	0.69	0.36	0.09

Table B-6. For Structure-6, nonlinear equivalent linear effective moduli data for Newberry limerock base layer.

Structure-6			
Base Layer Moisture Content			
	13%	11%	5.5%
E $_{max}$ (MPa)*	152.112	529.529	2457.19
Case 1: 50 MPa subgrade			
base E (MPa)	76	90	107
E/E$_{max}$	0.50	0.17	0.04
Case 2: 125 MPa subgrade			
base E (MPa)	103	180	187
E/E$_{max}$	0.68	0.34	0.08

Table B-7. For Structure-1, nonlinear equivalent linear effective moduli data for Georgia granite base layer.

	Structure-1		
	Base Layer Moisture Content		
	5.5%	4.5%	3.5%
E_{max} (MPa)	136.23	444.71	647.68
Case 1: 50 MPa subgrade			
base E (MPa)	76	135	152
E/E_{max}	0.56	0.30	0.23
Case 2: 30 MPa subgrade			
base E (MPa)	63	104	117
E/E_{max}	0.46	0.23	0.18
Case 3: 70 MPa subgrade			
base E (MPa)	86	155	178
E/E_{max}	0.63	0.35	0.27
Case 4: 125 MPa subgrade			
base E (MPa)	112	210	243
E/E_{max}	0.82	0.47	0.38

Table B-8. For Structure-2, nonlinear equivalent linear effective moduli data for Georgia granite base layer.

	Structure-2		
Base Layer Moisture Content			
	5.5%	4.5%	3.5%
E_{max} (MPa)	134.45	443.70	646.91
Case 1:	50 MPa subgrade		
base E (MPa)	70	112	124
E/E_{max}	0.52	0.25	0.19
Case 2:	30 MPa subgrade		
base E (MPa)	56	94	104
E/E_{max}	0.42	0.21	0.16
Case 3:	70 MPa subgrade		
base E (MPa)	82	135	150
E/E_{max}	0.61	0.30	0.23
Case 4:	125 MPa subgrade		
base E (MPa)	105	195	220
E/E_{max}	0.78	0.44	0.34

Table B-9. For Structure-3, nonlinear equivalent linear effective moduli data for Georgia granite base layer.

	Structure-3		
	Base Layer Moisture Content		
	5.5%	4.5%	3.5%
E_{max} (MPa)	133.87	443.37	646.63
Case 1: 50 MPa subgrade			
base E (MPa)	66	115	119
E/E_{max}	0.49	0.26	0.18
Case 2: 30 MPa subgrade			
base E (MPa)	54	88	100
E/E_{max}	0.40	0.20	0.15
Case 3: 70 MPa subgrade			
base E (MPa)	73	133	162
E/E_{max}	0.55	0.30	0.25
Case 4: 125 MPa subgrade			
base E (MPa)	90	207	220
E/E_{max}	0.67	0.47	0.34

Table B-10. For Structure-4, nonlinear equivalent linear effective moduli data for Georgia granite base layer.

	Structure-4		
	Base Layer Moisture Content		
	5.5%	4.5%	3.5%
E_{max} (MPa)	132.08	442.40	645.84
Case 1: 50 MPa subgrade			
base E (MPa)	60	100	106
E/E_{max}	0.45	0.23	0.16
Case 2: 30 MPa subgrade			
base E (MPa)	46	74	75
E/E_{max}	0.35	0.17	0.12
Case 3: 70 MPa subgrade			
base E (MPa)	67	123	137
E/E_{max}	0.51	0.28	0.21
Case 4: 125 MPa subgrade			
base E (MPa)	84	184	220
E/E_{max}	0.64	0.42	0.34

Table B-11. For Structure-1, nonlinear equivalent linear effective moduli data for Maimi
            limerock base layer.

	Structure-1		
	Base Layer Moisture Content		
	8.0%	6.0%	4.0%
E_{max} (MPa)	32.99	612.77	3474.36
Case 1: 50 MPa subgrade			
base E (MPa)	30	168	337
E/E_{max}	0.91	0.27	0.10
Case 2: 125 MPa subgrade			
base E (MPa)	31	260	545
E/E_{max}	0.94	0.42	0.16

Table B-12. For Structure-4, nonlinear equivalent linear effective moduli data for Miami
            limerock base layer.

	Structure-4		
	Base Layer Moisture Content		
	8.0%	6.0%	4.0%
E_{max} (MPa)	32.99	612.77	3474.36
Case 1: 50 MPa subgrade			
base E (MPa)	6	54	159
E/E_{max}	0.18	0.09	0.05
Case 2: 125 MPa subgrade			
base E (MPa)	7	122	320
E/E_{max}	0.21	0.20	0.09

APPENDIX C
COMPARISON OF NONLINEAR AND EQUIVALENT LINEAR RESPONSES FROM NONLINEAR BASE ANALYSIS

C.1   Newberry Limerock

C.1.1   Surface Deflection Profiles

C.1.1.1 Structure-1
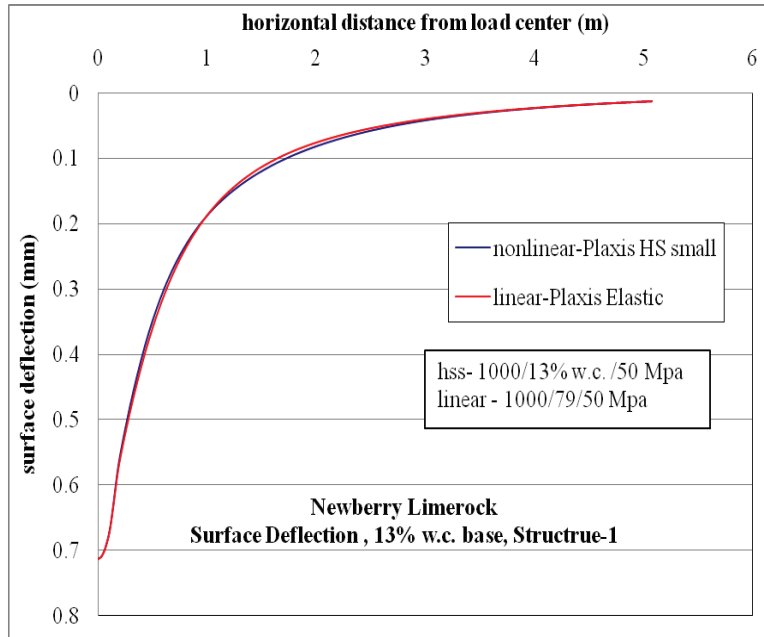
Figure C-1. Surface deflection comparison for nonlinear and linear cases, for Structure-1 with 13% w.c. base layer.
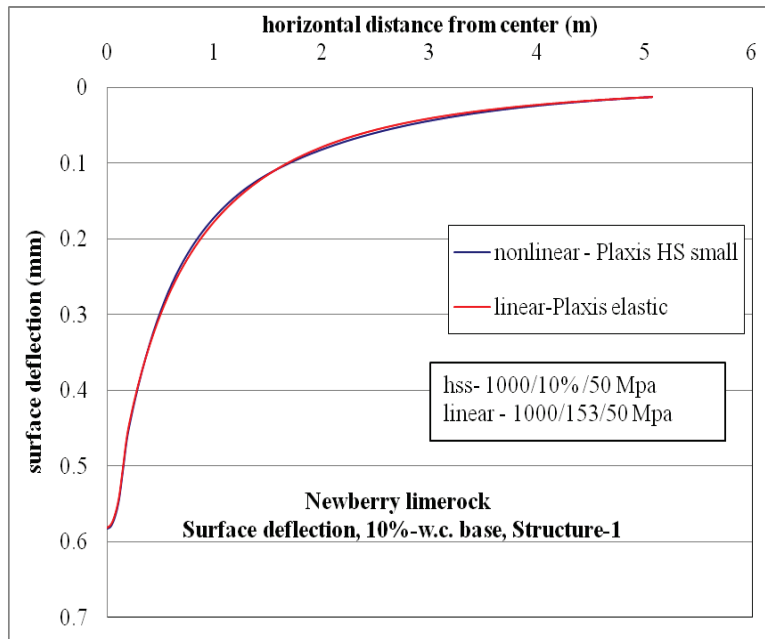
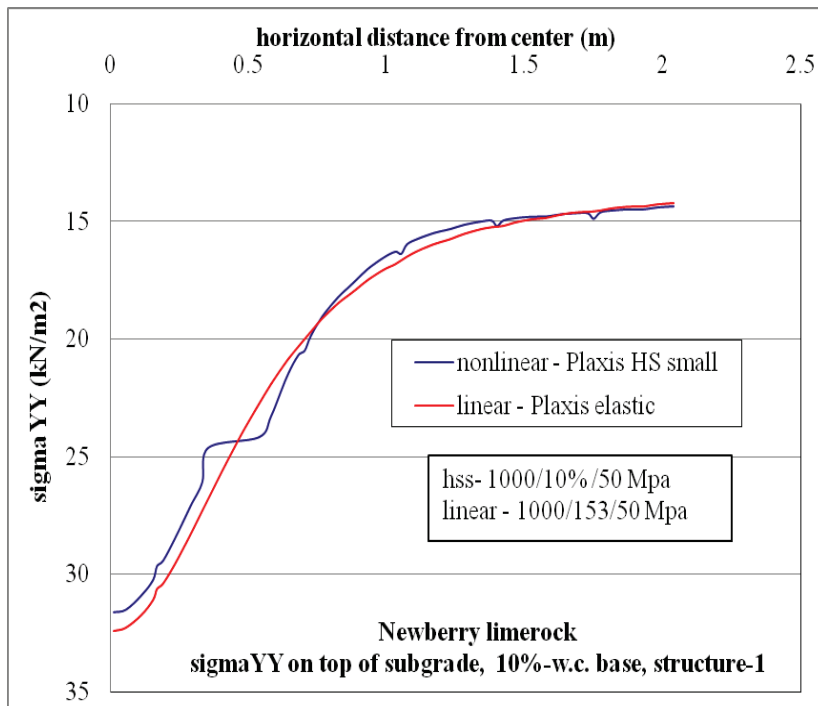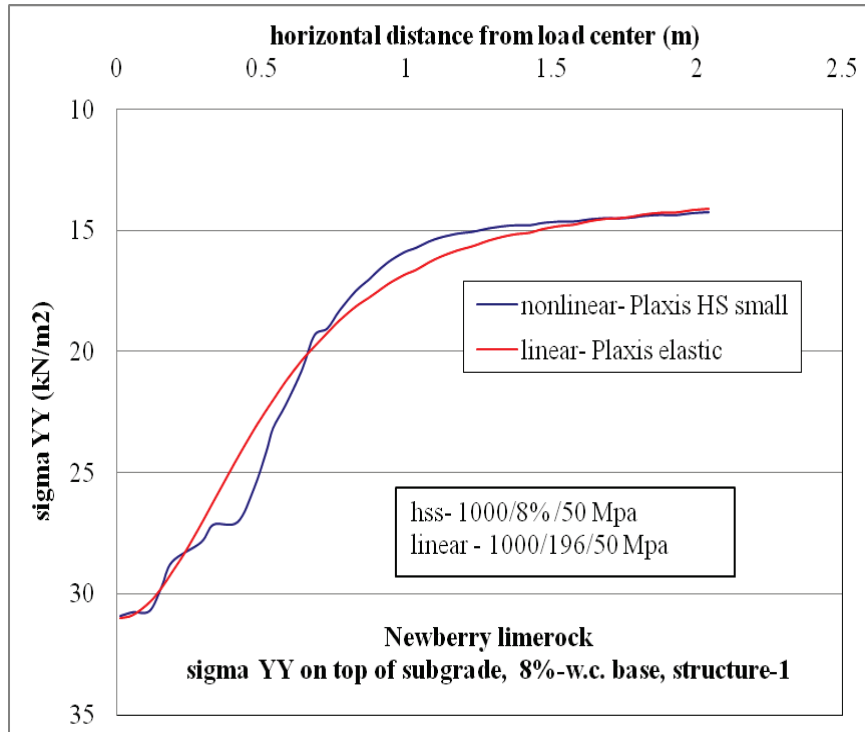Figure C-2 Surface deflection comparison for nonlinear and linear cases, for Structure-1 with 10% w.c. base layer.
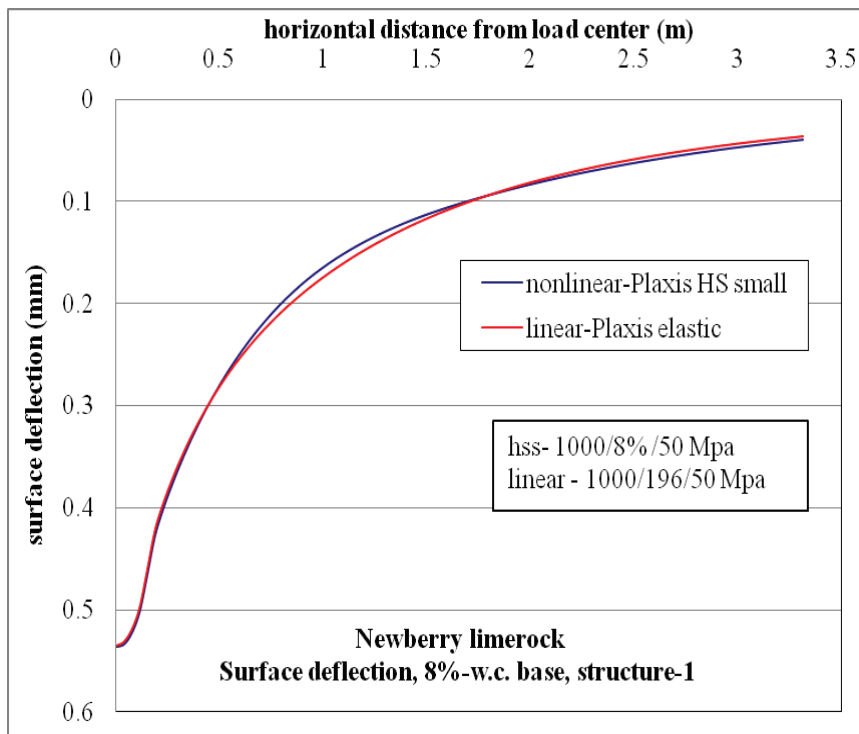
Figure C-3. Surface deflection comparison for nonlinear and linear cases, for Structure-1 with 8% w.c. base layer.
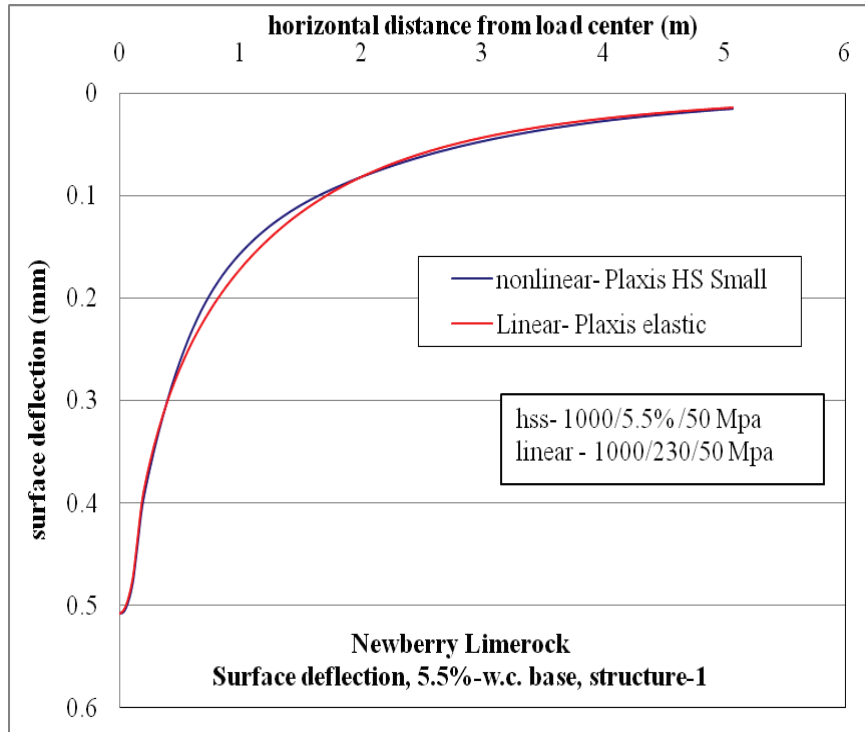
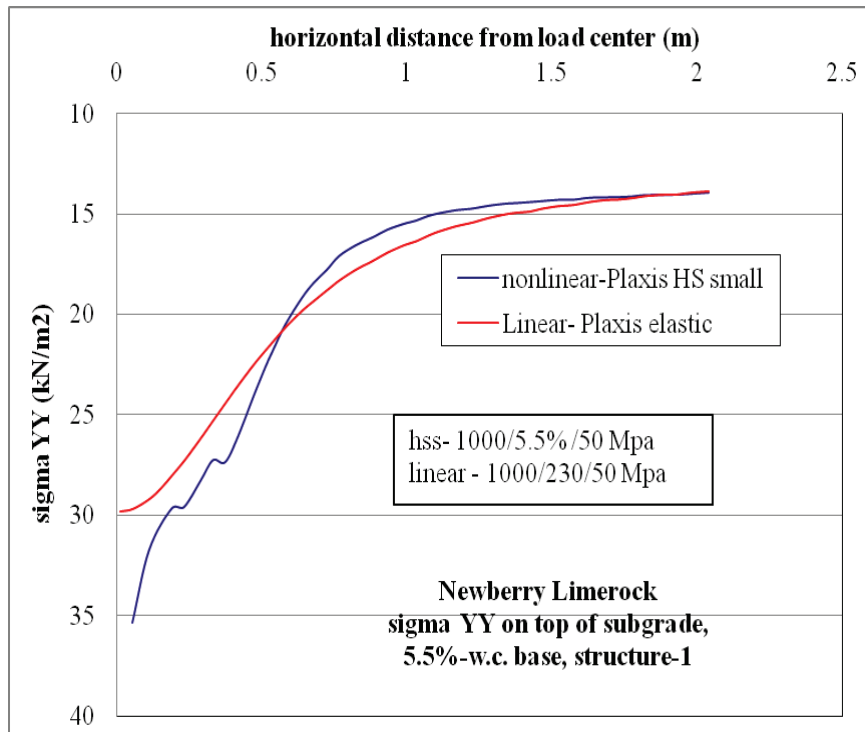Figure C-4. Surface deflection comparison for nonlinear and linear cases, for Structure-1 with 5.5% w.c. base layer.

C.1.1.2 Structure-4
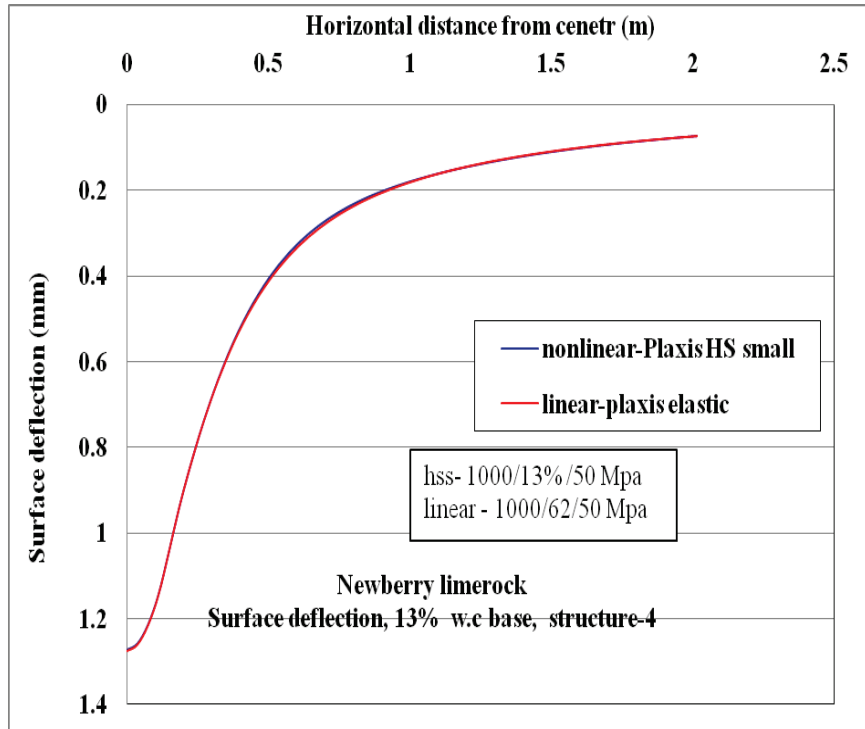
Figure C-5. Surface deflection comparison for nonlinear and linear cases, for Structure-4 with 13% w.c. base layer.
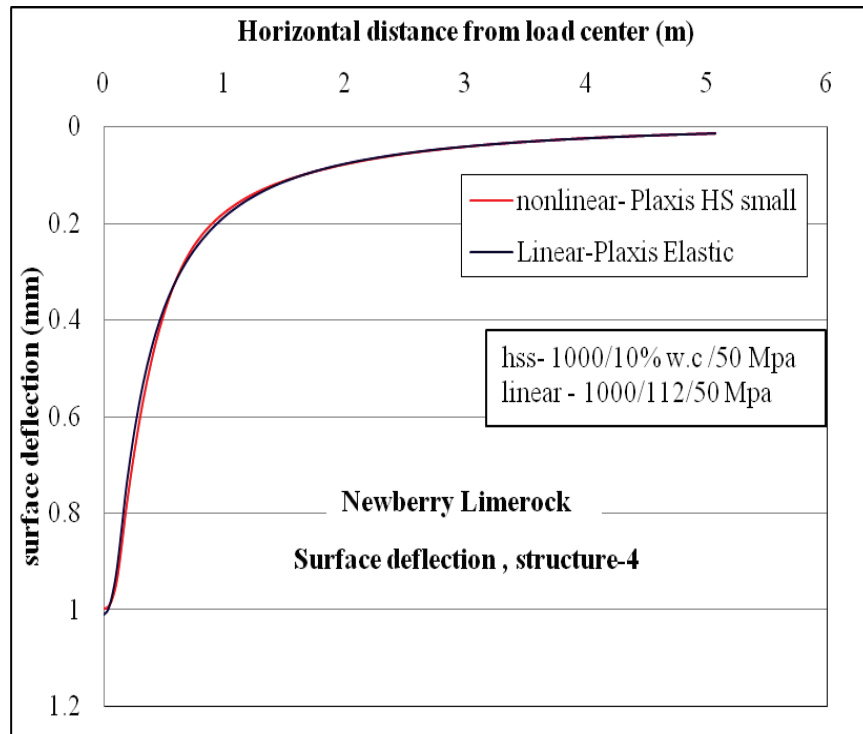
Figure C-6. Surface deflection comparison for nonlinear and linear cases, for Structure-4 with 10% w.c. base layer.
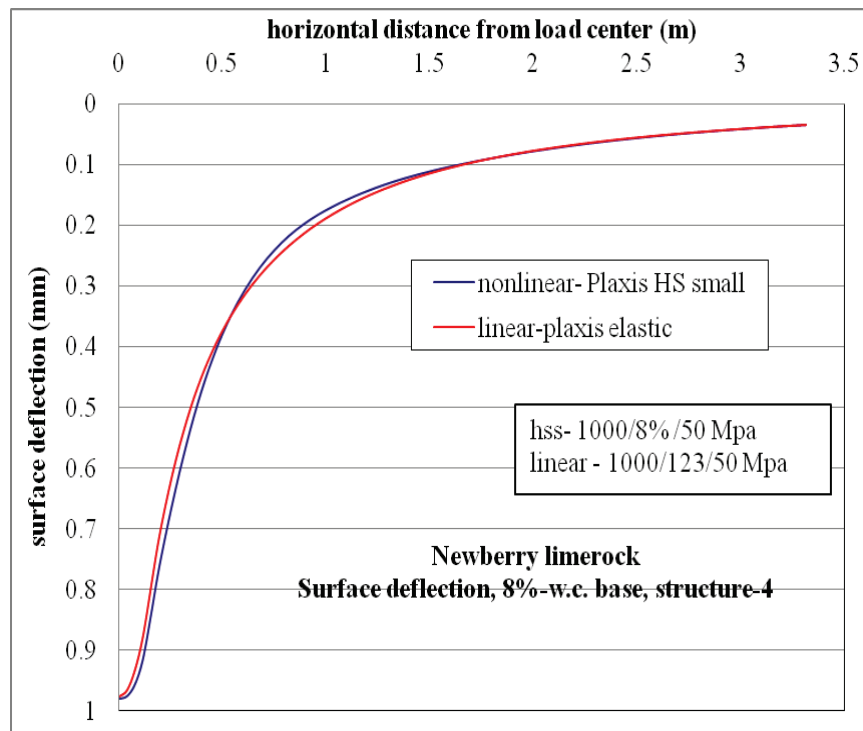
Figure C-7. Surface deflection comparison for nonlinear and linear cases, for Structure-4 with 8% w.c. base layer.
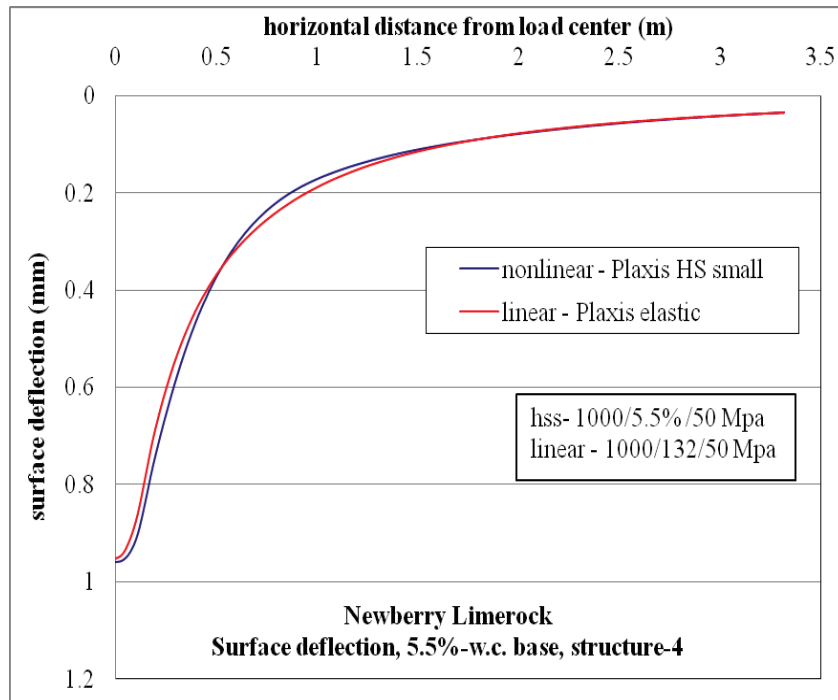
Figure C-8. Surface deflection comparison for nonlinear and linear cases, for Structure-4 with 5.5% w.c. base layer.

C.1.2 Horizontal Stress (σ$_{xx}$, Tensile Stress) at Top of AC Layer

C.1.2.1 Structure-1

Figure C-9. σ$_{xx}$ at top of AC layer comparison for nonlinear and linear cases, for Structure-1 with 13% w.c. base layer.

Figure C-10. σ$_{xx}$ at top of AC layer comparison for nonlinear and linear cases, for Structure-1 with 10% w.c. base layer.

Figure C-11. σ_{xx} at top of AC layer comparison for nonlinear and linear cases, for Structure-1 with 8% w.c. base layer.
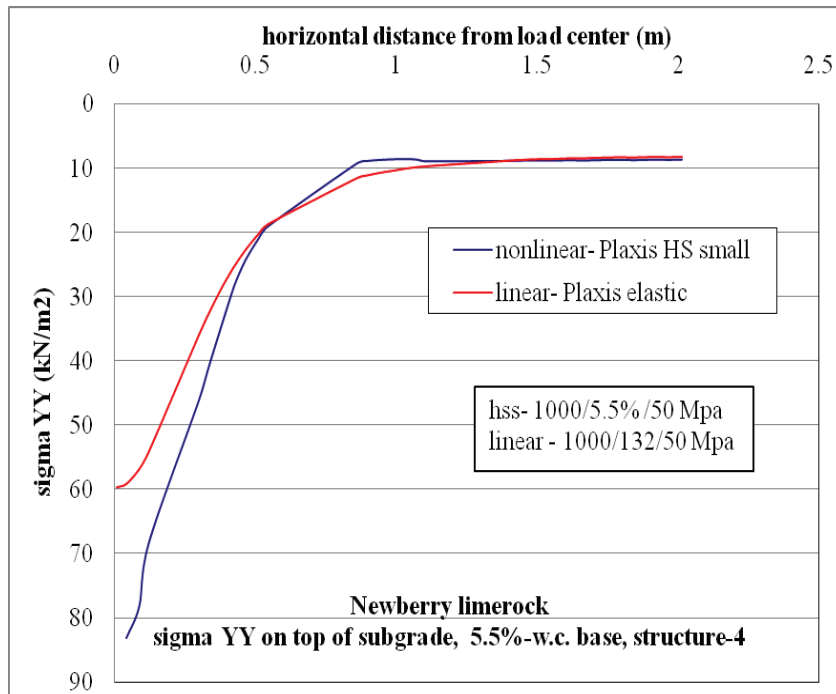

Figure C-12. σ_{xx} at top of AC layer comparison for nonlinear and linear cases, for Structure-1 with 5.5% w.c. base layer.
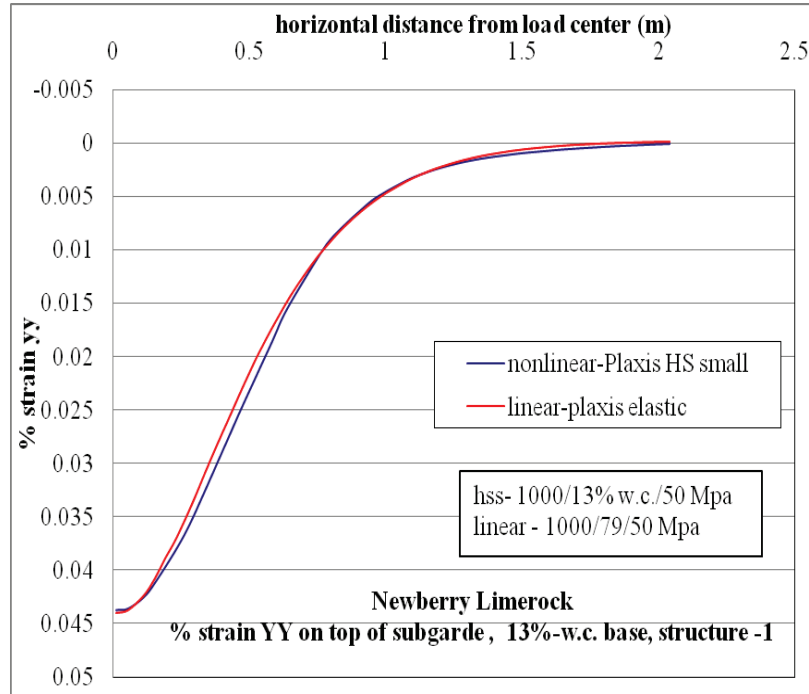
171
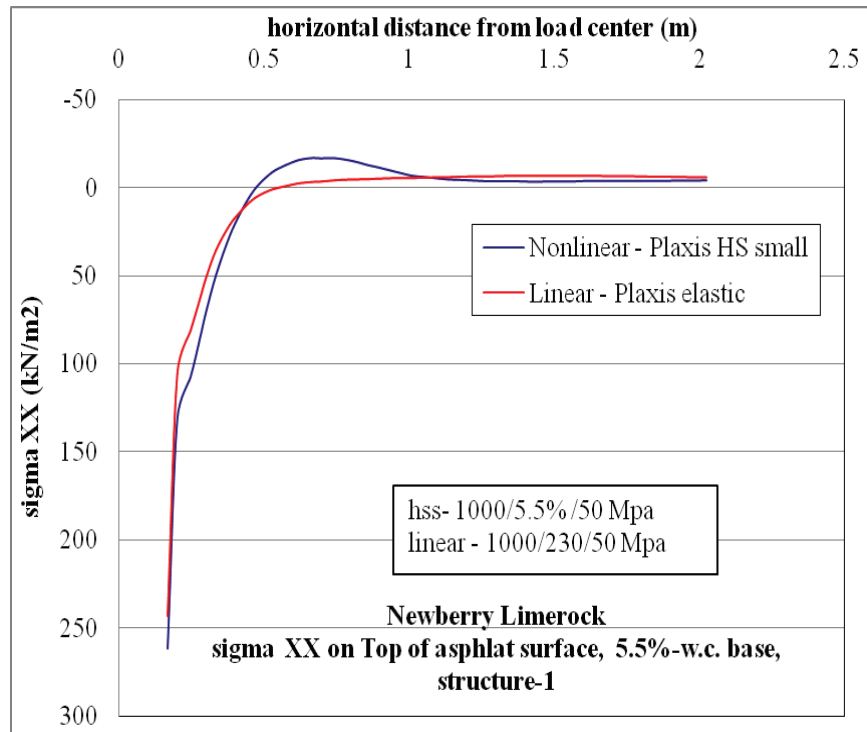
C.1.2.2 Structure-4

Figure C-13. σ_{xx} at top of AC layer comparison for nonlinear and linear cases, for Structure-4 with 13% w.c. base layer.
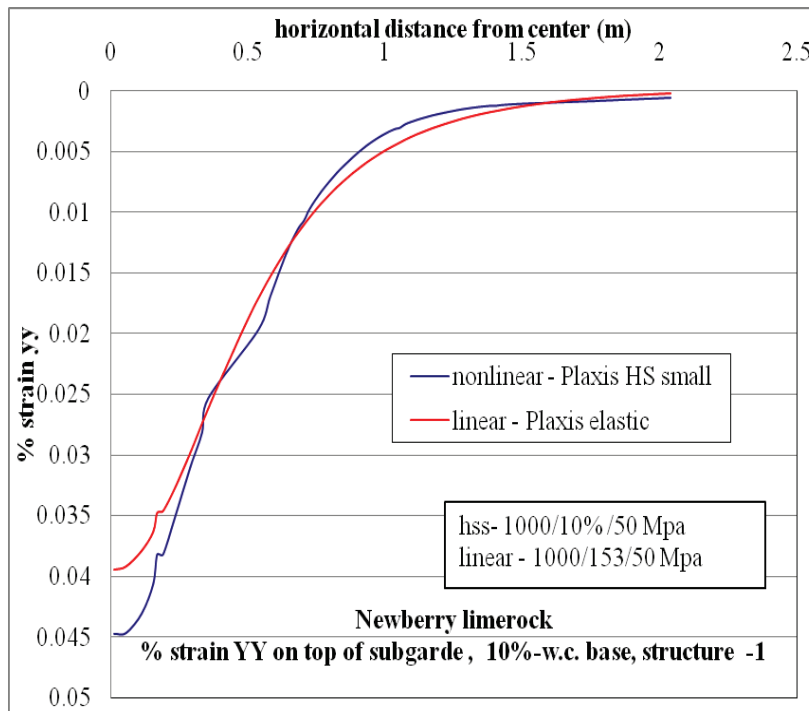

Figure C-14. σ_{xx} at top of AC layer comparison for nonlinear and linear cases, for Structure-4 with 10% w.c. base layer.

Figure C-15. σ_{xx} at top of AC layer comparison for nonlinear and linear cases, for Structure-4 with 8% w.c. base layer.

Figure C-16. σxx at top of AC layer comparison for nonlinear and linear cases, for Structure-4 with 5.5% w.c. base layer.

C.1.3 Horizontal Strain (ε_{xx}, Tensile Strain) at Top of AC Layer

C.1.3.1 Structure-1
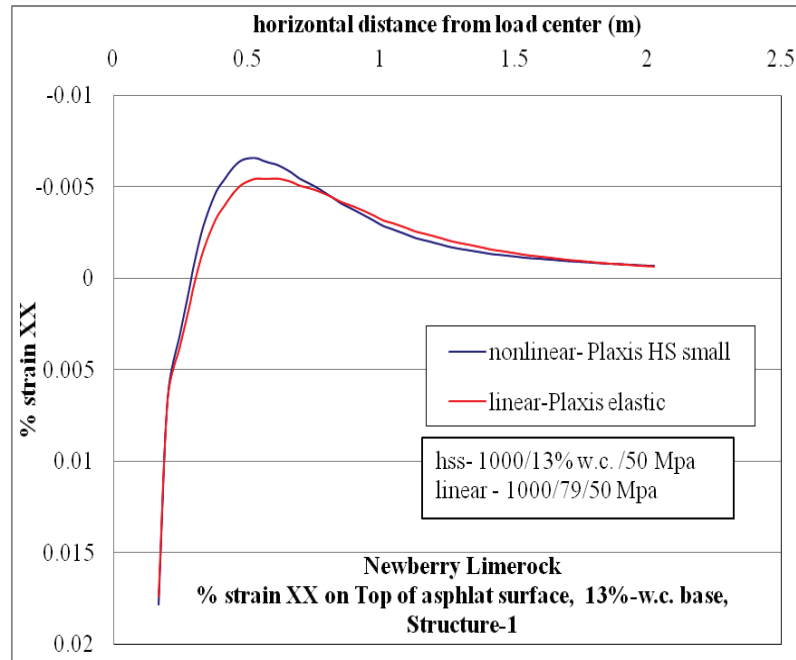
Figure C-17. ε_{xx} at top of AC layer comparison for nonlinear and linear cases, for Structure-1 with 13% w.c. base layer.

Figure C-18. ε_{xx} at top of AC layer comparison for nonlinear and linear cases, for Structure-1 with 10% w.c. base layer.
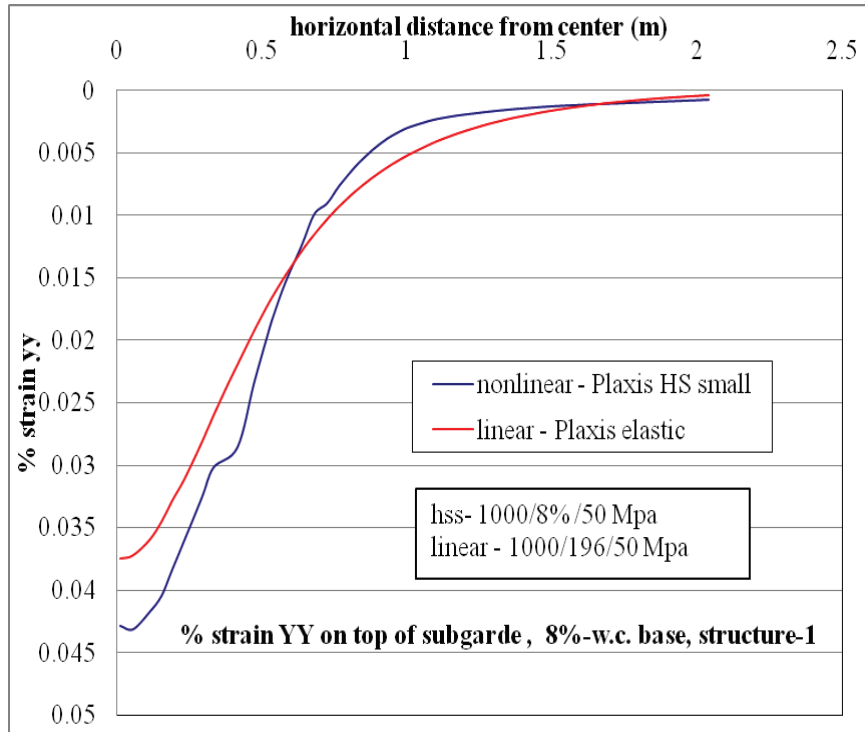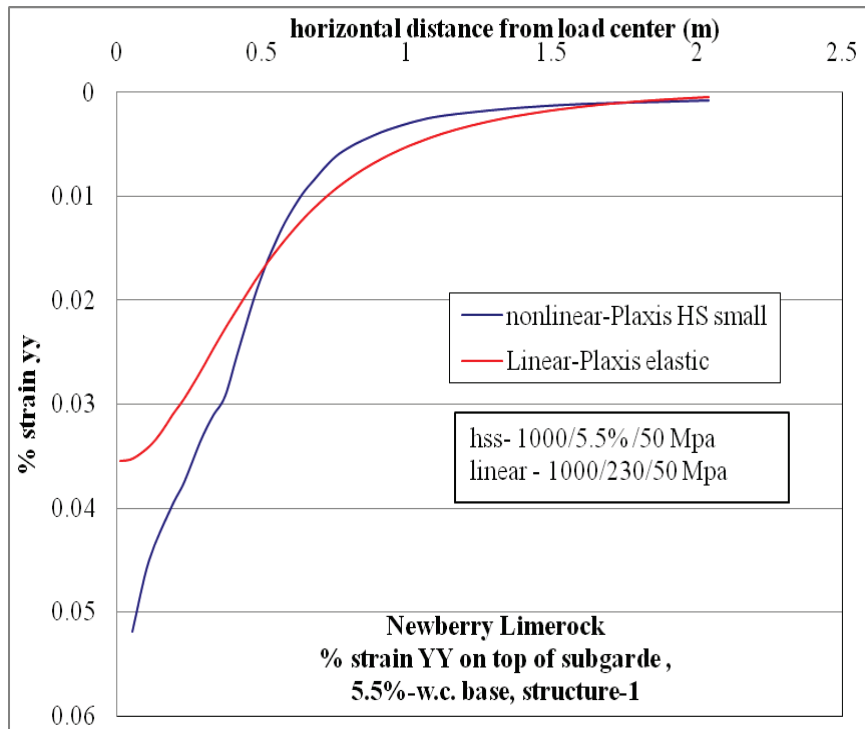
174
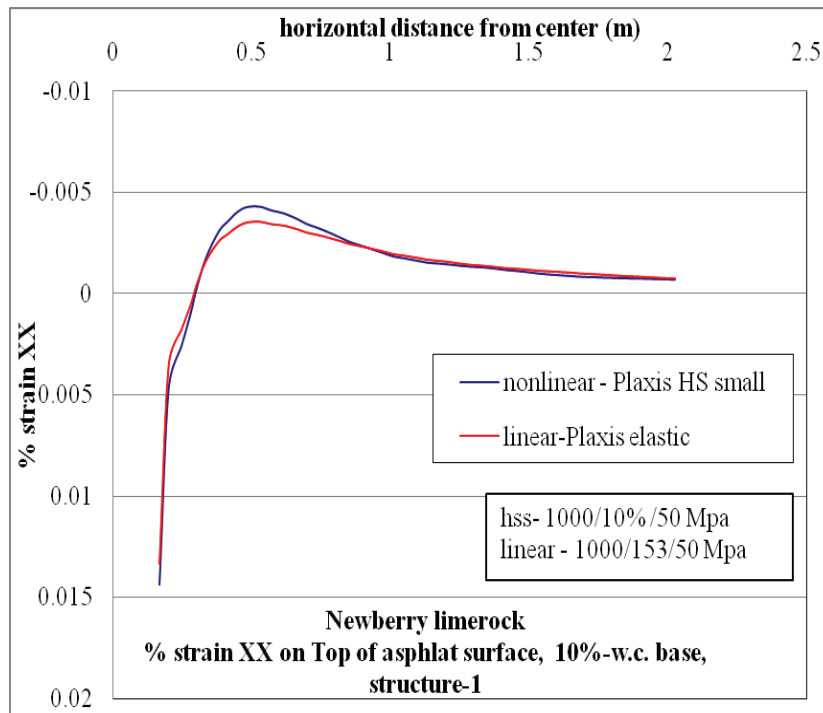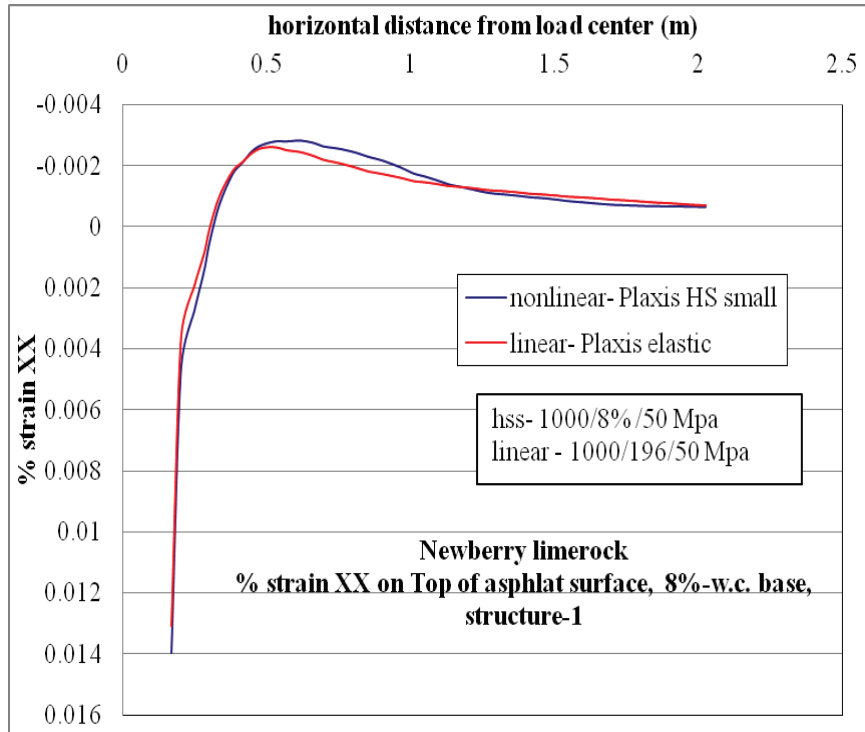
Figure C-19. ε_{xx} at top of AC layer comparison for nonlinear and linear cases, for Structure-1 with 8% w.c. base layer.
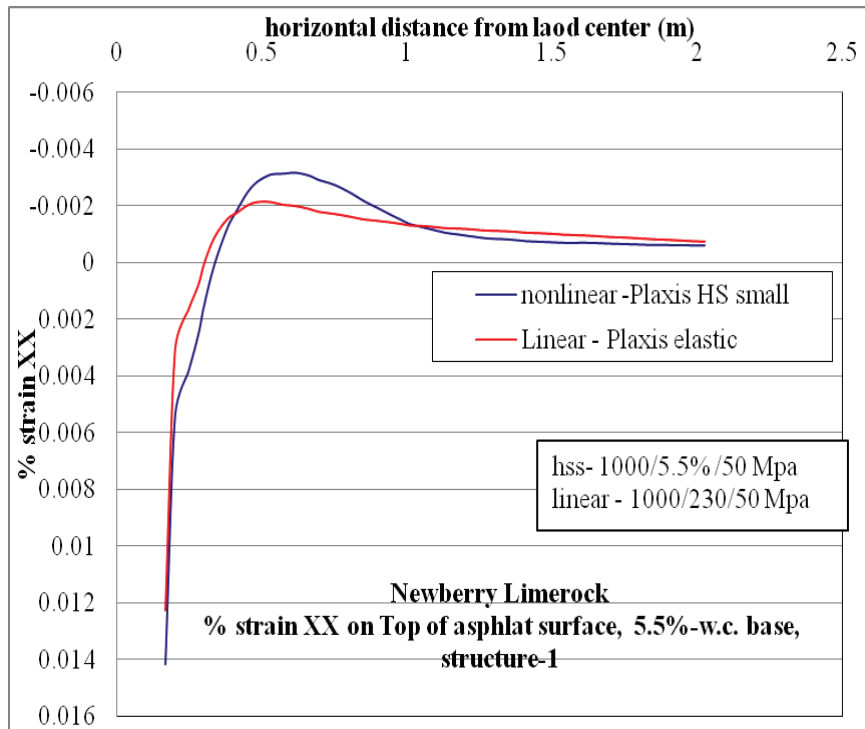
Figure C-20. ε_{xx} at top of AC layer comparison for nonlinear and linear cases, for Structure-1 with 5.5% w.c. base layer.
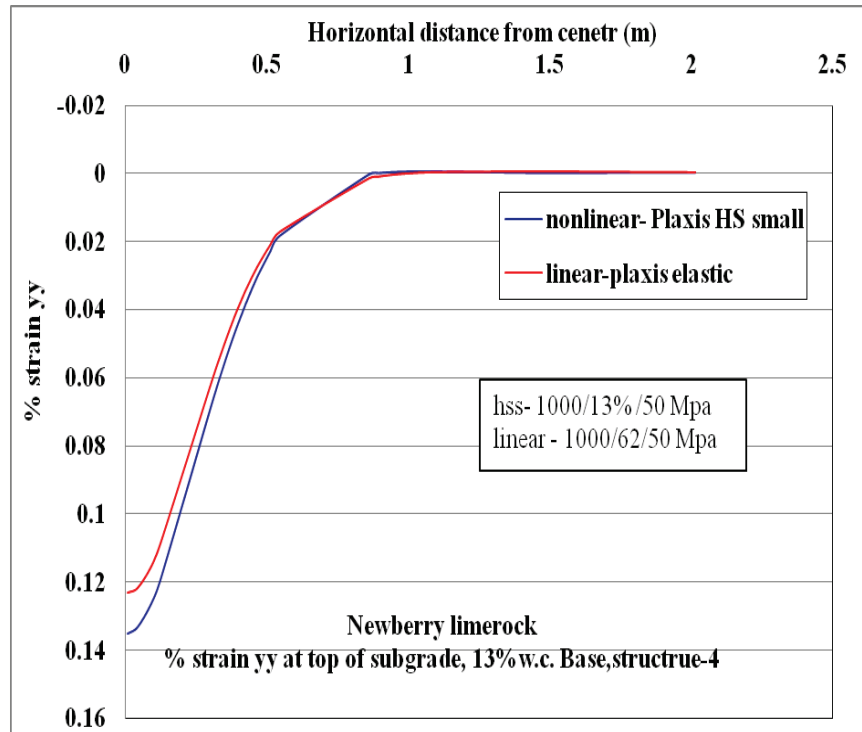
C.1.3.2 Structure-4
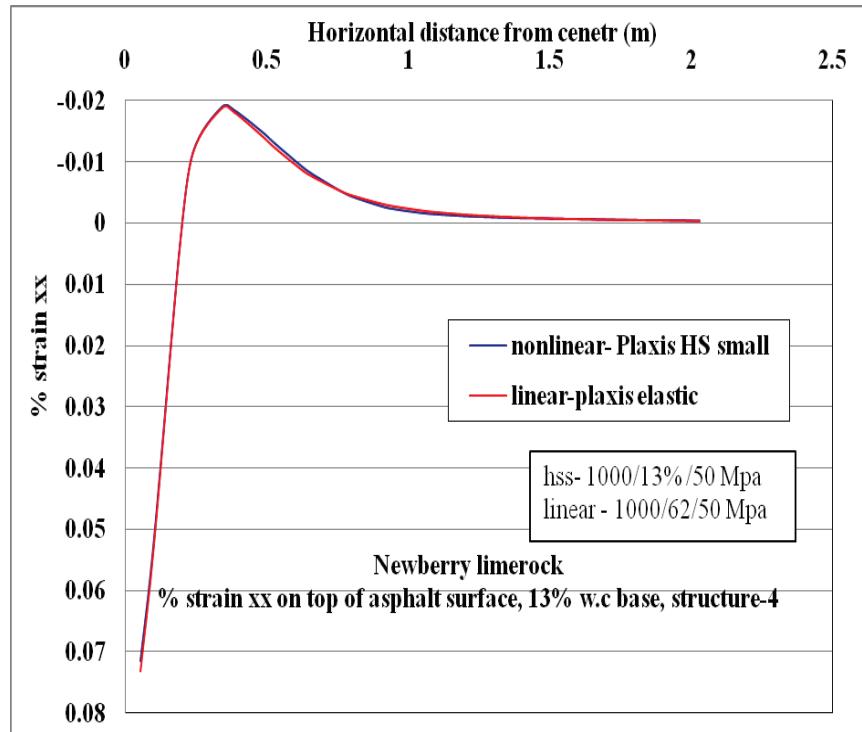
Figure C-21. ε_{xx} at top of AC layer comparison for nonlinear and linear cases, for Structure-4 with 13% w.c. base layer.
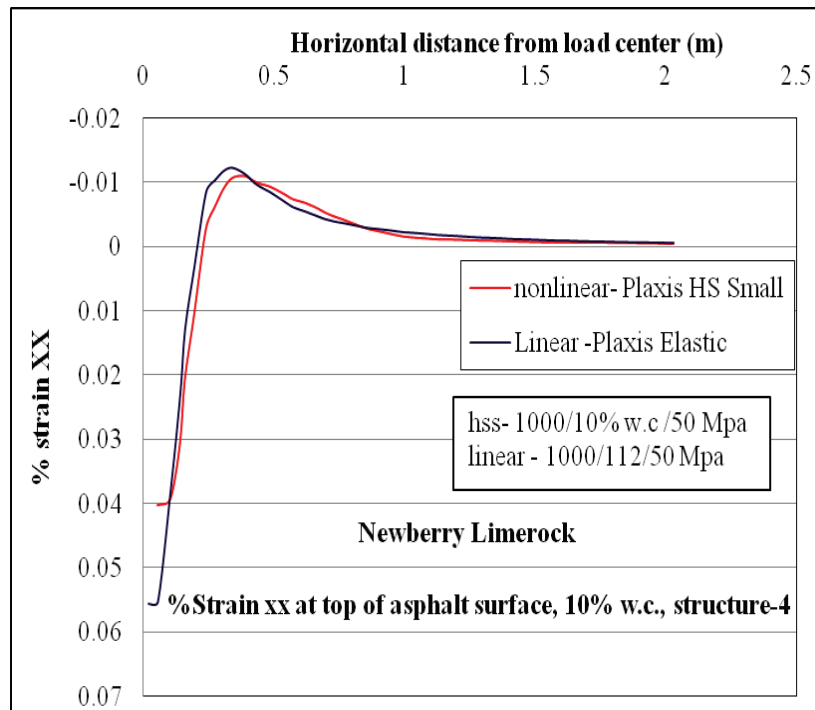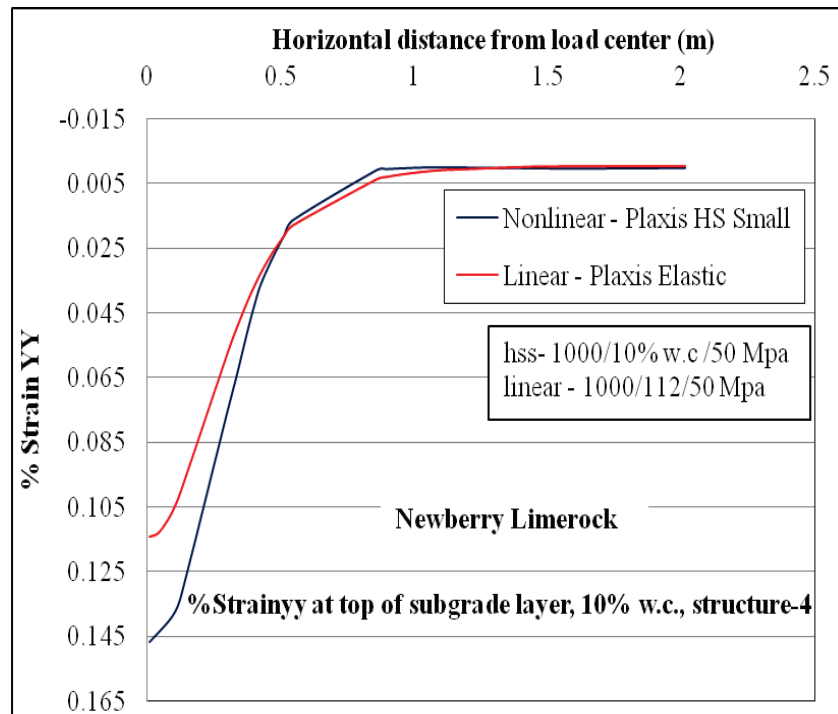

Figure C-22. ε_{xx} at top of AC layer comparison for nonlinear and linear cases, for Structure-4 with 10% w.c. base layer.
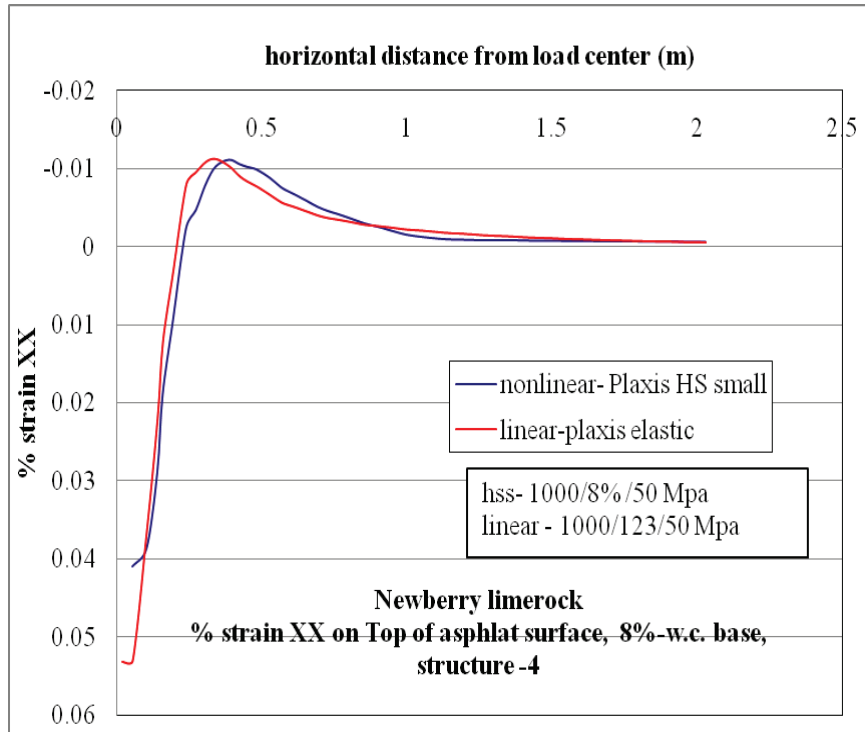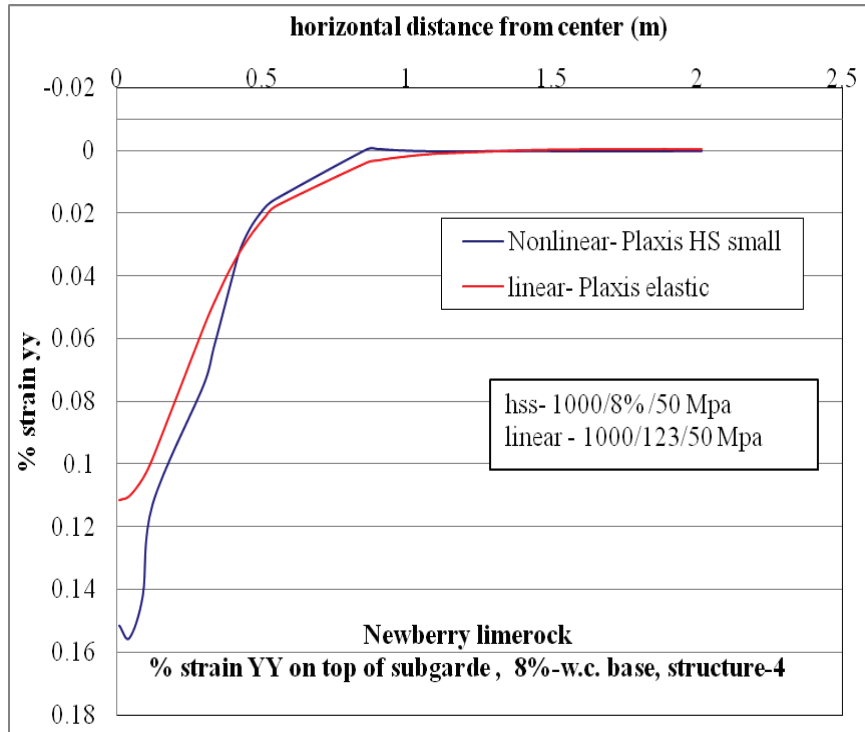
Figure C-23. ε_{xx} at top of AC layer comparison for nonlinear and linear cases, for Structure-4 with 8% w.c. base layer.
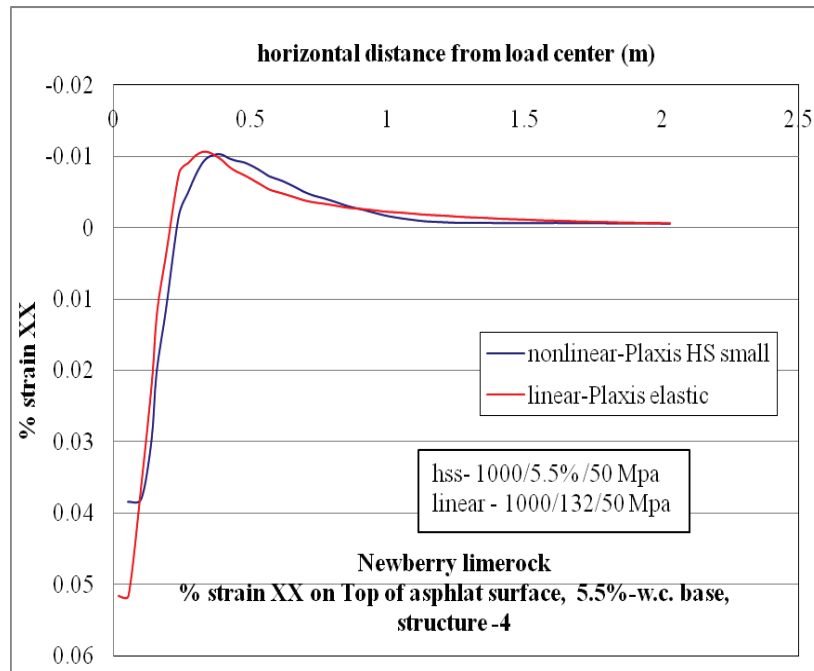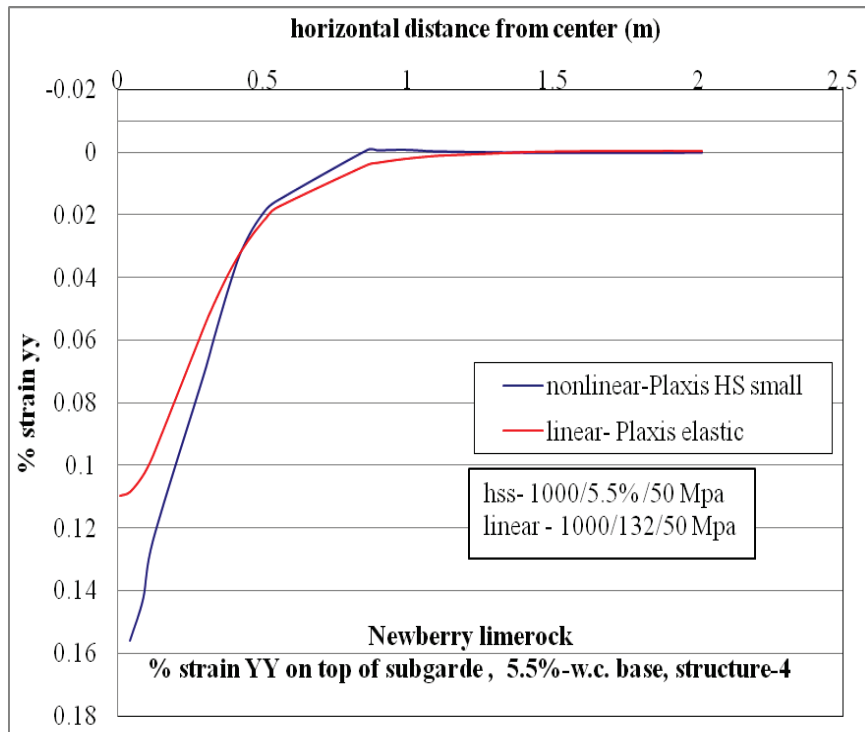

Figure C-24. ε_{xx} at top of AC layer comparison for nonlinear and linear cases, for Structure-4 with 5.5% w.c. base layer.

C.1.4 Horizontal Stress (σ_{xx}, Tensile Stress) at Bottom of AC Layer

C.1.4.1 Structure-1
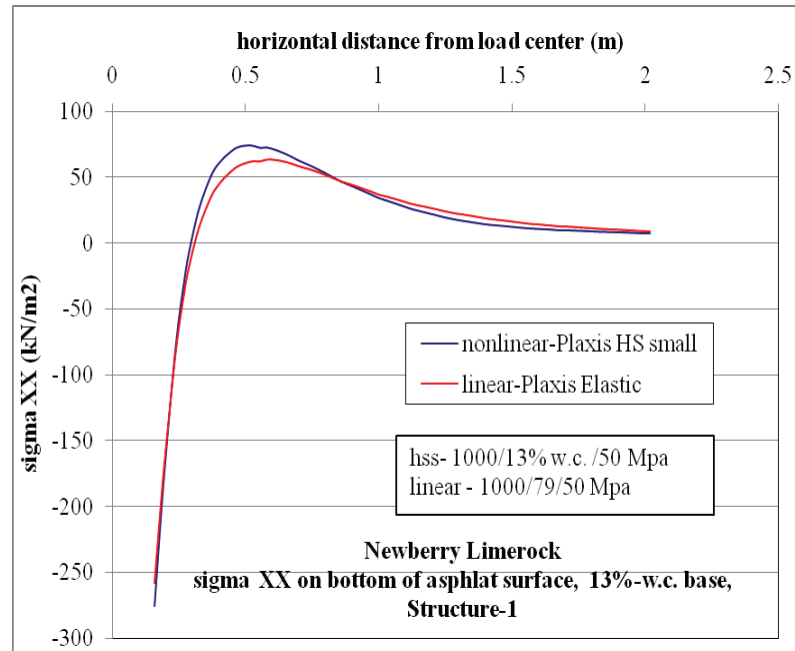
Figure C-25. σ_{xx} at bottom of AC layer comparison for nonlinear and linear cases, for Structure-1 with 13% w.c. base layer.
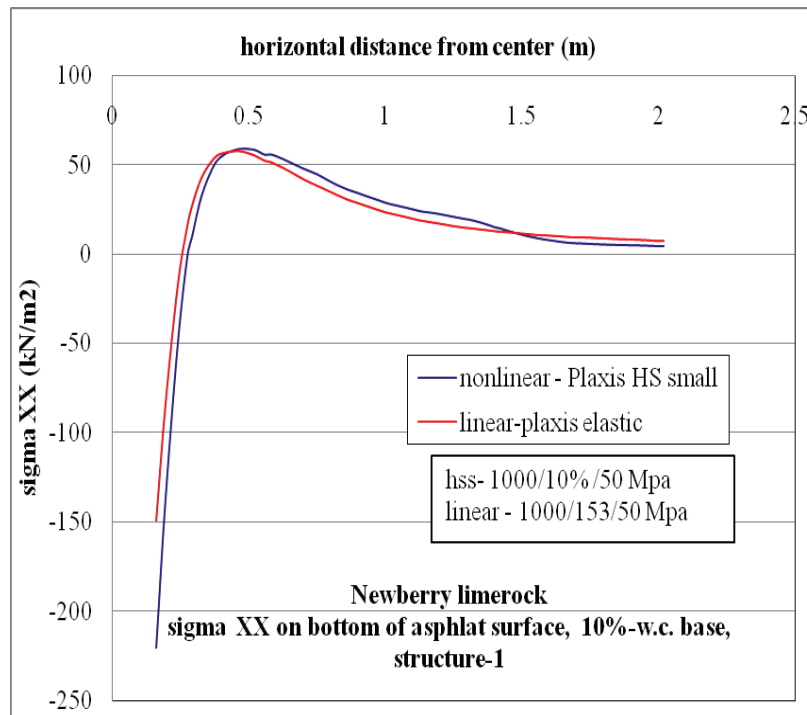
Figure C-26. σ_{xx} at bottom of AC layer comparison for nonlinear and linear cases, for Structure-1 with 10% w.c. base layer.
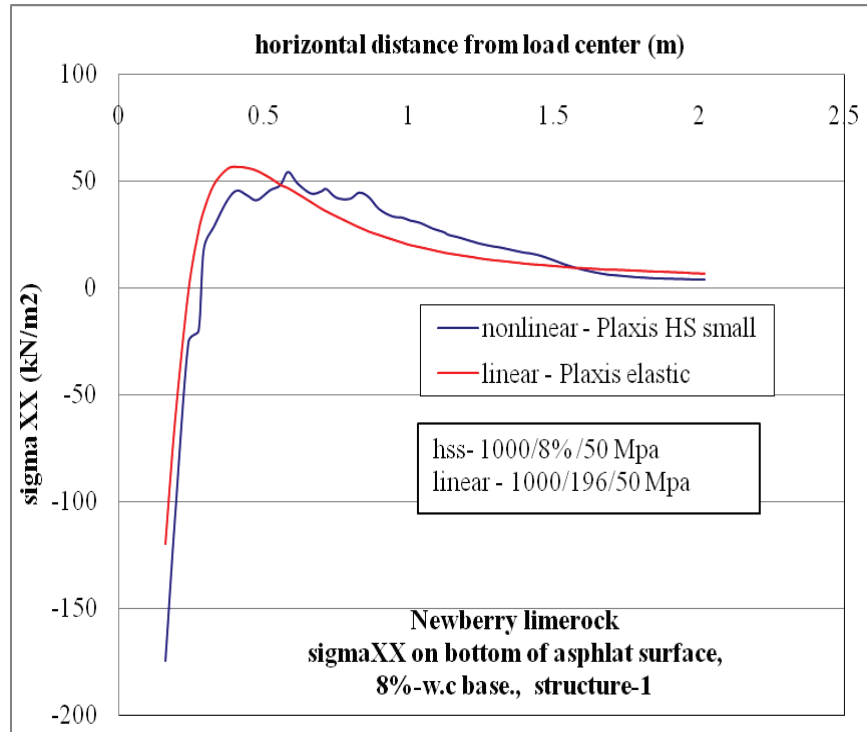
Figure C-27. σ_{xx} at bottom of AC layer comparison for nonlinear and linear cases, for Structure-1 with 8% w.c. base layer.
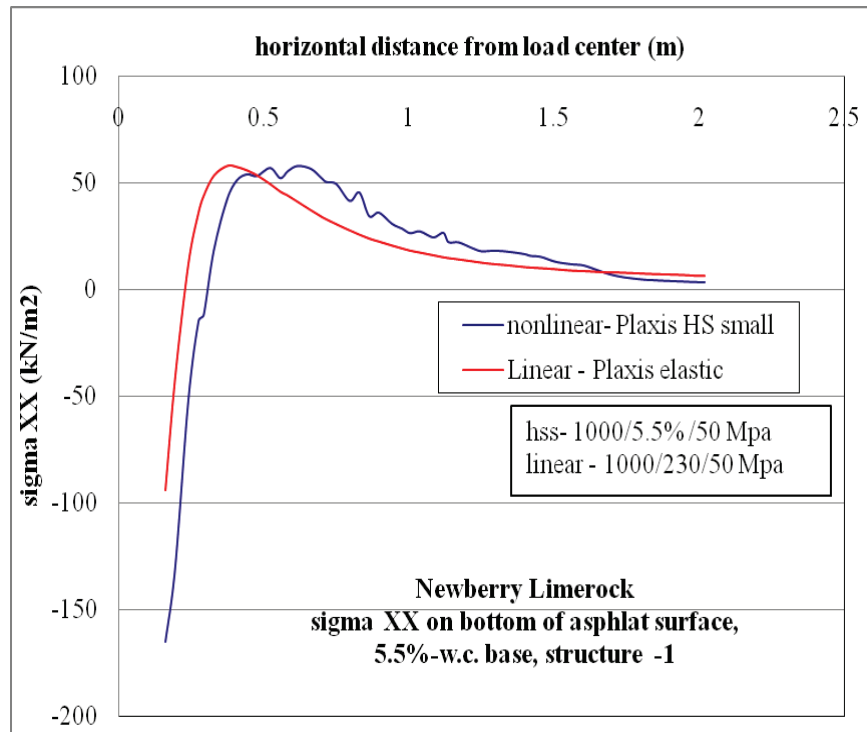
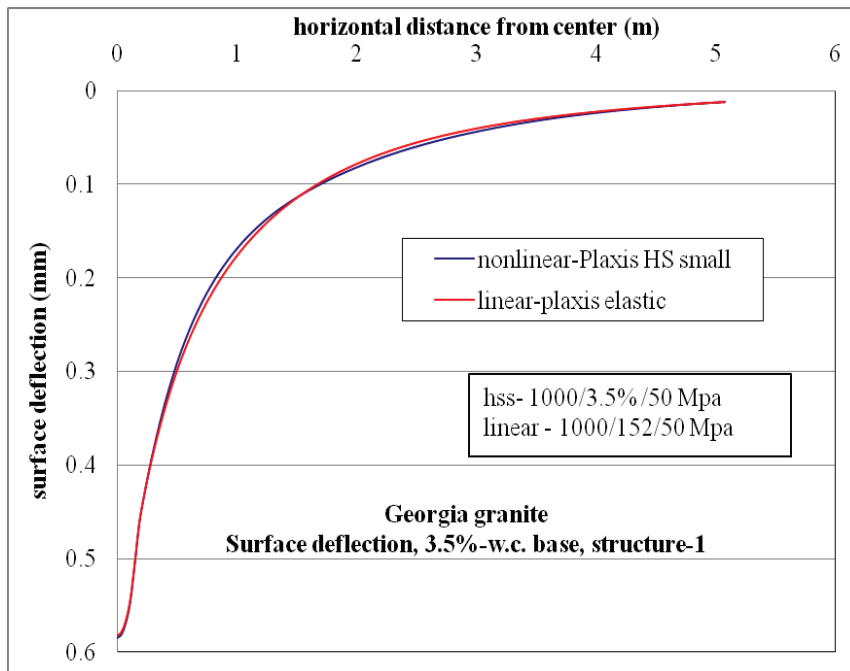Figure C-28. σ_{xx} at bottom of AC layer comparison for nonlinear and linear cases, for Structure-1 with 5.5% w.c. base layer.

C.1.4.2 Structure-4
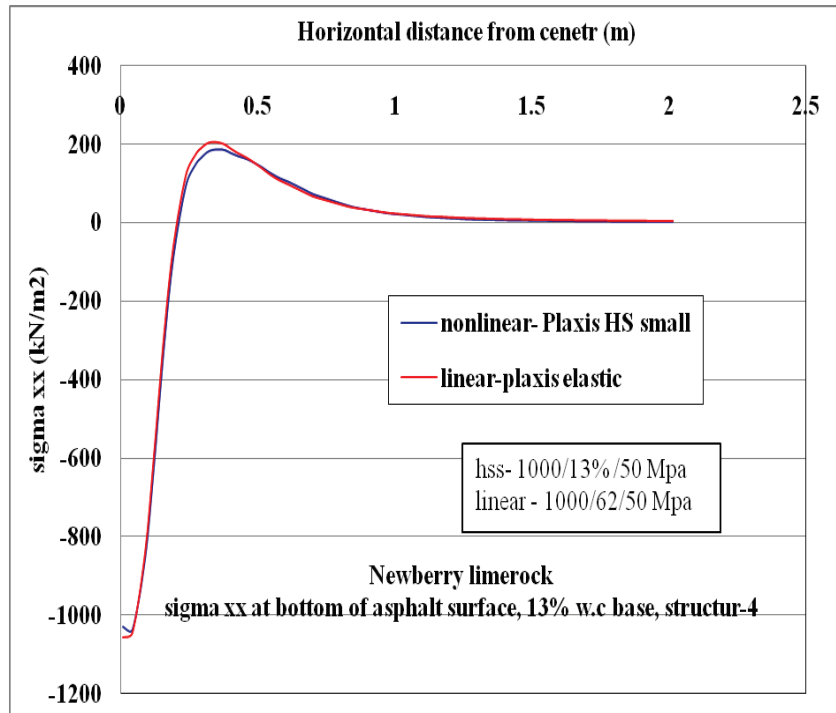
Figure C-29. σ_{xx} at bottom of AC layer comparison for nonlinear and linear cases, for Structure-4 with 13% w.c. base layer.
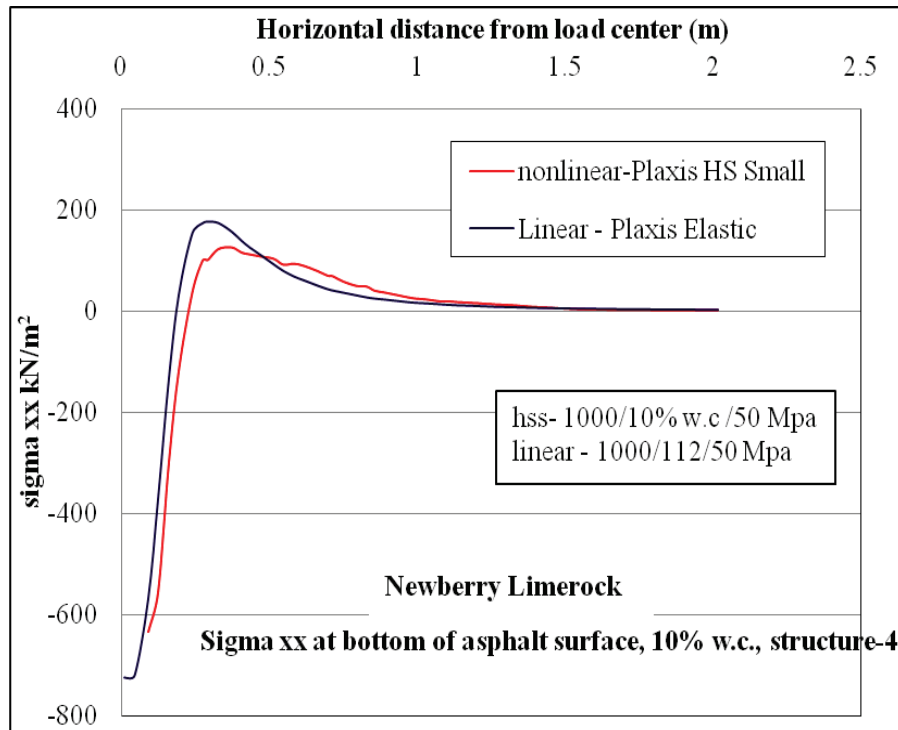
Figure C-30. σ_{xx} at bottom of AC layer comparison for nonlinear and linear cases, for Structure-4 with 10% w.c. base layer.
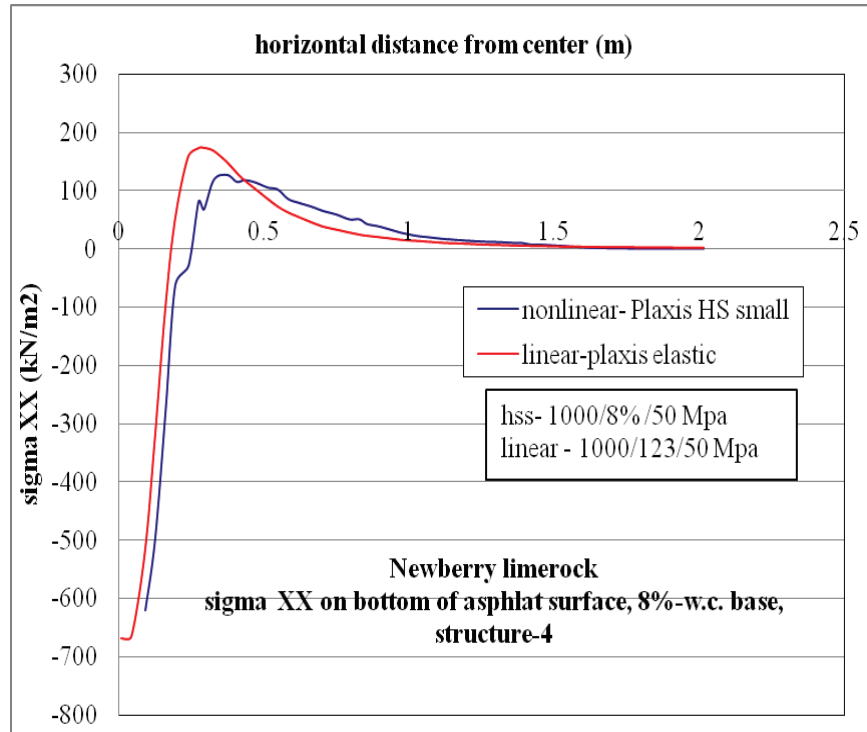
Figure C-31. σ_{xx} at bottom of AC layer comparison for nonlinear and linear cases, for Structure-4 with 8% w.c. base layer.
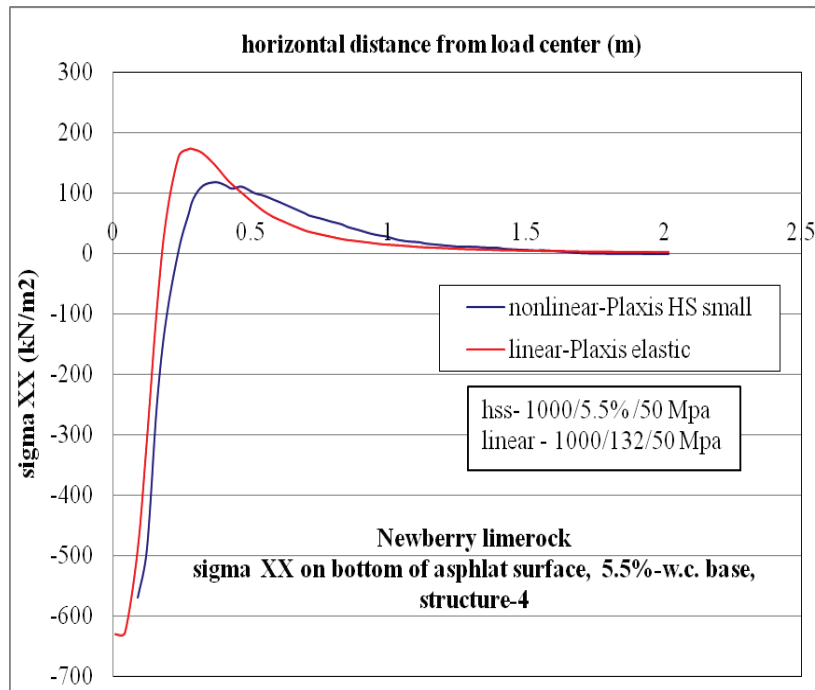
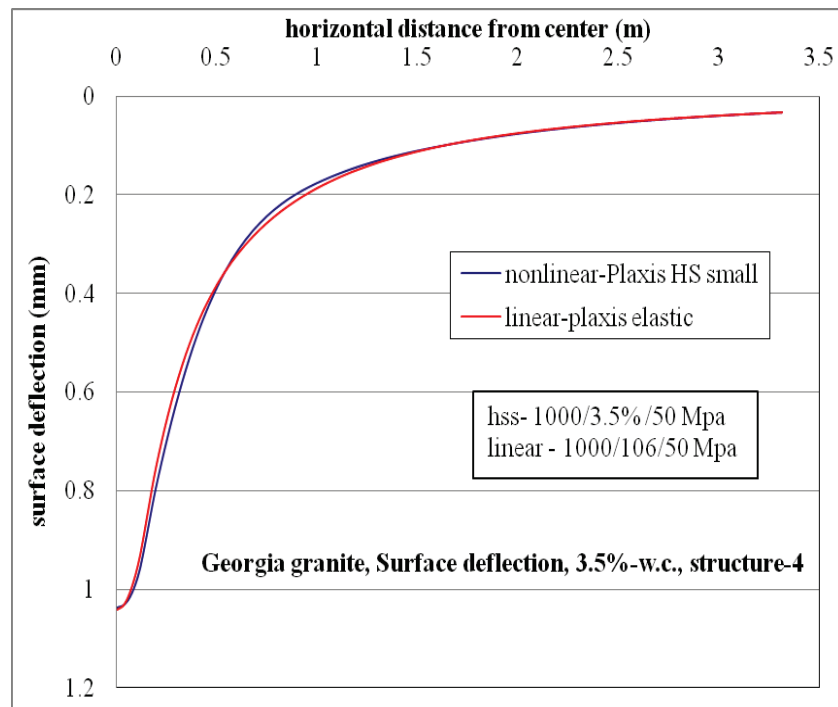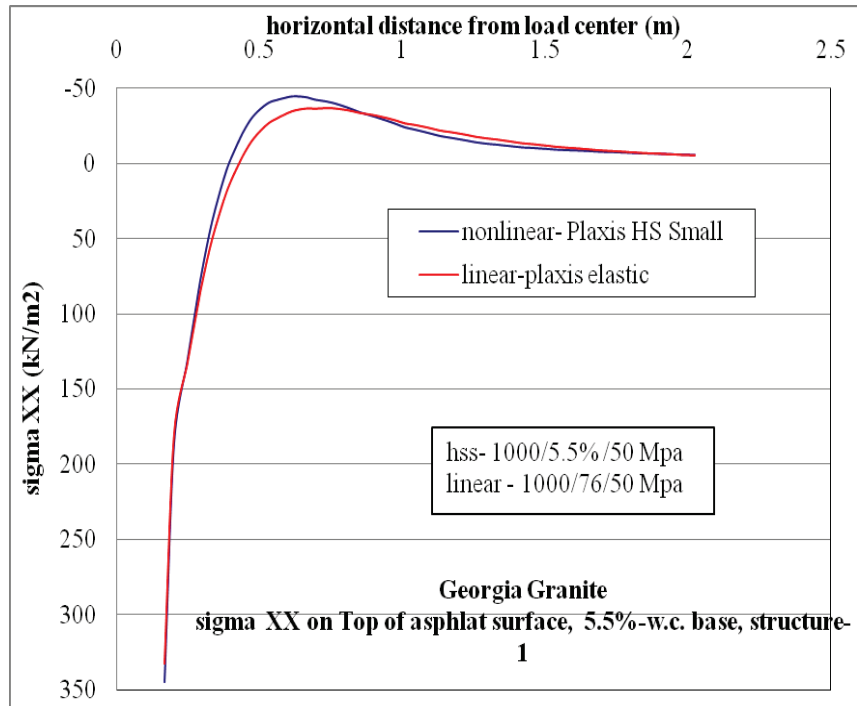Figure C-32. σ_{xx} at bottom of AC layer comparison for nonlinear and linear cases, for Structure-4 with 5.5% w.c. base layer.

C.1.5   Horizontal Strain (ε_{xx}, Tensile Strain) at Bottom of AC layer

C.1.5.1 Structure-1
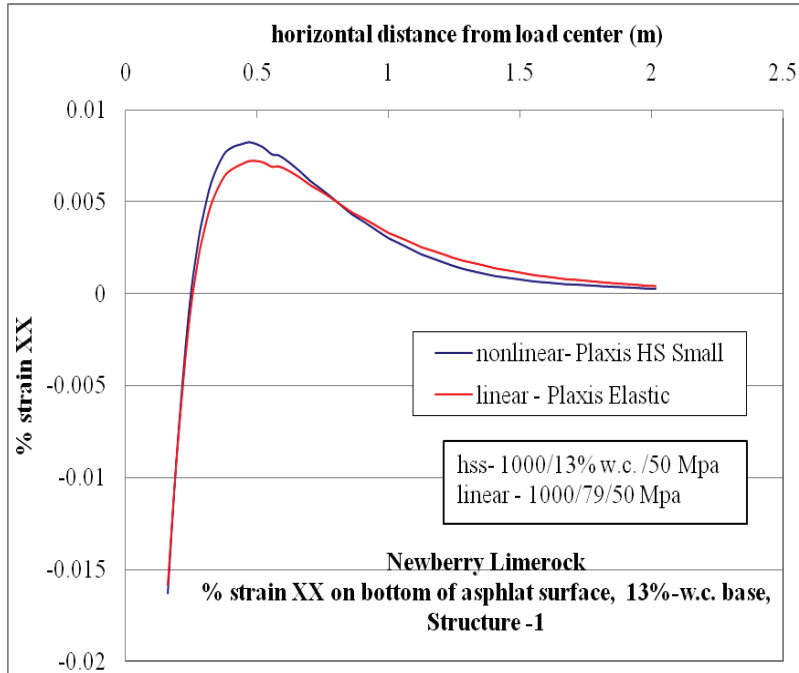
Figure C-33. ε_{xx} at bottom of AC layer comparison for nonlinear and linear cases, for Structure-1 with 13% w.c. base layer.
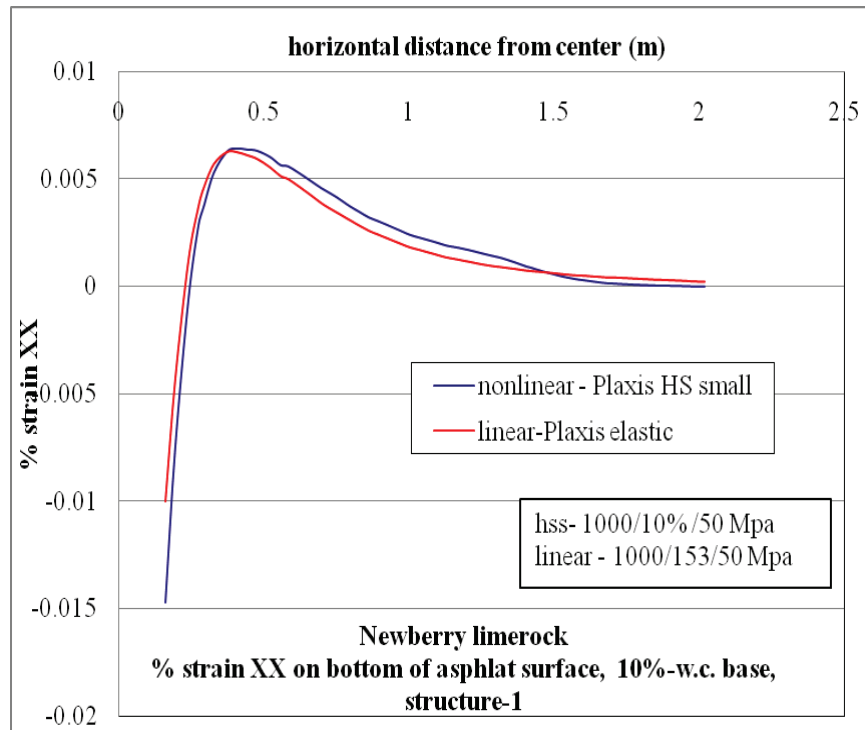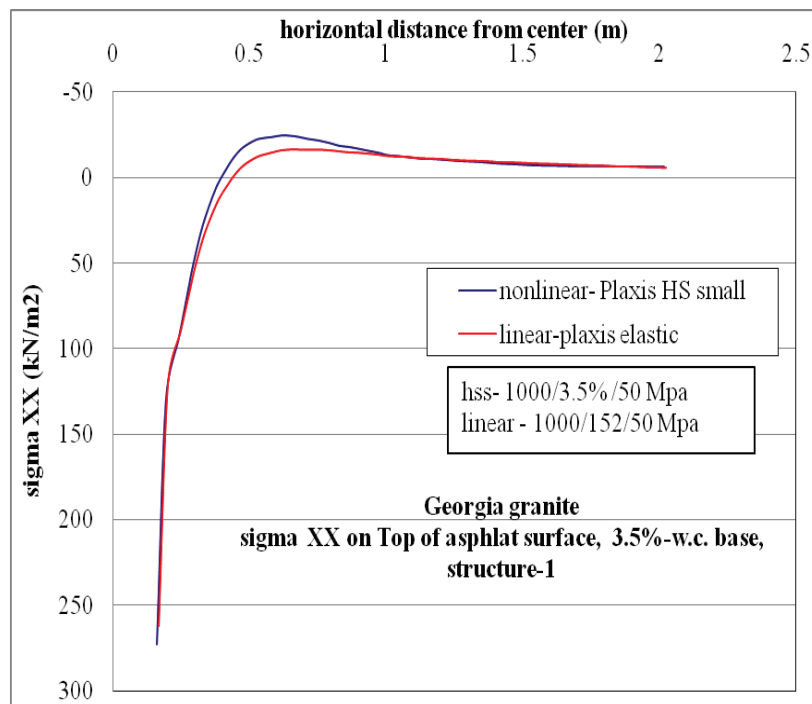

Figure C-34. ε_{xx} at bottom of AC layer comparison for nonlinear and linear cases, for Structure-1 with 10% w.c. base layer.
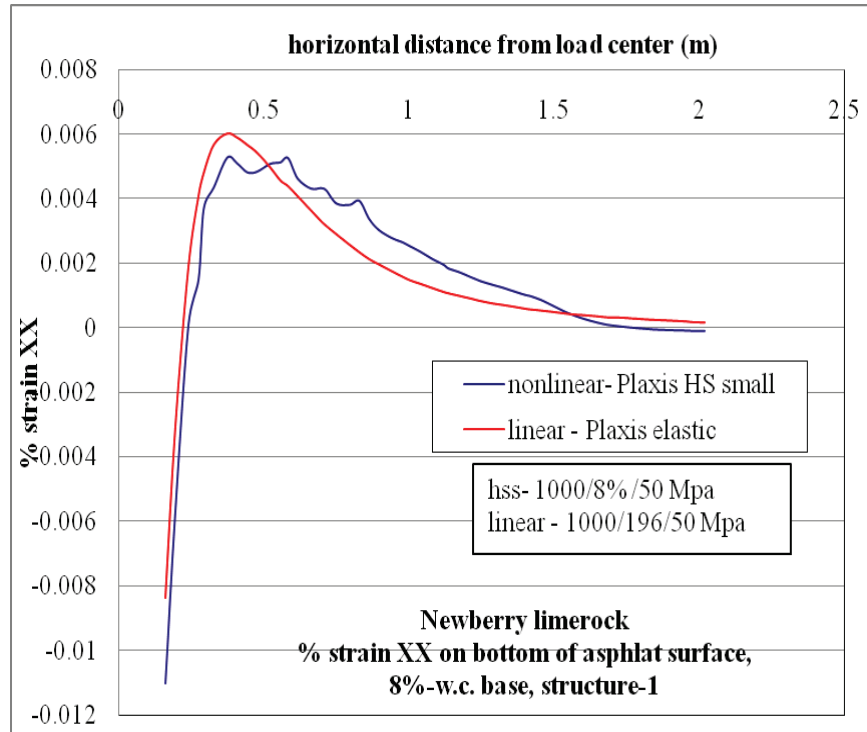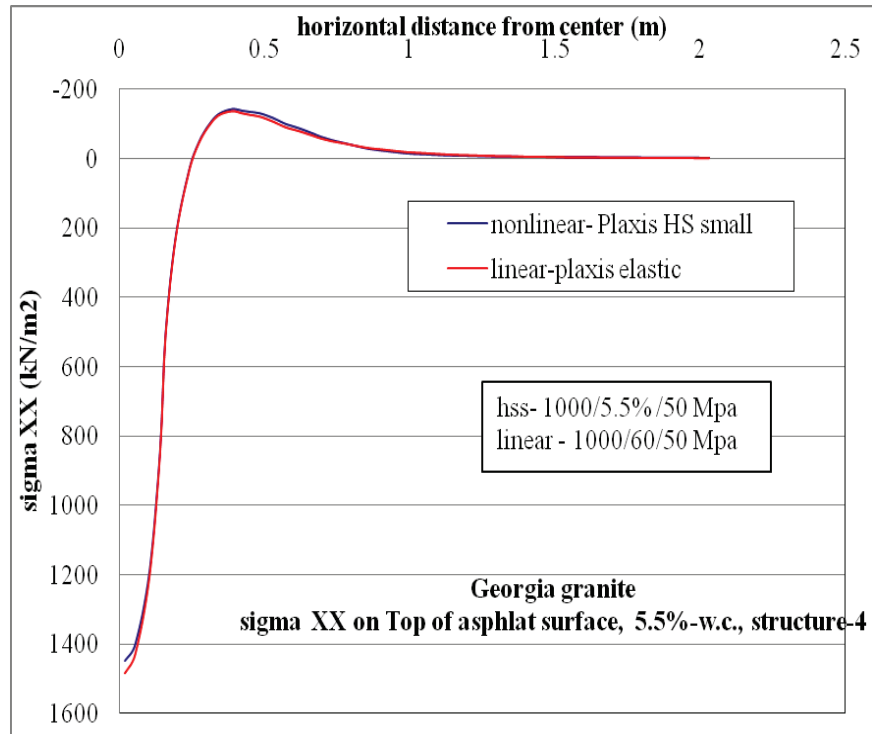
Figure C-35. ε_{xx} at bottom of AC layer comparison for nonlinear and linear cases, for Structure-1 with 8% w.c. base layer.

Figure C-36. ε_{xx} at bottom of AC layer comparison for nonlinear and linear cases, for Structure-1 with 5.5% w.c. base layer.

183
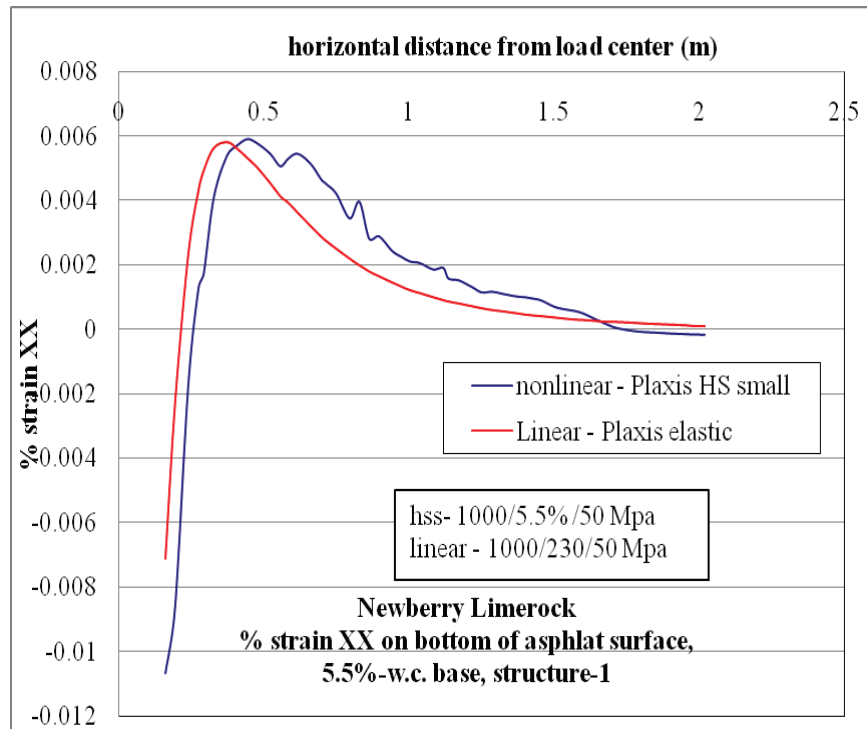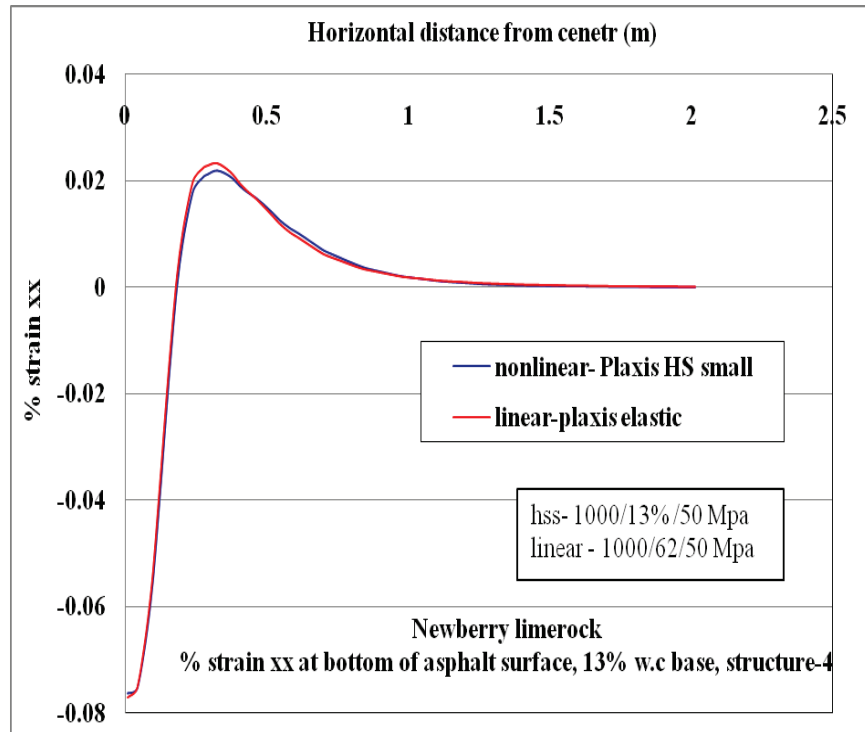
C.1.5.2 Structure-4

Figure C-37. ε_{xx} at bottom of AC layer comparison for nonlinear and linear cases, for Structure-4 with 13% w.c. base layer.
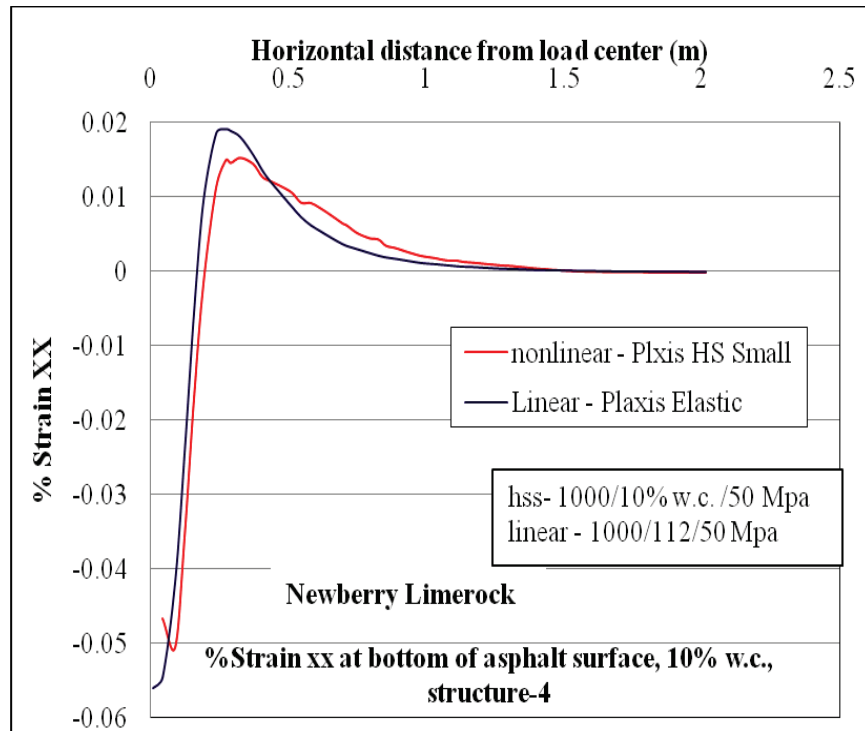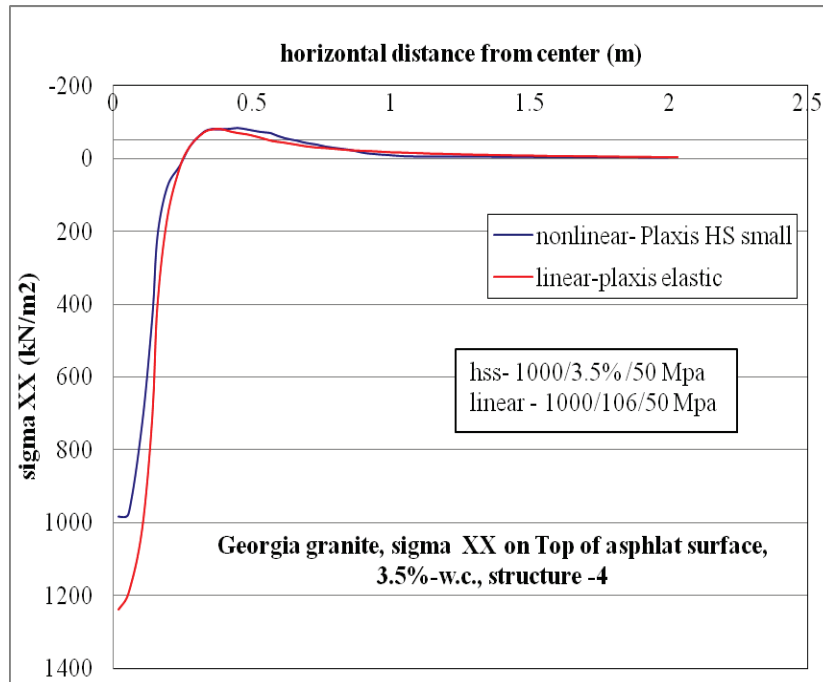

Figure C-38. ε_{xx} at bottom of AC layer comparison for nonlinear and linear cases, for Structure-4 with 10% w.c. base layer.
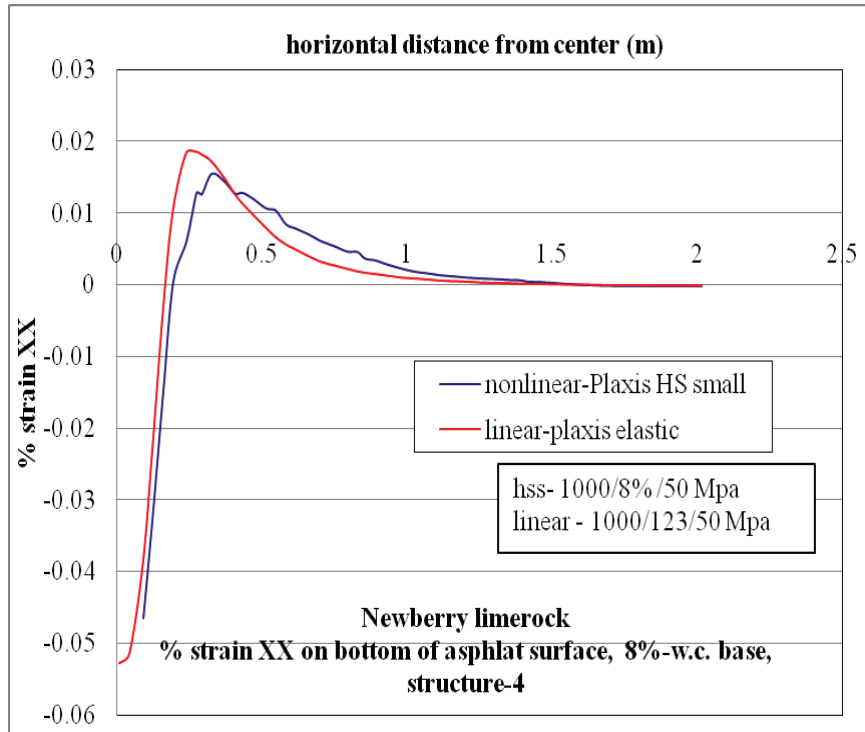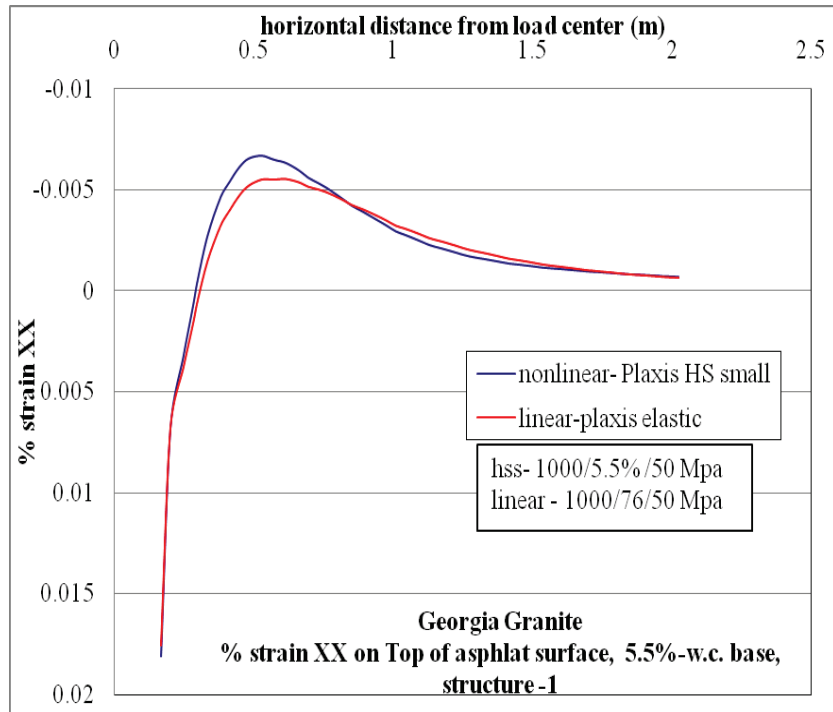
Figure C-39. ε_{xx} at bottom of AC layer comparison for nonlinear and linear cases, for Structure-4 with 8% w.c. base layer.
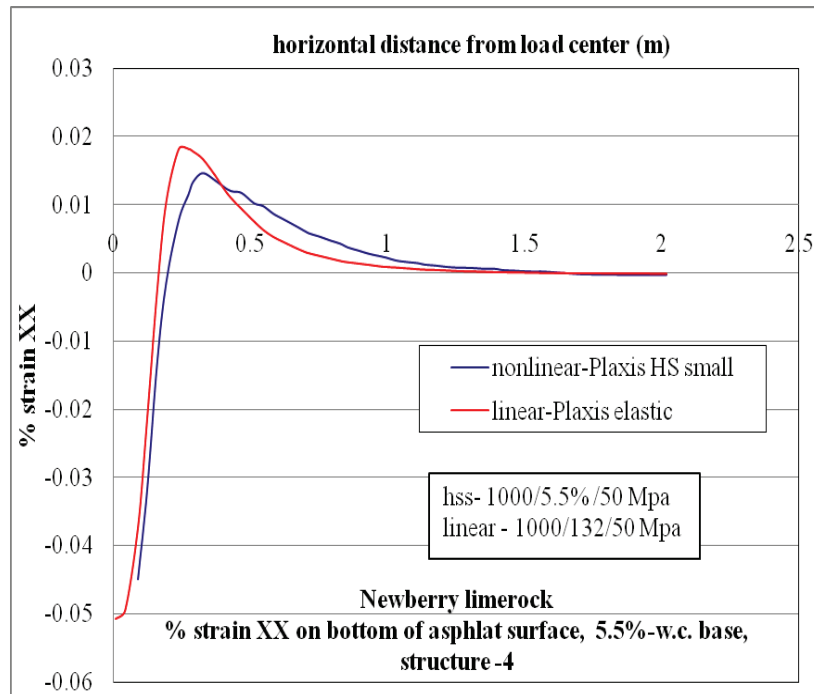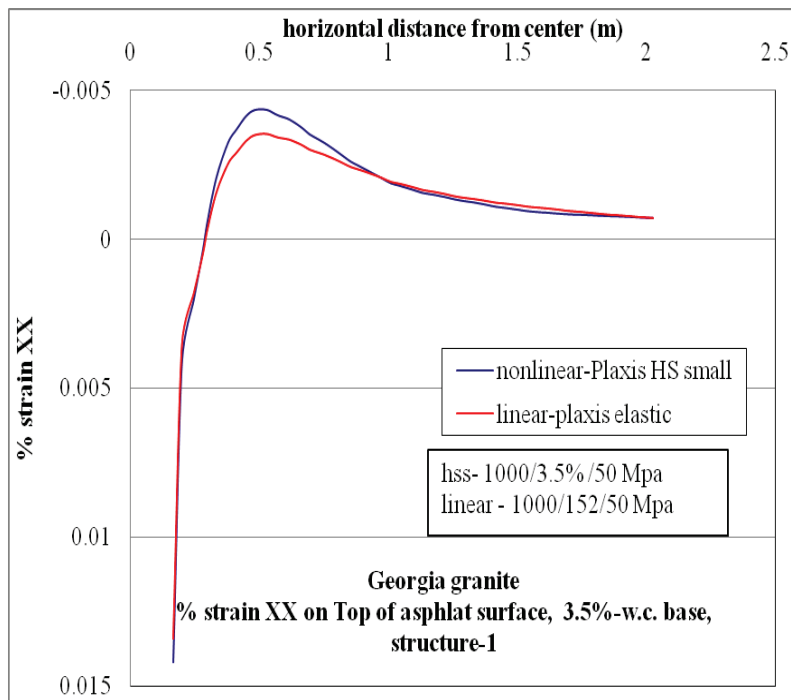

Figure C-40. ε_{xx} at bottom of AC layer comparison for nonlinear and linear cases, for Structure-4 with 5.5% w.c. base layer.

C.1.6 Vertical stress (σ_{yy}, compressive stress) at top of base layer

C.1.6.1 Structure-1
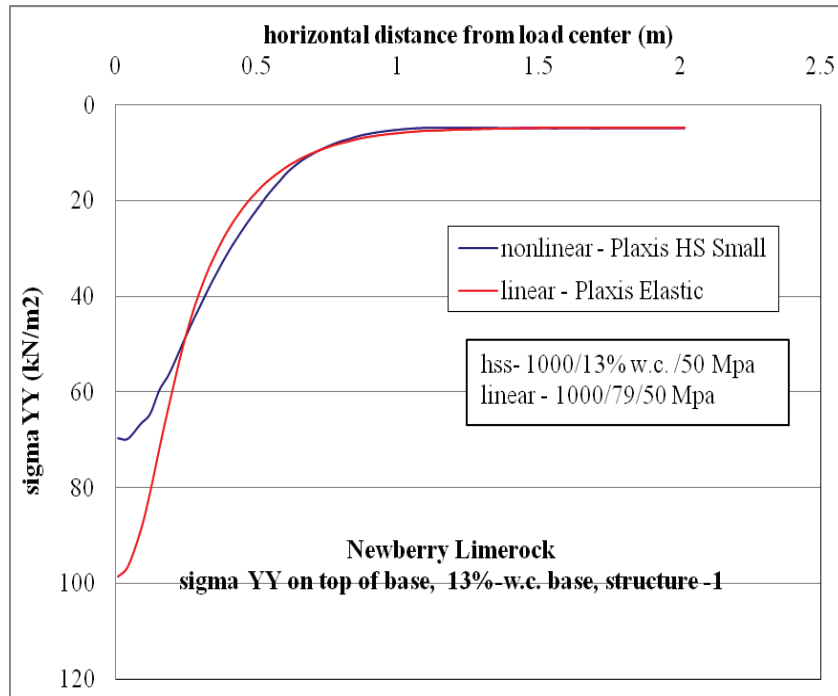
Figure C-41. σ_{yy} vertical stress at top of base layer comparison for nonlinear and linear cases, for Structure-1 with 13% w.c. base layer.
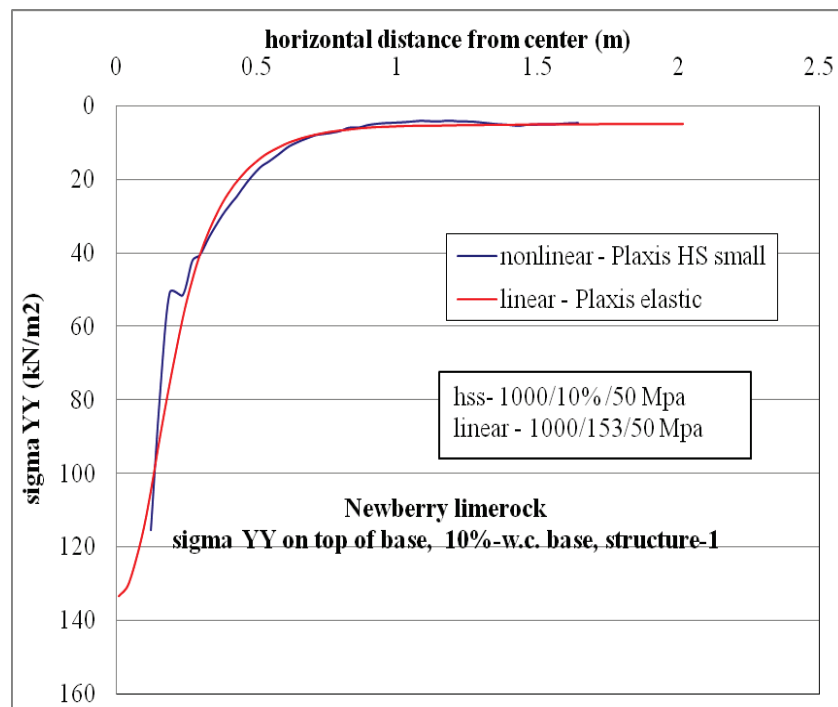
Figure C-42. σ_{yy} vertical stress at top of base layer comparison for nonlinear and linear cases, for Structure-1 with 10% w.c. base layer.
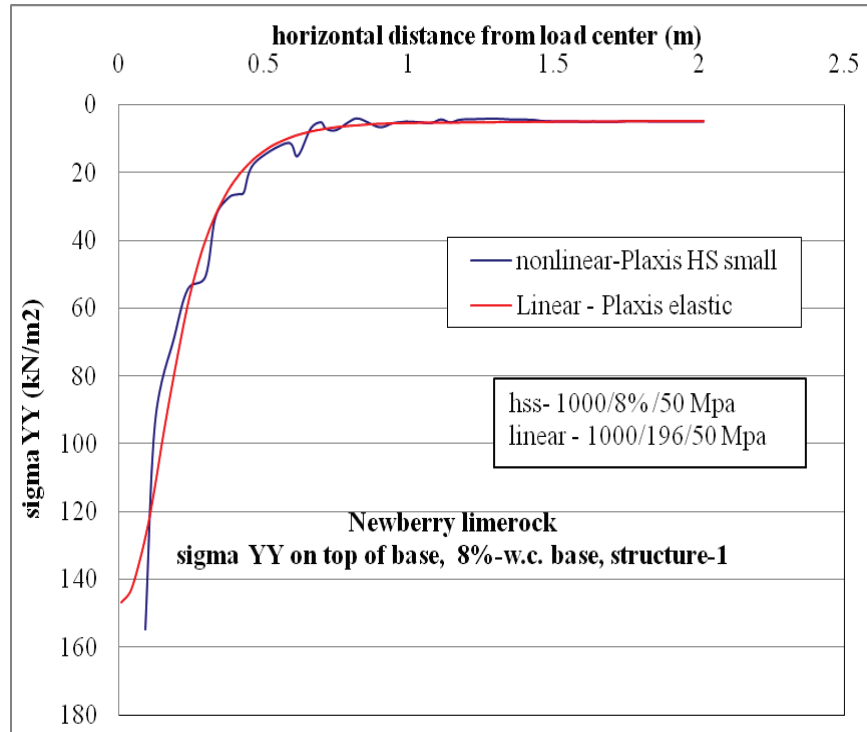
Figure C-43. σ_{yy} vertical stress at top of base layer comparison for nonlinear and linear cases, for Structure-1 with 8% w.c. base layer.
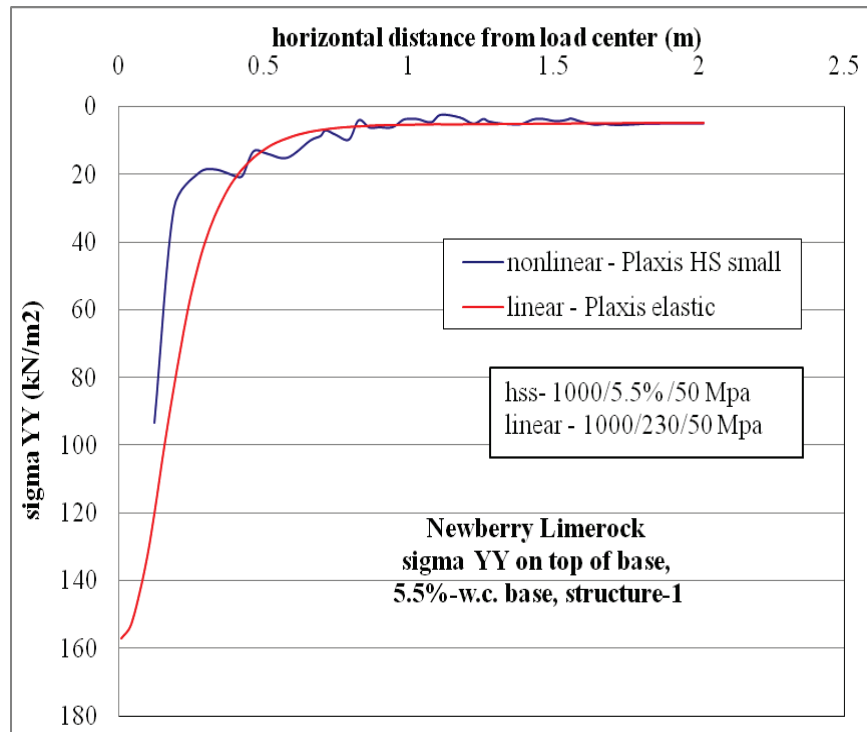
Figure C-44. σ_{yy} vertical stress at top of base layer comparison for nonlinear and linear cases, for Structure-1 with 5.5% w.c. base layer.
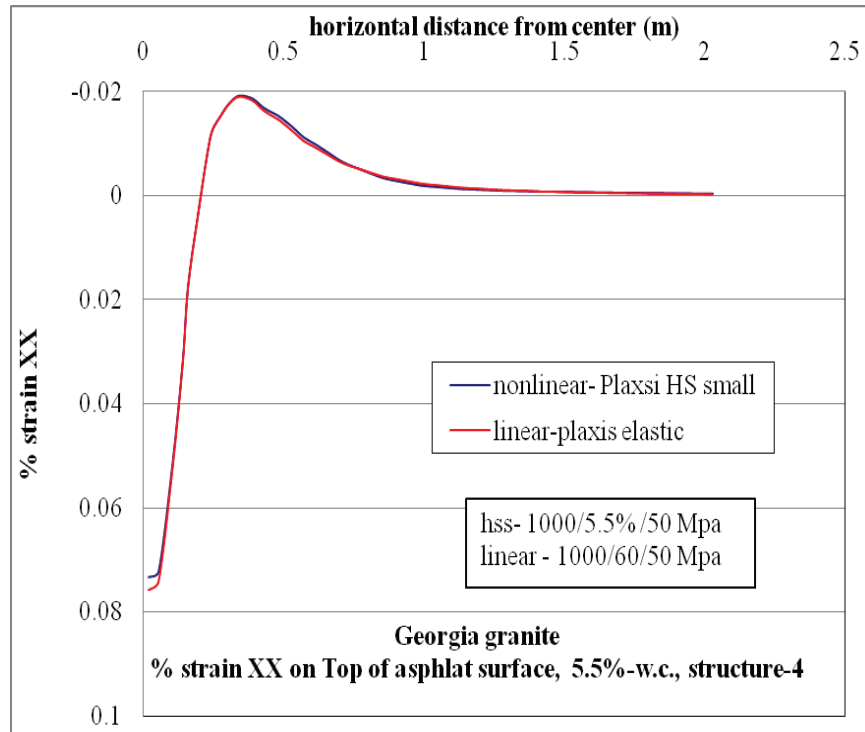
C.1.6.2 Structure-4
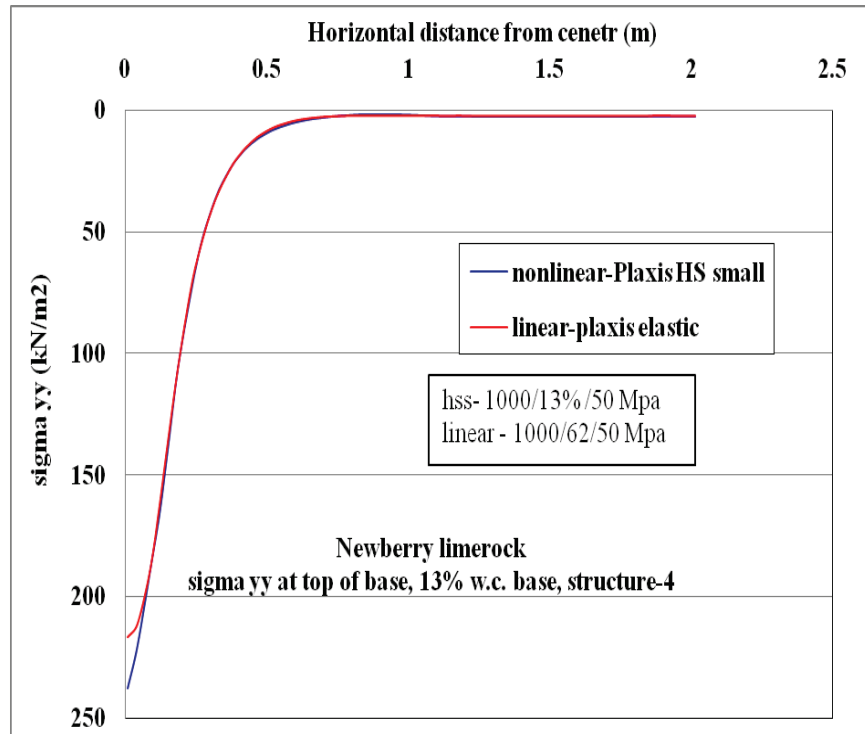
Figure C-45. σ_{yy} at top of base layer comparison for nonlinear and linear cases, for Structure-4 with 13% w.c. base layer.
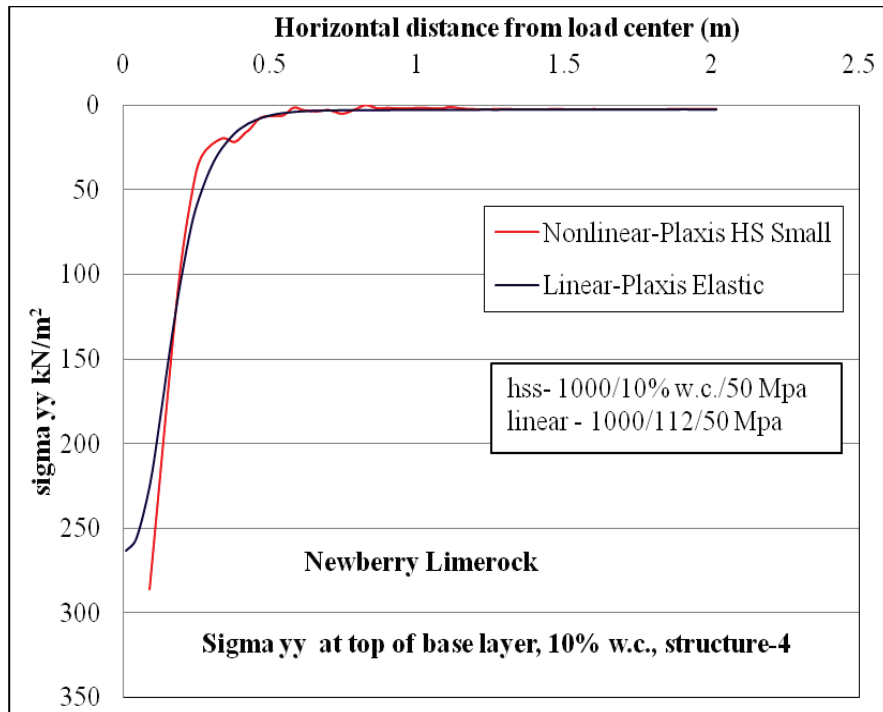

Figure C-46. σ_{yy} vertical stress at top of base layer comparison for nonlinear and linear cases, for Structure-4 with 10% w.c. base layer.
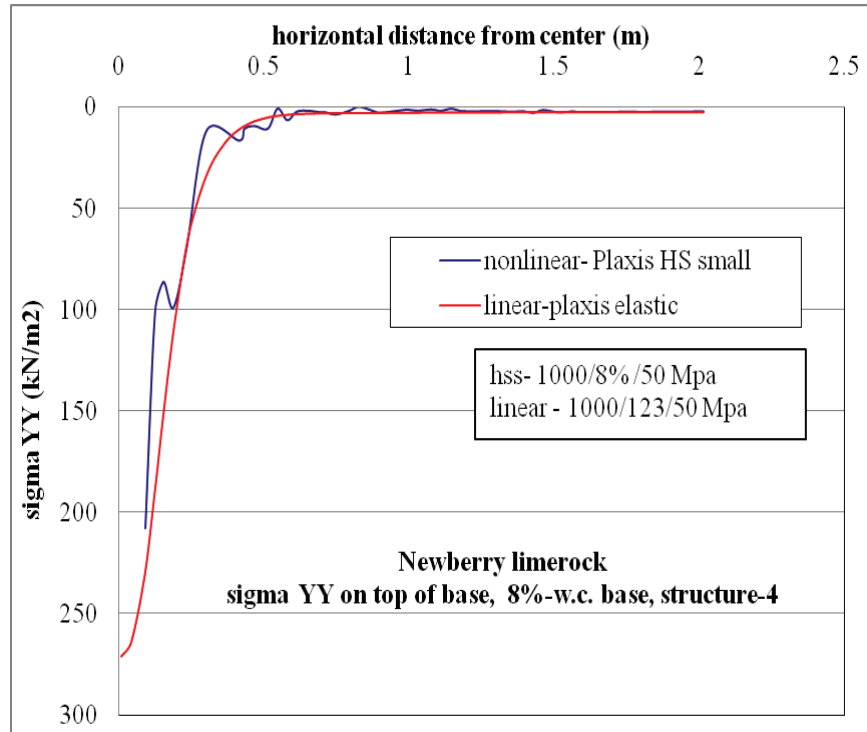
Figure C-47. σ_{yy} vertical stress at top of base layer comparison for nonlinear and linear cases, for Structure-4 with 8% w.c. base layer.
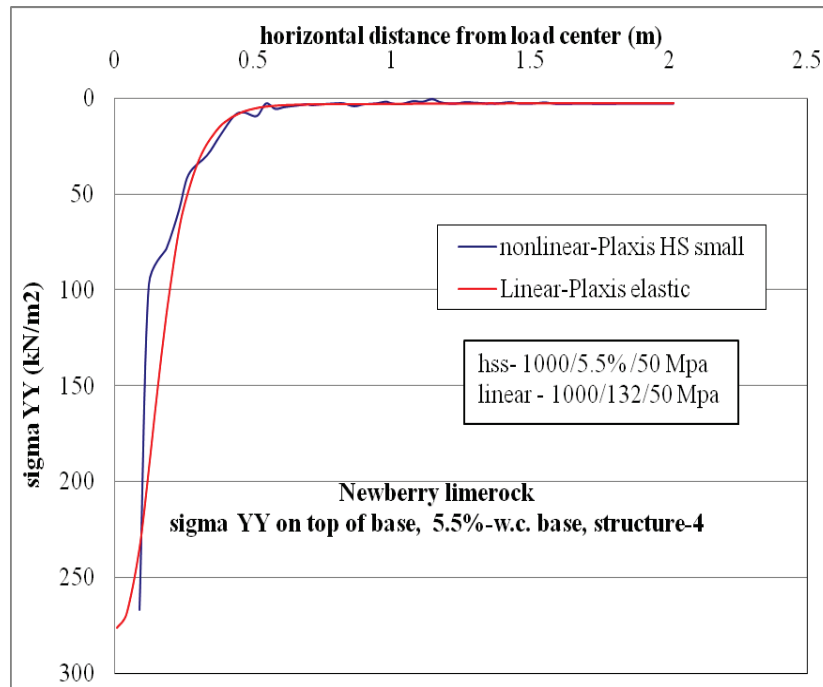
Figure C-48. σ_{yy} vertical stress at top of base layer comparison for nonlinear and linear cases, for Structure-4 with 5.5% w.c. base layer.

C.1.7   Vertical Strain (ε_{yy}, Compressive Strain) at Top of Base Layer
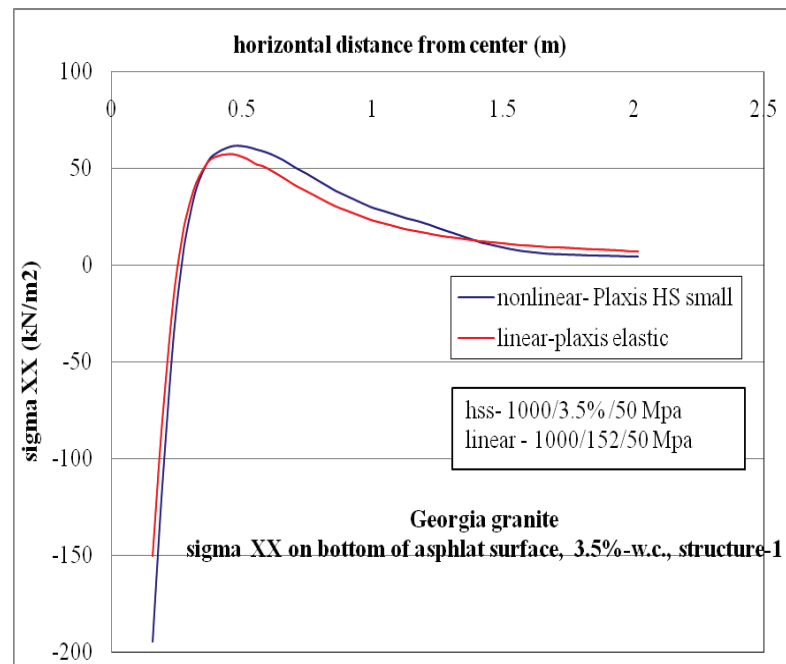
C.1.7.1 Structure-1
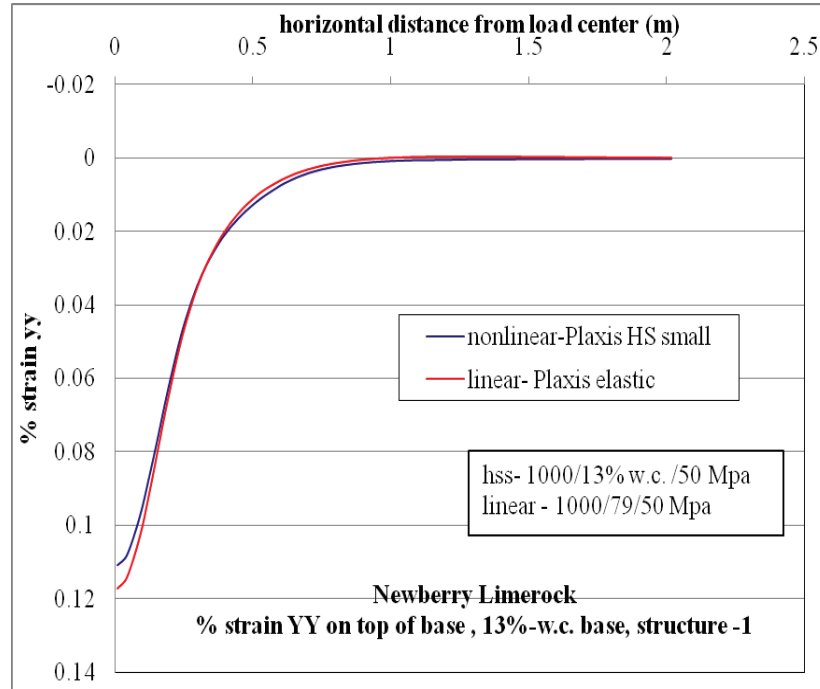
Figure C-49. ε_{yy} at top of base layer comparison for nonlinear and linear cases, for Structure-1 with 13% w.c. base layer.
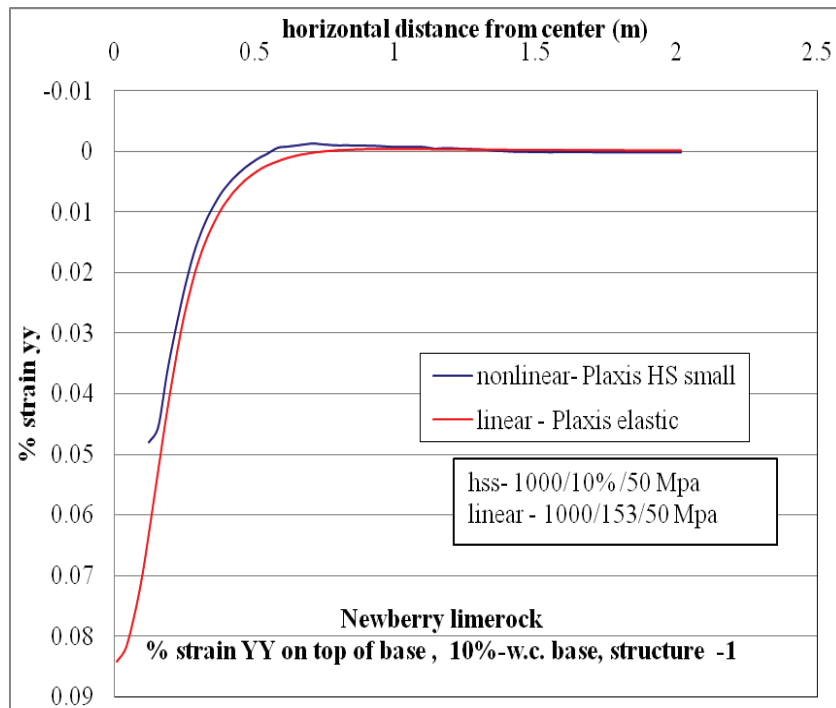
Figure C-50. ε_{yy} at top of base layer comparison for nonlinear and linear cases, for Structure-1 with 10% w.c. base layer.
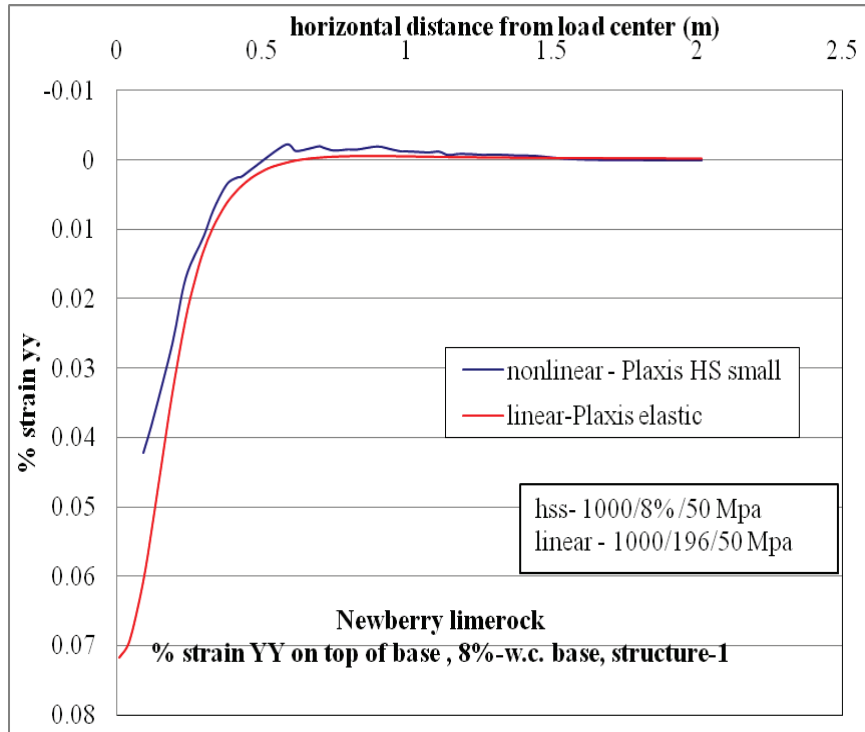
Figure C-51. ε_{yy} at top of base layer comparison for nonlinear and linear cases, for Structure-1 with 8% w.c. base layer.
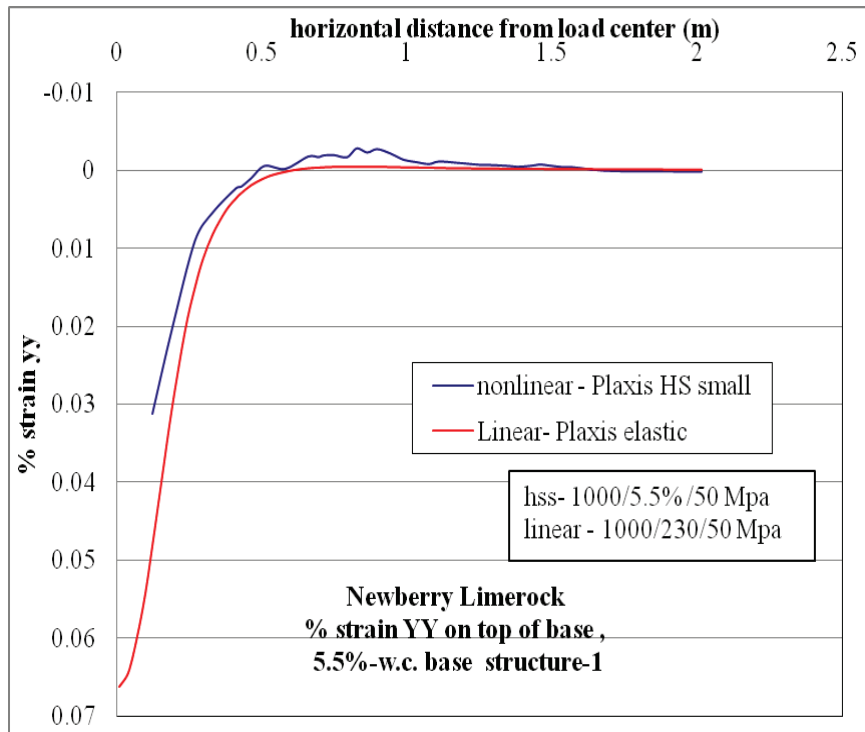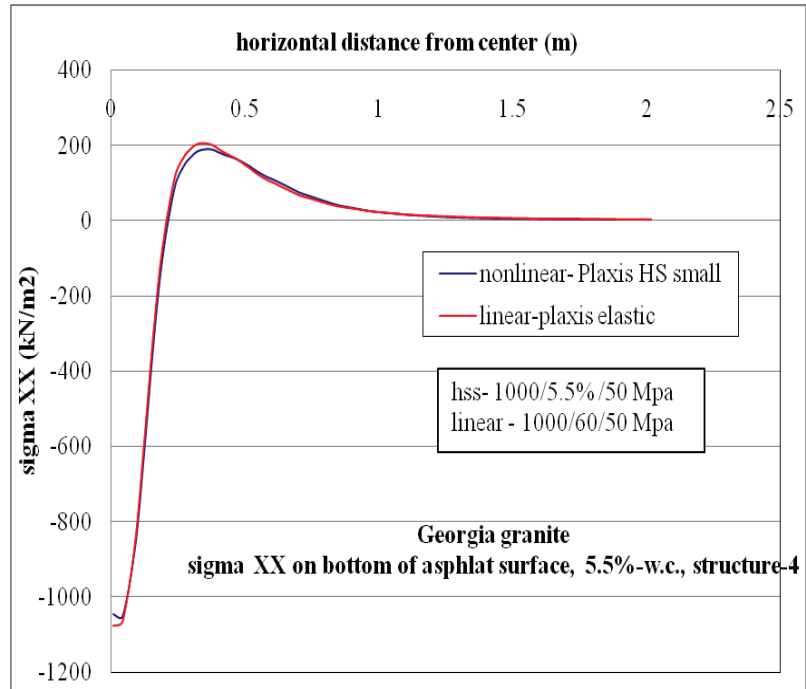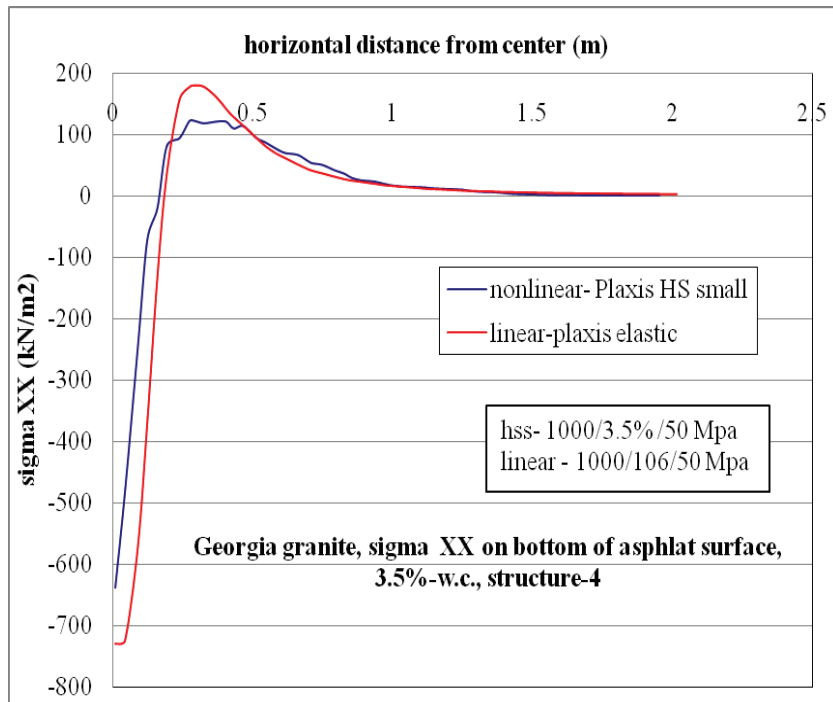

Figure C-52. ε_{yy} at top of base layer comparison for nonlinear and linear cases, for Structure-1 with 5.5% w.c. base layer.

C.1.7.2 Structure-4
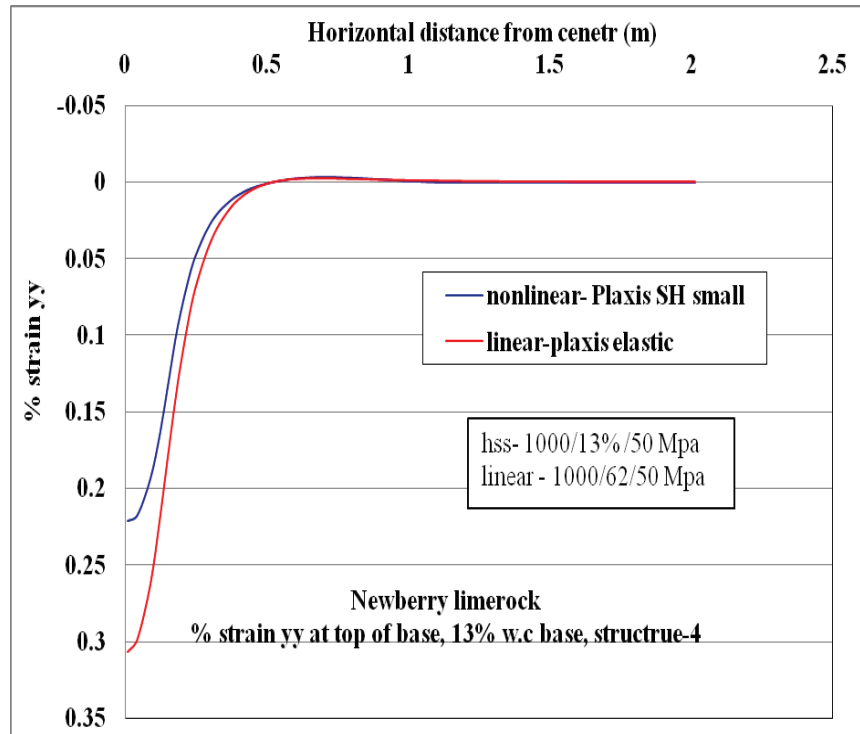
Figure C-53. ε_{yy} at top of base layer comparison for nonlinear and linear cases, for Structure-4 with 13% w.c. base layer.
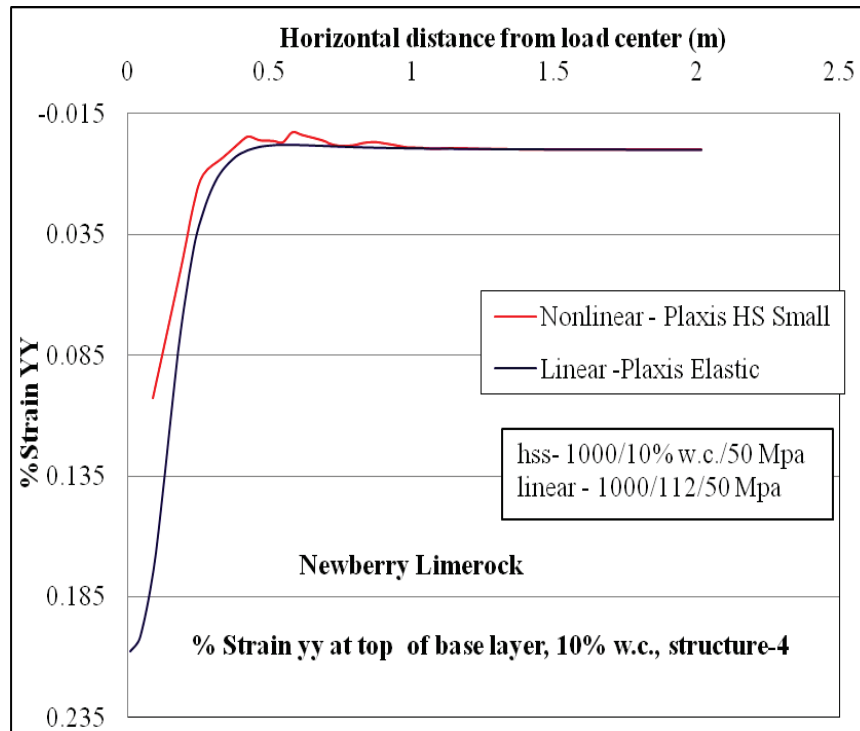
Figure C-54. ε_{yy} at top of base layer comparison for nonlinear and linear cases, for Structure-4 with 10% w.c. base layer.
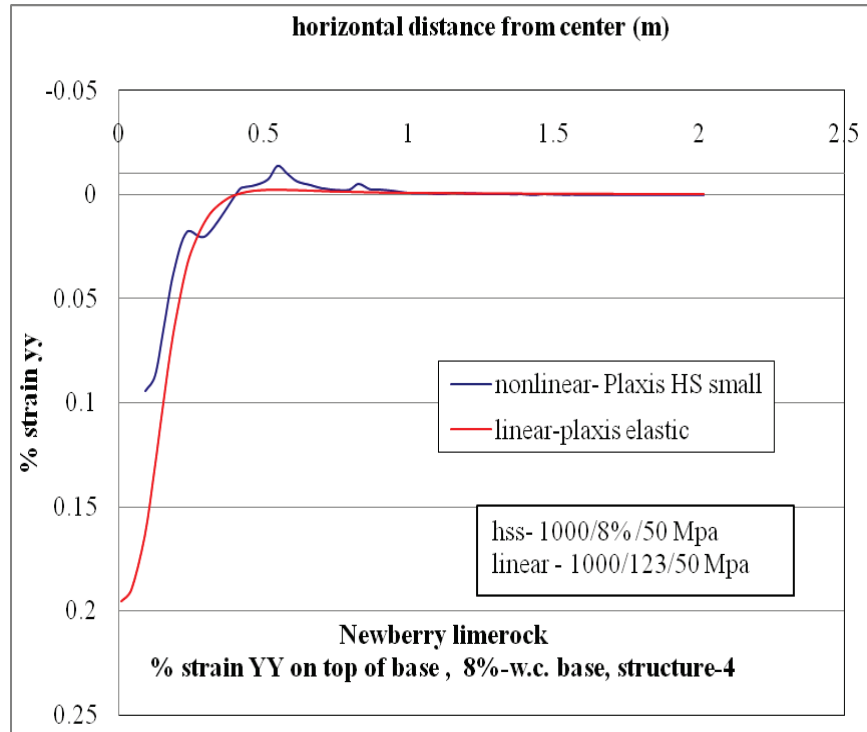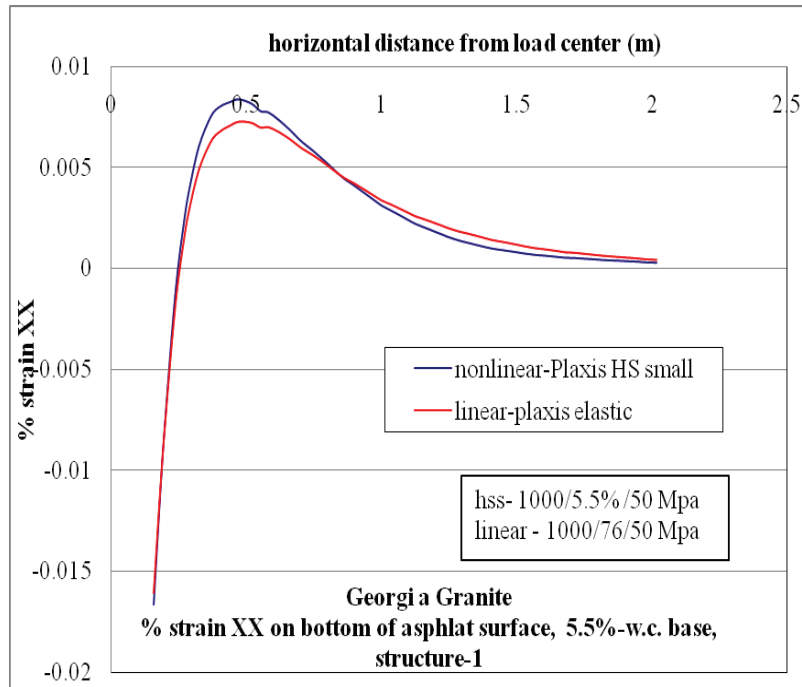
Figure C-55. ε_{yy} at top of base layer comparison for nonlinear and linear cases, for Structure-4 with 8% w.c. base layer.
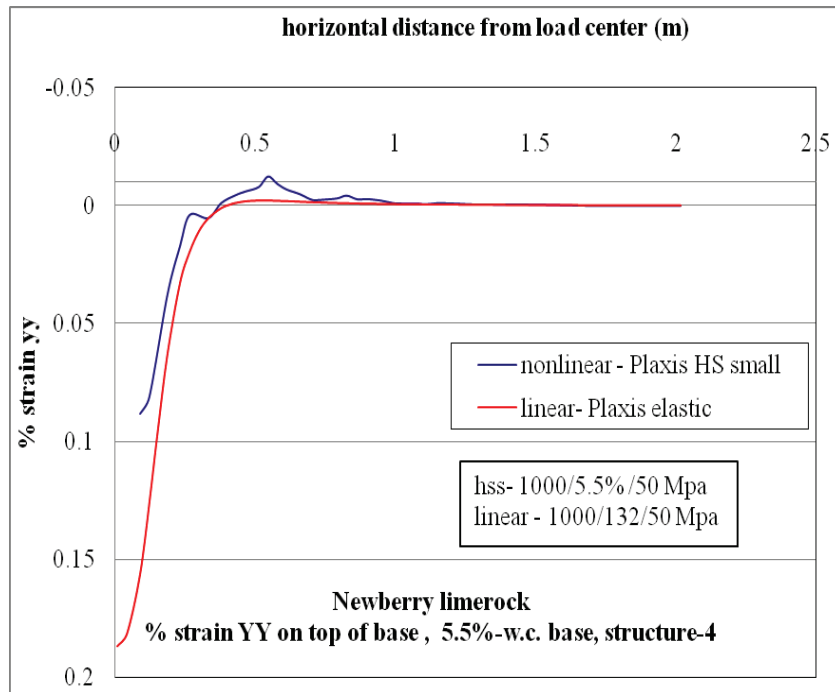
Figure C-56. ε_{yy} at top of base layer comparison for nonlinear and linear cases, for Structure-4 with 5.5% w.c. base layer.

C.1.8 Vertical Stress (σ_{yy}, Compressive Stress) at Bottom of Base Layer

C.1.8.1 Structure-1
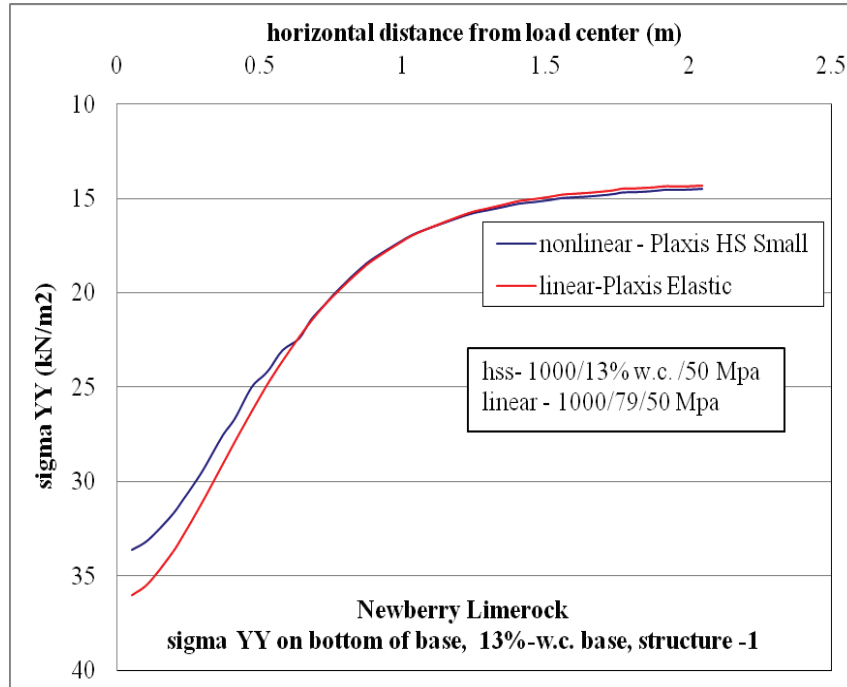
Figure C-57. σ_{yy} at bottom of base layer comparison for nonlinear and linear cases, for Structure-1 with 13% w.c. base layer.
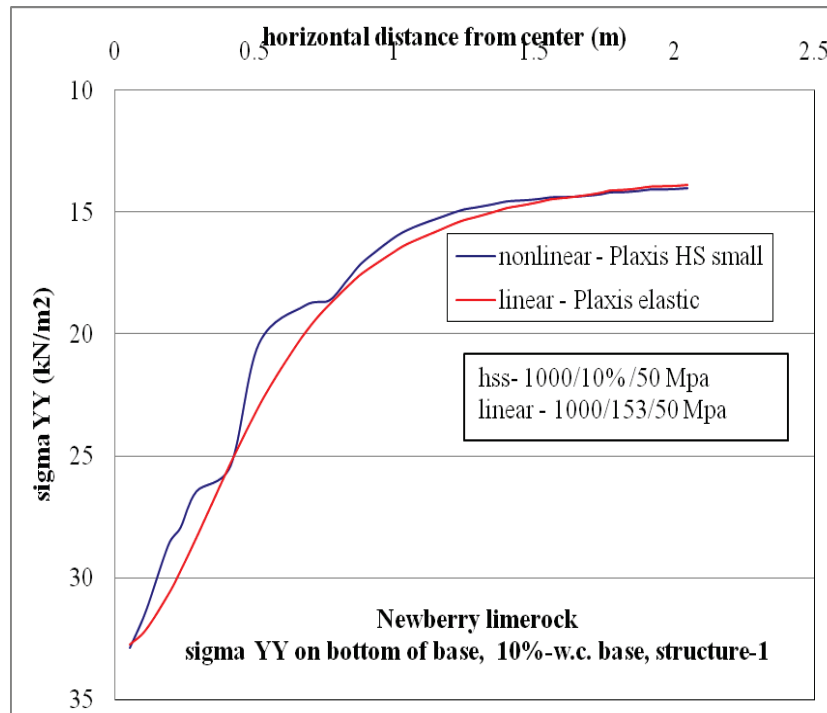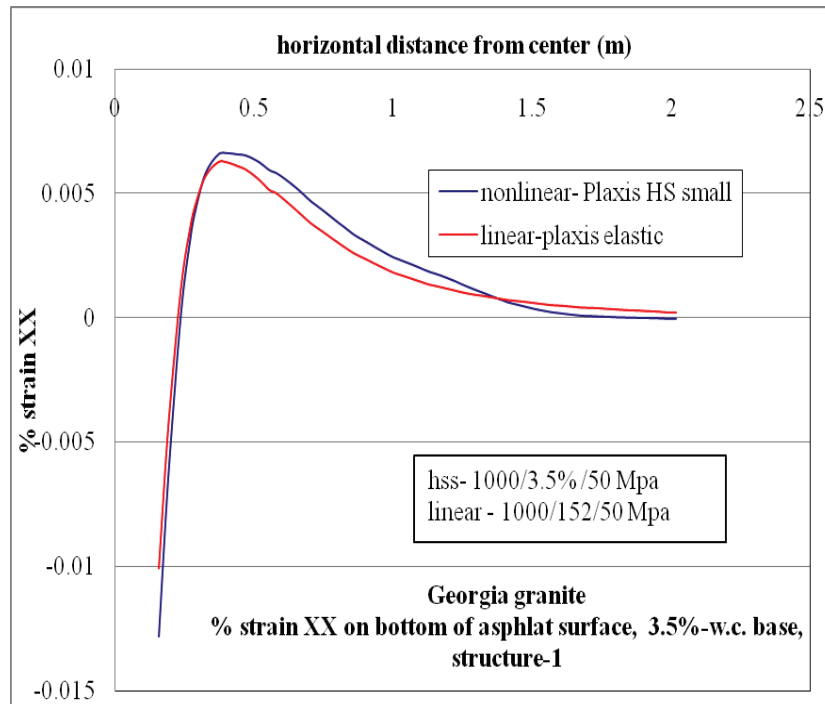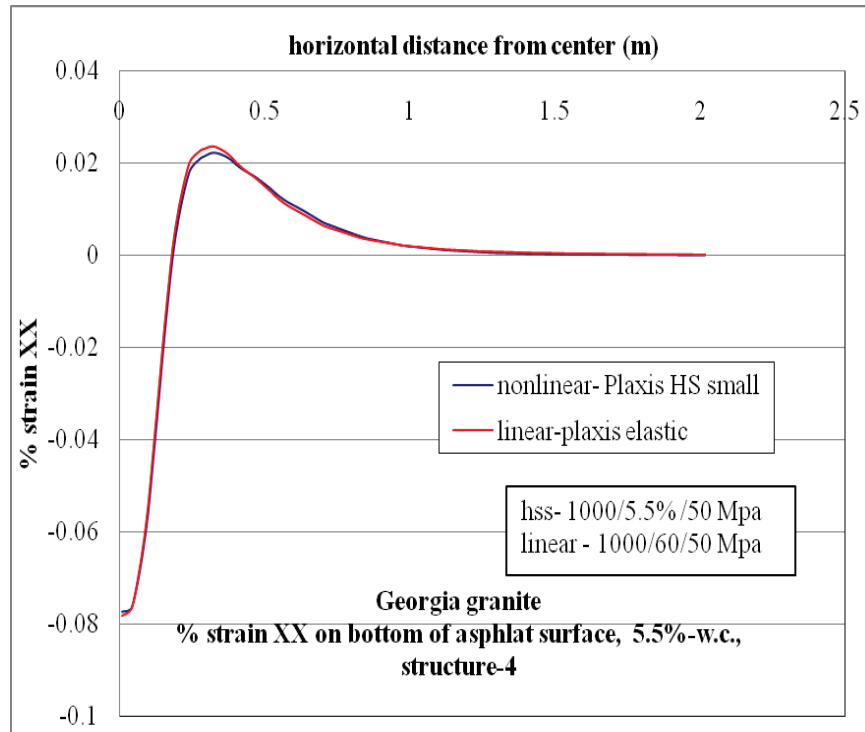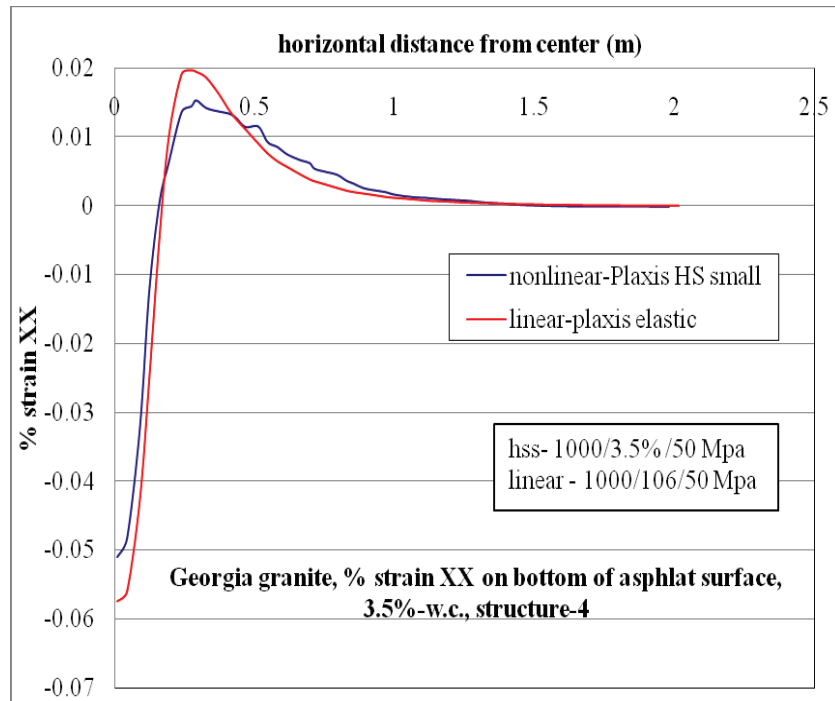

Figure C-58. σ_{yy} at bottom of base layer comparison for nonlinear and linear cases, for Structure-1 with 10% w.c. base layer.
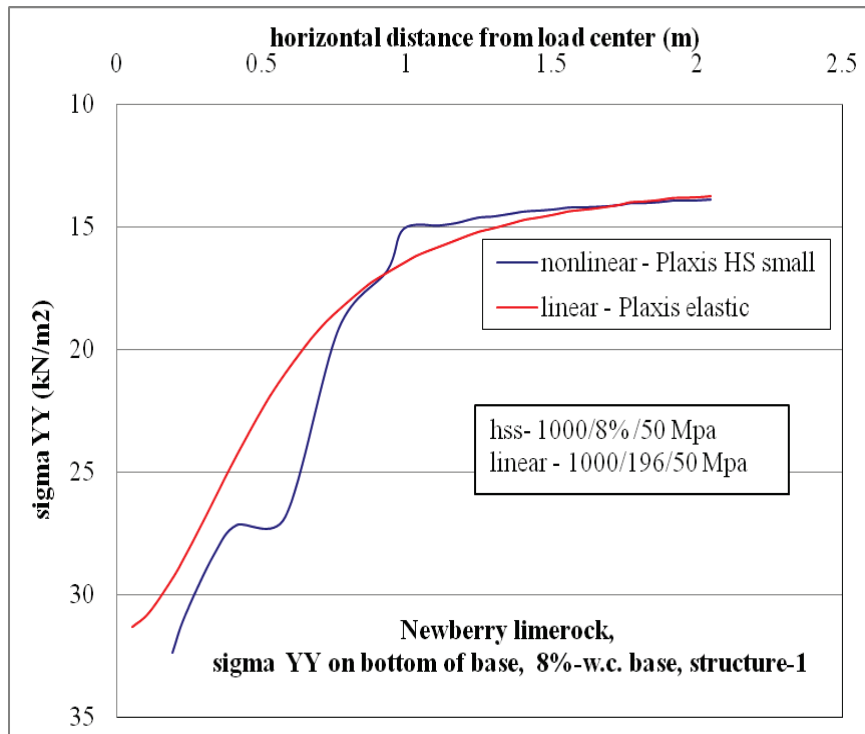
Figure C-59. σ_{yy} at bottom of base layer comparison for nonlinear and linear cases, for Structure-1 with 8% w.c. base layer.
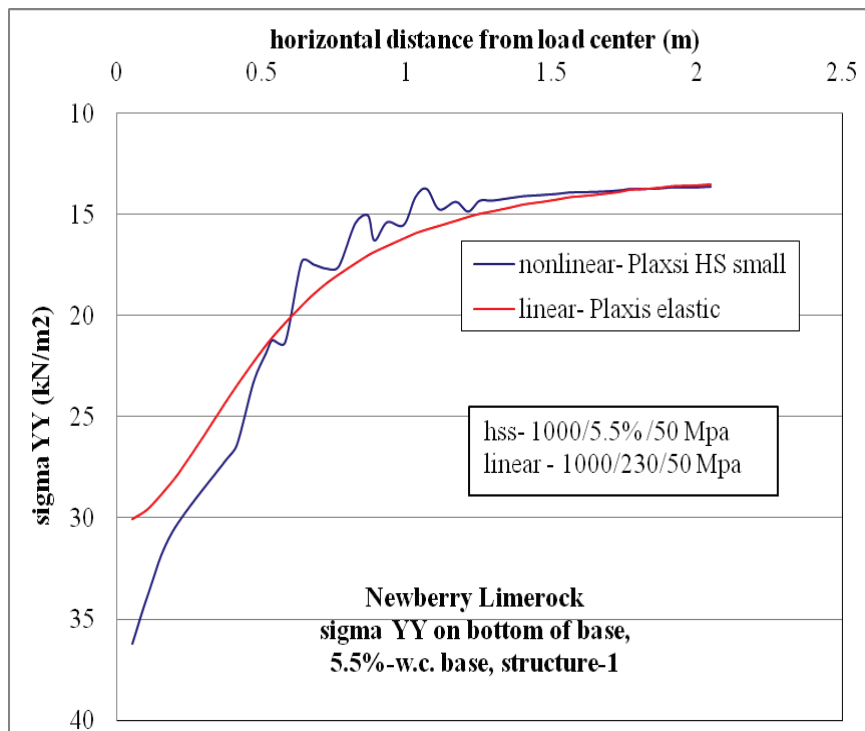
Figure C-60. σ_{yy} at bottom of base layer comparison for nonlinear and linear cases, for Structure-1 with 5.5% w.c. base layer.
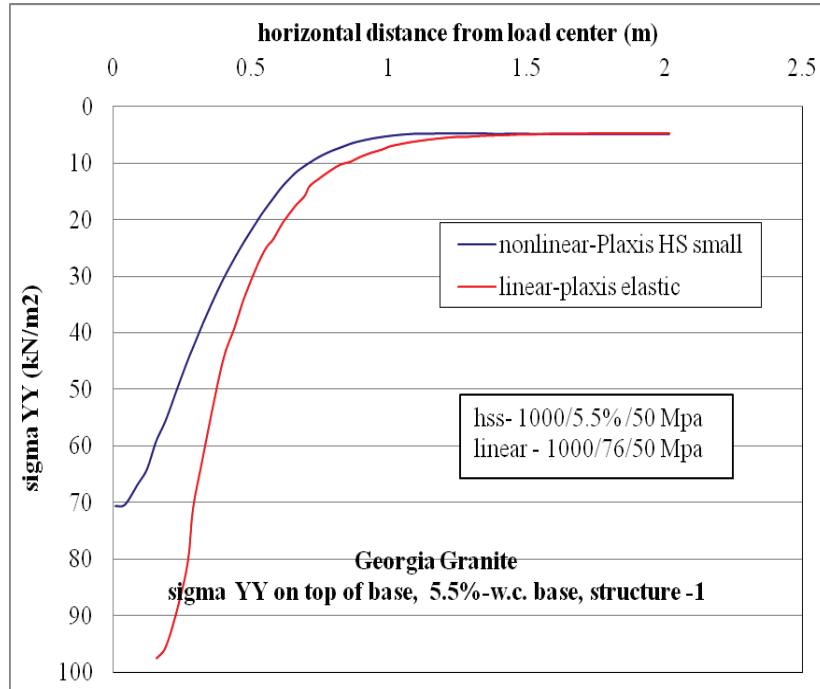
C.1.8.2 Structure-4
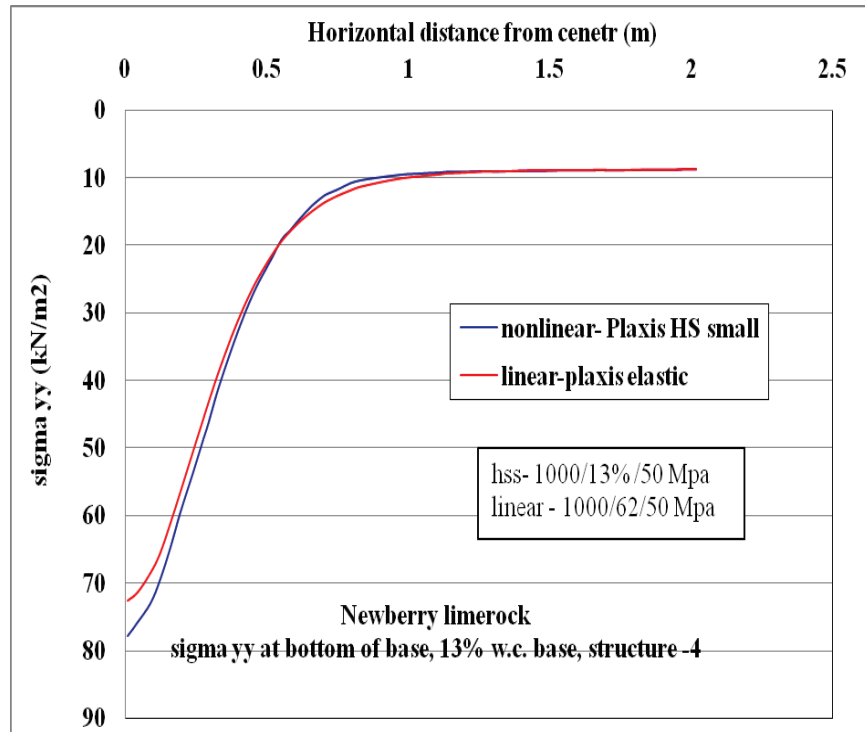
Figure C-61. σ_{yy} at bottom of base layer comparison for nonlinear and linear cases, for Structure-4 with 13% w.c. base layer.
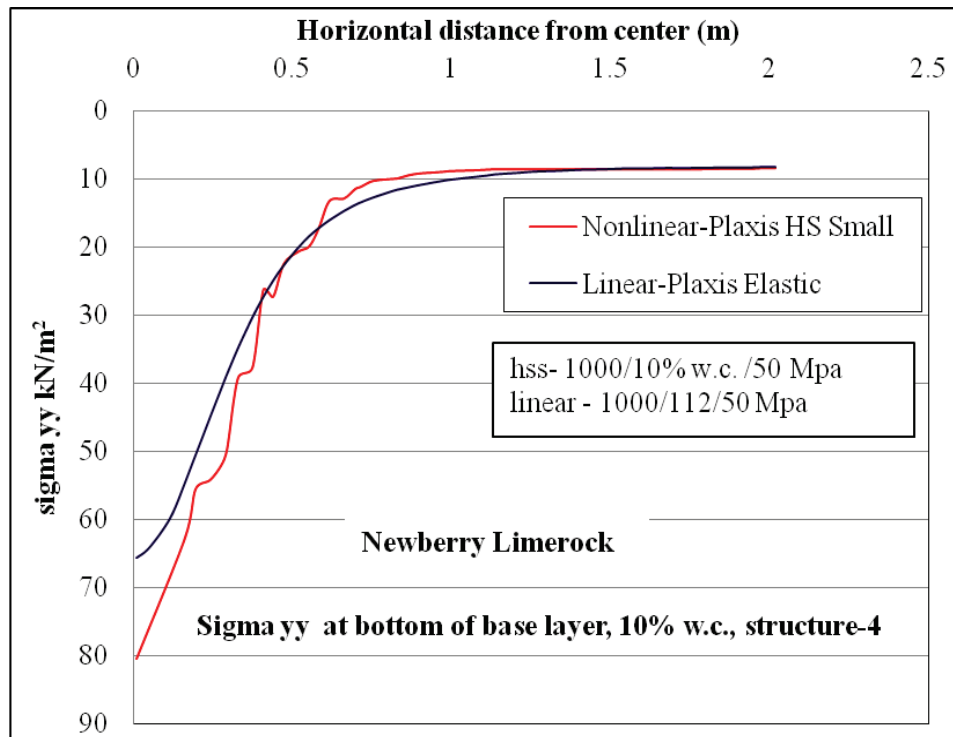
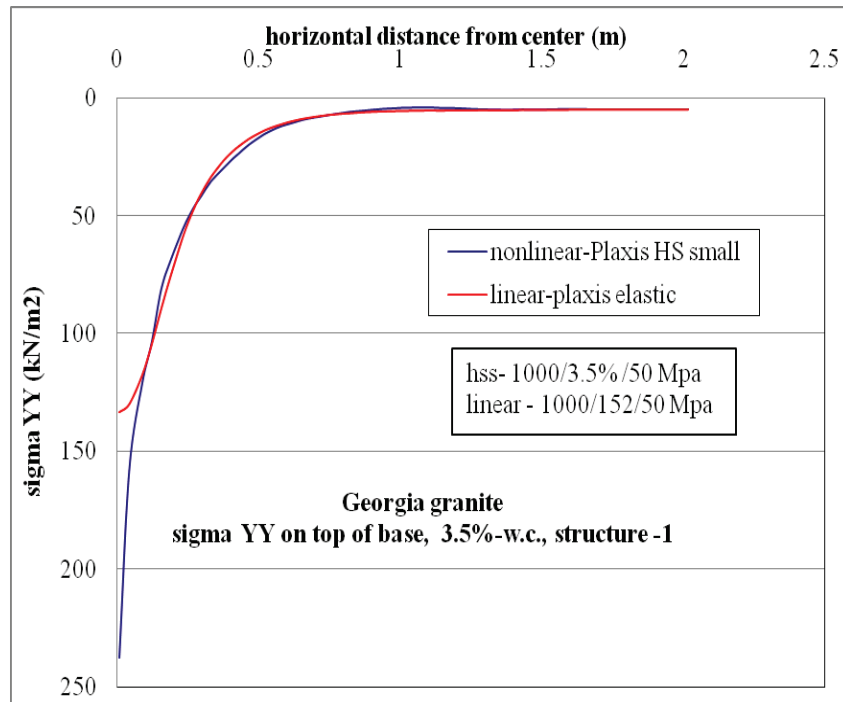Figure C-62. σ_{yy} at bottom of base layer comparison for nonlinear and linear cases, for Structure-4 with 10% w.c. base layer.
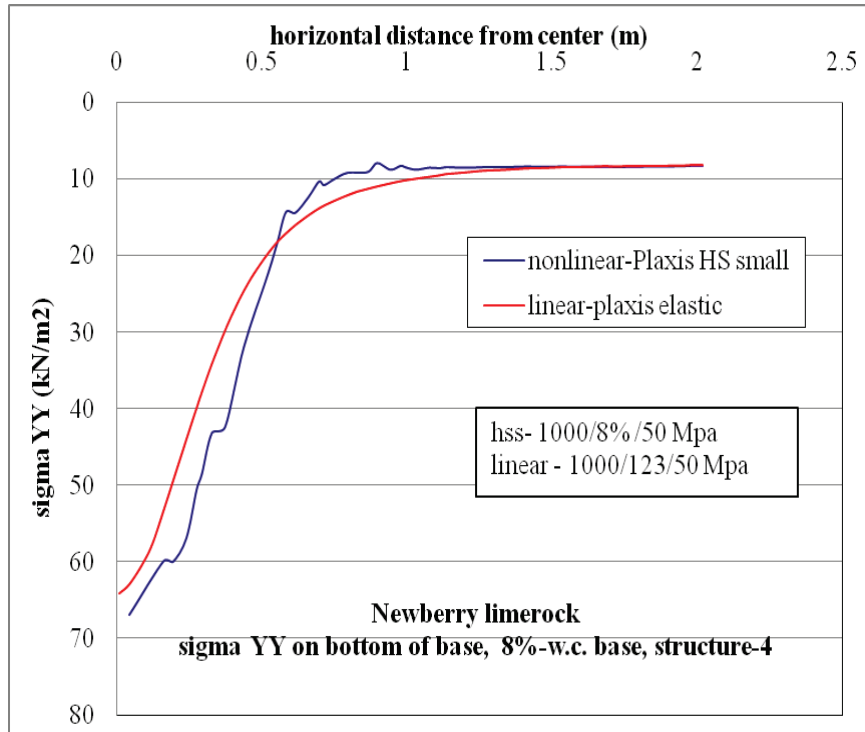
Figure C-63. σ_{yy} at bottom of base layer comparison for nonlinear and linear cases, for Structure-4 with 8% w.c. base layer.
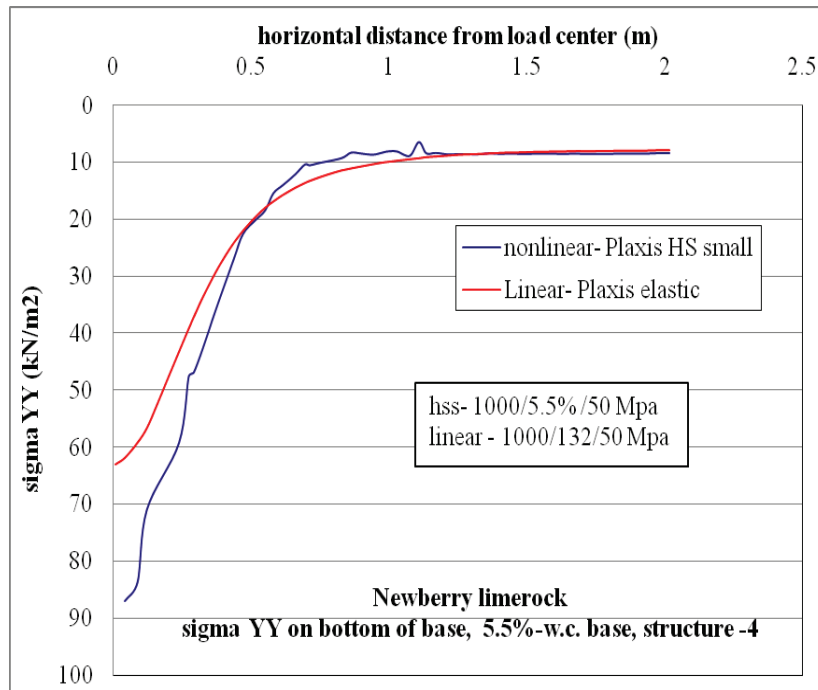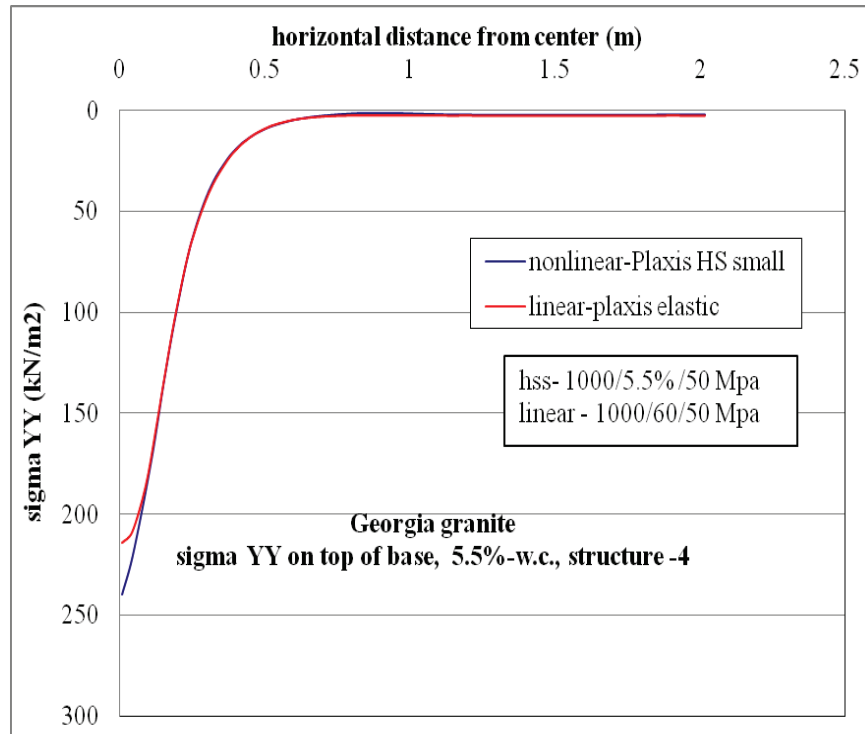

Figure C-64. σ_{yy} at bottom of base layer comparison for nonlinear and linear cases, for Structure-4 with 5.5% w.c. base layer.

C.1.9. Vertical Strain (ε$_{yy}$, Compressive Strain) at Bottom of Base Layer

C.1.9.1 Structure-1
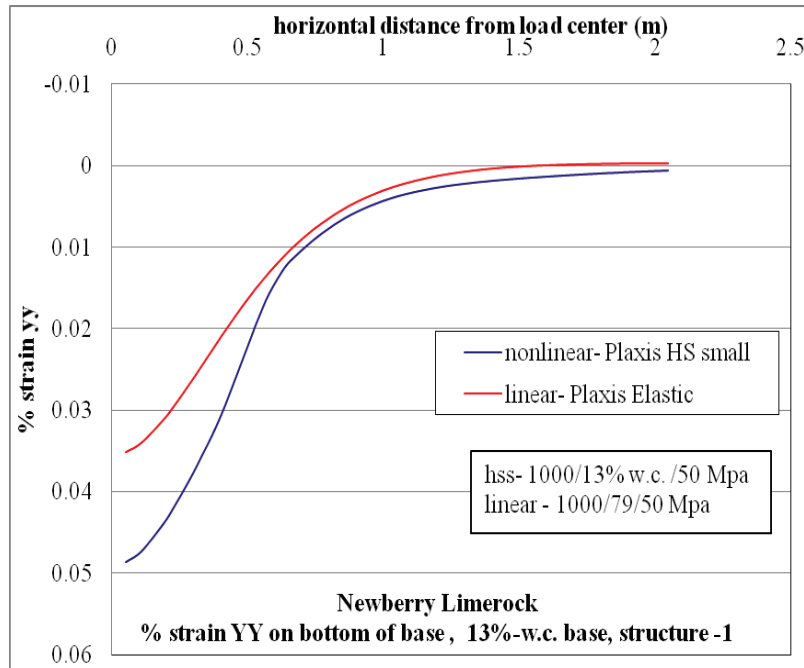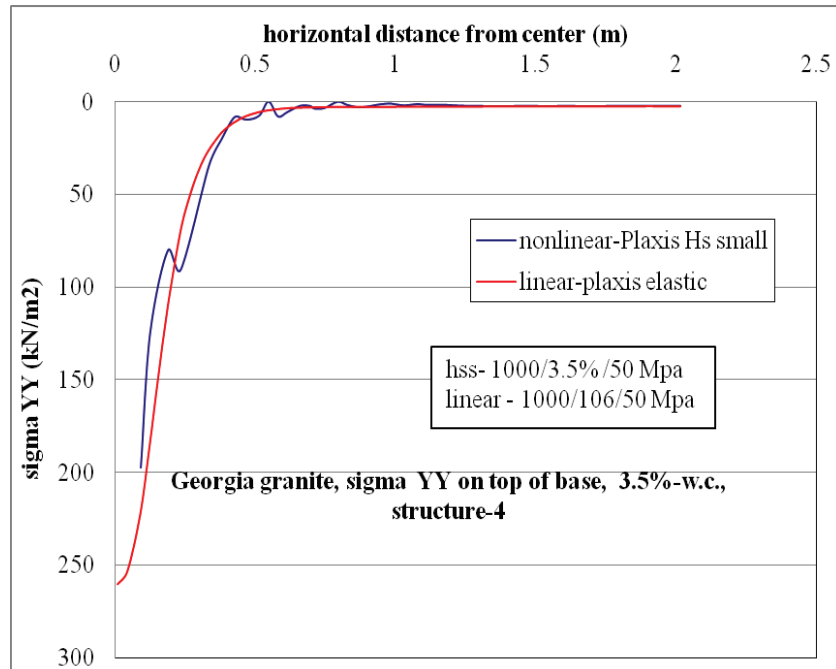

Figure C-65. ε$_{yy}$ at bottom of base layer comparison for nonlinear and linear cases, for Structure-1 with 13% w.c. base layer.
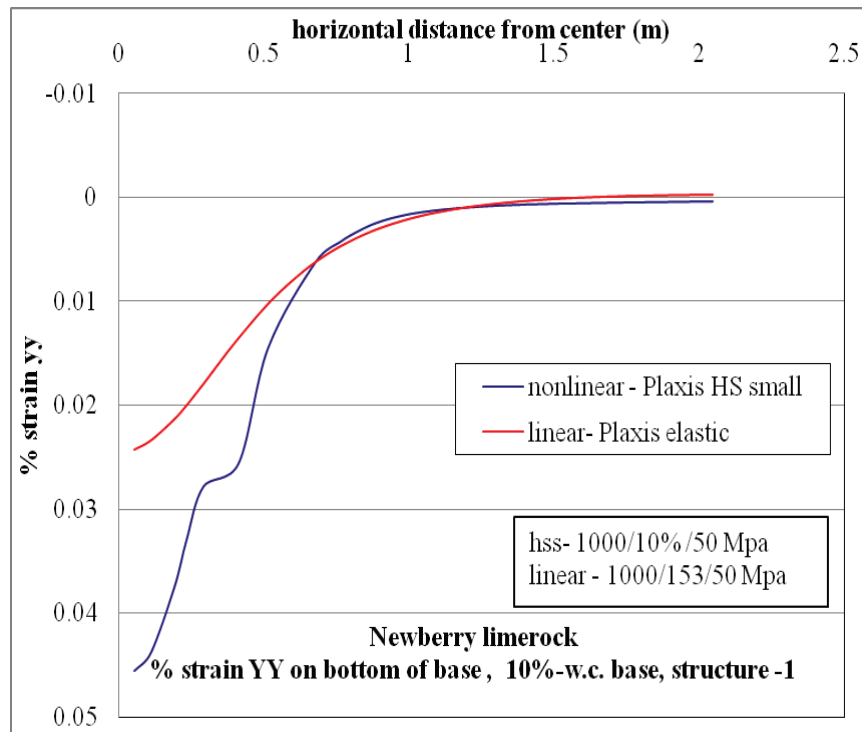
Figure C-66. ε$_{yy}$ at bottom of base layer comparison for nonlinear and linear cases, for Structure-1 with 10% w.c. base layer.
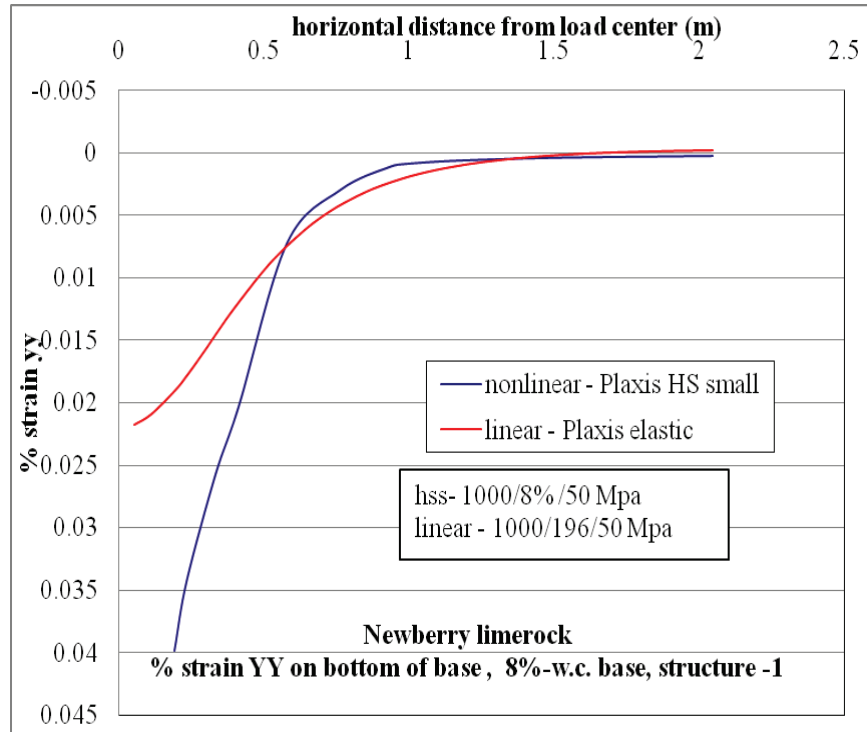
Figure C-67. ε_{yy} at bottom of base layer comparison for nonlinear and linear cases, for Structure-1 with 8% w.c. base layer.
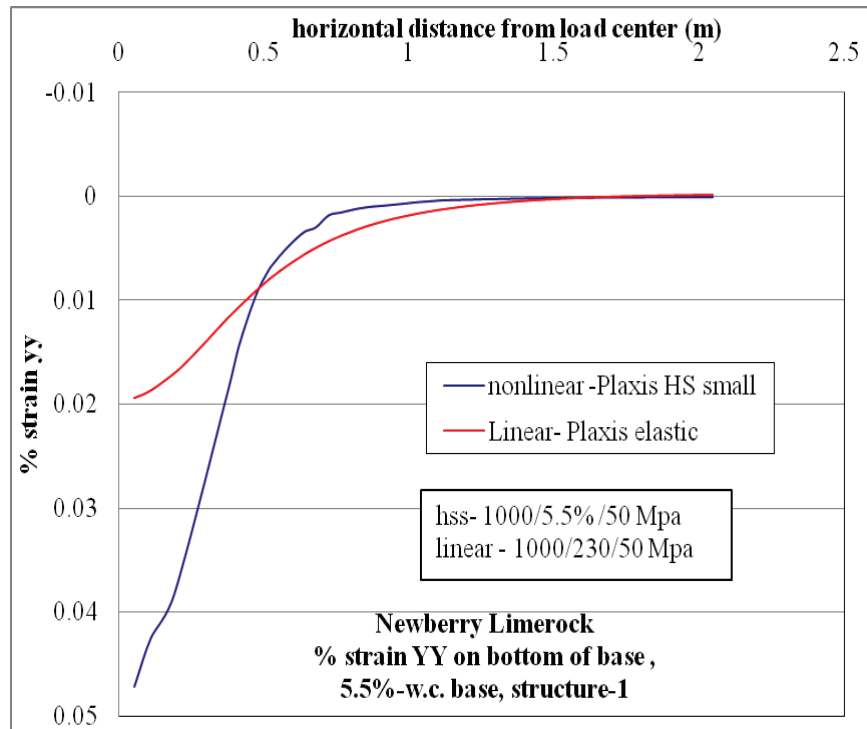
Figure C-68. ε_{yy} at bottom of base layer comparison for nonlinear and linear cases, for Structure-1 with 5.5% w.c. base layer.
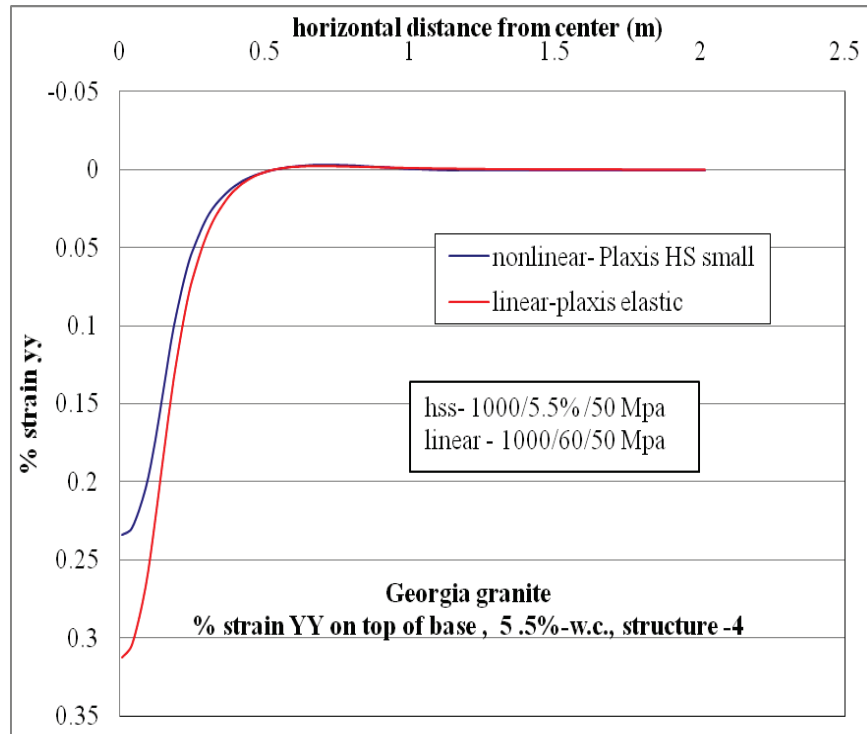
C.1.9.2 Structure-4
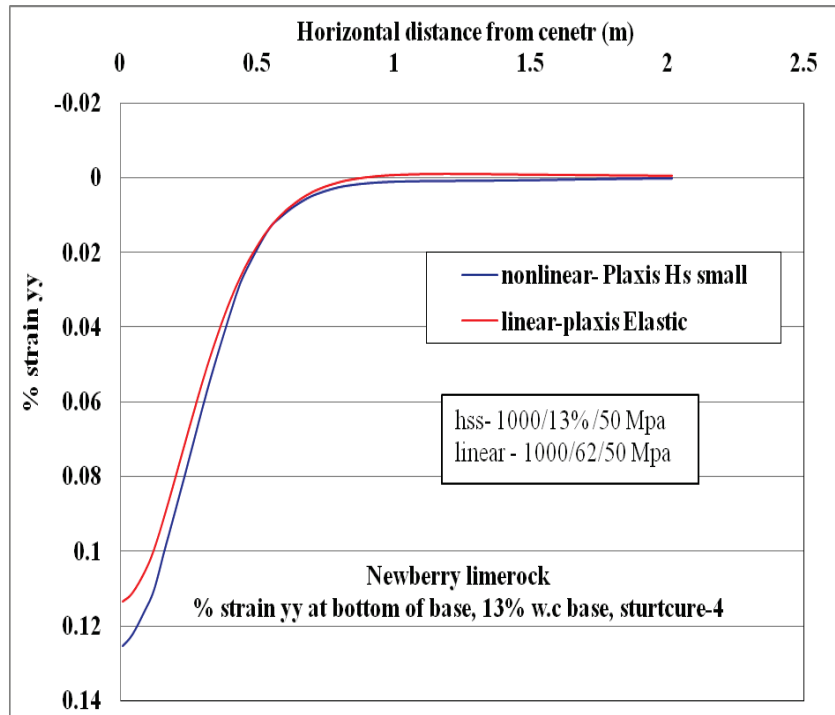
Figure C-69. ε_{yy} at bottom of base layer comparison for nonlinear and linear cases, for Structure-4 with 13% w.c. base layer.
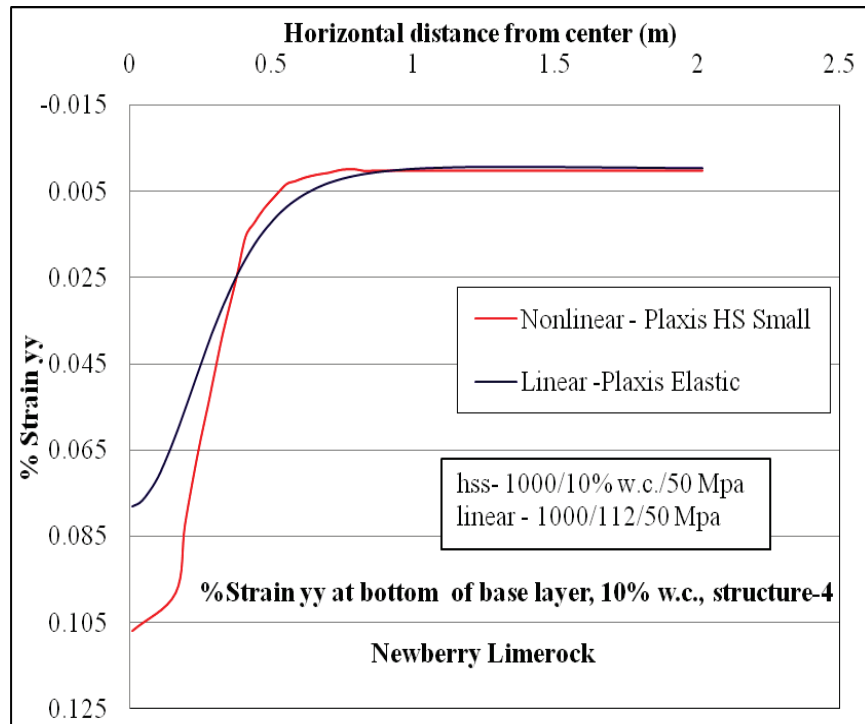
Figure C-70. ε_{yy} at bottom of base layer comparison for nonlinear and linear cases, for Structure-4 with 10% w.c. base layer.
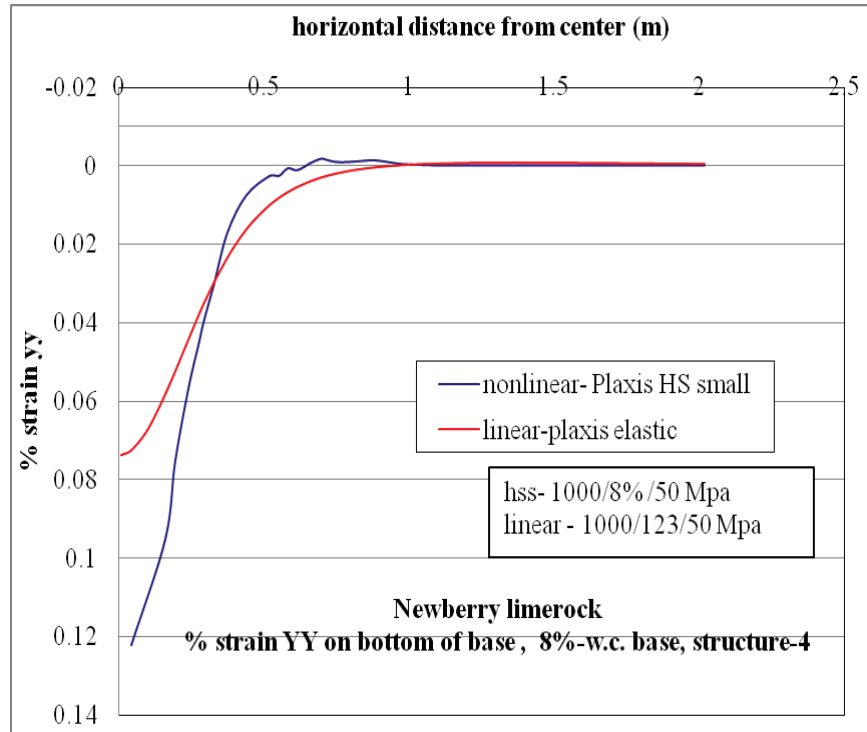
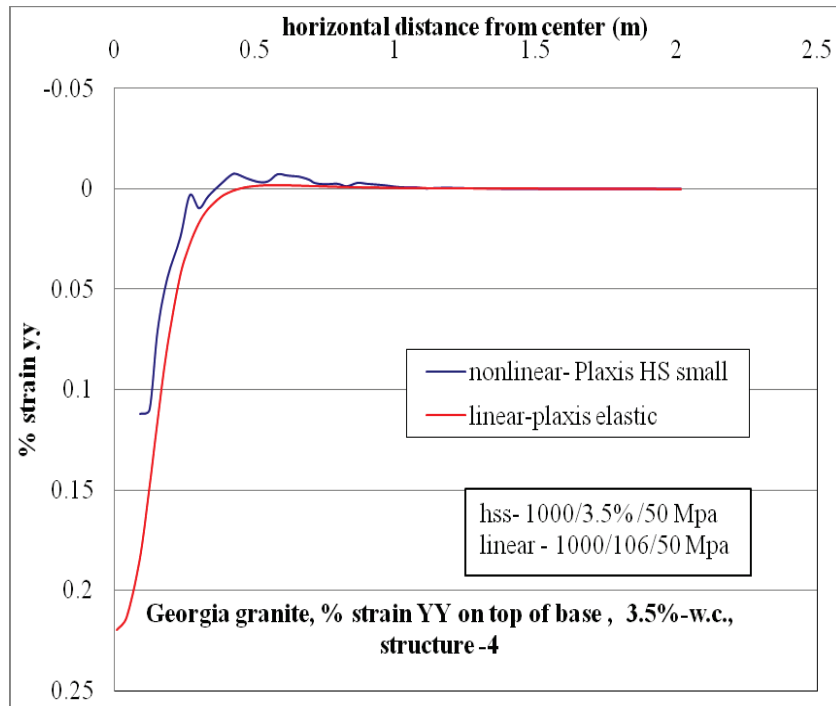Figure C-71. ε_{yy} at bottom of base layer comparison for nonlinear and linear cases, for Structure-4 with 8% w.c. base layer.
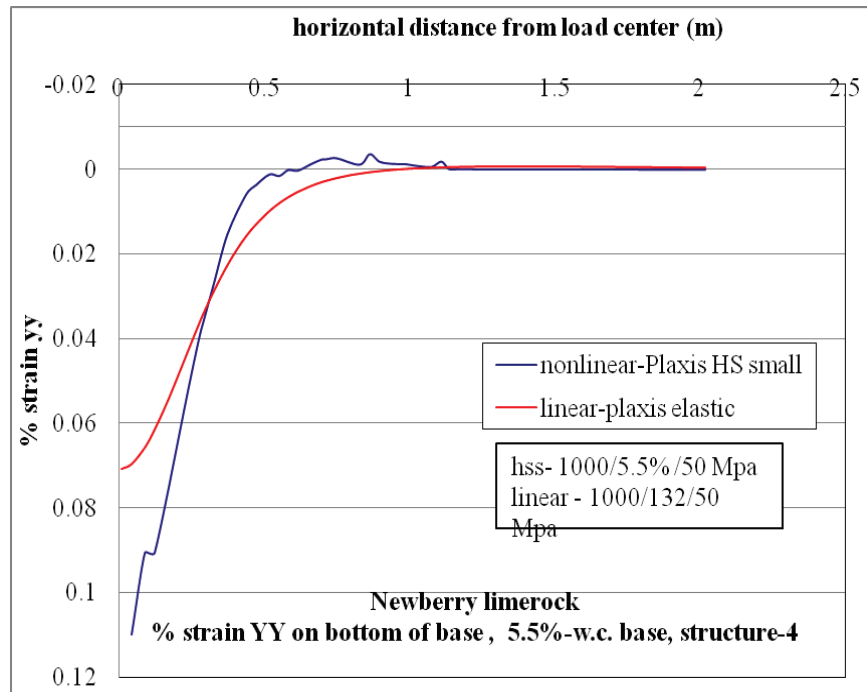
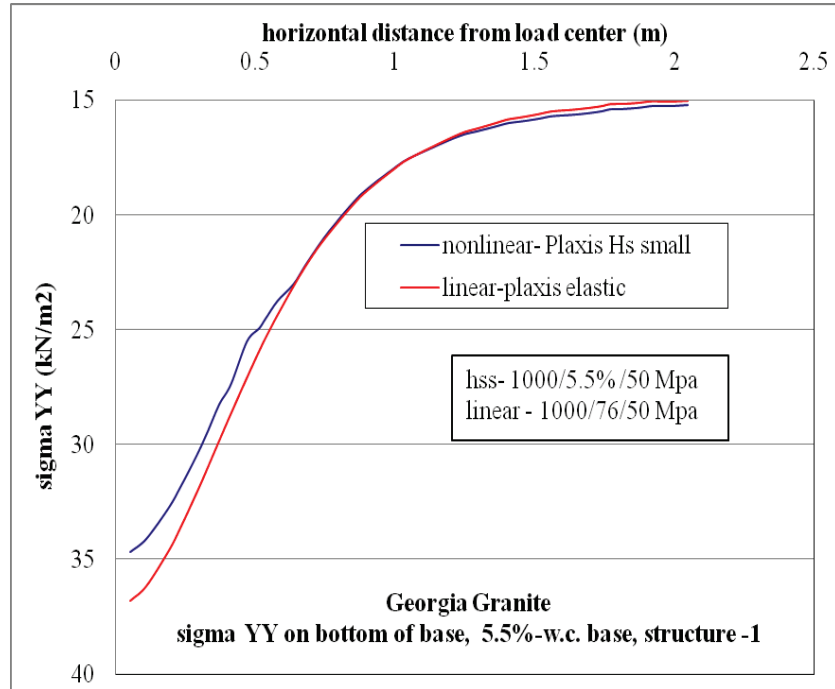

Figure C-72. ε_{yy} at bottom of base layer comparison for nonlinear and linear cases, for Structure-4 with 5.5% w.c. base layer.

C.1.10 Vertical Stress (σ$_{yy}$, Compressive Stress) at Top of Subgrade Layer

C.1.10.1 Structure-1
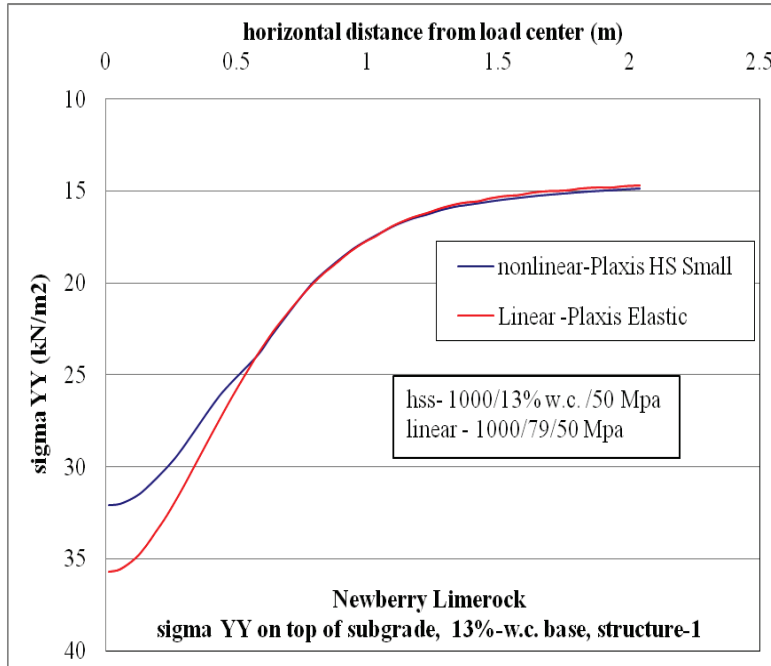
Figure C-73. σ$_{yy}$ at top of subgrade comparison for nonlinear and linear cases, for Structure-1 with 13% w.c. base layer.

Figure C-74. σ$_{yy}$ at top of subgrade comparison for nonlinear and linear cases, for Structure-1 with 10% w.c. base layer.

Figure C-75. σ_{yy} at top of subgrade comparison for nonlinear and linear cases, for Structure-1 with 8% w.c. base layer.
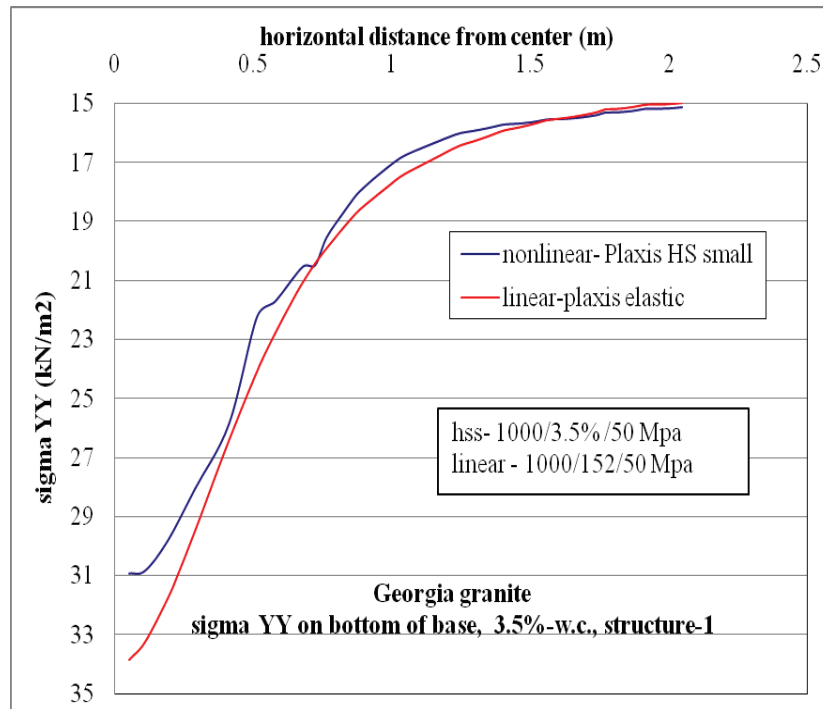

Figure C-76. σ_{yy} at top of subgrade comparison for nonlinear and linear cases, for Structure-1 with 5.5% w.c. base layer.

C.1.10.2 Structure-4
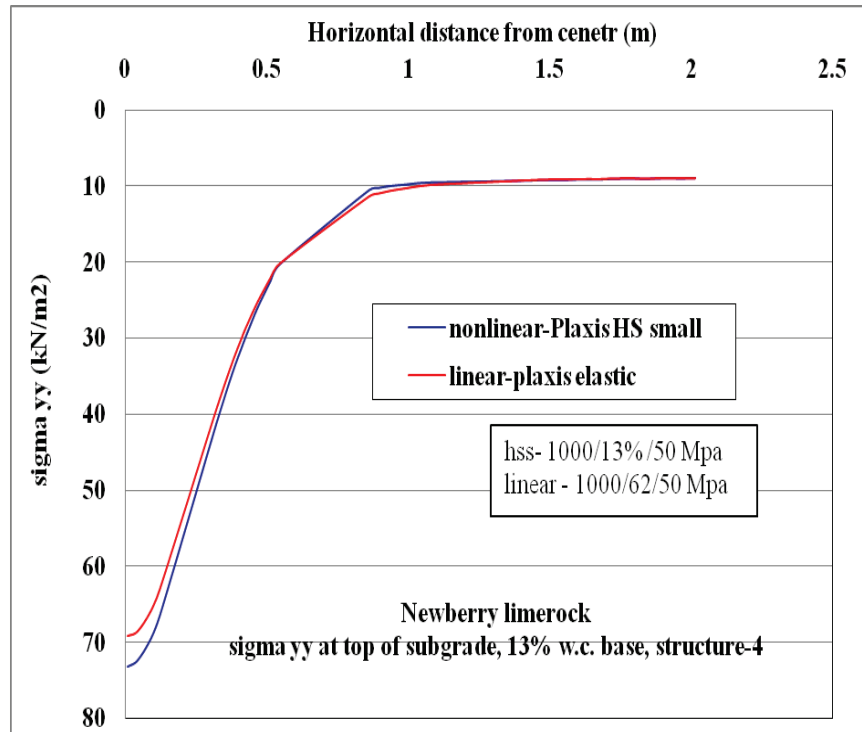
Figure C-77. σ_{yy} at top of subgrade comparison for nonlinear and linear cases, for Structure-4 with 13% w.c. base layer.
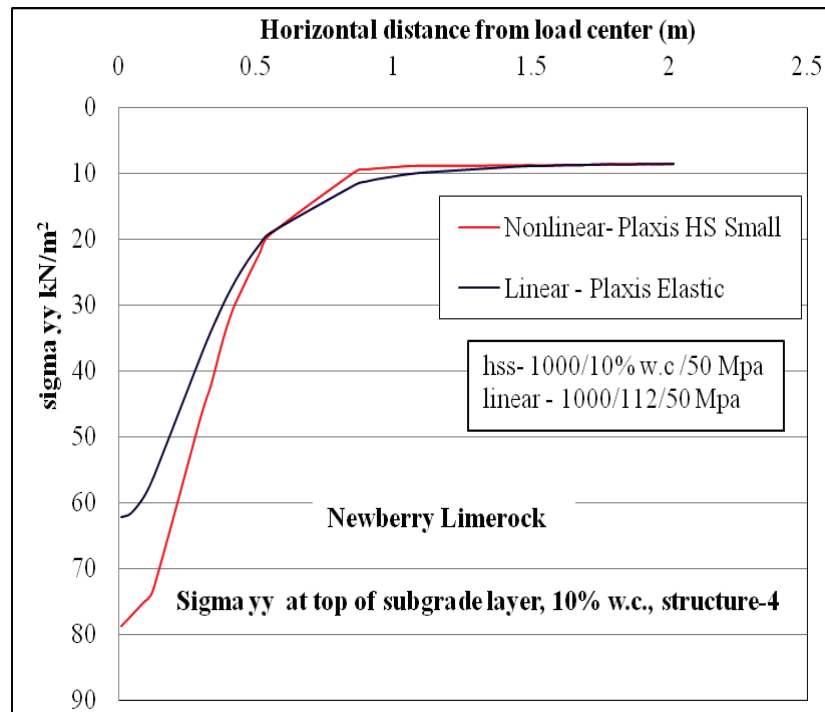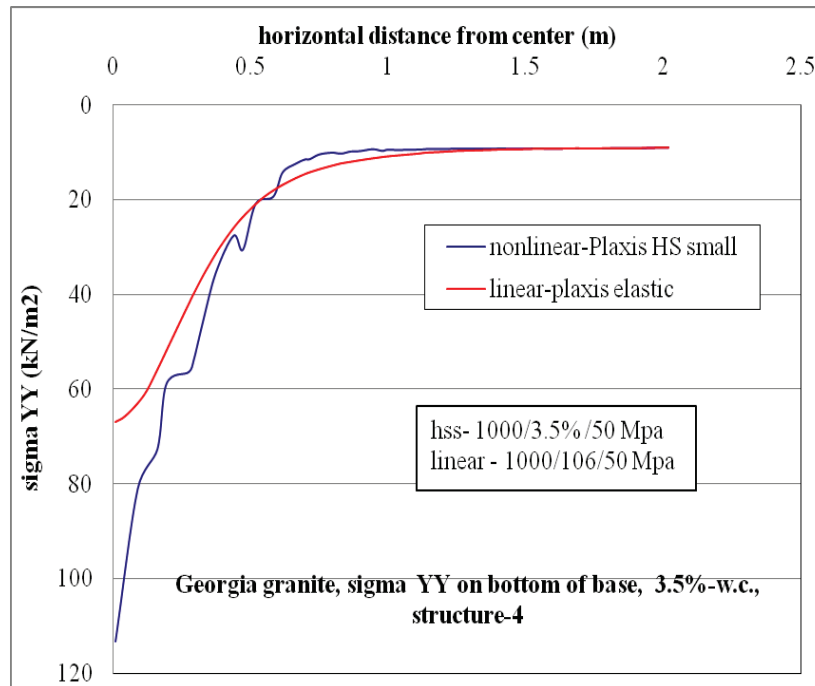

Figure C-78. σ_{yy} at top of subgrade comparison for nonlinear and linear cases, for Structure-4 with 10% w.c. base layer.
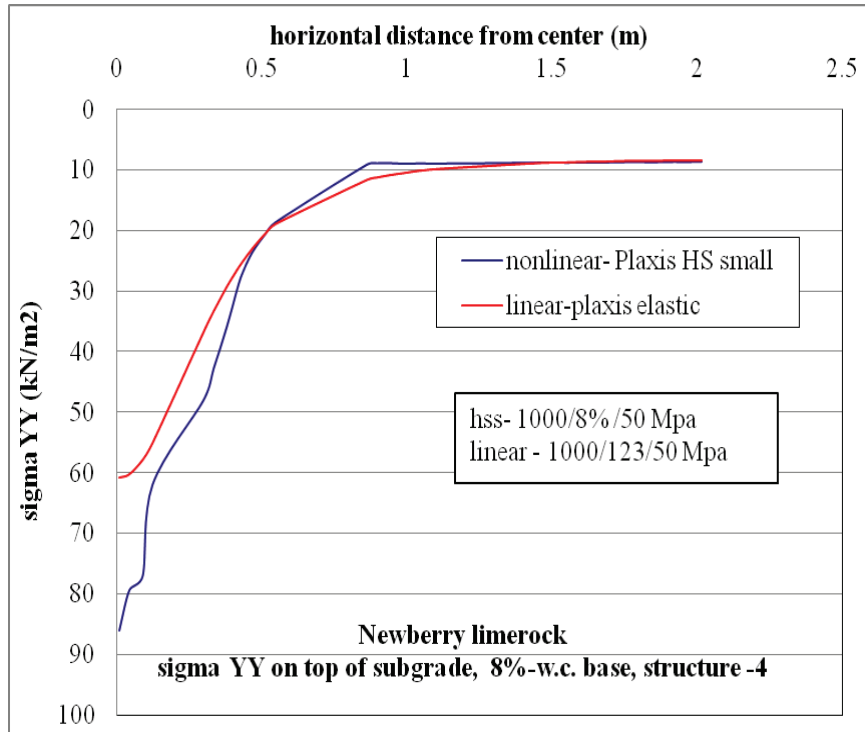
Figure C-79. σ_{yy} at top of subgrade comparison for nonlinear and linear cases, for Structure-4 with 8% w.c. base layer.

Figure C-80. σ_{yy} at top of subgrade comparison for nonlinear and linear cases, for Structure-4 with 5.5% w.c. base layer.

C.1.11 Vertical Strain (ε_{yy}, Compressive Strain) at Top of Subgrade Layer
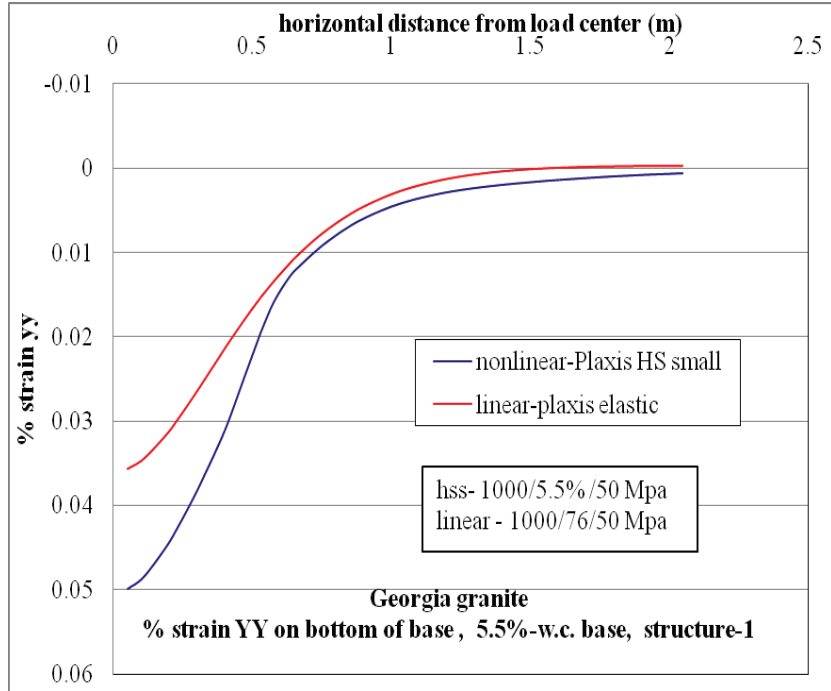
C.1.11.1 Structure-1

Figure C-81. ε_{yy} at top of subgrade layer comparison for nonlinear and linear cases for Structure-1 with 13% w.c. base layer.
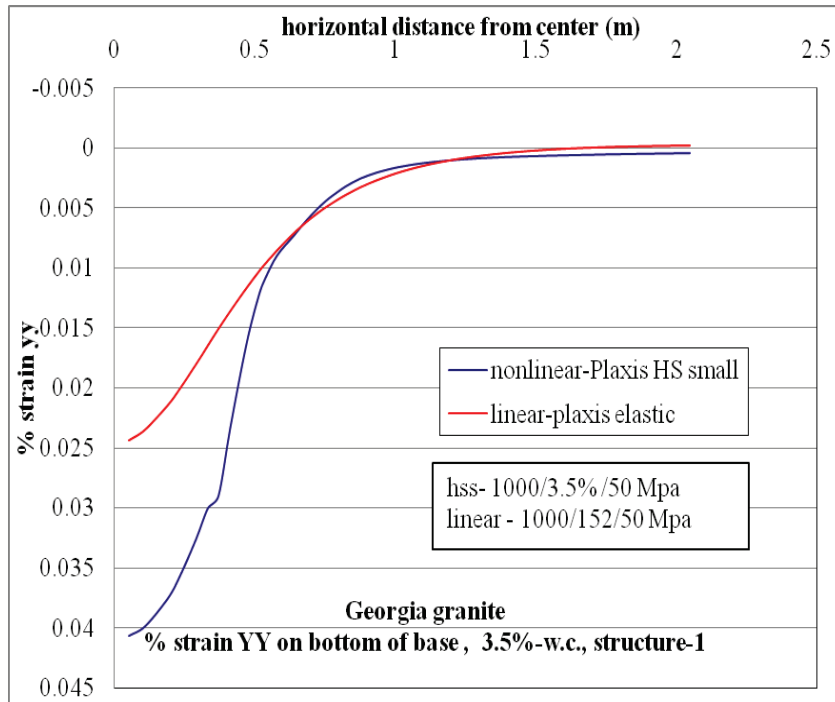

Figure C-82. ε_{yy} at top of subgrade layer comparison for nonlinear and linear cases for Structure-1 with 10% w.c. base layer.

Figure C-83. ε_{yy} at top of subgrade layer comparison for nonlinear and linear cases for Structure-1 with 8% w.c. base layer.

Figure C-84. ε_{yy} at top of subgrade layer comparison for nonlinear and linear cases for Structure-1 with 5.5% w.c. base layer.
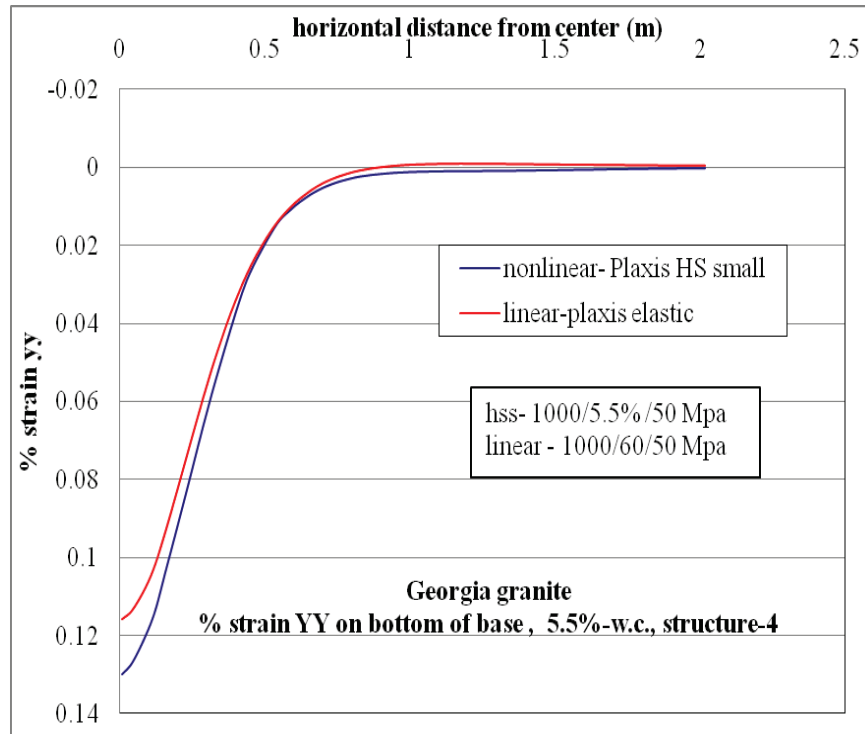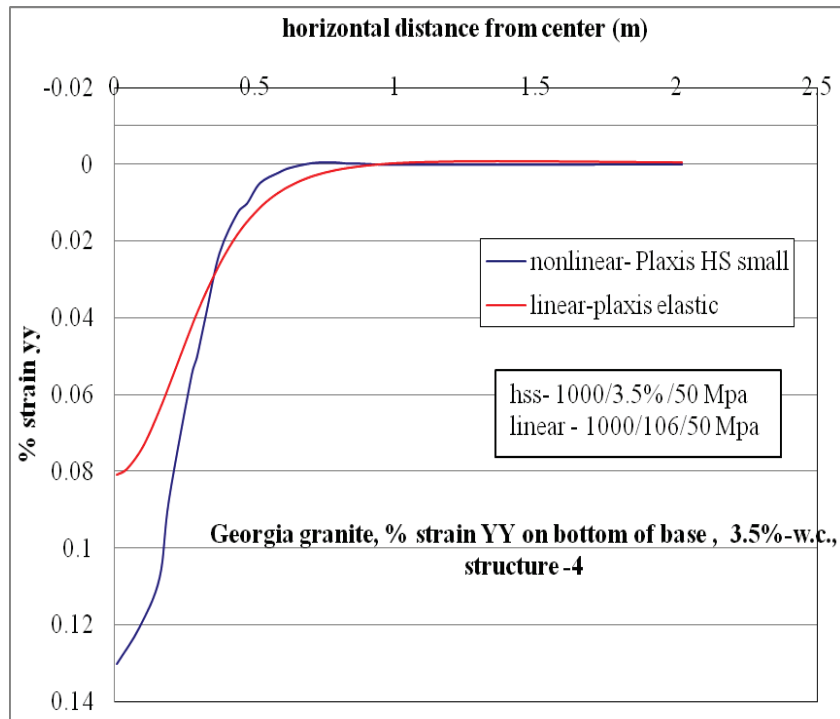
C.1.11.2 Structure-4

Figure C-85. ε_{yy} at top of subgrade layer comparison for nonlinear and linear cases for Structure-4 with 13% w.c. base layer.

Figure C-86. ε_{yy} at top of subgrade layer comparison for nonlinear and linear cases for Structure-4 with 10% w.c. base layer.
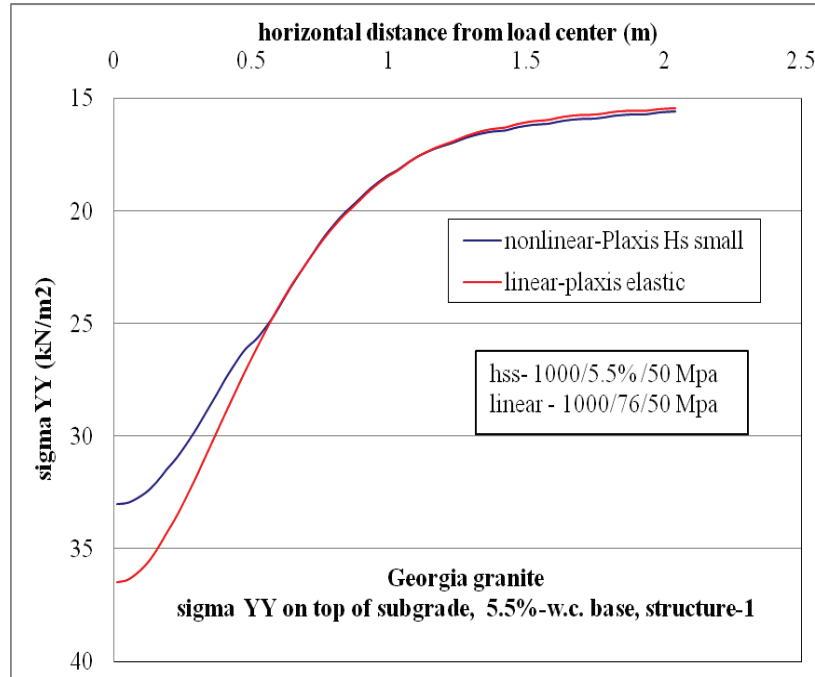
Figure C-87. ε_{yy} at top of subgrade layer comparison for nonlinear and linear cases for Structure-4 with 8% w.c. base layer.

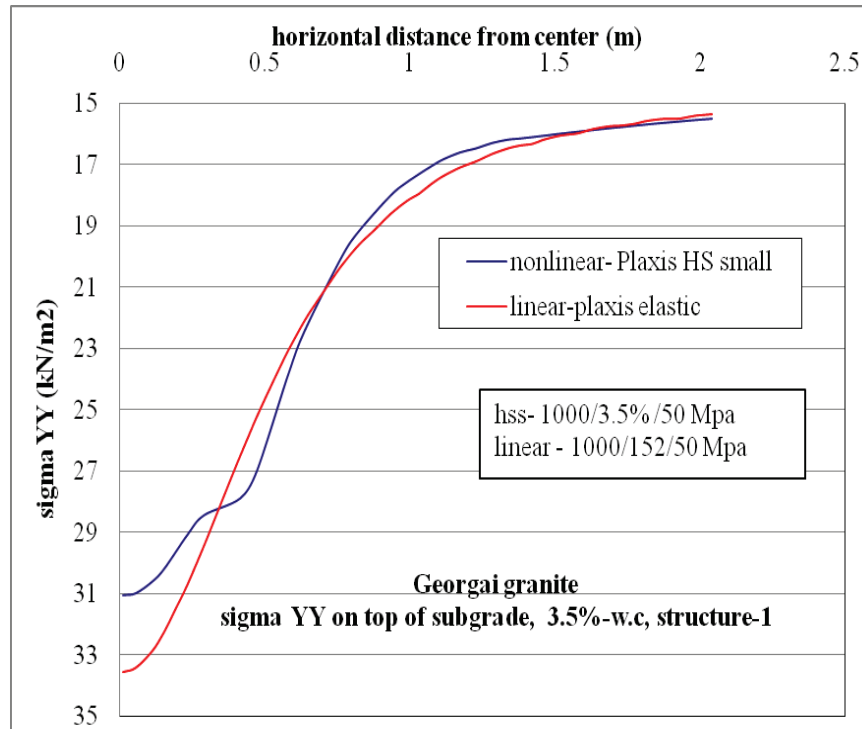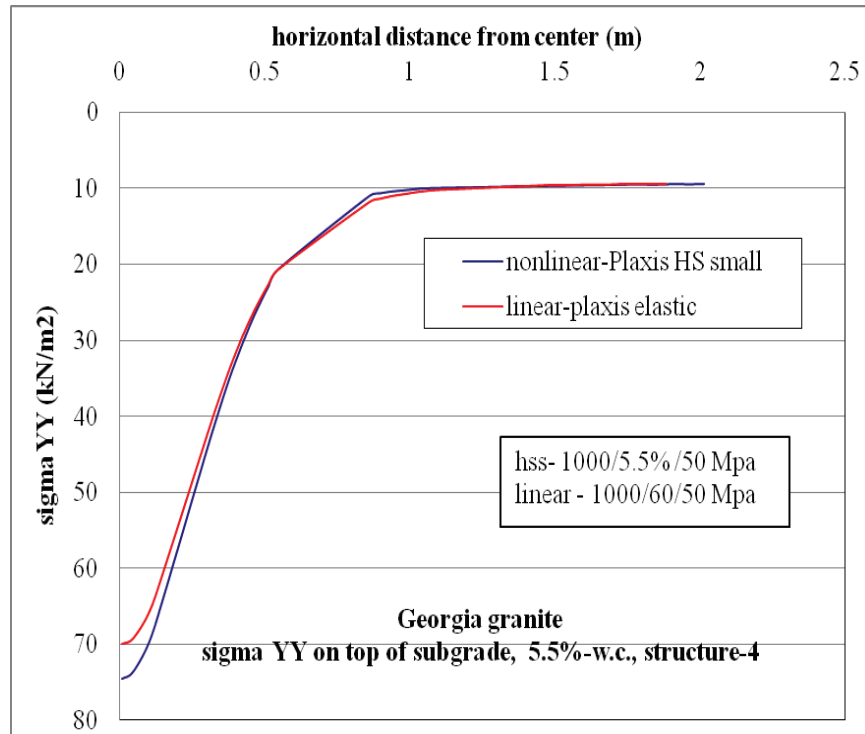

Figure C-88. ε_{yy} at top of subgrade layer comparison for nonlinear and linear cases for Structure-4 with 5.5% w.c. base layer.

209

C.2 Georgia Granite

C.2.1 Surface Deflection Profiles

C.2.1.1 Structure-1
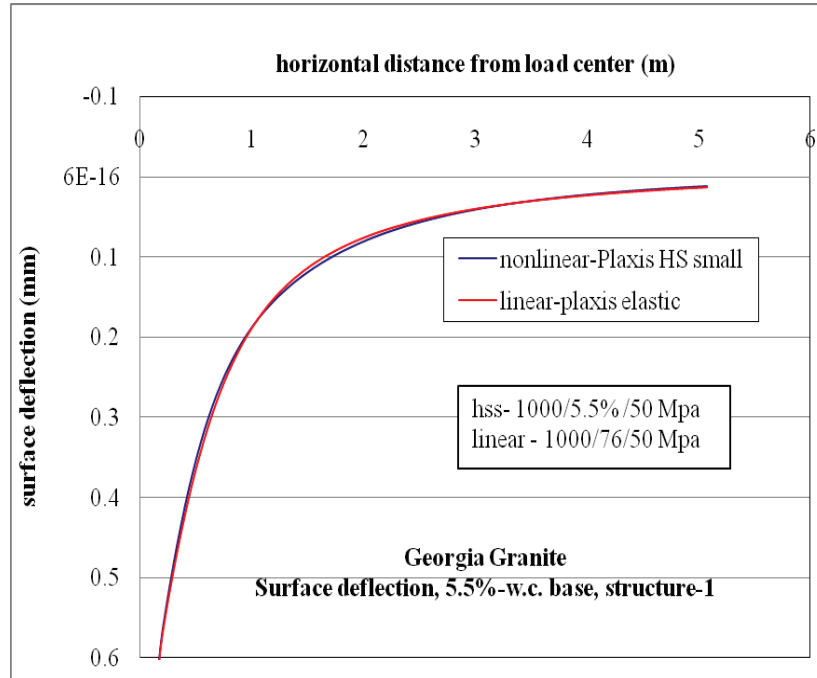
Figure C-89. Surface deflection comparison for nonlinear and linear cases, for Structure-1 with 5.5% w.c. base layer.

Figure C-90. Surface deflection comparison for nonlinear and linear cases, for Structure-1 with 3.5% w.c. base layer.

C.2.1.2 Structure-4
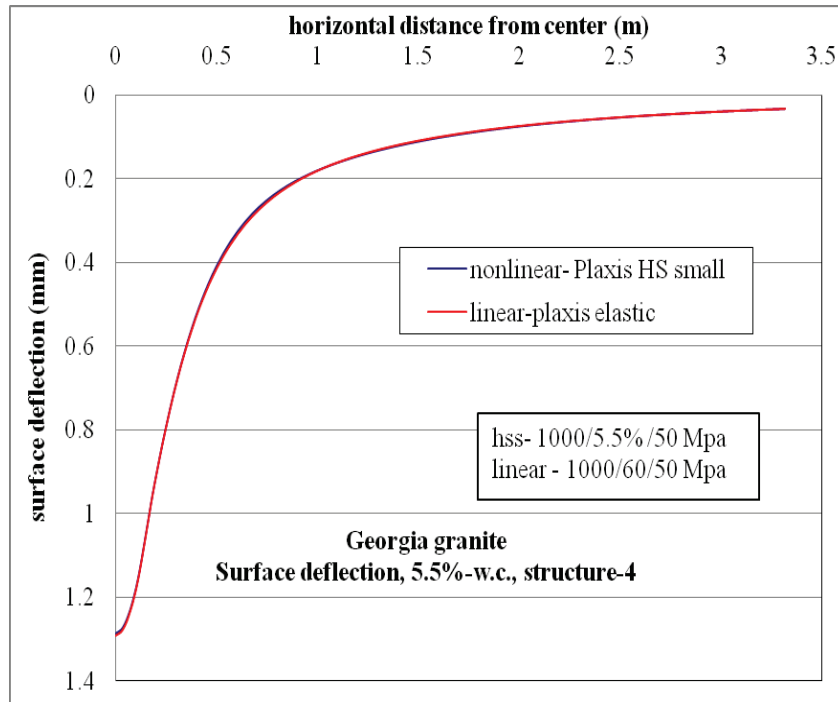
Figure C-91. Surface deflection comparison for nonlinear and linear cases, for Structure-4 with 5.5% w.c. base layer.

Figure C-92. Surface deflection comparison for nonlinear and linear cases, for Structure-4 with 3.5% w.c. base layer.

C.2.2   Horizontal Stress (σ$_{xx}$, Tensile Stress) at Top of AC Layer

C.2.2.1 Structure-1

Figure C-93. σ$_{xx}$ at top of AC layer comparison for nonlinear and linear cases, for Structure-1 with 5.5% w.c. base layer.
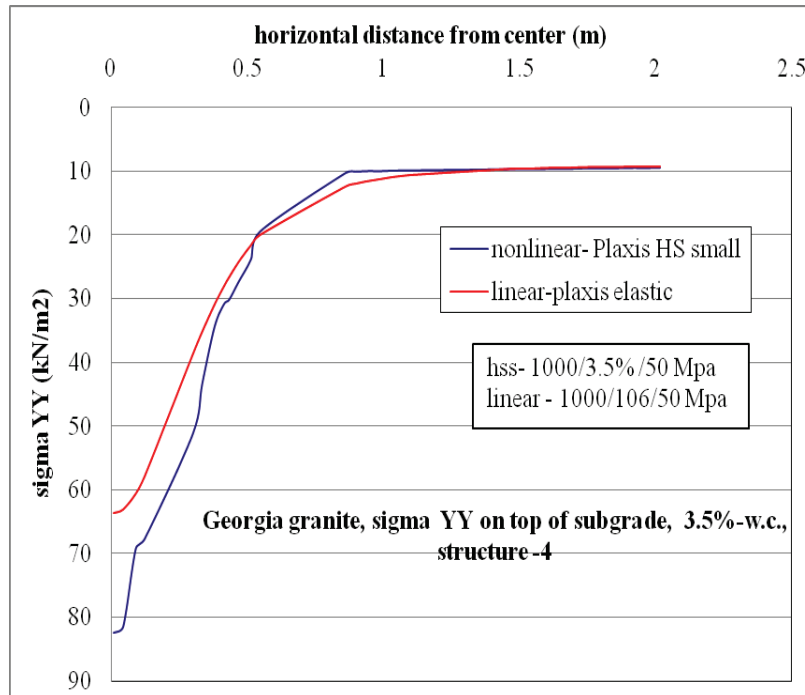

Figure C-94. σ$_{xx}$ at top of AC layer comparison for nonlinear and linear cases, for Structure-1 with 3.5% w.c. base layer.
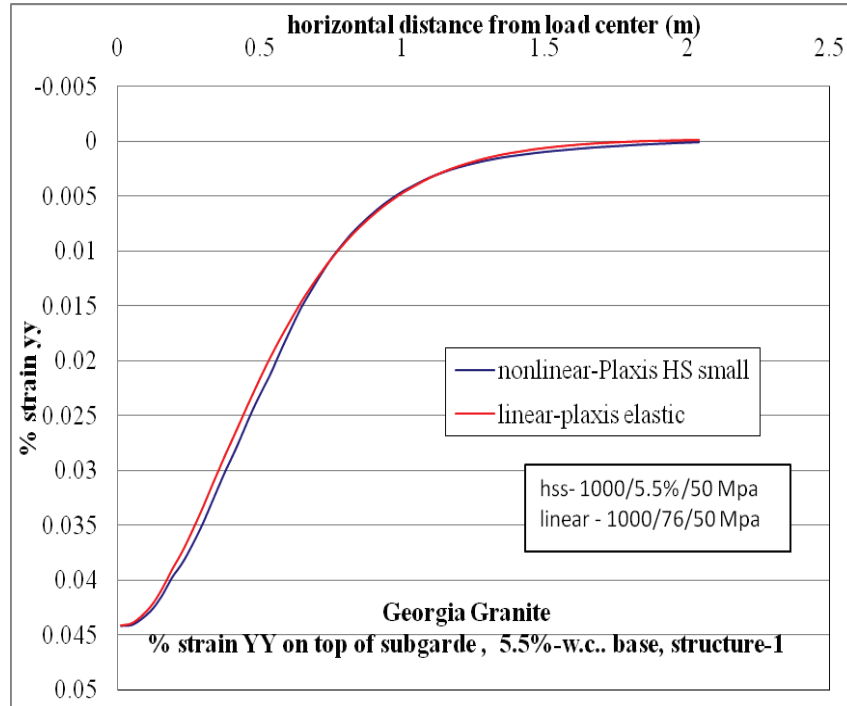
C.2.2.2 Strcutrue-4

Figure C-95. σ_{xx} at top of AC layer comparison for nonlinear and linear cases, for Structure-4
with 5.5% w.c. base layer.

Figure C-96. σ_{xx} at top of AC layer comparison for nonlinear and linear cases, for Structure-4
with 3.5% w.c. base layer.

C.2.3   Horizontal Strain (ε_{xx}, Tensile Strain) at Top of AC Layer

C.2.3.1 Structure-1

Figure C-97. ε_{xx} at top of AC layer comparison for nonlinear and linear cases, for Structure-1 with 5.5% w.c. base layer.
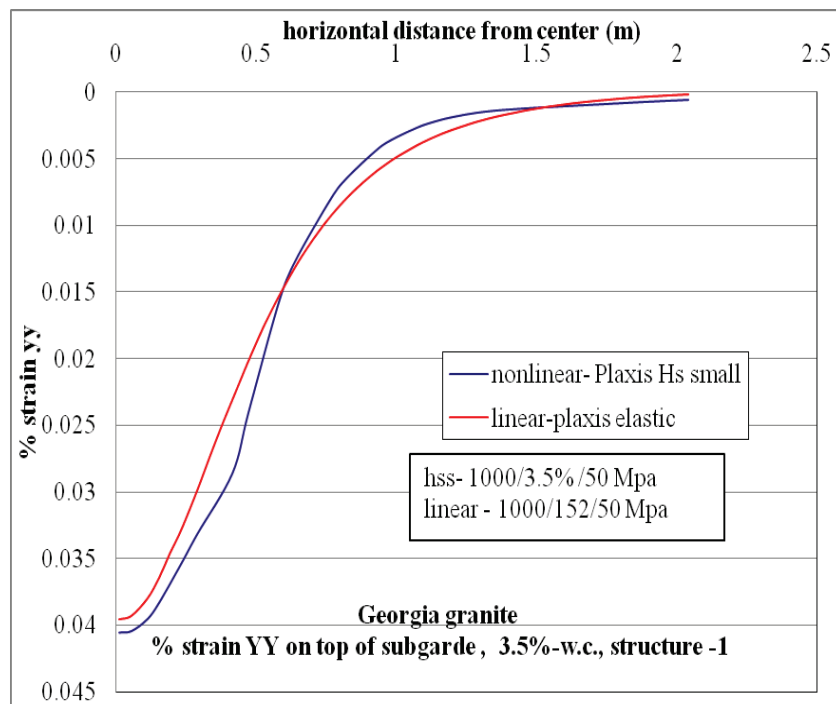

Figure C-98. ε_{xx} at top of AC layer comparison for nonlinear and linear cases, for Structure-1 with 3.5% w.c. base layer.
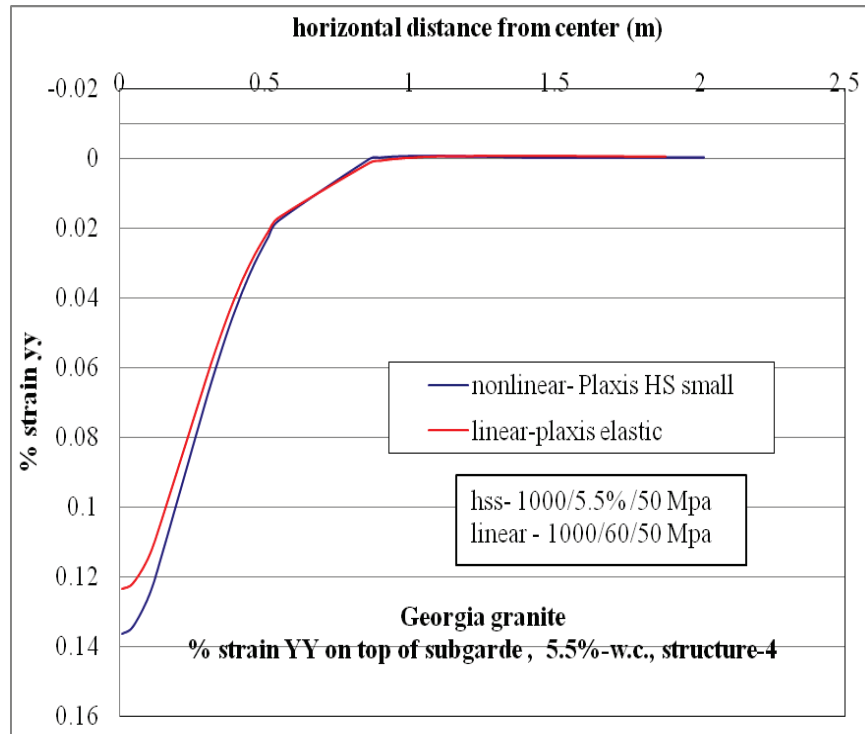
C.2.3.2 Structure-4

Figure C-99. ε_{xx} at top of AC layer comparison for nonlinear and linear cases, for Structure-4 with 5.5% w.c. base layer.
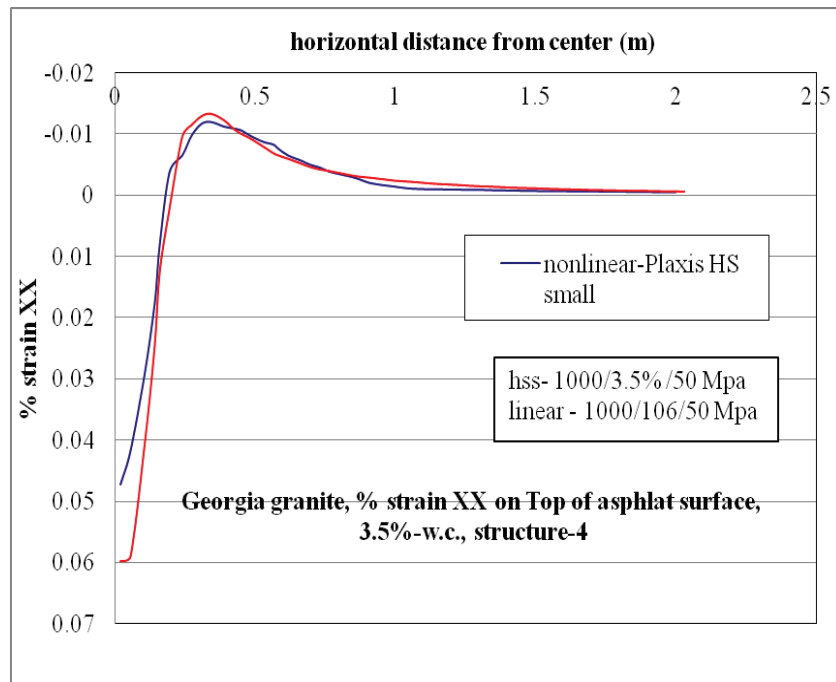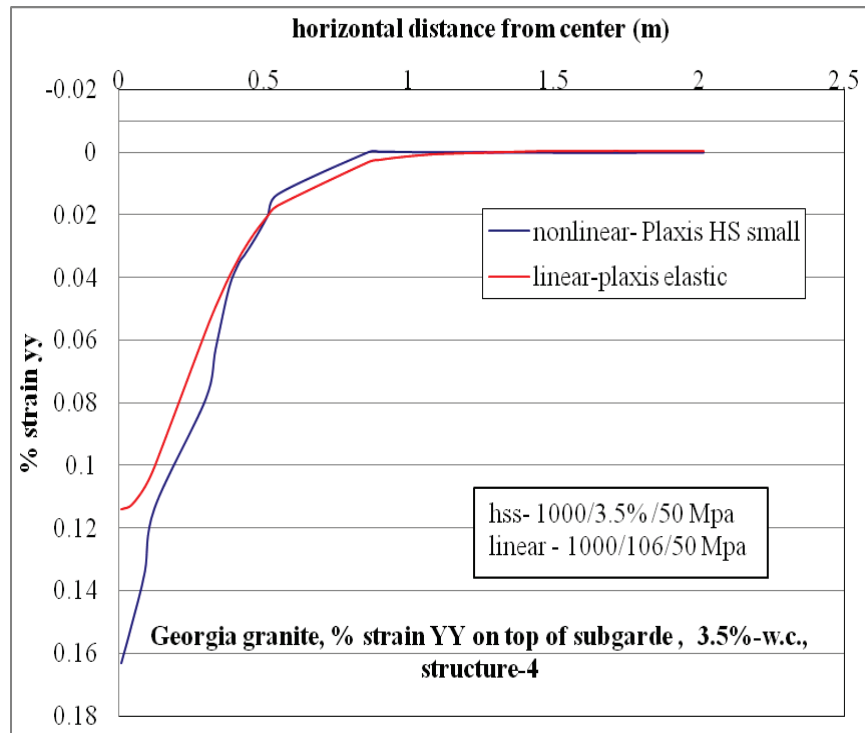

Figure C-100. ε_{xx} at top of AC layer comparison for nonlinear and linear cases, for Structure-4 with 3.5% w.c. base layer.

C.2.4 Horizontal Stress (σ$_{xx}$, Tensile Stress) at Bottom of AC Layer

C.2.4.1 Structure-1
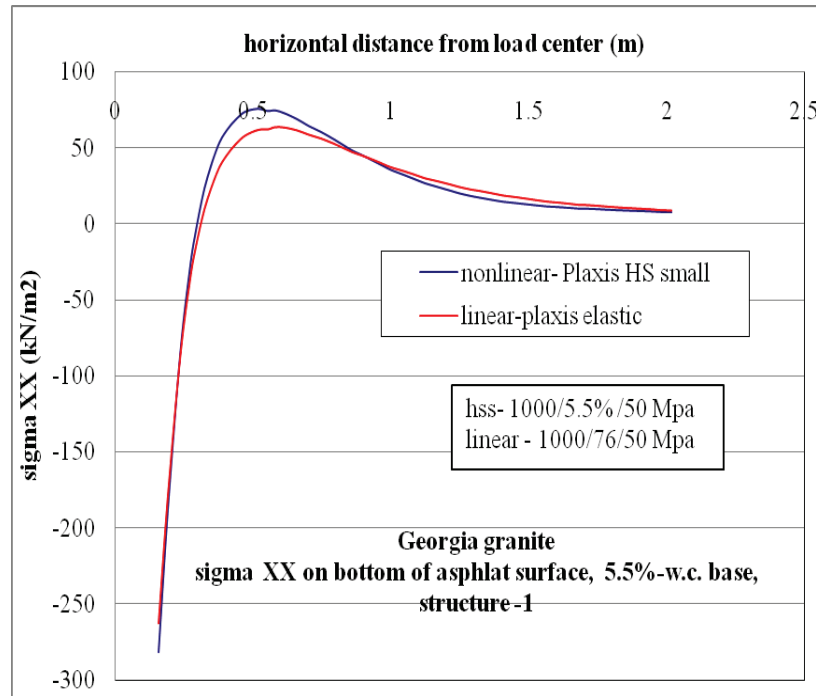
Figure C-101. σ$_{xx}$ at bottom of AC layer comparison for nonlinear and linear cases, for Structure-1 with 5.5% w.c. base layer.

Figure C-102. σ$_{xx}$ at bottom of AC layer comparison for nonlinear and linear cases, for Structure-1 with 3.5% w.c. base layer.

216

Figure C-103. σ_{xx} at bottom of AC layer comparison for nonlinear and linear cases, for Structure-4 with 5.5% w.c. base layer.

Figure C-104. σ_{xx} at bottom of AC layer comparison for nonlinear and linear cases, for Structure-4 with 3.5% w.c. base layer.

C.2.5. Horizontal Strain (ε_{xx}, Tensile Strain) at Bottom of AC Layer

C.2.5.1 Structure-1

Figure C-105. ε_{xx} at bottom of AC layer comparison for nonlinear and linear cases, for Structure-1 with 5.5% w.c. base layer.

Figure C-106. ε_{xx} at bottom of AC layer comparison for nonlinear and linear cases, for Structure-1 with 3.5% w.c. base layer.

C.2.5.2 Structure-4

Figure C-107. ε_{xx} at bottom of AC layer comparison for nonlinear and linear cases, for Structure-4 with 5.5% w.c. base layer.

Figure C-108. ε_{xx} at bottom of AC layer comparison for nonlinear and linear cases, for Structure-4 with 3.5% w.c. base layer.

C.2.6 Vertical Stress (σ_yy, Compressive Stress) at Top of Base Layer

C.2.6.1 Structure-1

Figure C-109. σ_{yy} vertical stress at top of base layer comparison for nonlinear and linear cases, for Structure-1 with 5.5% w.c. base layer.

Figure C-110. σ_{yy} vertical stress at top of base layer comparison for nonlinear and linear cases, for Structure-1 with 3.5% w.c. base layer.

C.2.6.2 Structure-4

Figure C-111. σ_{yy} vertical stress at top of base layer comparison for nonlinear and linear cases, for Structure-4 with 5.5% w.c. base layer.

Figure C-112. σ_{yy} vertical stress at top of base layer comparison for nonlinear and linear cases, for Structure-4 with 3.5% w.c. base layer.

C.2.7 Vertical Strain (ε_{yy}, Compressive Strain) at Top of Base Layer
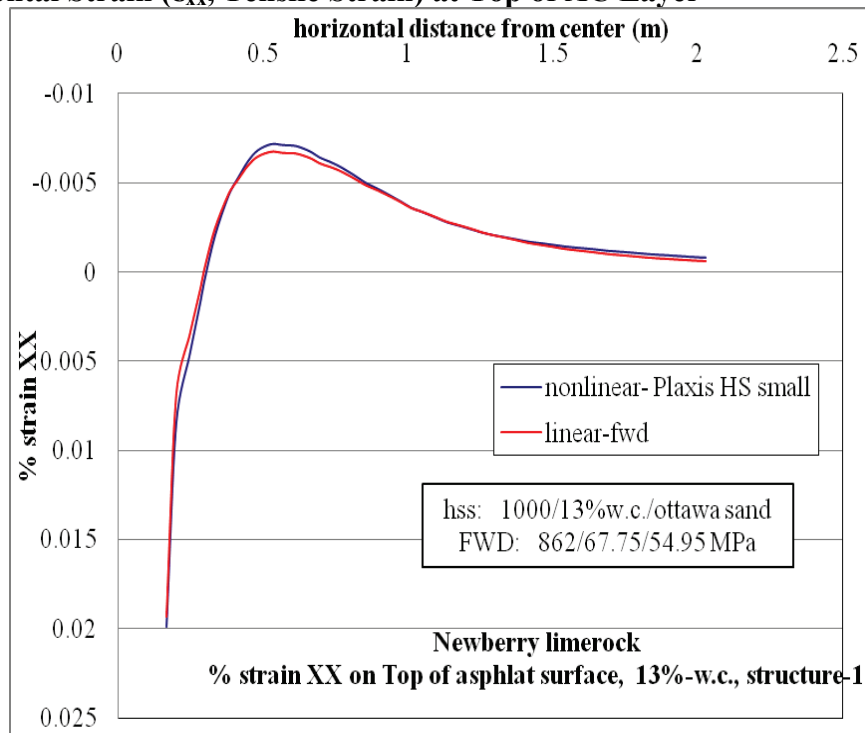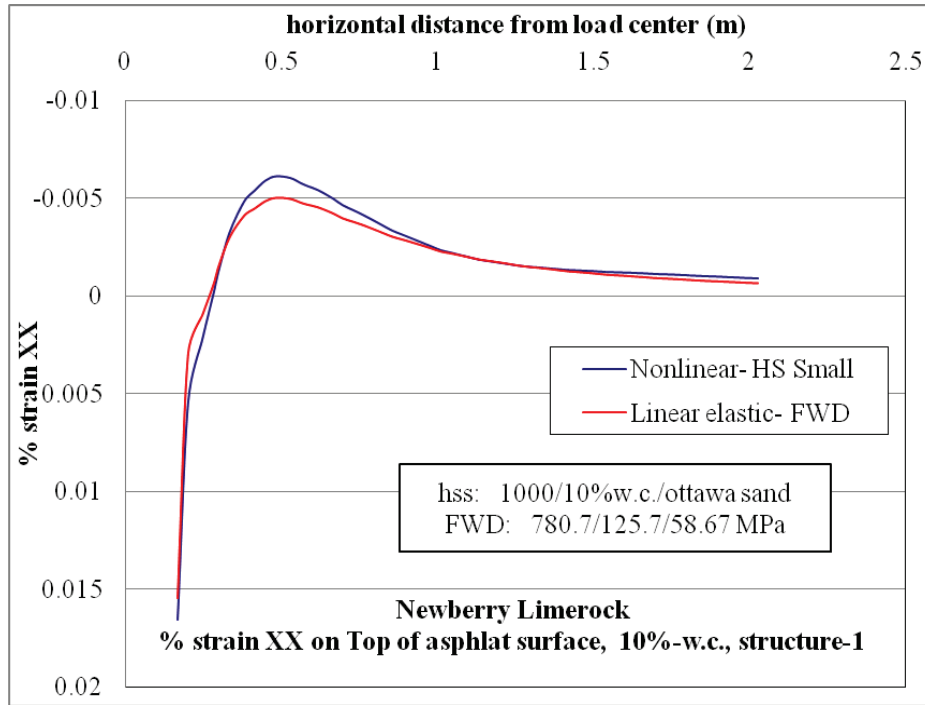
C.2.7.1 Structure-1

Figure C-113. ε_{yy} at top of base layer comparison for nonlinear and linear cases, for Structure-1 with 5.5% w.c. base layer.

Figure C-114. ε_{yy} at top of base layer comparison for nonlinear and linear cases, for Structure-1 with 3.5% w.c. base layer.

C.2.7.2 Structure-4

Figure C-115. ε_{yy} at top of base layer comparison for nonlinear and linear cases, for Structure-4 with 5.5% w.c. base layer.

Figure C-116. ε_{yy} at top of base layer comparison for nonlinear and linear cases, for Structure-4 with 3.5% w.c. base layer.

C.2.8 Vertical Stress (σ$_{yy}$, Compressive Stress) at Bottom of Base Layer

C.2.8.1 Structure-1
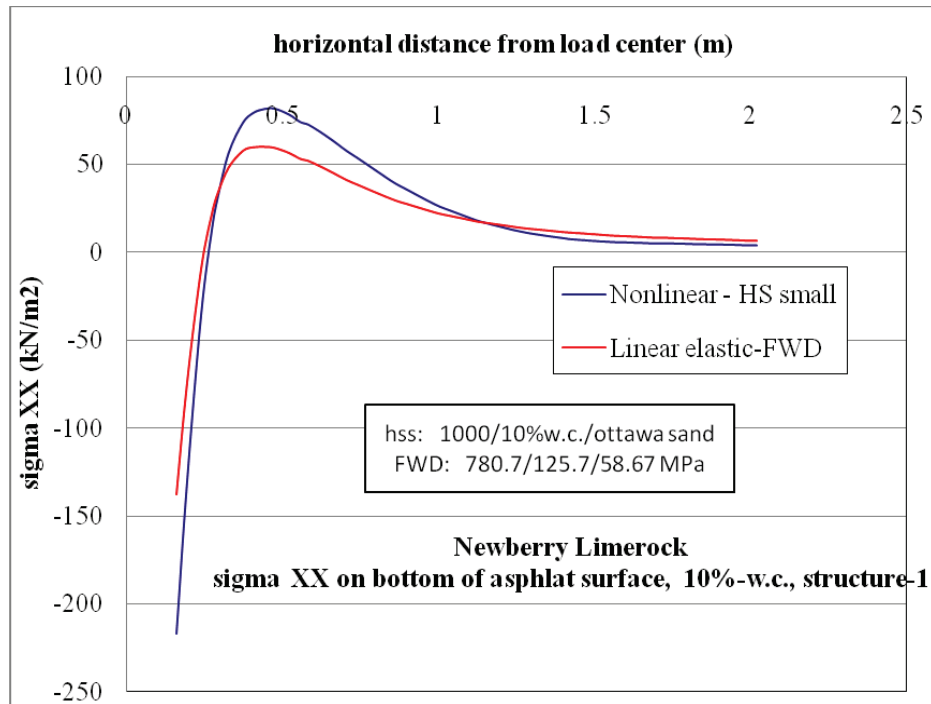

Figure C-117. σ$_{yy}$ at bottom of base layer comparison for nonlinear and linear cases, for Structure-1 with 5.5% w.c. base layer.

Figure C-118. σ$_{yy}$ at bottom of base layer comparison for nonlinear and linear cases, for Structure-1 with 3.5% w.c. base layer.

C.2.8.2 Structure-4
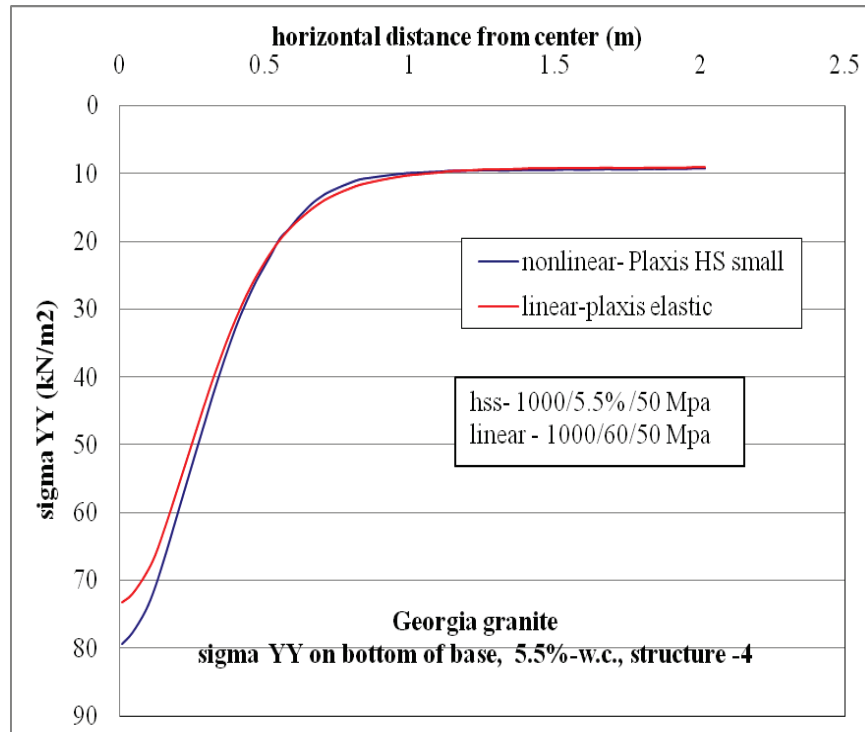
Figure C-119. σ_{yy} at bottom of base layer comparison for nonlinear and linear cases, for Structure-4 with 5.5% w.c. base layer.
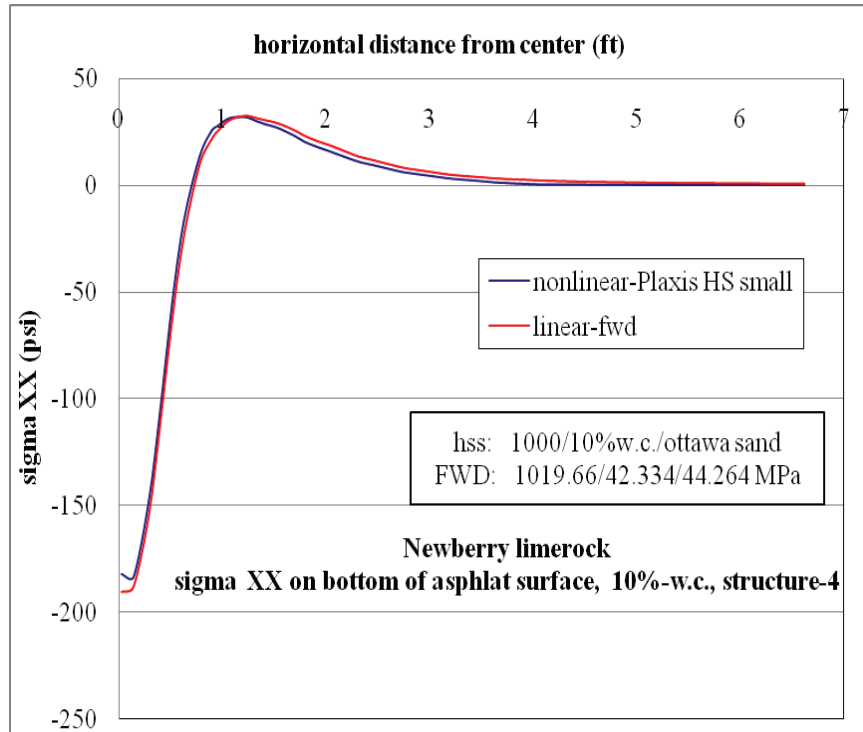

Figure C-120. σ_{yy} at bottom of base layer comparison for nonlinear and linear cases, for Structure-4 with 3.5% w.c. base layer.

C.2.9   Vertical Strain (ε_{yy}, Compressive Strain) at Bottom of Base Layer

C.2.9.1 Structure-1

Figure C-121. ε_{yy} at bottom of base layer comparison for nonlinear and linear cases, for Structure-1 with 5.5% w.c. base layer.
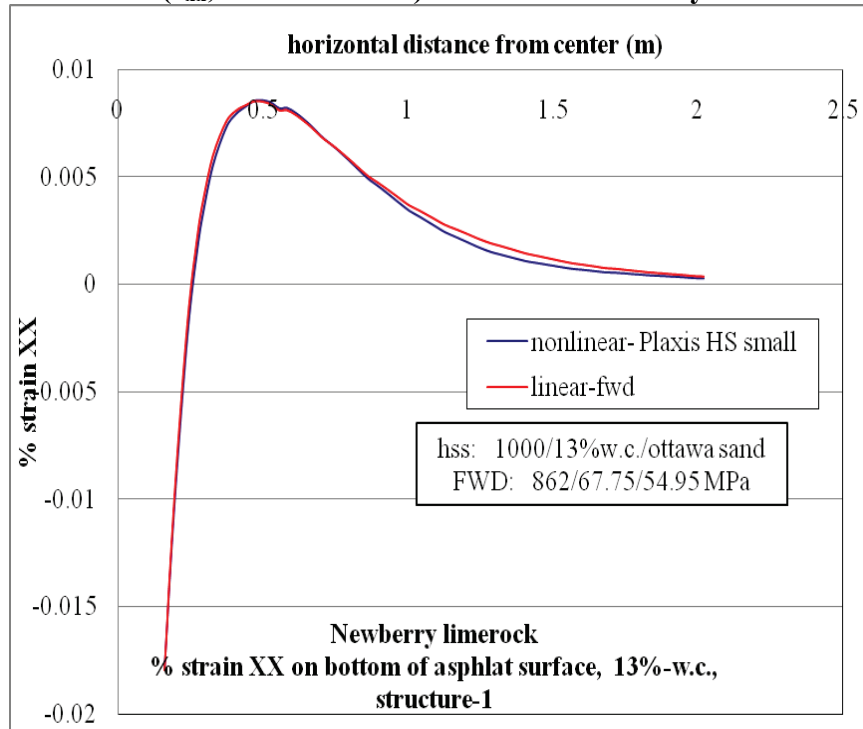

Figure C-122. ε_{yy} at bottom of base layer comparison for nonlinear and linear cases, for Structure-1 with 3.5% w.c. base layer.

C.2.9.2 Structure-4

Figure C-123. ε_{yy} at bottom of base layer comparison for nonlinear and linear cases, for Structure-4 with 5.5% w.c. base layer.

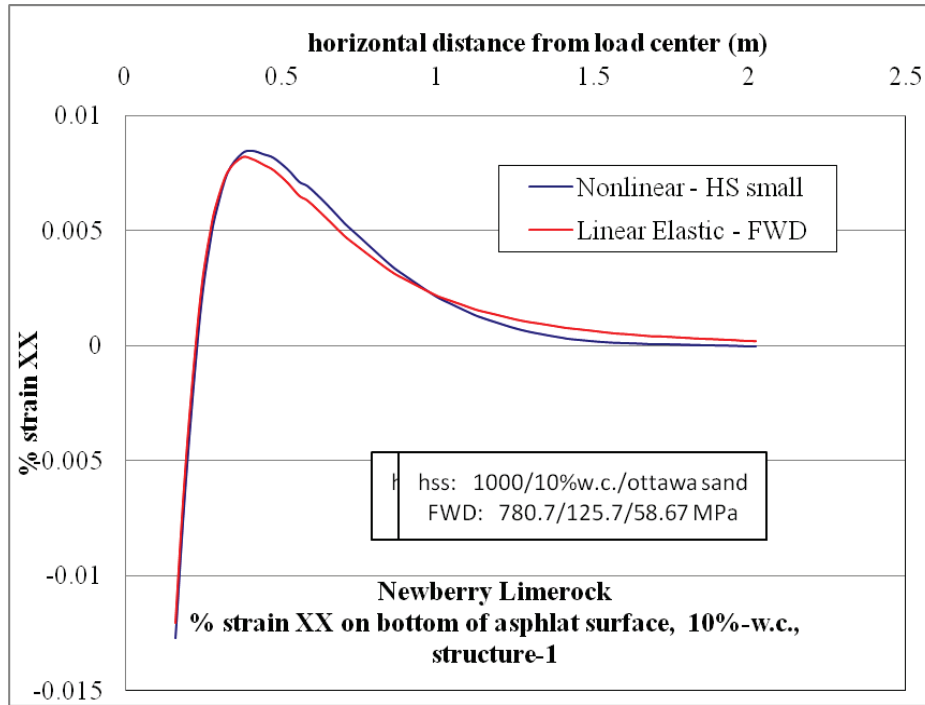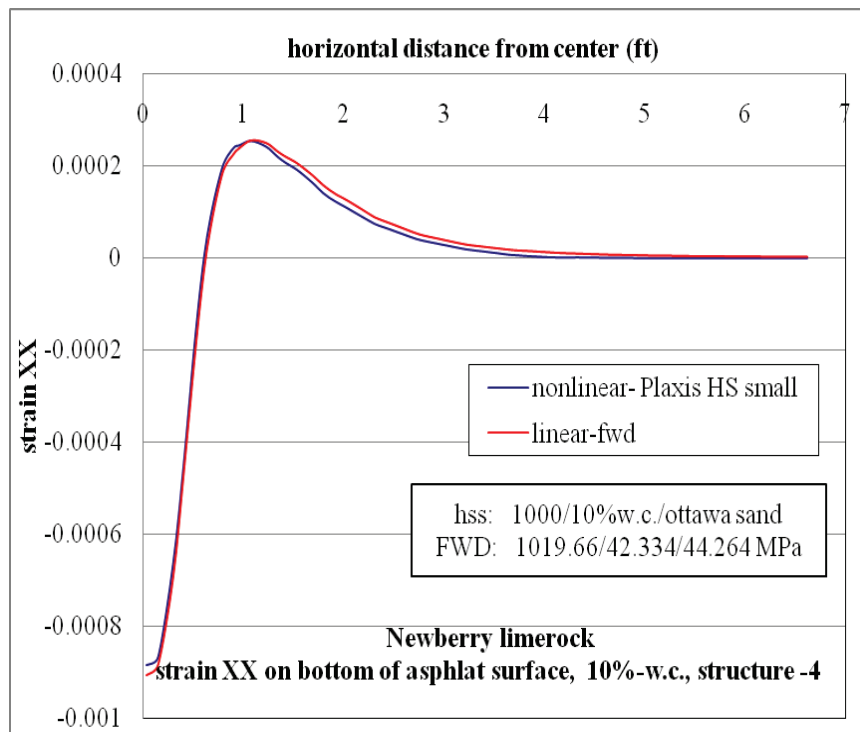

Figure C-124. ε_{yy} at bottom of base layer comparison for nonlinear and linear cases, for Structure-4 with 3.5% w.c. base layer.

C.2.10 Vertical Stress (σ_{yy}, Compressive Stress) at Top of Subgrade Layer

C.2.10.1 Structure-1

Figure C-125. σ_{yy} at top of subgrade comparison for nonlinear and linear cases, for Structure-1 with 5.5% w.c. base layer.

Figure C-126. σ_{yy} at top of subgrade layer comparison for nonlinear and linear cases for Structure-1 with 3.5% w.c. base layer.
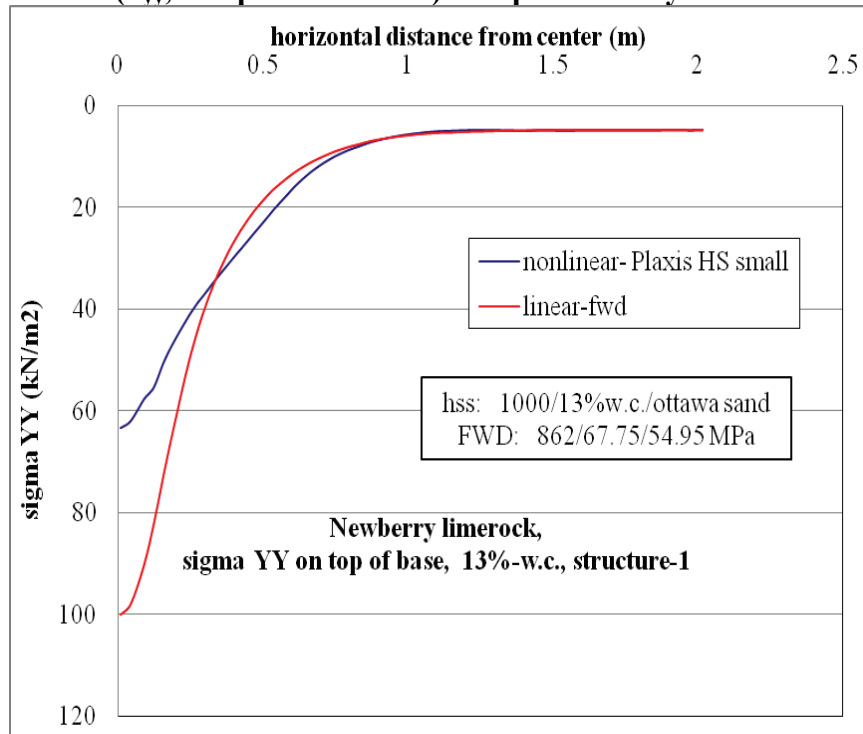
C.2.10.2 Structure-4

Figure C-127. σ_{yy} at top of subgrade layer comparison for nonlinear and linear cases, for Structure-4 with 5.5% w.c. base layer.

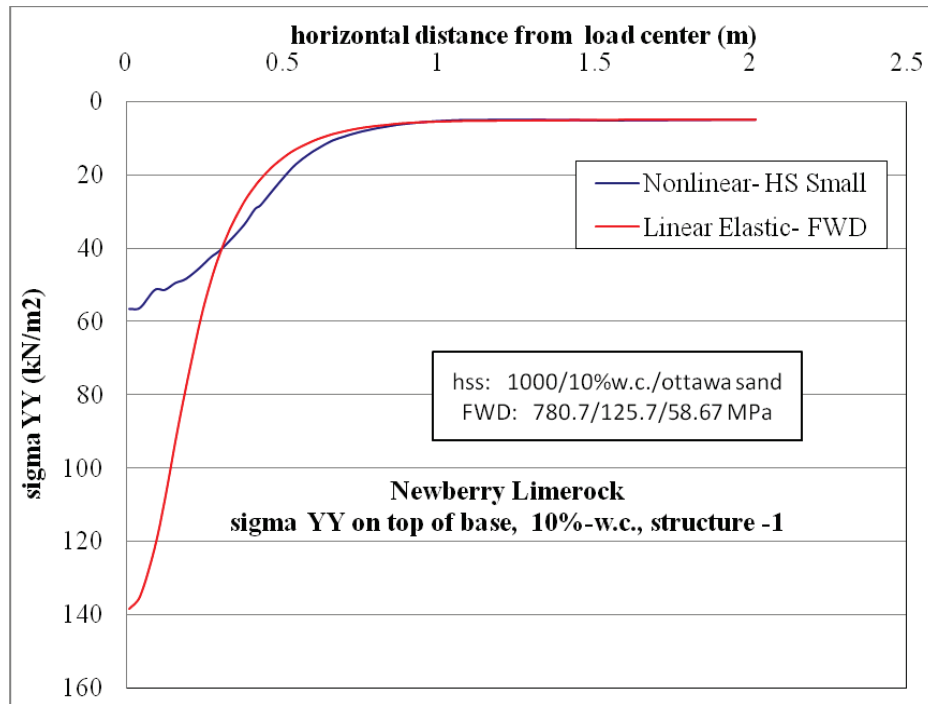Figure C-128. σ_{yy} at top of subgrade layer comparison for nonlinear and linear cases for Structure-4 with 3.5% w.c. base layer.

C.2.11 Vertical Strain (ε_{yy}, Compressive Strain) at Top of Subgrade Layer

C.2.11.1 Structure-1

Figure C-129. ε_{yy} at top of subgrade layer comparison for nonlinear and linear cases for Structure-1 with 5.5% w.c. base layer.

Figure C-130. ε_{yy} at top of subgrade layer comparison for nonlinear and linear cases for Structure-1 with 3.5% w.c. base layer.

C.2.11.1 Structure-4

Figure C-131. ε_{yy} at top of subgrade layer comparison for nonlinear and linear cases for Structure-4 with 5.5% w.c. base layer.
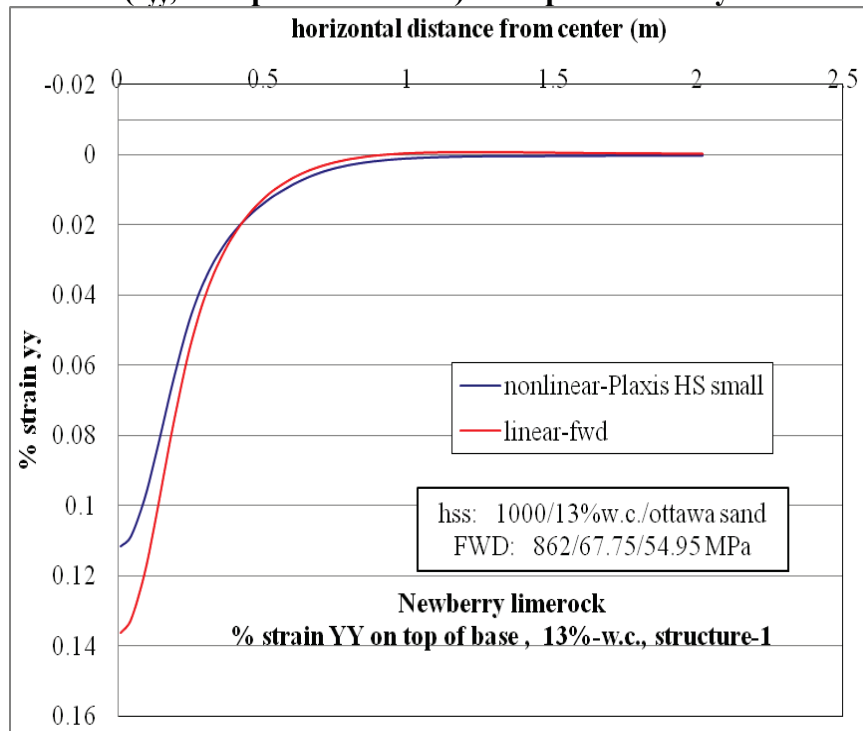

Figure C-132. ε_{yy} at top of subgrade layer comparison for nonlinear and linear cases for Structure-4 with 3.5% w.c. base layer.

APPENDIX D
COMPARISON OF NONLINEAR AND EQUIVALENT LINEAR RESPONSES FROM NONLINEAR BASE AND NONLINEAR SUBGRADE ANALYSIS

D.1   Newberry Limerock

D.1.1   Surface Deflection Profiles
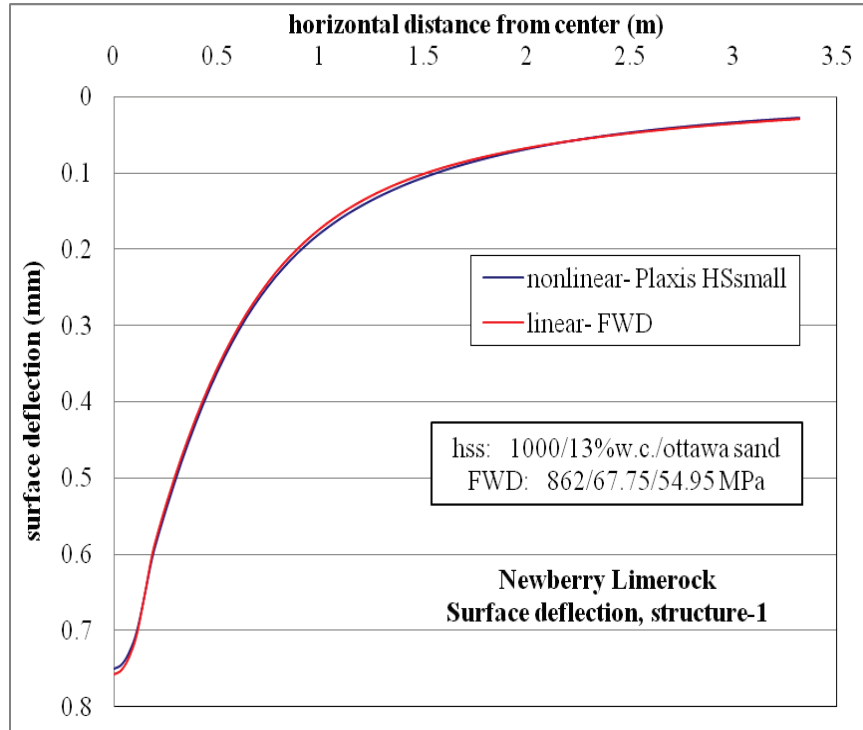
Figure D-1. Surface deflection comparison for nonlinear and linear cases, for Structure-1 with 13% w.c. base layer and nonlinear Ottawa sand subgrade.
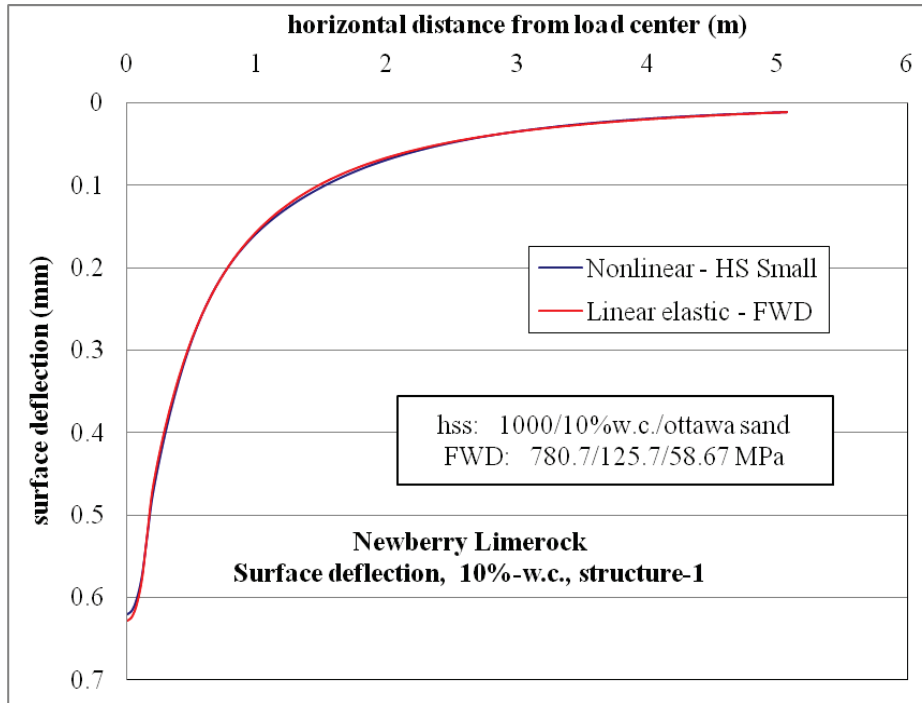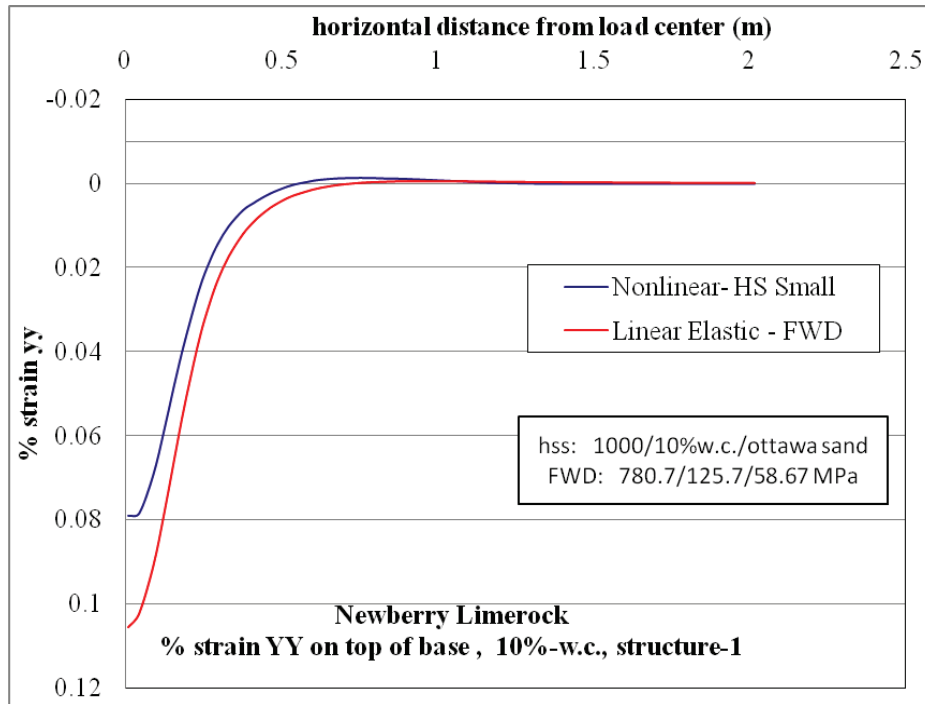
Figure D-2. Surface deflection comparison for nonlinear and linear cases, for Structure-1 with 10% w.c. base layer and nonlinear Ottawa sand subgrade.
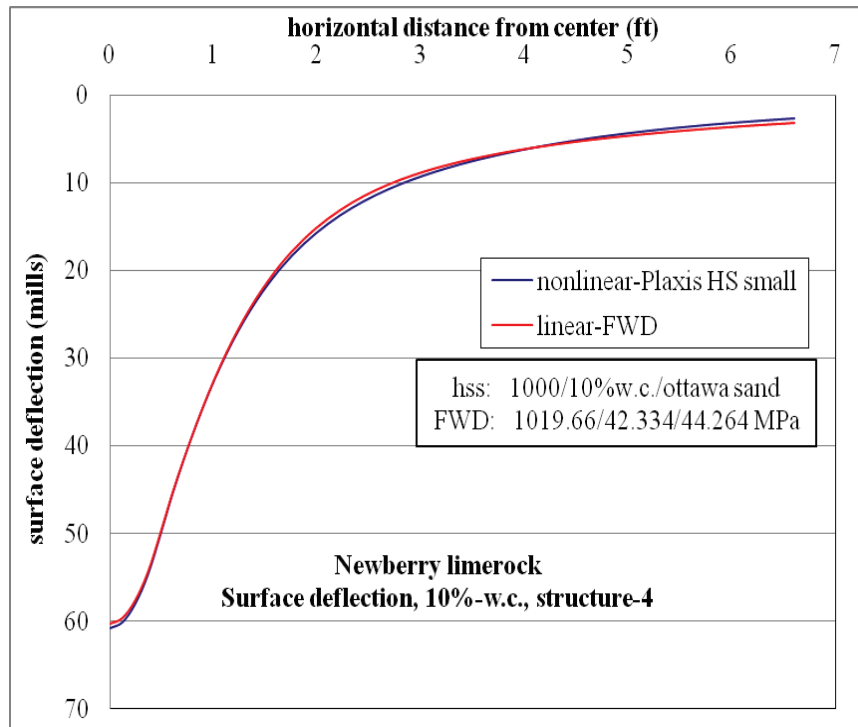
Figure D-3. Surface deflection comparison for nonlinear and linear cases, for Structure-4 with 10% w.c. base layer and nonlinear Ottawa sand subgrade.

D.1.2 Horizontal Stress (σ_xx, Tensile Stress) at Top of AC Layer
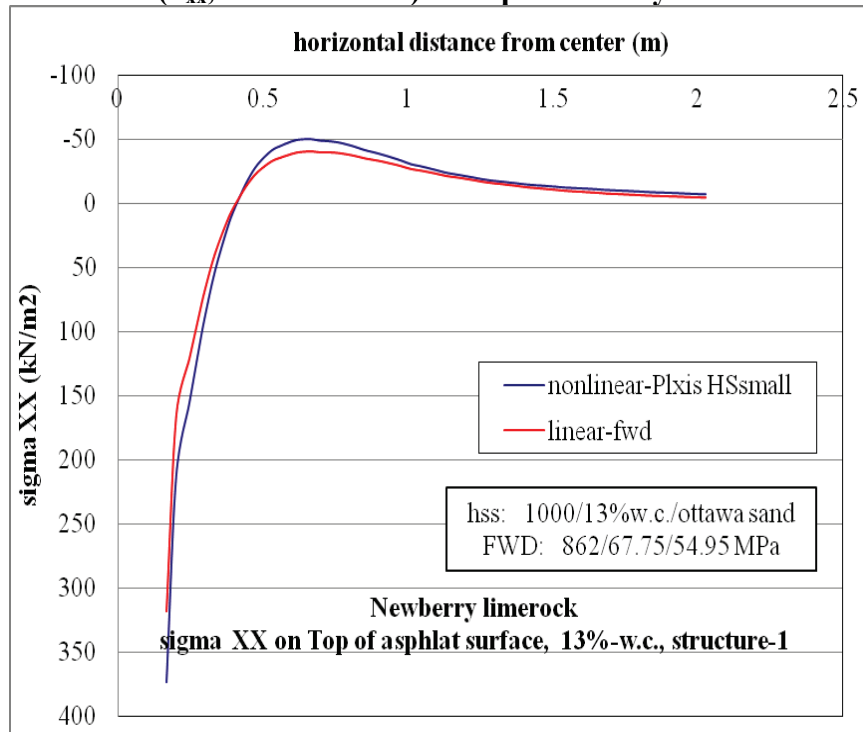
Figure D-4. σ_xx at top of AC layer comparison for nonlinear and linear cases, for Structure-1 with 13% w.c. base layer and nonlinear Ottawa sand subgrade.
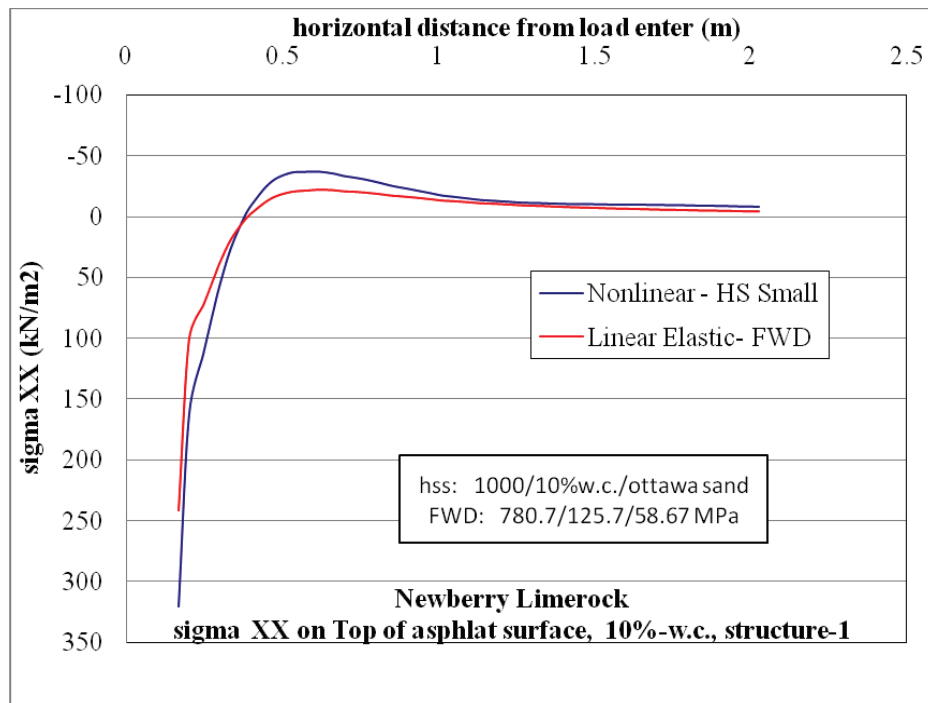
Figure D-5. σ_xx at top of AC layer comparison for nonlinear and linear cases, for Structure-1 with 10% w.c. base layer and nonlinear Ottawa sand subgrade.
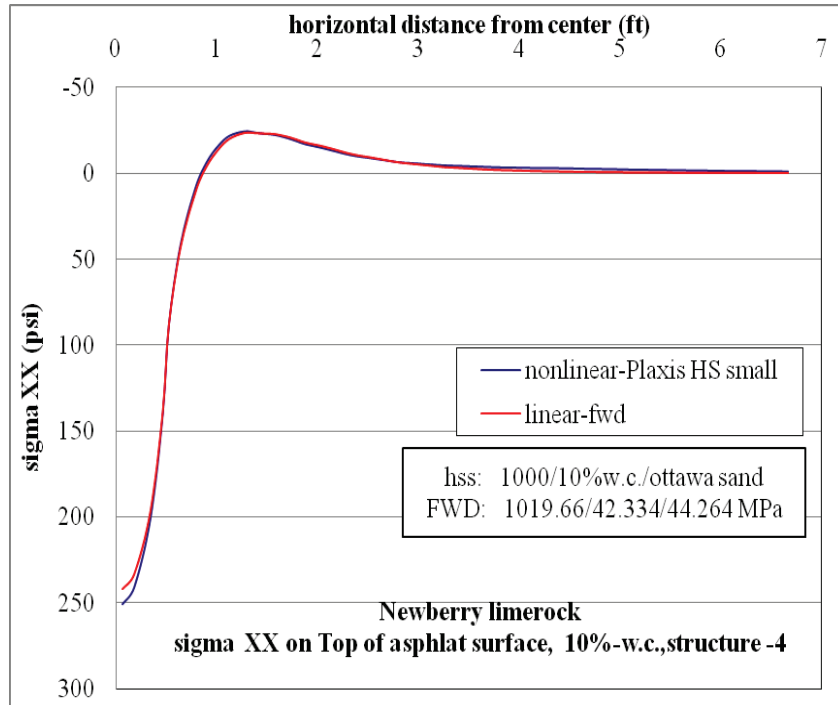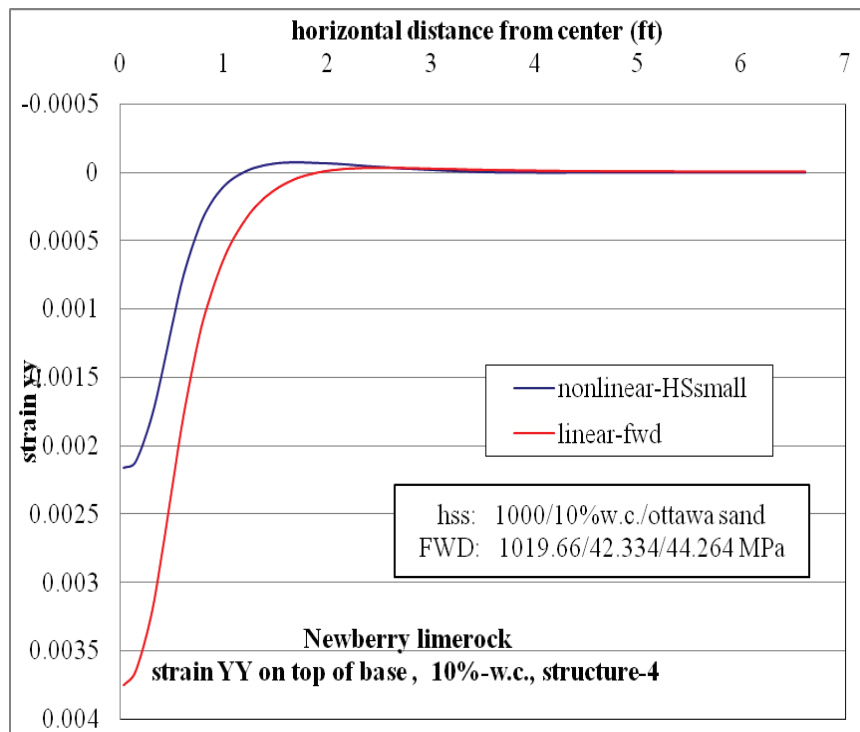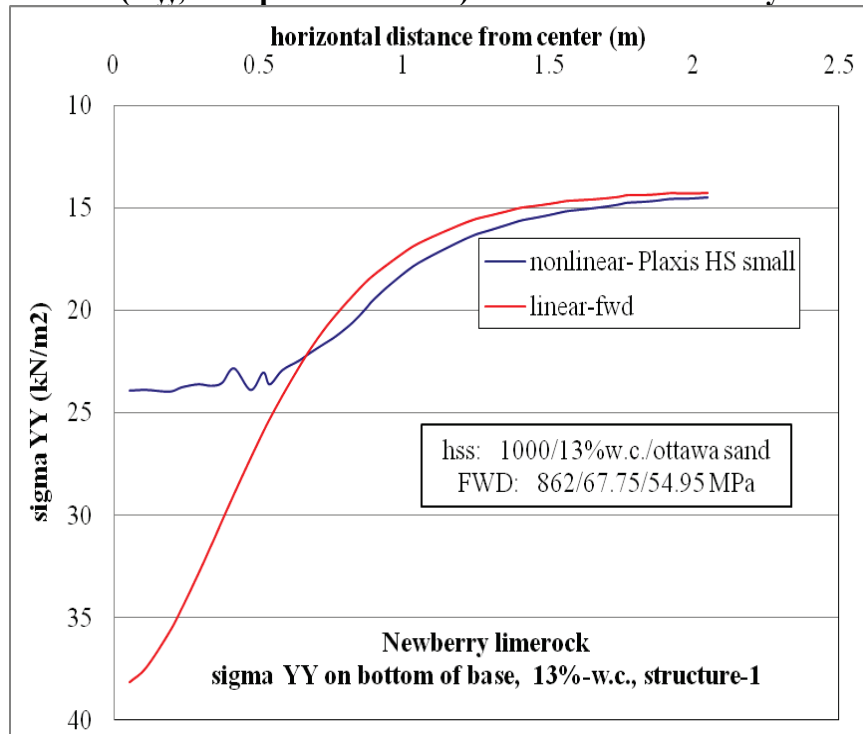
Figure D-6. σ_{xx} at top of AC layer comparison for nonlinear and linear cases, for Structure-4 with 10% w.c. base layer and nonlinear Ottawa sand subgrade.

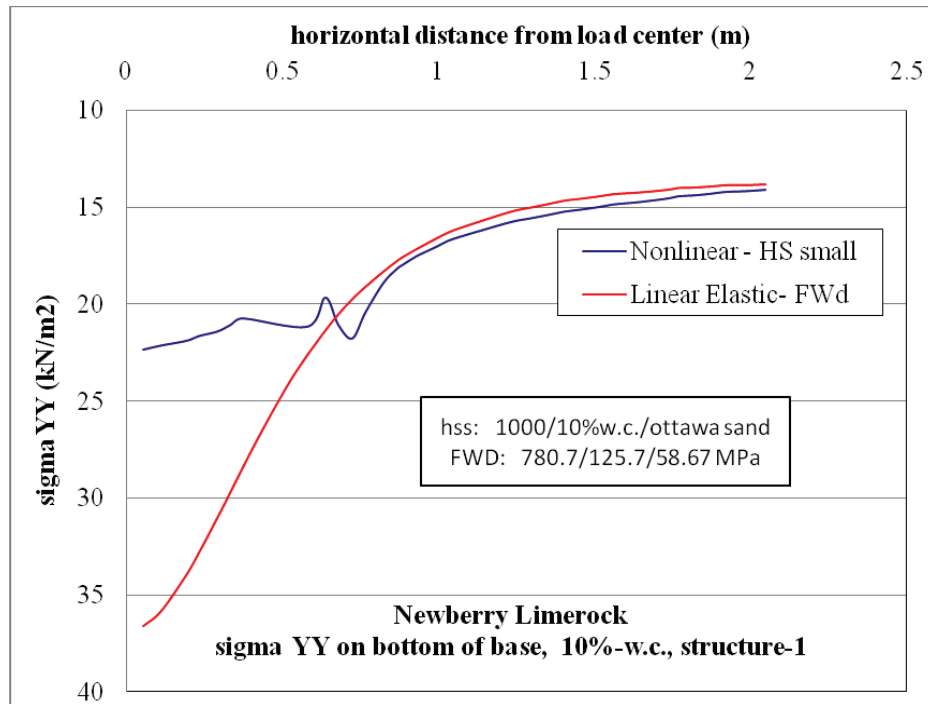### D.1.3 Horizontal Strain (ε_{xx}, Tensile Strain) at Top of AC Layer

Figure D-7. ε_{xx} at top of AC layer comparison for nonlinear and linear cases, for Structure-1 with 13% w.c. base layer and nonlinear Ottawa sand subgrade.

Figure D-8. ε_{xx} at top of AC layer comparison for nonlinear and linear cases, for Structure-1 with 10% w.c. base layer and nonlinear Ottawa sand subgrade.
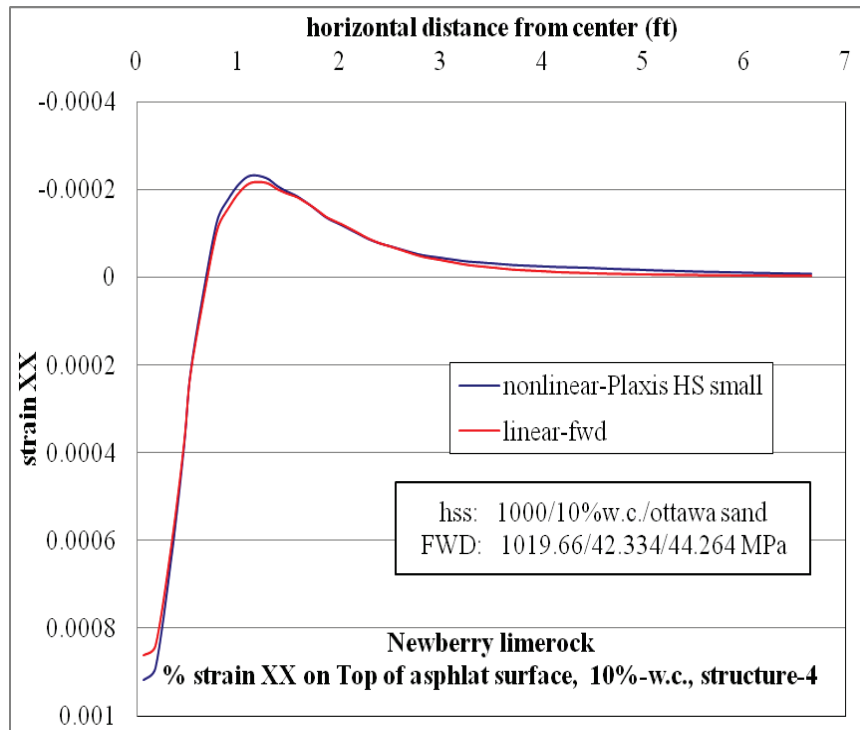
Figure D-9. ε_{xx} at top of AC layer comparison for nonlinear and linear cases, for Structure-4 with 10% w.c. base layer and nonlinear Ottawa sand subgrade.
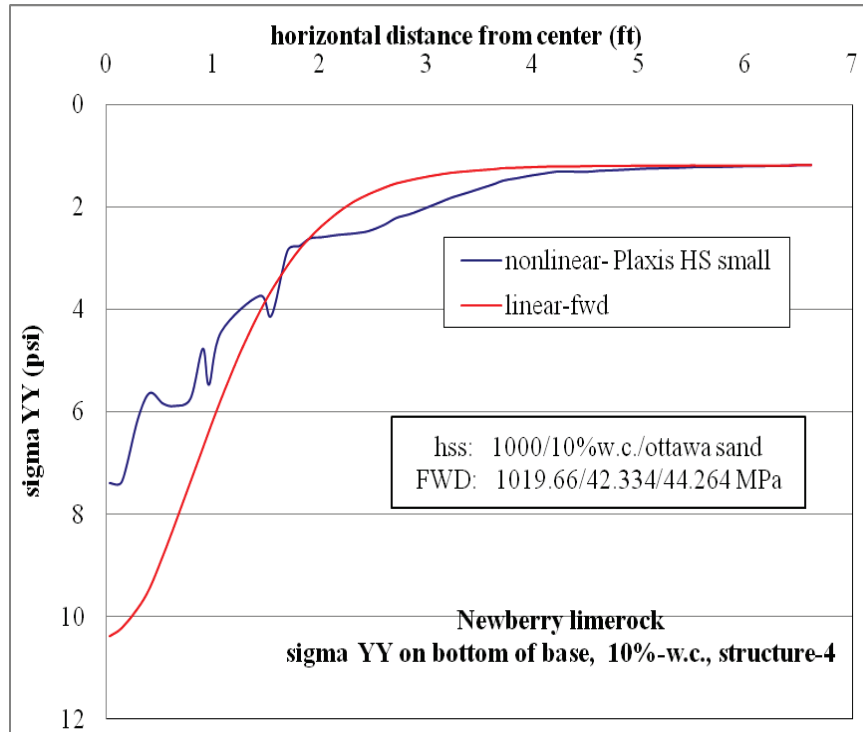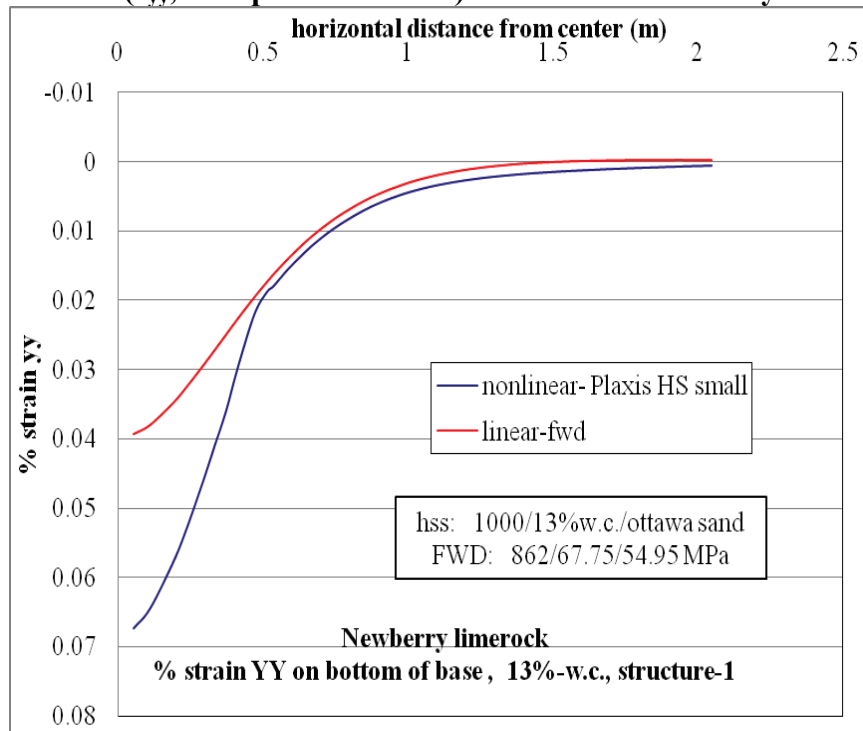
D.1.4 Horizontal Stress (σ$_{xx}$, Tensile Stress) at Bottom of AC Layer
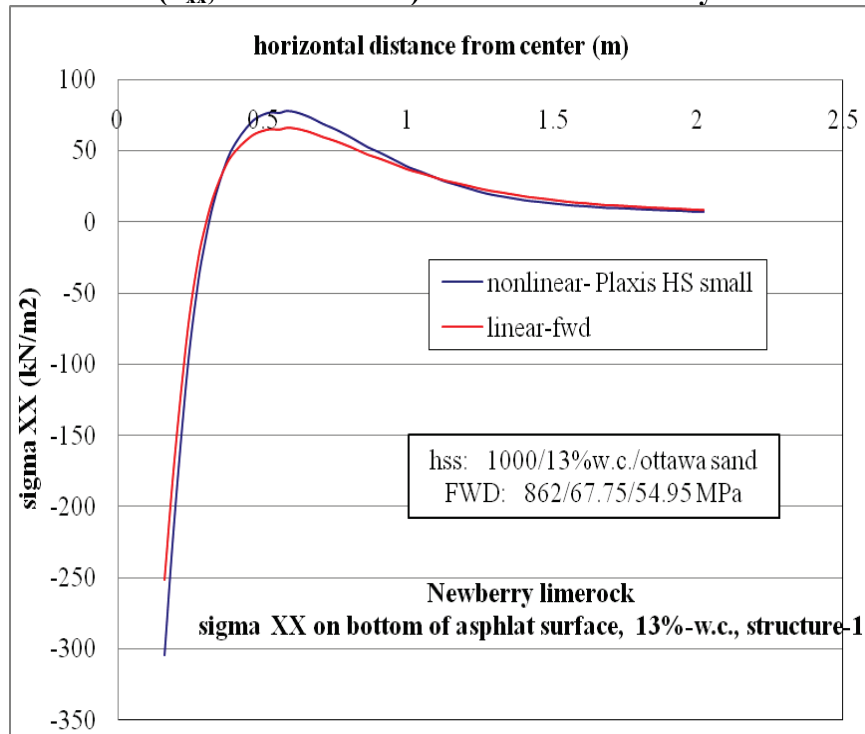
Figure D-10. σ$_{xx}$ at bottom of AC layer comparison for nonlinear and linear cases, for Structure-1 with 13% w.c. base layer and nonlinear Ottawa sand subgrade.

Figure D-11. σ$_{xx}$ at bottom of AC layer comparison for nonlinear and linear cases, for Structure-1 with 10% w.c. base layer and nonlinear Ottawa sand subgrade.

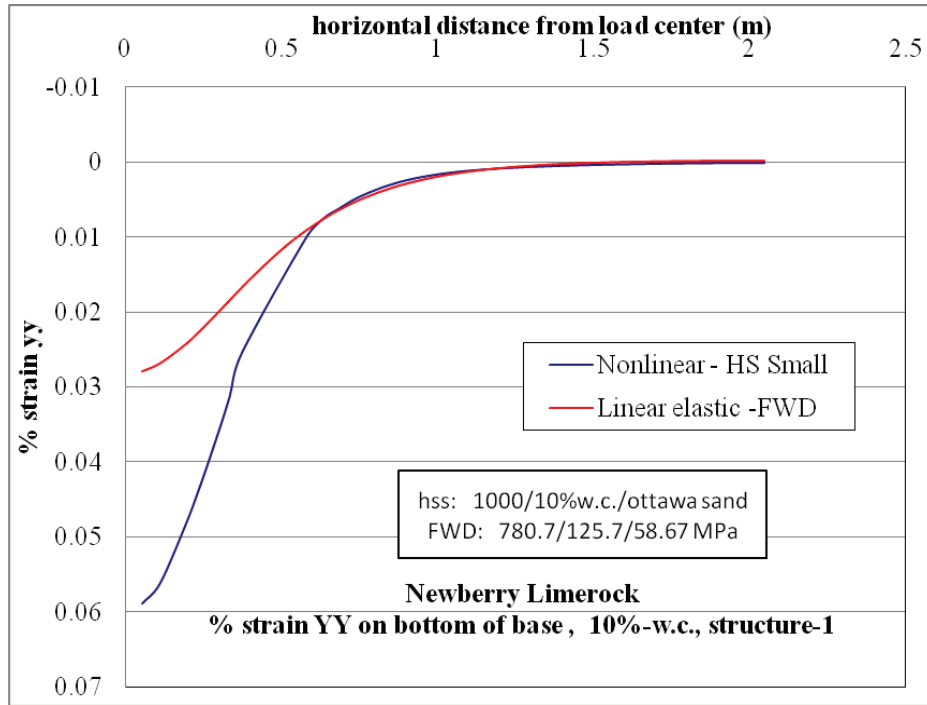Figure D-12. σ_{xx} at bottom of AC layer comparison for nonlinear and linear cases, for Structure-4 with 10% w.c. base layer and nonlinear Ottawa sand subgrade.

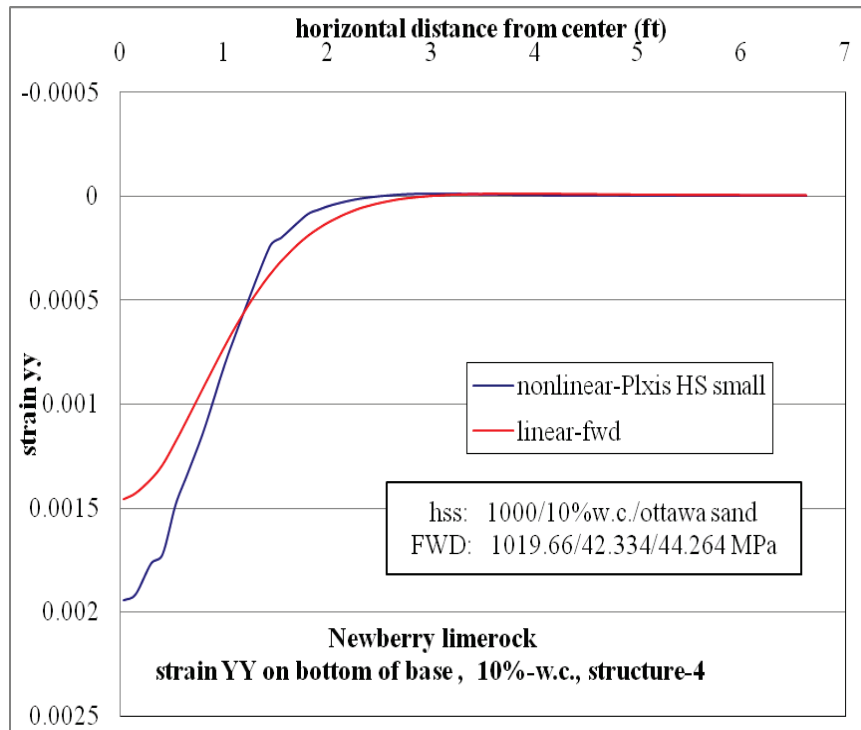### D.1.5 Horizontal Strain (ε_{xx}, Tensile Strain) at Bottom of AC layer

Figure D-13. ε_{xx} at bottom of AC layer comparison for nonlinear and linear cases, for Structure-1 with 13% w.c. base layer and nonlinear Ottawa sand subgrade.

Figure D-14. ε_{xx} at bottom of AC layer comparison for nonlinear and linear cases, for Structure-1 with 10% w.c. base layer and nonlinear Ottawa sand subgrade.

Figure D-15. ε_{xx} at bottom of AC layer comparison for nonlinear and linear cases, for Structure-4 with 10% w.c. base layer and nonlinear Ottawa sand subgrade.

D.1.6 Vertical stress (σᵧᵧ, compressive stress) at top of base layer

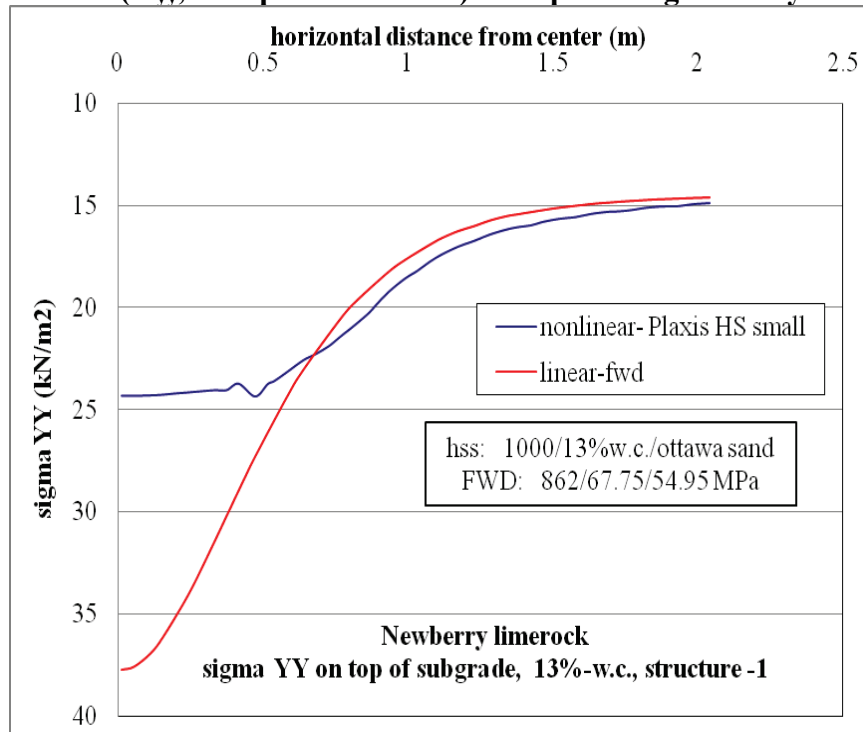Figure D-16. σ_{yy} vertical stress at top of base layer comparison for nonlinear and linear cases, for Structure-1 with 13% w.c. base layer and nonlinear Ottawa sand subgrade.

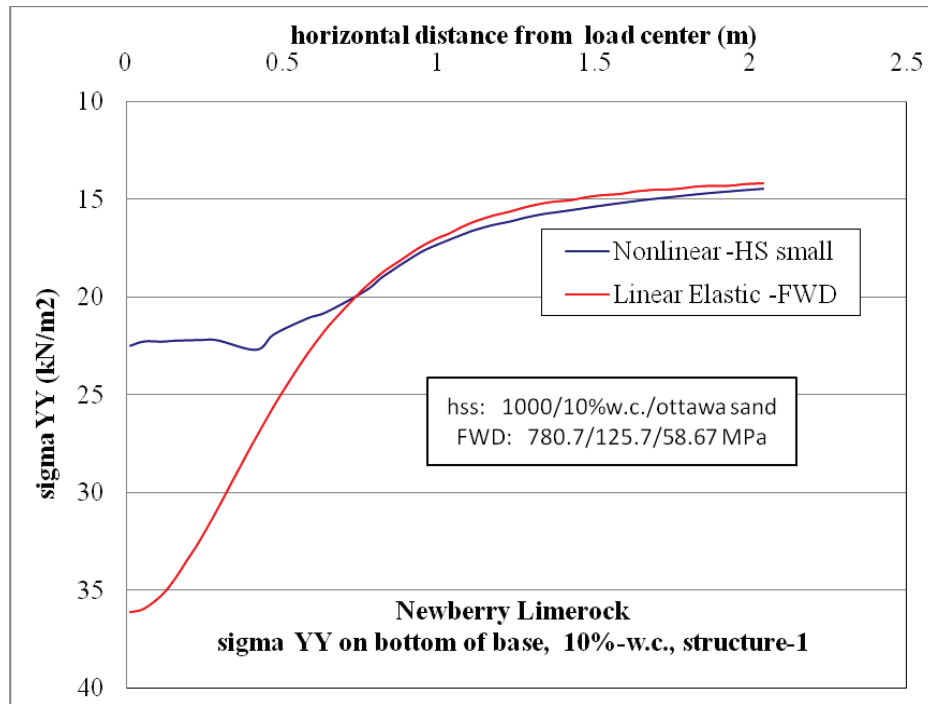Figure D-17. σ_{yy} vertical stress at top of base layer comparison for nonlinear and linear cases, for Structure-1 with 10% w.c. base layer and nonlinear Ottawa sand subgrade.
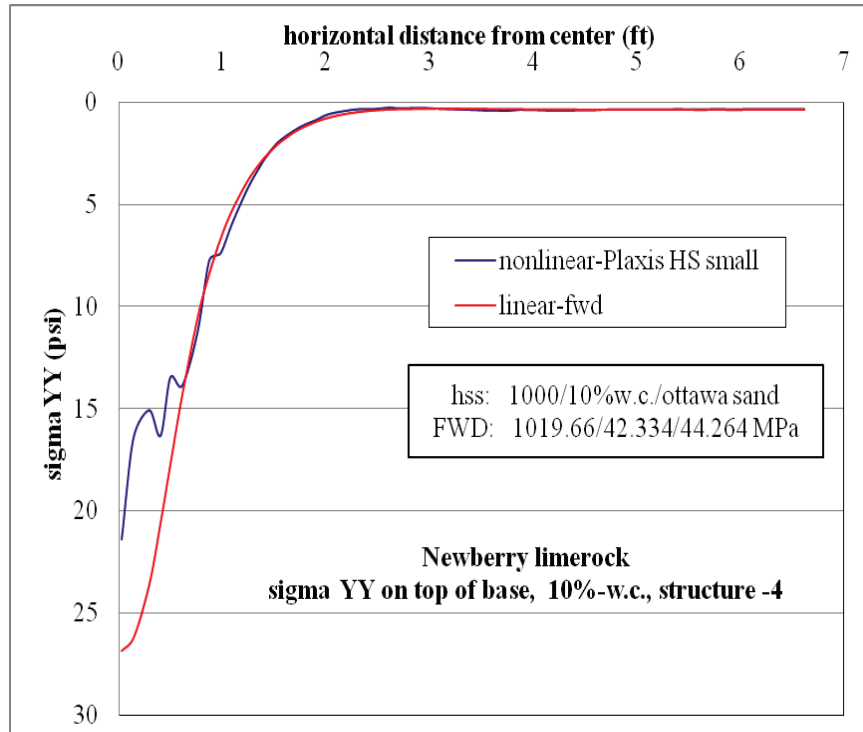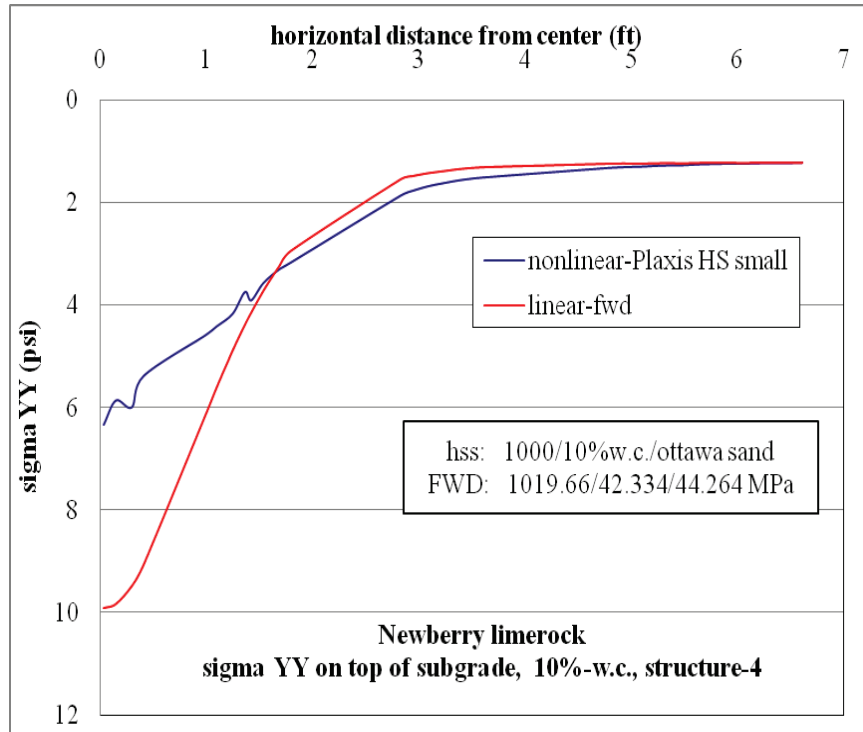
Figure D-18. σ_{yy} vertical stress at top of base layer comparison for nonlinear and linear cases, for Structure-4 with 10% w.c. base layer and nonlinear Ottawa sand subgrade.

D.1.7 Vertical Strain (ε_{yy}, Compressive Strain) at Top of Base Layer
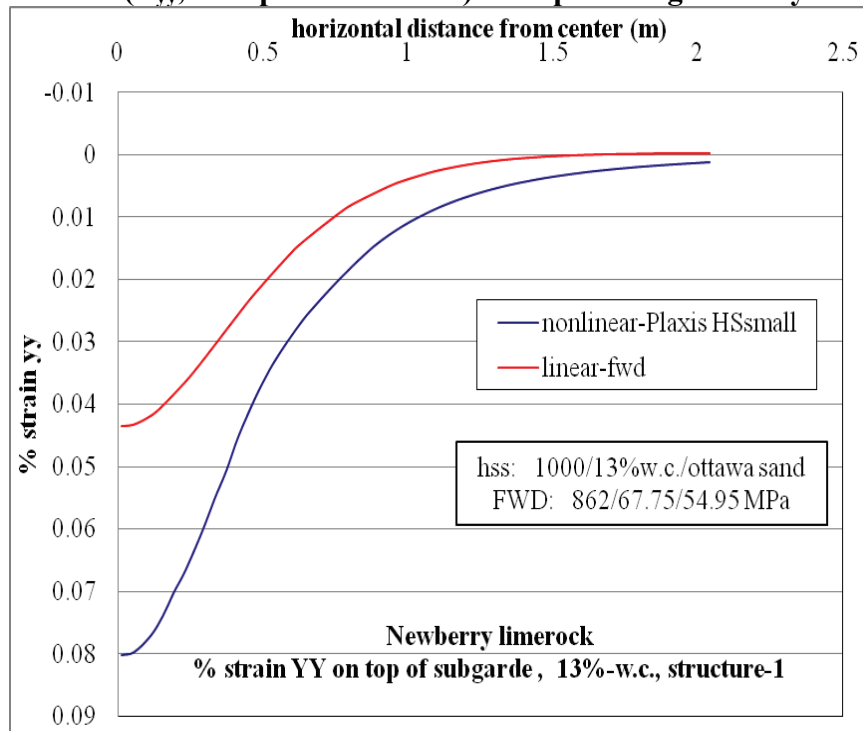

Figure D-19. ε_{yy} at top of base layer comparison for nonlinear and linear cases, for Structure-1 with 13% w.c. base layer and nonlinear Ottawa sand subgrade.

Figure D-20. ε_{yy} at top of base layer comparison for nonlinear and linear cases, for Structure-1 with 10% w.c. base layer and nonlinear Ottawa sand subgrade.

Figure D-21. ε_{yy} at top of base layer comparison for nonlinear and linear cases, for Structure-4 with 10% w.c. base layer and nonlinear Ottawa sand subgrade.

D.1.8   Vertical Stress (σ$_{yy}$, Compressive Stress) at Bottom of Base Layer

Figure D-22. σ$_{yy}$ at bottom of base layer comparison for nonlinear and linear cases, for Structure-1 with 13% w.c. base layer and nonlinear Ottawa sand subgrade.

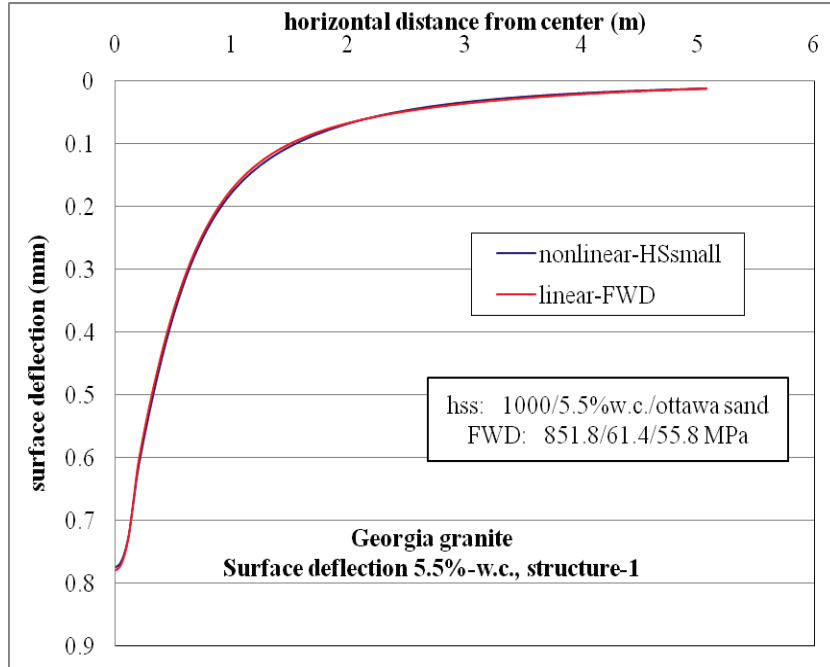Figure D-23. σ$_{yy}$ at bottom of base layer comparison for nonlinear and linear cases, for Structure-1 with 10% w.c. base layer and nonlinear Ottawa sand subgrade.

Figure D-24. σ_{yy} at bottom of base layer comparison for nonlinear and linear cases, for Structure-4 with 10% w.c. base layer and nonlinear Ottawa sand subgrade.

D.1.9. Vertical Strain (ε_{yy}, Compressive Strain) at Bottom of Base Layer
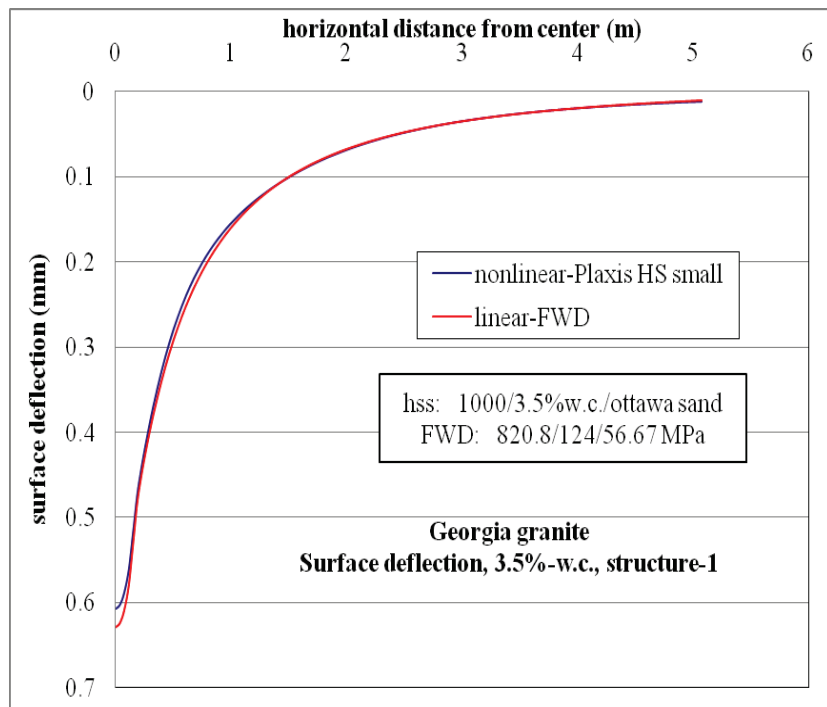

Figure D-25. ε_{yy} at bottom of base layer comparison for nonlinear and linear cases, for Structure-1 with 13% w.c. base layer and nonlinear Ottawa sand subgrade.
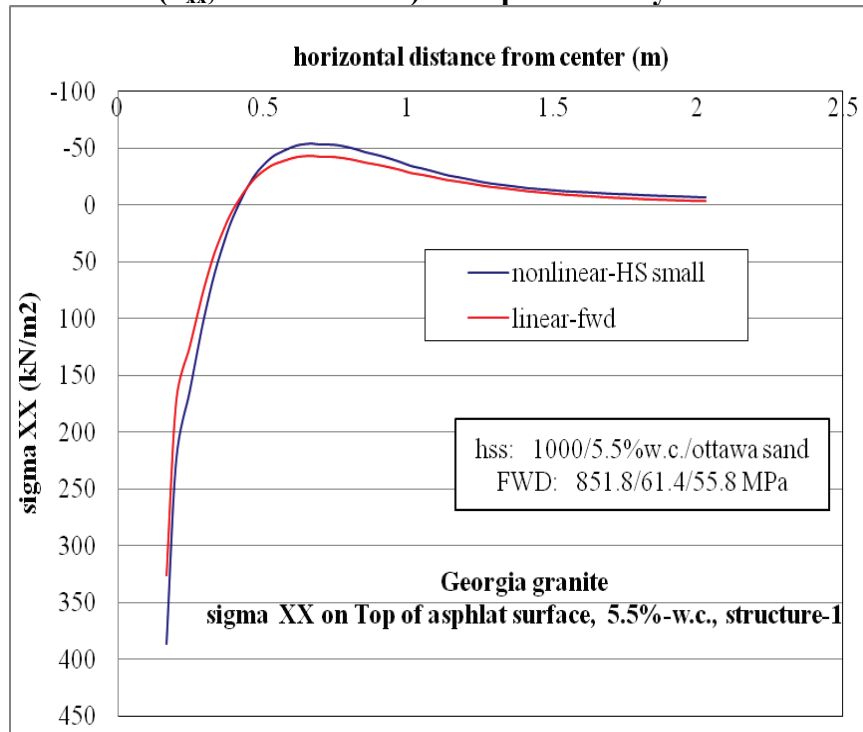
244

Figure D-26. ε_{yy} at bottom of base layer comparison for nonlinear and linear cases, for Structure-1 with 10% w.c. base layer and nonlinear Ottawa sand subgrade.

Figure D-27. ε_{yy} at bottom of base layer comparison for nonlinear and linear cases, for Structure-4 with 10% w.c. base layer and nonlinear Ottawa sand subgrade.

D.1.10 Vertical Stress (σ_{yy}, Compressive Stress) at Top of Subgrade Layer

Figure D-28. σ_{yy} at top of subgrade comparison for nonlinear and linear cases, for Structure-1 with 13% w.c. base layer and nonlinear Ottawa sand subgrade.
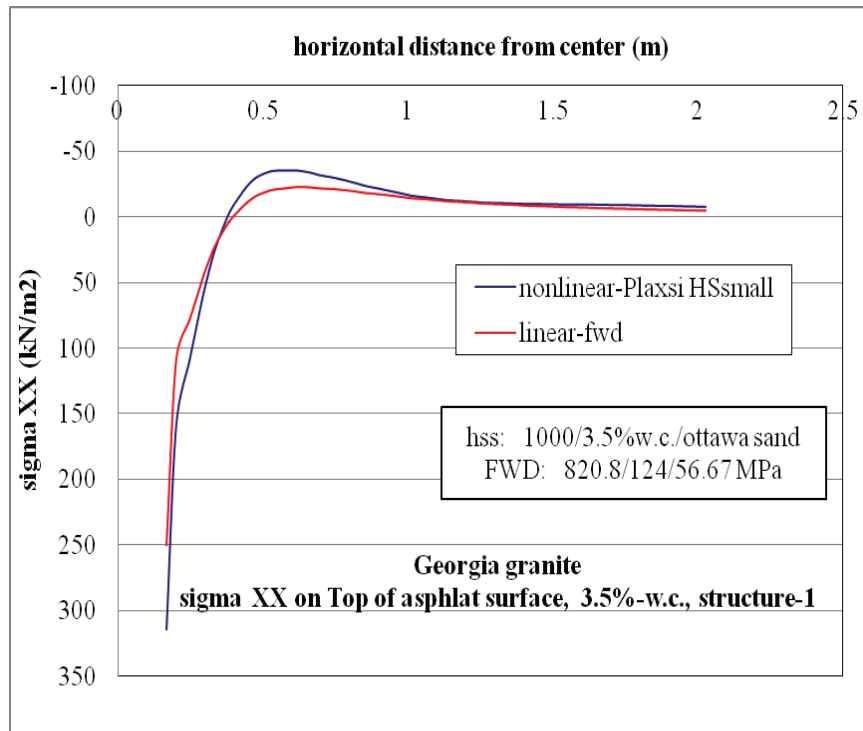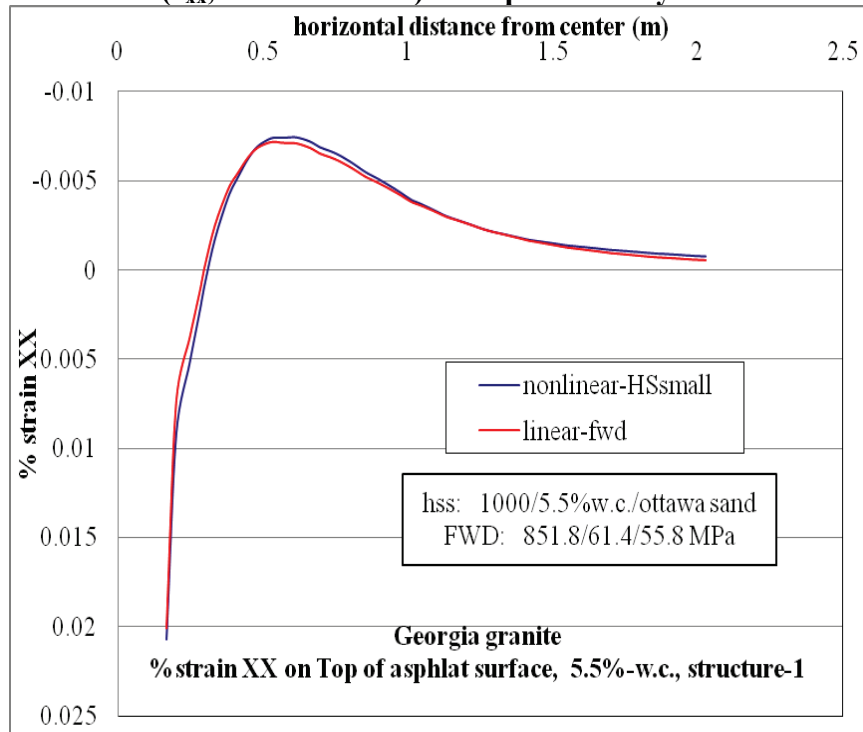

Figure D-29. σ_{yy} at top of subgrade comparison for nonlinear and linear cases, for Structure-1 with 10% w.c. base layer and nonlinear Ottawa sand subgrade.

Figure D-30. σ_{yy} at top of subgrade comparison for nonlinear and linear cases, for Structure-4 with 10% w.c. base layer and nonlinear Ottawa sand subgrade.

D.1.11 Vertical Strain (ε_{yy}, Compressive Strain) at Top of Subgrade Layer

Figure D-31. ε_{yy} at top of subgrade layer comparison for nonlinear and linear cases for Structure-1 with 13% w.c. base layer and nonlinear Ottawa sand subgrade.
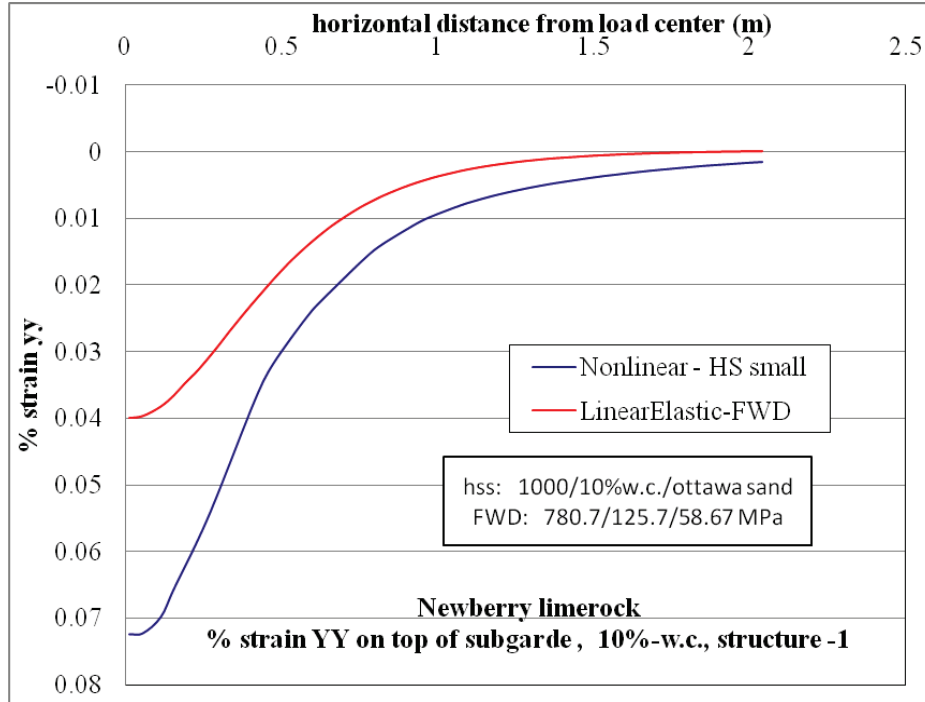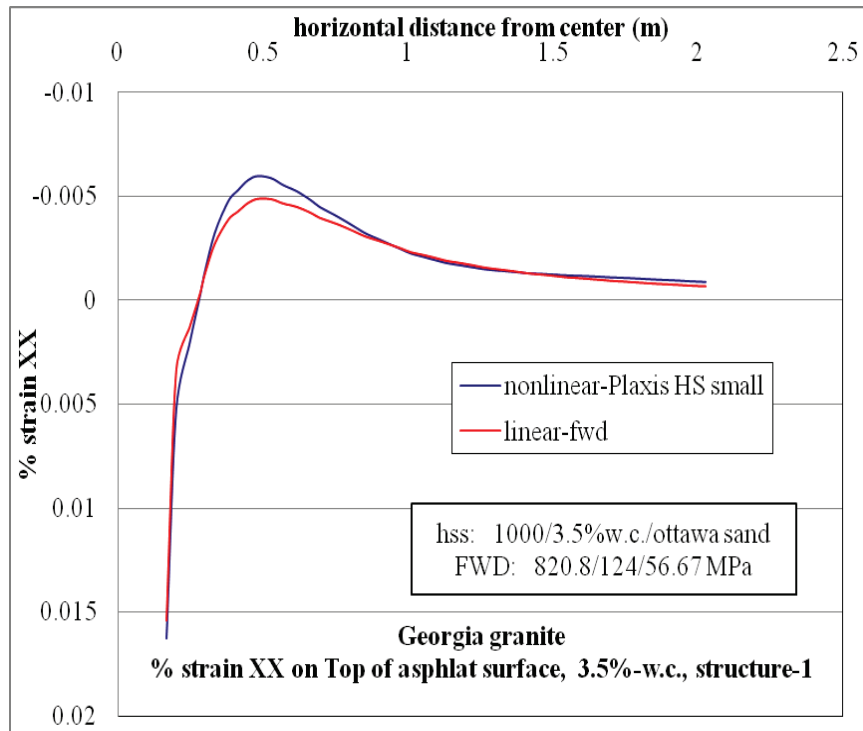
Figure D-32. ε_{yy} at top of subgrade layer comparison for nonlinear and linear cases for Structure-1 with 10% w.c. base layer and nonlinear Ottawa sand subgrade.
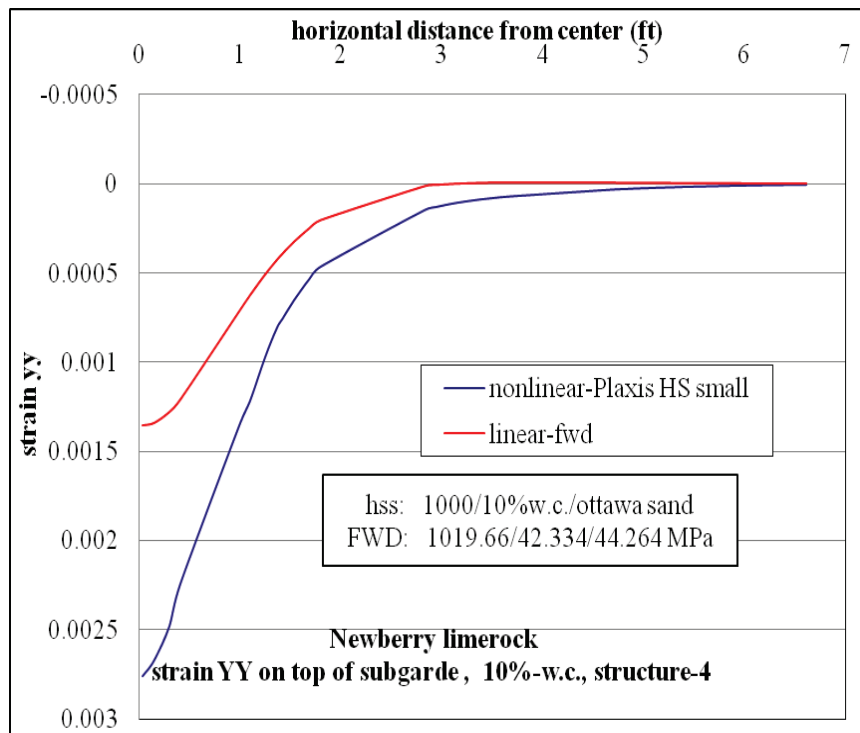
Figure D-33. ε_{yy} at top of subgrade layer comparison for nonlinear and linear cases for Structure-4 with 10% w.c. base layer and nonlinear Ottawa sand subgrade.

D.2   Georgia Granite
D.2.1   Surface Deflection Profiles

Figure D-34. Surface deflection comparison for nonlinear and linear cases, for Structure-1 with 5.5% w.c. base layer and nonlinear Ottawa sand subgrade.

Figure D-35. Surface deflection comparison for nonlinear and linear cases, for Structure-1 with 3.5% w.c. base layer and nonlinear Ottawa sand subgrade.

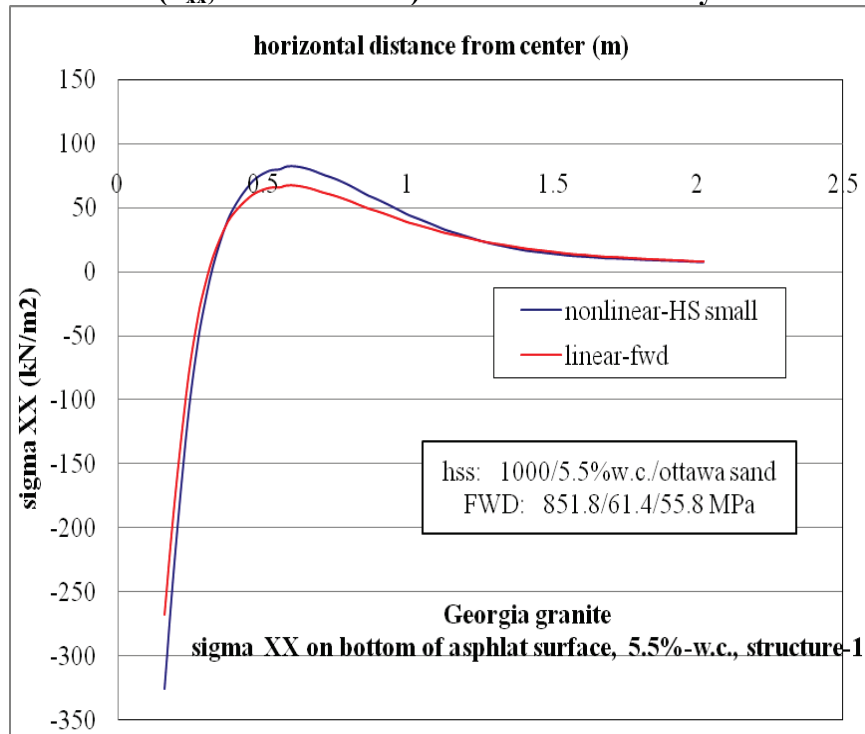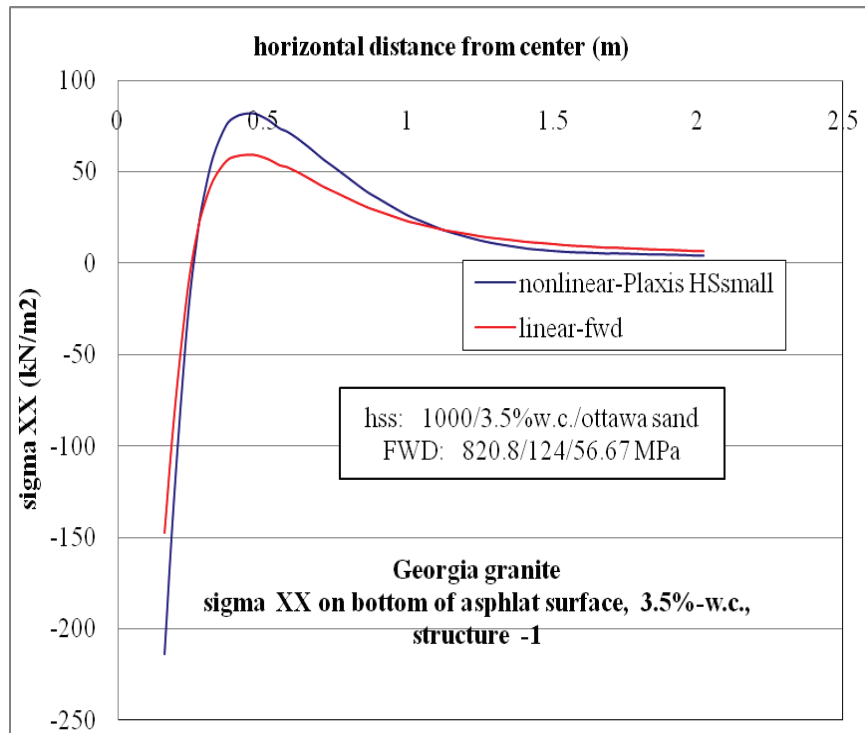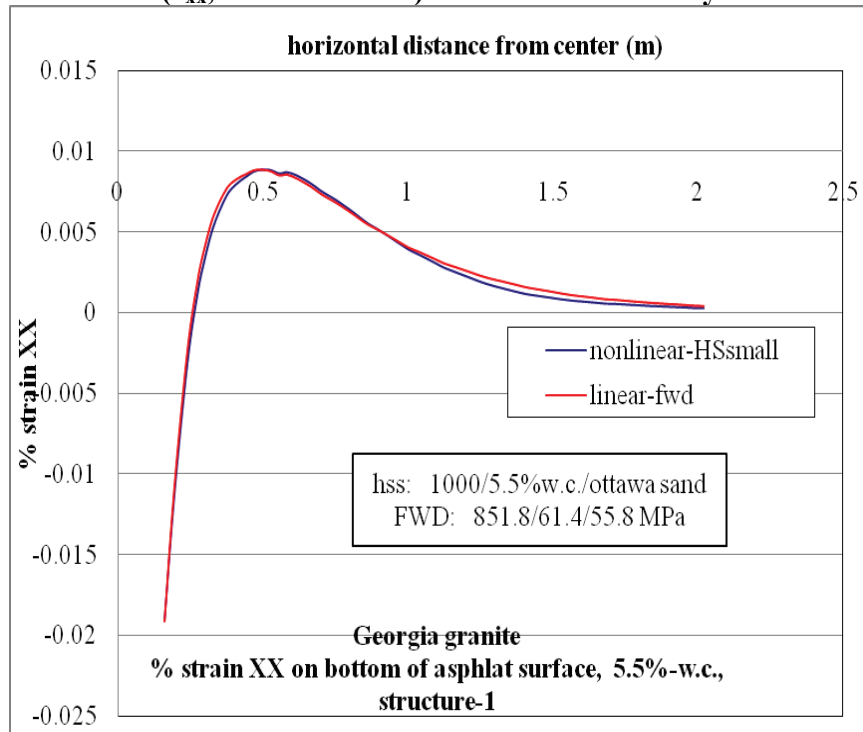## D.2.2 Horizontal Stress (σ$_{xx}$, Tensile Stress) at Top of AC Layer

Figure D-36. σ$_{xx}$ at top of AC layer comparison for nonlinear and linear cases, for Structure-1 with 5.5% w.c. base layer and nonlinear Ottawa sand subgrade.

Figure D-37. σ$_{xx}$ at top of AC layer comparison for nonlinear and linear cases, for Structure-1 with 3.5% w.c. base layer and nonlinear Ottawa sand subgrade.

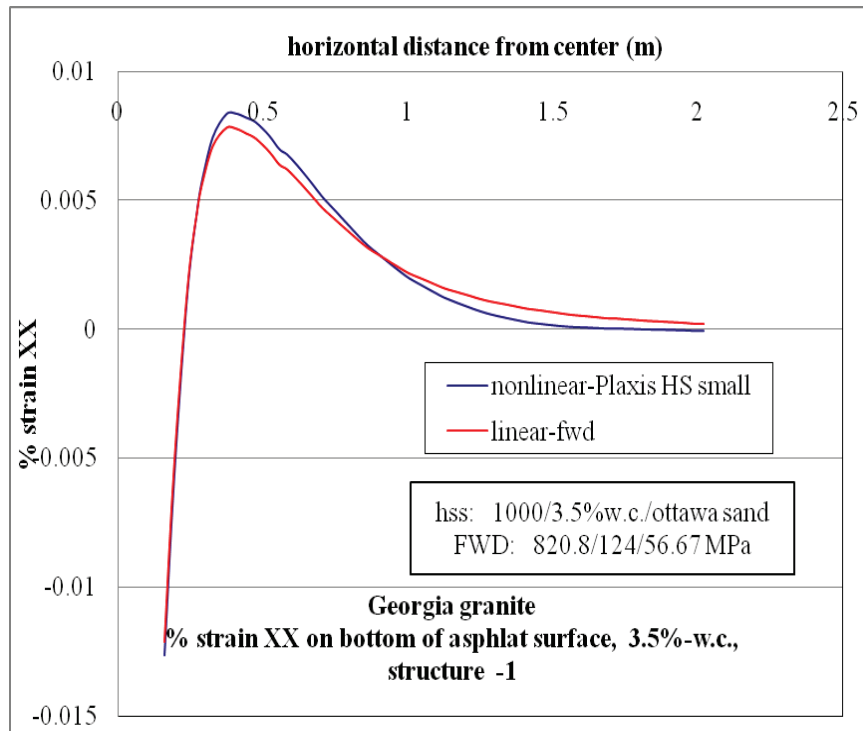### D.2.3 Horizontal Strain (ε_{xx}, Tensile Strain) at Top of AC Layer

Figure D-38. ε_{xx} at top of AC layer comparison for nonlinear and linear cases, for Structure-1 with 5.5% w.c. base layer and nonlinear Ottawa sand subgrade.

Figure D-39. ε_{xx} at top of AC layer comparison for nonlinear and linear cases, for Structure-1 with 3.5% w.c. base layer and nonlinear Ottawa sand subgrade.

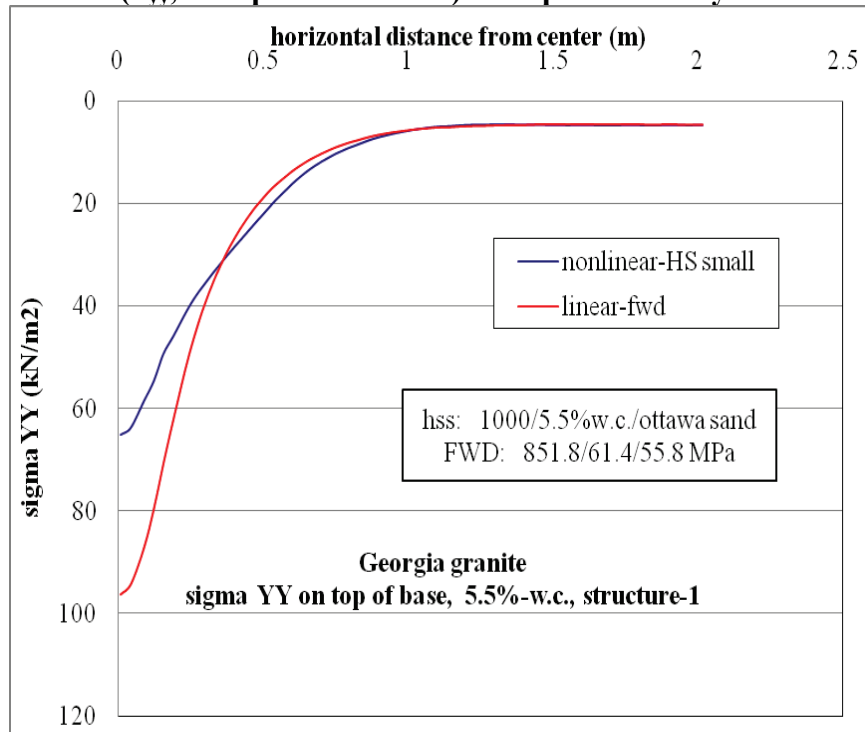### D.2.4 Horizontal Stress (σ_{xx}, Tensile Stress) at Bottom of AC Layer

Figure D-40. σ_{xx} at bottom of AC layer comparison for nonlinear and linear cases, for Structure-1 with 5.5% w.c. base layer and nonlinear Ottawa sand subgrade.

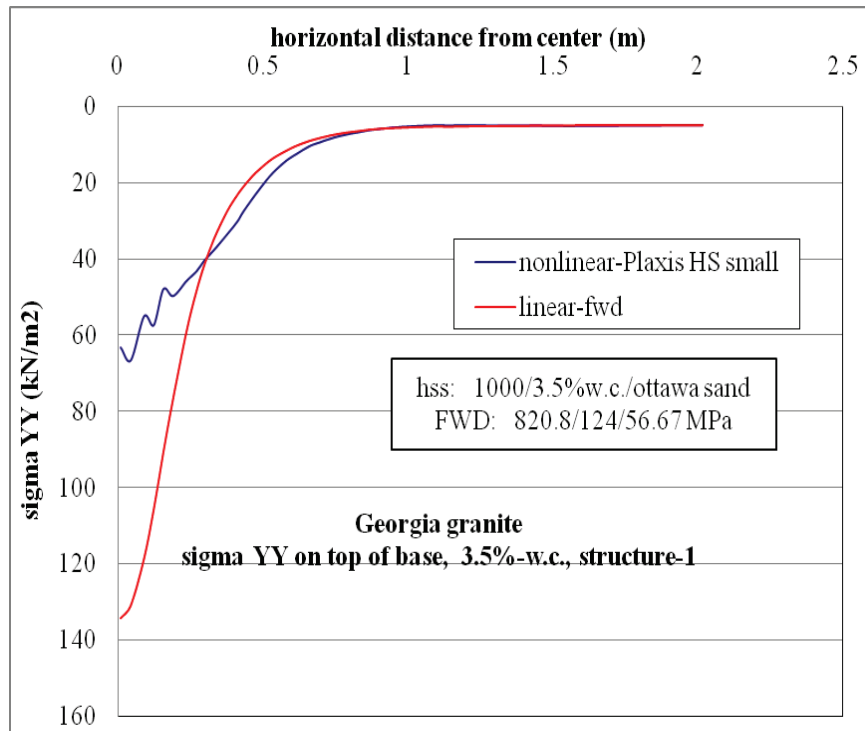Figure D-41. σ_{xx} at bottom of AC layer comparison for nonlinear and linear cases, for Structure-1 with 3.5% w.c. base layer and nonlinear Ottawa sand subgrade.

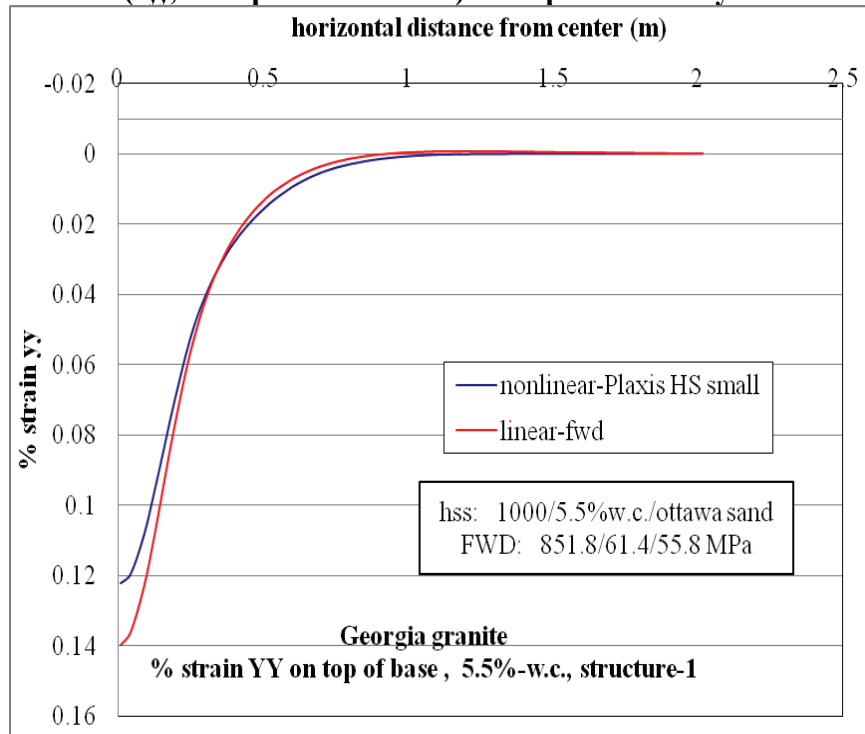**D.2.5. Horizontal Strain (ε_{xx}, Tensile Strain) at Bottom of AC Layer**

Figure D-42. ε_{xx} at bottom of AC layer comparison for nonlinear and linear cases, for Structure-1 with 5.5% w.c. base layer and nonlinear Ottawa sand subgrade.

Figure D-43. ε_{xx} at bottom of AC layer comparison for nonlinear and linear cases, for Structure-1 with 3.5% w.c. base layer and nonlinear Ottawa sand subgrade.
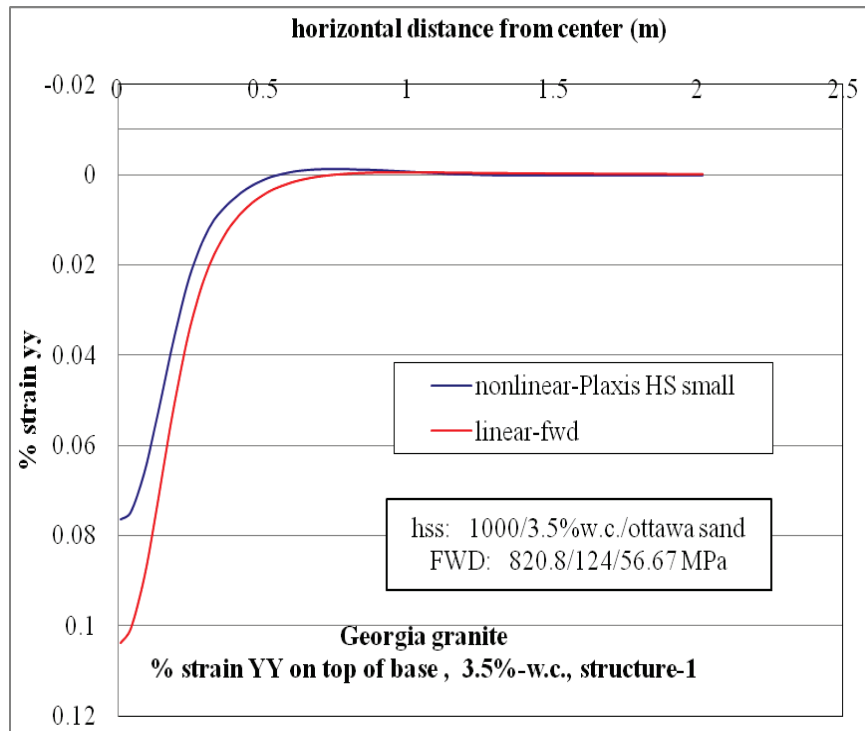
D.2.6 Vertical Stress (σ$_{yy}$, Compressive Stress) at Top of Base Layer

Figure D-44. σ$_{yy}$ vertical stress at top of base layer comparison for nonlinear and linear cases, for Structure-1 with 5.5% w.c. base layer and nonlinear Ottawa sand subgrade.

Figure D-45. σ$_{yy}$ vertical stress at top of base layer comparison for nonlinear and linear cases, for Structure-1 with 3.5% w.c. base layer and nonlinear Ottawa sand subgrade.

D.2.7 Vertical Strain (ε_{yy}, Compressive Strain) at Top of Base Layer
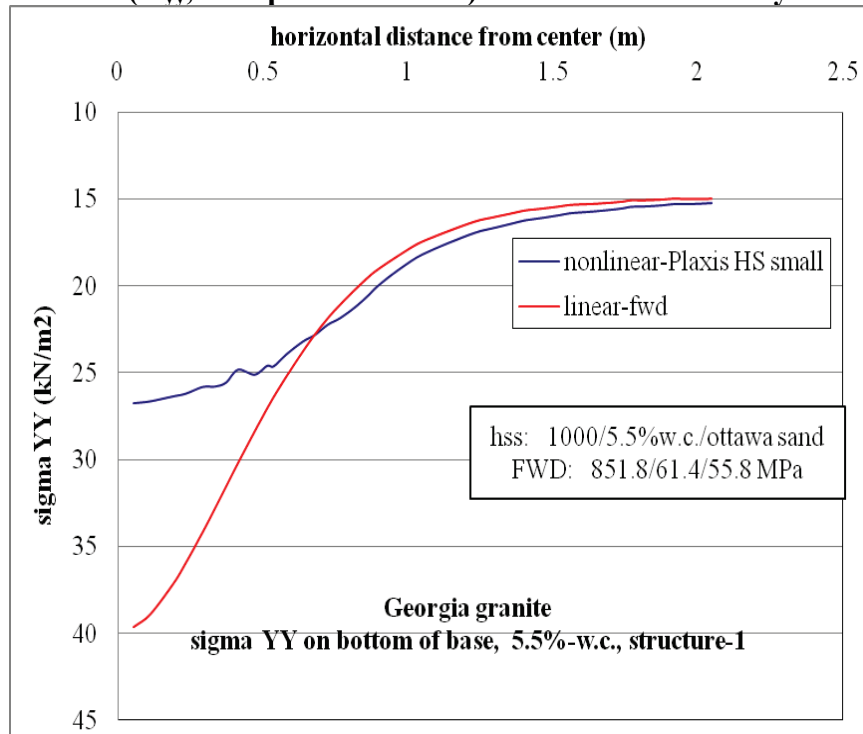

Figure D-46. ε_{yy} at top of base layer comparison for nonlinear and linear cases, for Structure-1 with 5.5% w.c. base layer and nonlinear Ottawa sand subgrade.
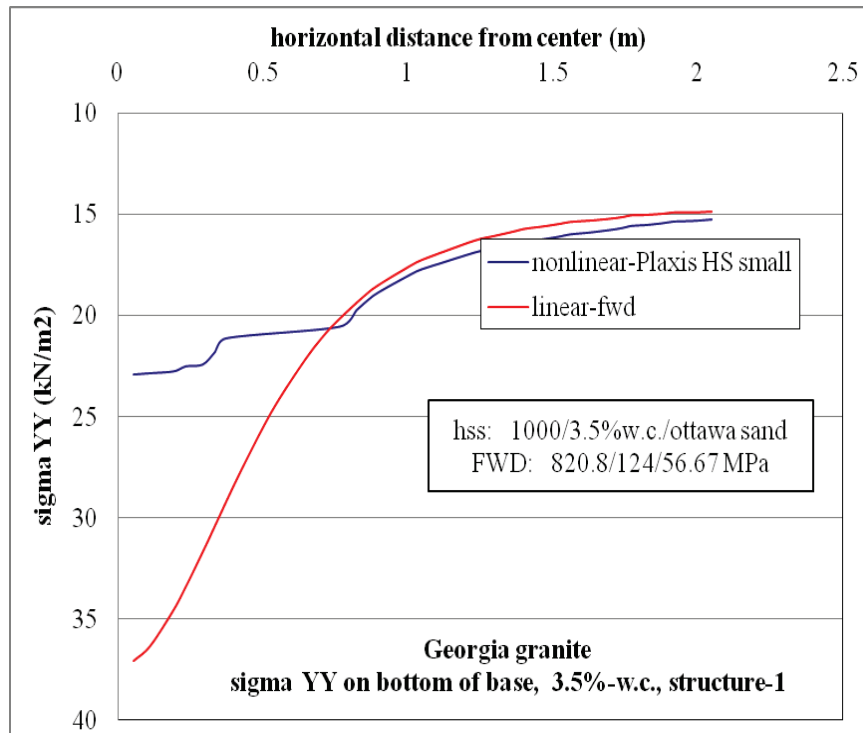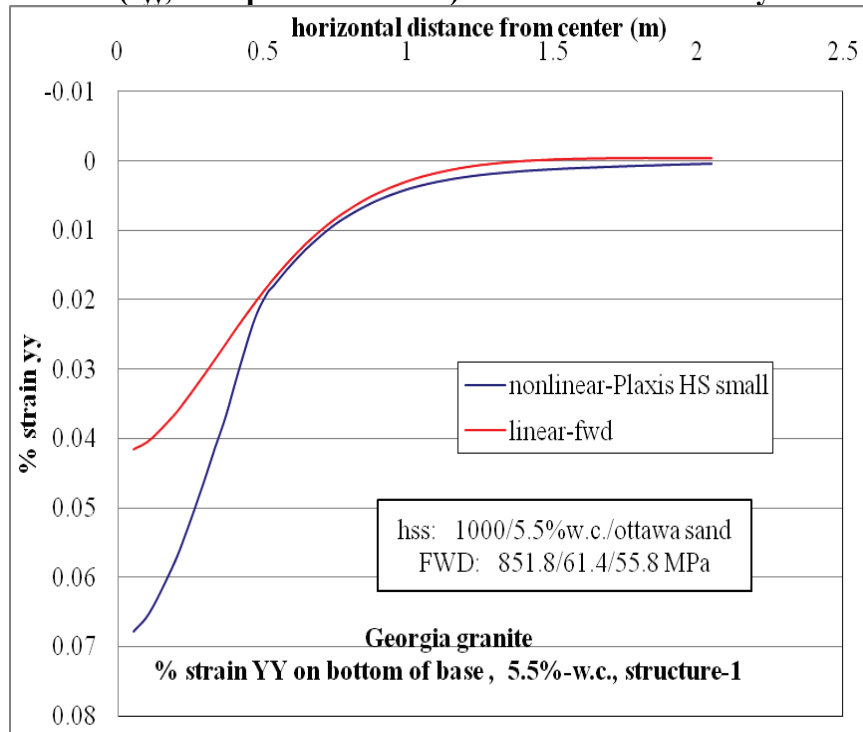

Figure D-47. ε_{yy} at top of base layer comparison for nonlinear and linear cases, for Structure-1 with 3.5% w.c. base layer and nonlinear Ottawa sand subgrade.

D.2.8　Vertical Stress (σ_{yy}, Compressive Stress) at Bottom of Base Layer

Figure D-48. σ_{yy} at bottom of base layer comparison for nonlinear and linear cases, for Structure-1 with 5.5% w.c. base layer and nonlinear Ottawa sand subgrade.

Figure D-49. σ_{yy} at bottom of base layer comparison for nonlinear and linear cases, for Structure-1 with 3.5% w.c. base layer and nonlinear Ottawa sand subgrade.
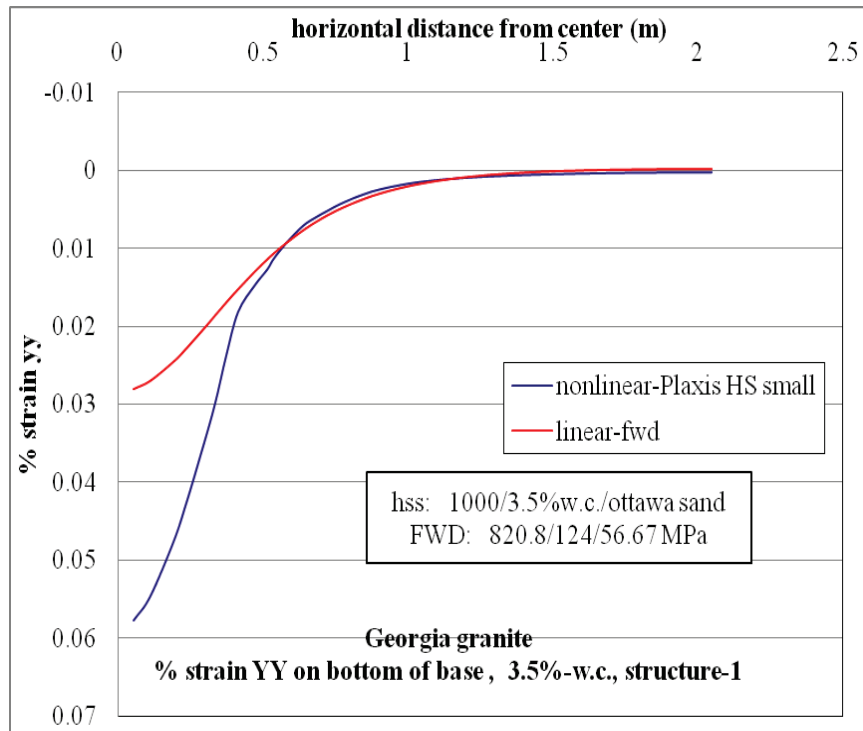
D.2.9 Vertical strain (ε_{yy}, Compressive Strain) at Bottom of Base Layer

Figure D-50. ε_{yy} at bottom of base layer comparison for nonlinear and linear cases, for Structure-1 with 5.5% w.c. base layer and nonlinear Ottawa sand subgrade.

Figure D-51. ε_{yy} at bottom of base layer comparison for nonlinear and linear cases, for Structure-1 with 3.5% w.c. base layer and nonlinear Ottawa sand subgrade.

D.2.10 Vertical Stress (σ_{yy}, Compressive Stress) at Top of Subgrade Layer
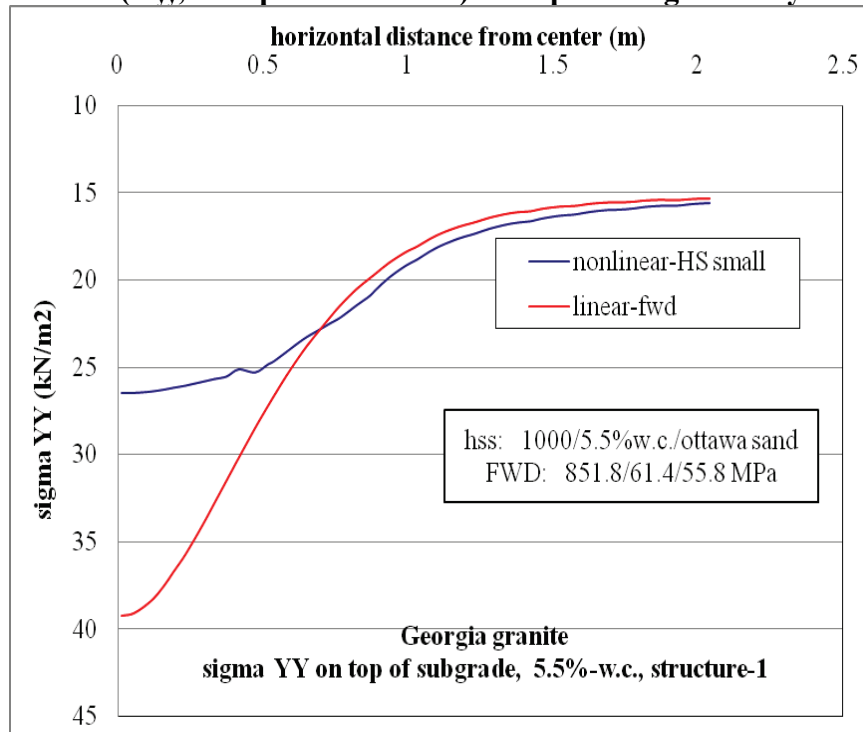

Figure D-52. σ_{yy} at top of subgrade comparison for nonlinear and linear cases, for Structure-1 with 5.5% w.c. base layer and nonlinear Ottawa sand subgrade.
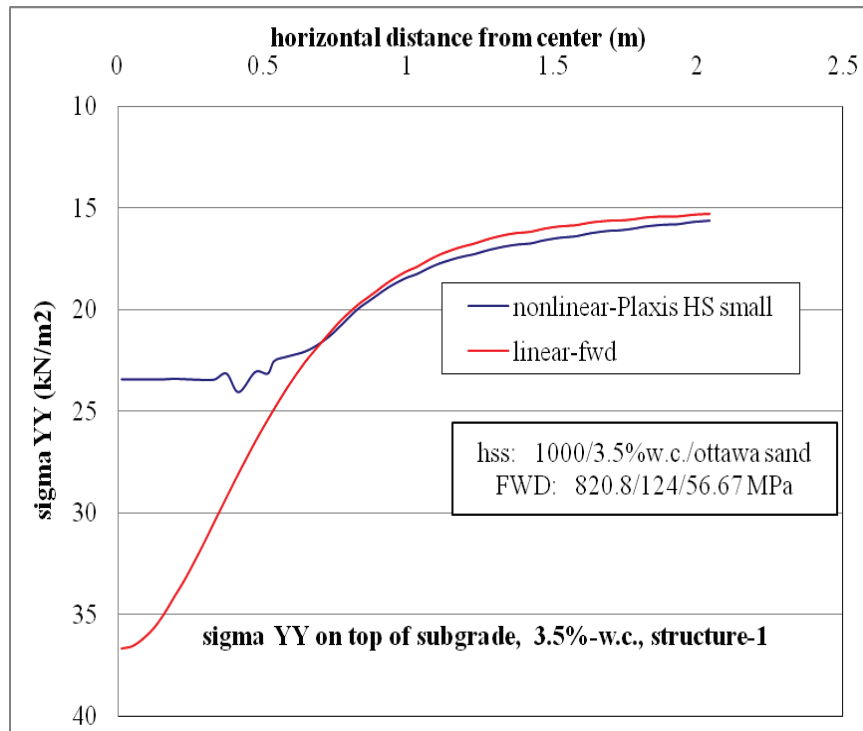

Figure D-53. σ_{yy} at top of subgrade comparison for nonlinear and linear cases, for Structure-1 with 3.5% w.c. base layer and nonlinear Ottawa sand subgrade.

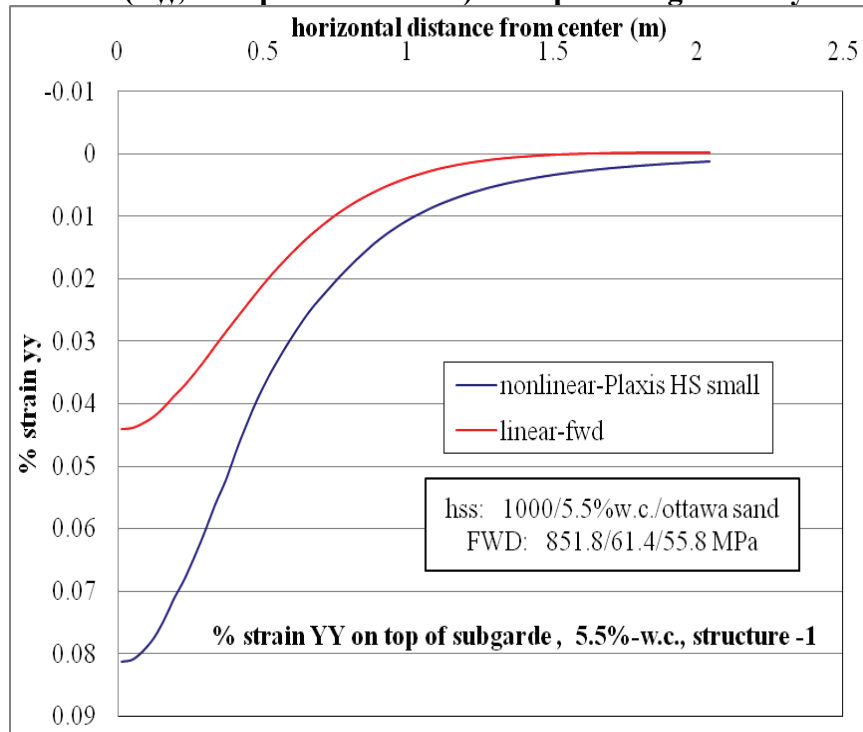**D.2.11 Vertical Strain (ε_{yy}, Compressive Strain) at Top of Subgrade Layer**

Figure D-54. ε_{yy} at top of subgrade layer comparison for nonlinear and linear cases for Structure-1 with 5.5% w.c. base layer and nonlinear Ottawa sand subgrade.
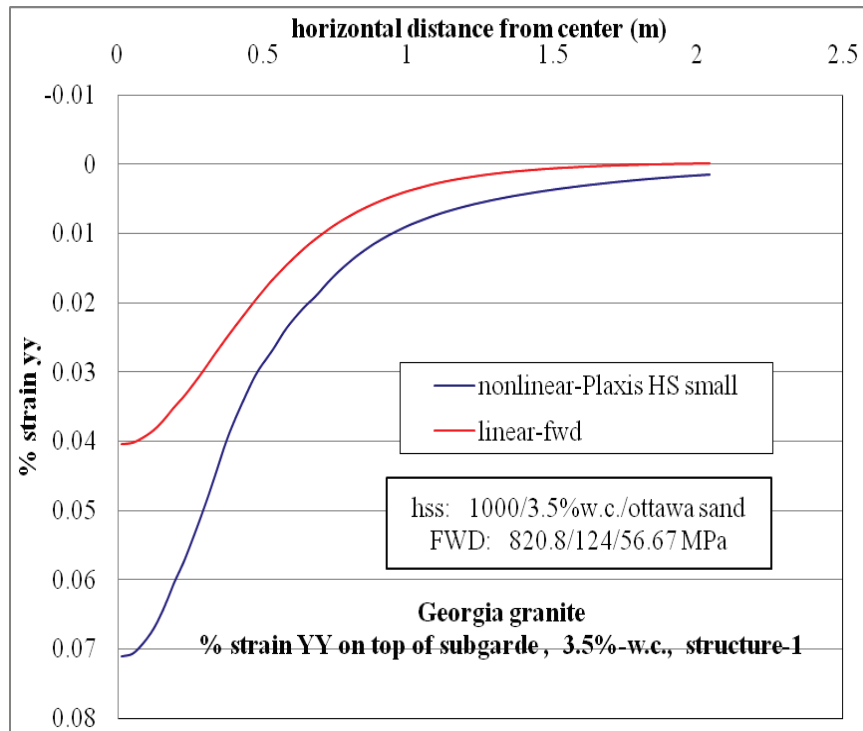

Figure D-55. ε_{yy} at top of subgrade layer comparison for nonlinear and linear cases for Structure-1 with 3.5% w.c. base layer and nonlinear Ottawa sand subgrade.